DOT/FAA/TC-18/1

Federal Aviation Administration
William J. Hughes Technical Center
Aviation Research Division
Atlantic City International Airport
New Jersey 08405

An Assessment of Cloud Total Water Content and Particle Size from Flight Test Campaign Measurements in High Ice Water Content, Mixed Phase/Ice Crystal Icing Conditions: Primary In-Situ Measurements

June 2020

Version 3

U.S. Department of Transportation
Federal Aviation Administration

NOTICE

This report is available at the Federal Aviation Administration William J. Hughes Technical Center’s Full-Text Technical Reports page: actlibrary.tc.faa.gov in Adobe Acrobat portable document format (PDF).

Technical Report Documentation Page

1. Report No.	2. Government Accession No.	3. Recipient's Catalog No.
DOT/FAA/TC-18/1		

4. Title and Subtitle	5. Report Date
An Assessment of Cloud Total Water Content and Particle Size from Flight Test Campaign Measurements in High Ice Water Content, Mixed Phase/Ice Crystal Icing Conditions: Primary In-Situ Measurements	June 2020
	6. Performing Organization Code

7. Author(s)	8. Performing Organization Report No.
Strapp, J.W., Schwarzenboeck, A. , Bedka, K. , Bond, T. , Calmels, A. , Delanoë, J. , Dezitter, F. , Grzych, M. , Harrah, S. , Korolev, A. , Leroy, D. , Lilie, L. , Mason, J. , Potts, R. , Protat, A. , Ratvasky, T. , Riley, J. , and Wolde, M.	

9. Performing Organization Name and Address	10. Work Unit No. (TRAIS)
Met Analytics Inc. 88 Whispering Pine Trail Aurora, ON, Canada L4G4Y1	11. Contract or Grant No.

12. Sponsoring Agency Name and Address	13. Type of Report and Period Covered
U.S. Department of Transportation Federal Aviation Administration William J. Hughes Technical Center Aviation Research Division ****BRANCH**** Atlantic City International Airport, NJ 08405	Project Science and Technical Plan
	14. Sponsoring Agency Code

15. Supplementary Notes

The Federal Aviation Administration Aviation Research Division COR was James Riley.

16. Abstract

The Federal Aviation Administration and the European Aviation Safety Agency (EASA) issued new certification requirements for flight in mixed-phase and glaciated cloud conditions in 2014 and 2015. The atmospheric conditions are described in the Title 14 Code of Federal Regulations Part 33 Appendix D mixed-phase/glaciated environmental envelopes, with identical Appendix P envelopes in the corresponding EASA CS-25 regulations. The environmental envelopes are hereinafter referred to as Appendix D/P.

The envelopes were developed by an international government/industry working group using a database of conditions during which ice-crystal icing engine events occurred. The working group concluded that the events were driven by high concentrations of ice particles in the atmosphere, not requiring the presence of supercooled liquid water. For estimation of total water content, only a data set collected in the 1950s was available, and information on particle size and mixed-phase levels was very meager. The FAA and EASA implemented the rules, but recommended a later assessment with new atmospheric data using modern instrumentation and data collection techniques.

This report summarizes and analyzes results from an international effort to collect data to assess the Appendix D/P environmental envelopes. The European High Altitude Ice Crystals (HAIC) and North American High Ice Water Content (HIWC) projects combined efforts to collect airborne in-situ and remote sensing data from deep convective clouds. Collaborative HAIC-HIWC flight campaigns were performed using the French Falcon-20 out of Darwin, Australia in 2014 and Cayenne, French Guiana in 2015. The HIWC-RADAR flight campaign out of Florida in 2015, using the NASA DC-8 research aircraft, contributed additional data for the assessment of Appendix D/P.

The flight campaigns collected a unique, modern, and high-quality data set describing the microphysical properties of deep convective clouds. This report compares the flight campaign data to Appendix D/P, and documents differences for consideration by regulators and industry.

17. Key Words	18. Distribution Statement
Ice crystal icing, jet-engine icing, Appendix D, NPRM 10-10	This document is available to the U.S. public through the National Technical Information Service (NTIS), Springfield, Virginia 22161. This document is also available from the Federal Aviation Administration William J. Hughes Technical Center at actlibrary.tc.faa.gov.

19. Security Classif. (of this report)	20. Security Classif. (of this page)	21. No. of Pages	22. Price
Unclassified	Unclassified		

ACKNOWLEDGEMENTS

The activities of Science Engineering Associates and Met Analytics Inc. were supported by The Federal Aviation Administration William Hughes Technical Center, contracts DTFACT-14-C-00003 and DTFACT-15-C-00011, and the NASA Glenn Research Center. Major North American funding for flight campaigns and associated research was provided by the FAA William Hughes Technical Center and Aviation Weather Research Program, the NASA Aeronautics Research Mission Directorate Aviation Safety Program, the Boeing Co., Environment Canada, the National Research Council of Canada, and Transport Canada. Major European campaign and research funding was provided from the European Commission Seventh Framework Program in research, technological development, and demonstration under grant agreement n°ACP2-GA-2012-314314, and from the European Aviation Safety Agency (EASA) Research Program under service contract n° EASA.2013.FC27. Further funding was provided by the Ice Crystal Consortium.

The authors wish to thank the following for additional project management support: Tom Bond, Jim Riley, and Chris Dumont, Federal Aviation Administration; Ron Colantonio, NASA Aerosciences Evaluation & Test Capabilities Project Manager; Fabien Dezitter, Airbus Ind; Peter May, Rod Potts, Australian Bureau of Meteorology; and Jeanne Mason, the Boeing Company.

Operational support for the research aircraft is acknowledged, as follows. For the Falcon-20, primary support was provided by the Service des Avions Français Instrumentés Pour la Recherche en Environnement (SAFIRE) facility for the scientific airborne operations. SAFIRE (http://www.safire.fr), is a joint facility of CNRS, Météo-France and CNES. For the Convair-580, primary support was provided by the National Research Council of Canada Institute for Aerospace Research, and the Environment and Climate Change Canada Cloud Physics Research Division. For the NASA DC-8, primary support was provided by the NASA Armstrong DC-8 crew, including Tim Moes, NASA DC-8 project manager. Additional aircraft operational support was provided by Airbus SAS Operations, and Kurt Blankenship, NASA Glenn icing research pilot. Primary instrument support was provided by the SAFIRE technical team, Science Engineering Associates, Ed Emery, the NASA Glenn icing instrumentation lead, ECCC, National Research Council of Canada, the Université Blaise Pascal Laboratoire de Météorologie Physique, Laboratoire Atmosphères, Milieux, Observations Spatiales, and Airbus Ind.

Other operational support during flight campaigns was provided by the Australian Bureau of Meteorology (local facilities in Darwin, dedicated and Northern Territories Weather Office forecasters), Meteo France, the NASA Langley Cloud and Radiation Research Group (nowcasting and real-time and archive of satellite products), the National Center for Atmospheric Research (nowcasting and data archiving), the NASA Langley Electromagnetic Sensors Branch (nowcasting and campaign planning), and the Boeing Company, ATMOSPHERE, Coriolis Weather, and Leading Edge Atmospherics (dedicated real-time forecasting).

During the projects, important scientific advice and support was generally provided by those already listed above, and also by participating members of the HAIC-HIWC Science team, including Ed Zipser and Adam Varble of the U. Utah, Greg McFarquhar of the U. Illinois, Pat Minnis, and Chris Yost of the representatives of the NASA Langley Cloud and Radiation Research Group, Peter May of the Australian Bureau of Meteorology, Andy Ackerman and Ann Fridlind of

the NASA Goddard Institute of Space Studies, Meteo France, Biagio Esposito of the Centro Italiano Ricerche Aerospaziali, and Patrick King of Coriolis Weather.

The Japan Meteorological Agency is specially thanked for providing rapid-scan visible and infrared Multifunctional Transport Satellites-1R satellite data during the Darwin campaign. Data from the Global Position and Tracking Systems Pty. Ltd. lightning network was provided by the Australian Bureau of Meteorology for research associated with the HIWC Study.

TABLE OF CONTENTS

LIST OF FIGURES

LIST OF TABLES

ACRONYMNS AND DEFINITIONS

2D-S	Two-Dimensional Stereo Optical Array Spectrometer (Stratton Park Engineering Co.)
AIMMS-20	Aircraft Integrated Meteorological Measurements System (Aventech)
ARAC	Aviation Rulemaking Advisory Committee
BWV	Background water vapor
CDP-2	Cloud Droplet Probe (Droplet Measurement Technologies)
CCN	Cloud condensation nuclei
D	Diameter, Or Size (Particle)
D_{eq}	Area Equivalent Diameter (Particle)
D_{max}	Maximum Diameter Or Size (Particle)
df	Distance Factor
DMT	Droplet Measurement Technologies
DOF	Depth of field
EASA	European Aviation Safety Agency
EHWG	Engine Harmonization Working Group
EIWG	Engine Icing Working Group
ELO	Equilibrium Level Overshoot
ECCC	Environment And Climate Change Canada
FSSP	Forward Scattering Spectrometer Probe
GPATS	Global Position And Tracking Systems
HAIC	High Altitude Ice Crystals (Project)
HIWC	High Ice Water Content
HSI	High Speed Imager
ICT	Ice capture tube
IKP-1	Isokinetic Evaporator Probe (Prototype)
IKP-2	Isokinetic Evaporator Probe (Flight Campaigns)
IR	Infrared
IRT	Icing Research Tunnel (Nasa Glenn)
ISA	International standard atmosphere
IWC	Ice Water Content
LaMP	Laboratoire De Météorologie Physique
LWC	Liquid water content
MCS	Mesoscale Convective System
MSD	Mass size distribution (Particle)
MMD	Median mass diameter
MTSAT	Multifunctional Transport Satellites (Japan)
NRC	National Research Council (Canada)
OAP	Optical Array Probe
PIP	Precipitation Imaging Probe (Droplet Measurement Technologies)
PW	Precipitable Water
PSD	Particle Size Distribution
RATFac	Research Altitude Test Facility
RAE	Royal Aircraft Establishment
SAFIRE	Service Des Avions Français Instrumentés Pour La Recherche En Environnement
SAT	Static air temperature

SEA	Science Engineering Associates
SLD	Supercooled Large Droplets
SPEC	Stratton Park Engineering Co.
TAT	Total Air Temperature
T_{eff}	Cloud top satellite infrared effective temperature
TRMM	Tropical Rainfall Measurement Mission
TWC	Total Water Content
TWC_{99}	99th Percentile TWC
TWC_n	Nth Percentile TWC

EXECUTIVE SUMMARY

This report summarizes results from an international effort to collect in-situ cloud data to assess the new Federal Aviation Administration Title 14 Code of Federal Regulations Part 33 Appendix D mixed-phase/glaciated environmental envelope, and the corresponding identical European Aviation Safety Agency Appendix P envelope (hereinafter "Appendix D/P"). Appendix D/P consists of a temperature-altitude envelope, a 99th percentile total water content (TWC_{99}) envelope at the 17.4 Nm distance scale, a distance factor to estimate TWC_{99} values at other distance scales, ice crystal characteristic size, and recommended liquid water content (LWC) levels in mixed-phase icing conditions. The effort was initiated in 2004, when the Engine Harmonization Working Group (EHWG) recognized that the primary issue related to flight in mixed-phase/glaciated conditions at the time was jet-engine power loss due to suspected ice-crystal icing, which has since been shown to occur in high mass concentrations of ice crystals, and without the requirement of supercooled liquid water in the atmosphere. The EHWG efforts also have led to improved understanding that air data probe measurement errors also occur in such conditions. The EHWG established a Technical Plan recommending, among other things, improvement of cloud measurement instrumentation, and a flight campaign to make in-situ measurements up to current cruise altitudes and cloud types that caused engine power-loss events. The High Ice Water Content (HIWC) study was started in North America in 2006, initially concentrating on instrument development and the outfitting of a flight campaign aircraft. In 2012, the European High Altitude Ice Crystal (HAIC) project and HIWC collaborated to perform the first HAIC-HIWC flight campaign in 2014 in Darwin, Australia using the French Falcon-20 cloud research aircraft. A second HAIC-HIWC flight campaign was conducted in May 2015 in Cayenne, French Guiana to collect additional data, where the Falcon-20 was joined by a Canadian Convair-580 aircraft, also equipped for cloud in-situ measurements. A third campaign, the NASA/FAA HIWC-RADAR campaign, was conducted by HIWC in August 2015 out of Fort Lauderdale, Florida with a NASA DC-8 aircraft. The flight campaigns were conducted by scientists and engineers from the international atmospheric science and aviation community highly experienced in making airborne cloud measurements.

Instrumentation efforts for improvement of total water content (TWC) and particle size distribution (PSD) measurements were significant. Due to the lack of a reliable instrument with defensible accuracy, a new bulk TWC instrument was developed specifically for the high ice water content (IWC) environment. In addition, extensive modifications were made to particle-measuring probes to improve performance and reduce artifacts. Calibration and performance testing in wind tunnels was extensive. Cloud remote-sensing instrumentation provided spatial context to the in-situ measurements and the potential for additional TWC measurements. The instruments performed well in the flight campaigns, providing a unique data set for Appendix D/P assessment and scientific research.

The flight campaign specifications were determined in consultation with the EHWG and its successor the Engine Icing Working Group in meetings between 2006 and 2015, and were driven by meteorological studies of engine-event clouds by industry. The project targeted tropical Mesoscale Convective Systems (MCSs) with a characteristic diameter of 100 Nm or larger, ideally with cloud tops reaching the tropopause or level of convective equilibrium. Active convective cells were directly sampled in the more benign systems, and from a safe distance in the more vigorous systems. In all, about 92% of the in-cloud data were collected in such tropical MCS, including six flights in tropical storms.

Cloud TWC was dominated by ice crystals. Although identification of mixed phase was challenging, it was estimated that at -10 C, the spatial fraction of mixed-phase zones with LWC greater than 0.1 gm^{-3} was only about 5%, with LWC never exceeding about 0.25 gm^{-3}. The width of such zones was usually less than a few nautical miles. The spatial fraction decreased with decreasing temperature as expected. There were no mixed-phase zones colder than -35 C. These observations are well below the guideline maximum LWC exposures provided in Appendix D/P (e.g., 0 to -20 C range, LWC $\leq$ 1.0 gm^{-3} for a cloud length of $\leq$ 50 Nm). However, it is important to note that the flight campaign clouds, representative of engine-event clouds, had tops typically colder than -60 C with high ice concentrations that could mix to lower altitudes and grow at the expense of the liquid content of any embedded updraft. Shallower clouds may well contain more significant mixed-phase regions. One also would expect higher LWC concentrations in convective core regions at low altitudes, which commercial aircraft would typically avoid due to flight radar red echo.

TWC values were averaged over 13 distance scales from 0.5 Nm to 100 Nm, including the 17.4 Nm reference distance scale of Appendix D/P. The maximum TWCs at the 0.5 and 50 Nm scales were 4.1 gm^{-3} and 2.4 gm^{-3}, respectively. For comparison to Appendix D/P, the data were also analyzed to provide TWC_{99} values for all distance scales with at least 100 data points. TWC_{99} at the 17.4 Nm reference distance ($TWC_{99}(17.4)$) was found to increase with temperature, from 1.84 gm^{-3} at -50 C to 2.66 gm^{-3} at -10 C. The ratios of observed $TWC_{99}(17.4)$ to Appendix D/P values were fairly constant with temperature, varying from about 0.49 to 0.58 (average 0.56), providing some support for the adiabatic TWC calculations that are the basis for the Appendix D/P envelope. Appendix D/P TWCs are based on simple adiabatic calculations for deep lift, scaled by a factor of 0.65 to match the $TWC_{99}(17.4)$ values of an industry data set collected in the 1950s. If the same approach had been taken using the data set of this report, the calculated scale factor would have been about 0.36 rather than 0.65. TWC_{99} values were found to decrease with increasing distance scale in a manner similar to the Appendix D/P distance factor. However, below the 4.5 Nm minimum Appendix D/P distance scale, the extrapolated Appendix D/P distance factor overestimated the observed TWC_{99} values by as much as 25% at 0.5 Nm. A new polynomial distance factor was provided in this report for consideration.

The characteristic size of particles provided in Appendix D/P was based on best estimates available at the time, but instrumentation was not optimum for this purpose and possibly subject to bias. For this data set, a much larger body of PSD data were collected, using modern instrumentation and processing techniques commonly used and accepted in the atmospheric research community. The sizes of cloud ice particles were found to span from sub-50 microns to larger than 5 mm. The images of particles were generally irregular in shape, likely composed of individual and aggregates particles, with varying degrees of riming. Heavily rimed particles such as graupel were rarely observed, and hail was never encountered. The data were analyzed to characterize the mass distributions of high IWC regions with TWC greater than or equal to 1 gm^{-3}. Less than 10% of the mass was found at sizes smaller than 100 µm. median mass diameter (MMD) was found to increase with temperature from about 320 µm at -50 C to 690 µm at -10 C. Although higher than those specified in Appendix D/P, MMDs are still relatively low, particularly in the -30 to -50 C range, as had been suspected at the outset of the flight campaigns.

A number of inter-location and inter-aircraft data set differences are discussed in the report, including the uneven distribution of temperature-interval data between the three locations,

differences in the sizes and depths of clouds, and possible differences in the way the clouds were sampled by the different aircraft. The HAIC-HIWC Science team also discussed the representativeness of the data set in defining aviation global exposure to high IWC, and identified three factors for consideration. First, although it was known that oceanic convection would be most intense in the early morning hours, for reasons of flight safety (HAIC-HIWC) and operational convenience (HIWC-RADAR), the data were collected only in daytime hours. An analysis of Darwin satellite imagery suggested that the flights were performed on the average about 2.6 hours after the suspected optimum sampling time for TWC. The implications to the data set maximum short-distance-scale TWC values are not clear. However, it does seem likely that high TWC would have been sustained over longer distance scales if sampled earlier. Second, the three flight campaigns were conducted in relatively unpolluted environments, especially the Darwin and Cayenne campaigns. A speculative argument presented in this report indicates that clouds forming in polluted atmospheres such as those found near continental southeast Asia may favor higher TWCs at high altitude. Third, the HAIC-HIWC Science team noted that there are no measurements from large vigorous continental storms in the data set. Such storms represent some of the most intense convection observed on earth. Although only 7% of engine events were associated with such storms in a 2011 study, a more recent 2015 study reveals that the percentage may be rising. Further investigation of these events may be warranted.

The HAIC-HIWC and HIWC-RADAR campaigns provided a high-quality and unique data set of the in-situ properties of deep convective clouds at common commercial aircraft flight levels, for which there is no current equivalent from the aviation industry or the atmospheric science community. The data set is from 45 flight missions in three flight campaigns, with 472 runs in approximately 115 clouds, providing about 29,600 Nm of in-cloud data in deep convection over four targeted temperature intervals: -10, -30, -40, and -50 ± 5 C. This compares with about 3500 Nm of cloud data used to develop the FAR Part 25 Appendix C envelope. The measurements span altitudes from about 17,000’ to 39,000’. In addition to the primary in-situ cloud measurements, the Darwin and Cayenne data also include measurements from research cloud radars that may extend TWC statistics once remote TWC estimates are fully assessed. The flight campaigns sampled mostly large tropical MCS clouds, from three specific geographical locations separated by a large distance, and are subject to the qualifications noted above while limited by the technical challenges and practical constraints of making such measurements The authors responsible for the FAR Part 25 Appendix C envelope similarly noted that their “results are only applicable to the United States,” but “should provide a framework for placing the data on a statistical basis that is not limited in scope to the United States.” As recommended by those authors for Appendix C, it would be prudent to review the results of this report if and when future data sets become available, and as commercial aircraft experience accumulates.

1. INTRODUCTION

The HAIC-HIWC international field campaigns are the result of an international collaboration conducted between the High Altitude Ice Crystals (HAIC) and High Ice Water Content (HIWC) projects. The purpose of the campaigns was to collect in-situ and remotely sensed data of deep convective clouds to fulfill industry objectives focused on the characterization and improved understanding of the high altitude and high concentration ice crystal environment, and to explore a variety of supporting scientific objectives detailed in the HIWC Science Plan [1] and the HAIC Description of Work [2]. In addition to this report, HAIC for the European Aviation Safety Agency (EASA) [3-6] prepared separate reports on the flight campaign measurements. This report and the EASA reports were created almost concurrently, with some differences in content and focus due to particular agency interests, though with the intent of providing consistent results. The reports contain some shared results, figures, tables, and sections of text.

This report summarizes work performed by an international group over the last decade to collect and analyze a modern in-situ cloud dataset for the assessment of Federal Aviation Administration (FAA) Title 14 Code of Federal Regulations Part 33 Appendix D [7], and the identical EASA Appendix P [8] (hereinafter "Appendix D/P"), a new ice crystal icing envelope that became law with the FAA and EASA in November 2014 and March 2015, respectively. The work was initiated within the Engine Harmonization Work Group (EHWG) in 2004, and has continued since 2009 within the Engine Icing Working Group (EIWG). The study addresses the characterization of total water content (TWC) and ice particle size in deep convective clouds that have caused over the last three decades in excess of 160 jet-engine power-loss events, and more recently, air-data probe malfunctions. The North American HIWC Study was initiated by the FAA, the National Aeronautics and Space Administration (NASA), and partners in 2006 to modify in-situ instrumentation for the high ice water content (IWC) environment, and design and execute a flight campaign to collect in-situ data in suitable clouds. In 2012, the HIWC Study partnered with the European HAIC Project to perform two flight campaigns in 2014 and 2015 to collect in-situ data in deep convective clouds for the Appendix D/P assessment. In 2015, the NASA/FAA HIWC-RADAR flight campaign provided additional data in similar clouds. This report is a culmination of these international efforts, with contributions from multiple partners. The report contains the primary information on the in-situ TWC and particle size measurements. Additional information and analyses unavailable at the time of delivery of this report may follow in future reports.

1.1 PURPOSE

In 2006, the EHWG recommended flight test measurements to help assess the new proposed regulatory Appendix D/P envelope developed for the high altitude, high concentration ice crystal environment. The total water content (TWC) envelope of Appendix D/P was based on theoretical calculations of estimated maximum TWC scaled to the only extensive in-situ TWC data set available at the time. Furthermore, little was known about the sizes of ice particles in the Appendix D/P environment. Three dedicated flight campaigns were specifically designed and executed to collect data in deep tropical clouds, similar to those in which engine events have been observed. New instrumentation was developed specifically for the high IWC environment. The most modern and accurate in-situ airborne cloud instrumentation available to date was employed. The data from the three campaigns are combined in this report and compared to Appendix D/P values, in order

to provide the FAA, EASA, other regulators, and industry, validated data with which to assess the Appendix D/P envelope.

1.2 BACKGROUND

1.2.1 A Brief History of Ice Crystal Icing in Aviation

This report focuses on an aircraft icing issue resulting from exposure to ice crystals in the atmosphere, one that does not require the presence of atmospheric, supercooled liquid water. Ice accretion results from interaction between ice crystals and a hot environment, the physics of which is the subject of continuing research and is not yet fully understood. The phenomenon has been commonly termed "ice crystal icing." Ice crystal icing was first recognized in the 1950s, when the Bristol Britannia aircraft Proteus engines experienced engine failures that were eventually linked to ice formation in a warm engine air inlet duct with a reverse flow. Bristol attributed the ice accretion to the melting of ice particles on the duct walls, leading to a liquid film into which ice crystals coalesced and formed pieces of solid ice that subsequently shed into the compressor. An extensive effort was launched to solve not only the engine problem, but also to investigate the cloud conditions in which the events occurred. New airborne cloud measuring instrumentation was developed and flown in a series of cloud measurement campaigns by the Royal Aircraft Establishment (RAE) and the UK Met Office in Darwin, Entebbe, and Singapore between 1956 and 1958 [9]. The flights targeted the Inter Tropical Convergence Zone, where deep convective clouds were frequent and abundant. From these measurements, researchers at the time noted that a new form of icing had been discovered, in conditions with total water contents much higher than observed for conventional supercooled cloud icing (and that today we know are higher than Code of Federal Regulations (CFR) Part 25, Appendix C [10]), and over much larger distance scales. The authors of this report could find little further record of ice crystal icing until the 1990s. A 1998 FAA review of mixed-phase icing conditions (coexisting supercooled liquid water and ice crystals) concluded that such conditions were frequent and widespread, but there was no evidence that performance effects due to structural icing on aircraft were enhanced in mixed-phase conditions relative to pure supercooled liquid conditions [11]. The review did note technical reports from the 1960s related to engine icing in mixed-phase and glaciated conditions, a reference to the Bristol Britannia experiences noted above. It also noted warnings that thermal anti-icing systems on aircraft surfaces might be overtaxed by the increased heat needed first to melt the ice crystals and then to warm and evaporate the water, possibly resulting in runback beyond the protected area. However, it was clear that ice crystal icing was not at this time seen as a major emerging issue. Around the same time as this report, a commuter-class aircraft experienced in excess of ten engine rollback events near deep convective clouds [12]. The events included simultaneous power loss in multiple engines, and loss of altitude before return to normal operation. The FAA issued a series of related airworthiness directives limiting the flight envelope and requiring changes to the aircraft engine [13-17]. Flight test measurements including in-situ cloud measurements were performed in 1997, and during one flight while orbiting in a thunderstorm anvil, ice accretion on the second stage stator in the low-pressure compressor created a flow blockage resulting in an engine rollback [18]. The engine manufacturer and airframer successfully instituted remedial changes and demonstrated the efficacy of a modified engine in the flight test previously noted. During the flight test rollback event, measurements indicated that the cloud was composed of high ice water content with little or no supercooled LWC. This was the first modern evidence that engine icing could result primarily from ice crystals, although the presences of small amounts of supercooled liquid

cloud could not be discounted. In later observations of engine events on other aircraft, the requirement for atmospheric supercooled liquid water was discounted when engine events were documented at temperatures colder than -40 C [18], where supercooled liquid water cannot exist.

The recognition that ice crystal icing in engines was an industry-wide problem, and the development of the environmental envelope for ice crystal conditions, actually resulted from the industry's response to the 1994 Roselawn Indiana Avions de transport régional ATR-72 accident [19,20]. After the Roselawn accident, which was ultimately attributed to flight in supercooled large drop (SLD) conditions outside the CFR Part 25 Appendix C icing envelope, the Ice Protection Harmonization Working Group (IPHWG), an Aviation Rulemaking Advisory Committee (ARAC) was created to address NTSB recommendations to "expand the Appendix C icing certification envelope to include freezing drizzle/freezing rain and mixed water/ice crystal conditions, as necessary" [21]. In response, the joint Engine Harmonization and Power Plant Installation Working Groups (EHWG/PPIHWG – hereinafter the EHWG) examined the impact of SLD and mixed phase/glaciated conditions on Part 33 and Part 25 (the certification rules for engines and power plant installations, respectively). The first task of the IPHWG was to review and classify an extensive database of in-service events encompassing all types of in-flight icing conditions. A summary of the technical discussions of the EHWG is given in [22]. During these discussions, it became evident that engine power loss in suspected mixed-phase and/or glaciated conditions was at the time the dominant engine icing issue. The EHWG examined the history of over 100 engine and power plant-related events thought to be due to weather, where engine damage, compressor stall, power loss or roll-back had occurred. The vast majority of events occurred during conditions suspected to be dominated by ice particles rather than conventional supercooled LWC or SLD. Engine power loss in ice crystal conditions was now recognized to be not just a problem in one commuter-class aircraft, but rather an industry-wide problem. Most of the events occurred in conditions outside the Federal Aviation Regulations (FAR) Part 25 Appendix C temperature-altitude envelope, generally between the lines defining a standard atmosphere and a Military Standard 210 hot day [23]. Since the initial report of the EHWG[1], engine events have continued to occur. Figure 1 shows the most recent depiction of the geographical location of 162 Boeing engine events [24], in which different colors indicate different engines, and large red asterisks that indicate the locations of the three flight campaigns. Events cluster in specific geographical regions, likely due to a complicated combination of a high frequency of suitable clouds, a high density of air traffic, and perhaps a reduced flexibility in making weather-related course changes. In addition to engine events, it is now recognized that ice crystal icing is responsible for measurement errors in air data probes (e.g., pitot probes, total air temperature probes) in cloud conditions that are similar or the same as those that cause engine events [25]. Qualification standards for pitot and pitot-static probes have recently been upgraded based on new understanding on the icing environment, including ice crystal icing [26].

In 2006, the EHWG developed a Technical Plan to advance understanding of ice crystal icing, and developed the new interim ice crystal environmental envelope "Appendix D" [27], that is described in section 1.2.3. In response to this Technical Plan, the High Ice Water Content (HIWC) [1] Study was initiated in 2006 to collect in-situ data in clouds similar to those that cause engine events in order to assess the proposed envelope. In 2010 and 2012, the first contemporary

[1] After fulfilling its Aviation Rulemaking Advisory Committee (ARAC) mandate, the EHWG continued to work on mixed-phase issues, now as the Engine Icing Working Group (EIWG).

exploratory in-situ measurements were made in deep convective clouds by Airbus Ind. [28], confirming many of the hypotheses that had been developed by the EHWG. In 2012, the North American-led HIWC study partnered with the European HAIC project [2], with joint objectives to collect in-situ flight measurements for science and regulatory objectives. The following section examines information gathered from the engine event database to identify the types of clouds that cause engine events, and reviews the hypothesis on what cloud conditions are conducive to such events. This is a necessary first step toward understanding the basis of the Appendix D/P interim icing envelope.

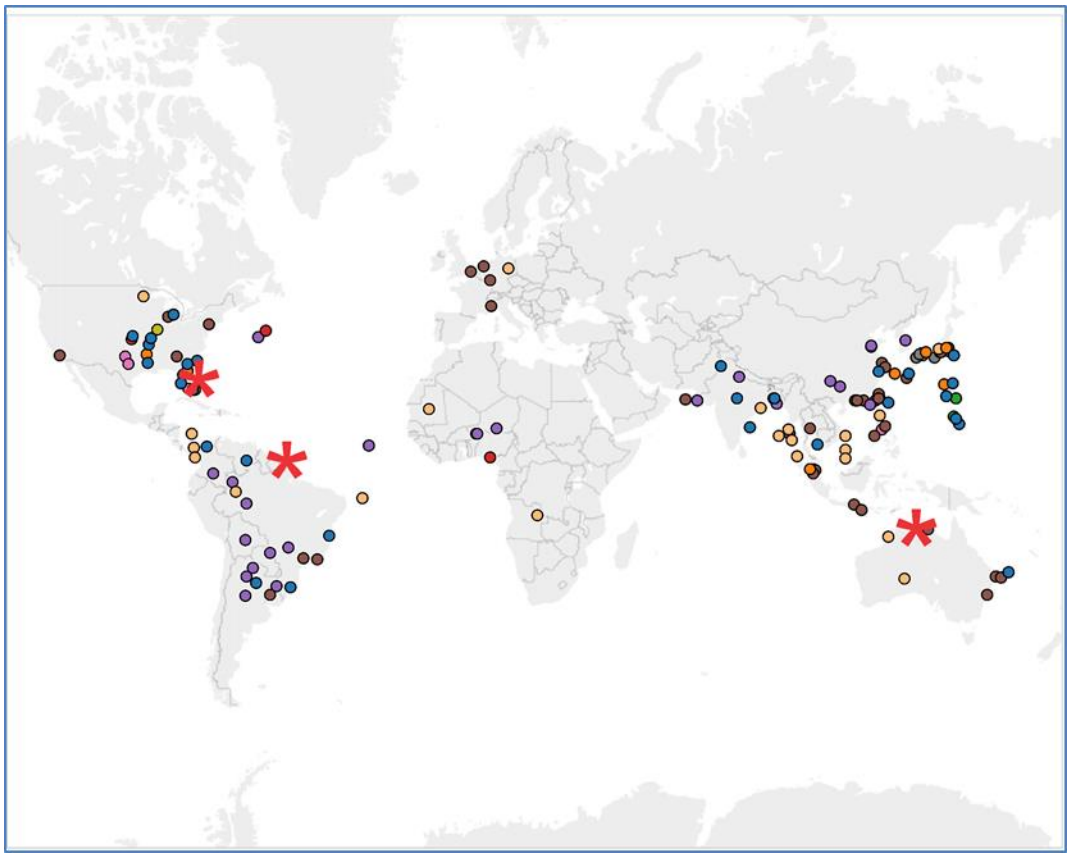

Figure 1. Location of 162 Boeing engine events as of June 2015 (adapted from [24])

1.2.2 Observations and Hypothesis of Meteorological Conditions Causing Engine Events

In 2006, the EHWG studied over 100 weather-related engine and power plant events, where compressor stall, power loss, rollback , and/or engine damage had occurred. Events occurred in or near deep convective clouds, however, in relatively innocuous conditions of low to moderate turbulence, little lightning, and in areas of cloud with only green (typically < 30 dBZ radar reflectivity) or no echoes (typically < 20 dBZ) on the pilot's radar [12,18]. Observations of airframe icing were rare. An anomaly was often observed on the Total Air Temperature (TAT) sensor, forcing the measurement towards 0 C. Pilots often observed "rain on the windscreen" around the time of the event. These latter two observations led early investigators to erroneously conclude that in the first case, the aircraft flew through a stratospheric intrusion and was thus exposed to unusually vigorous convection, and, in the second case, the aircraft flew through

supercooled rain at almost impossibly cold temperatures and without any observed airframe icing. In both cases, these confusing observations have since been linked to melting of ice crystals on heated surfaces in flight through high concentrations of ice crystals, and have been verified as such in the Airbus exploratory flights [28] and the three flight programs described in this report. It also was noted in engine event analyses that aircraft were often flying above heavy rain areas, which have since been concluded to be a more detectable manifestation of the high ice concentrations at flight altitude.

Events were found to occur in both the northern and southern hemispheres, and generally within the tropics and subtropics during periods of high frequency of deep convective cloud [18]. Several "hot spots" regions with a high frequency of events were observed in the earliest event inventory, the most notable being in the oceanic regions from tropical Southeast Asia to Japan. The reason for these hot spots has not been rigorously investigated, as many factors beyond the frequency of convective weather could contribute to a local concentration of engine events. The most recent map of event locations reveals some new hot spots, most notably over continental land masses [24].

The vast majority of engine events occurred in systems with broad cirrus shields formed by deep convective clouds, which are commonly characterized by lift of low-altitude air with high moisture content to high altitudes, where the air cannot retain the moisture and then condenses onto hydrometeors. The relatively short time and distance scales associated with this deep lift are conducive to retention of high local condensate concentrations relative to other cloud types. Figure 2 contains a photograph of an African cumulonimbus cloud taken from the NASA Space Shuttle. Although likely a smaller version of a cloud that might cause an engine event, it illustrates a broad stratiform cirrus shield with an embedded overshooting active cell on the right side. Figure 3 is a simplified schematic of a such a cloud cross-section. The active convective cells observed on the right contain multiple overshooting tops, caused by updrafts that penetrate past the level of neutral buoyancy (the "equilibrium level," which is often at or near the tropopause level)[2]. Cloud "enhanced region" is a term used in engine-event, meteorological analyses [e.g., 30]. Outflow from, and dissipation of, earlier active cells creates the broad "stratiform" cirrus layer surrounding the cells at the approximate equilibrium level[3]. Multiple active convective cells may exist at the same time, forming and dissipating over time and broadening the cirrus shield. The active cells may be randomly spaced, or may organize into structures such as lines. New cells may grow up into the cirrus shield, as exemplified on the far right of Figure 2 and Figure 3. An example image of a cirrus shield fed by multiple cells during the Darwin-14 flight campaign is contained in Figure 4. The image is a frame grab from a Falcon-20 GO-PRO video out the pilot's windscreen on 9 February 2014 at 21:39 UTC while approaching a small convective line of cells about 100 nautical miles (Nm) long by 20 Nm wide. The aircraft is beneath a broad cirrus canopy while individual cells feeding the canopy are observed ahead. The thick cirrus layer is seen through the windscreen just above the aircraft. The pilot's radar screen superimposed on the photo (tilt 3 degrees down) shows the radar signal from the multiple approaching cells. An aircraft crossing such a cirrus shield

[2] Past meteorological analyses of engine events have referred to the area of cloud at or above this level the "enhanced region," and ref. [24] uses the term "Enhanced Level Overshoot" (ELO) for satellite overshooting top areas with IR temperatures colder than this level by a threshold difference (e.g., Δ of -10 C for [24])

[3] The term stratiform here refers to the non-convective nature of this cloud area, and does not imply these cloud areas are similar to Appendix C stratiform clouds.

may intersect one or more of these cells if the radar reflectivity at flight altitude is low. If the precipitation areas formed in such clouds have a characteristic size larger than 100 km (~54 Nm), the cloud ensemble is called a Mesoscale Convective System[4] (MCS). In tropical regions, these systems can form a broad rotational circulation that can develop into a tropical storm, with cirrus shields hundreds of Nm in diameter.

Figure 2. African cumulonimbus taken from the NASA Space Shuttle

[4] A cloud system that occurs in connection with an ensemble of thunderstorms and produces a contiguous precipitation area on the order of 100 km or more in horizontal scale in at least one direction [29] (American Meteorological Society, "Mesoscale Convective System". Glossary of Meteorology 2014)

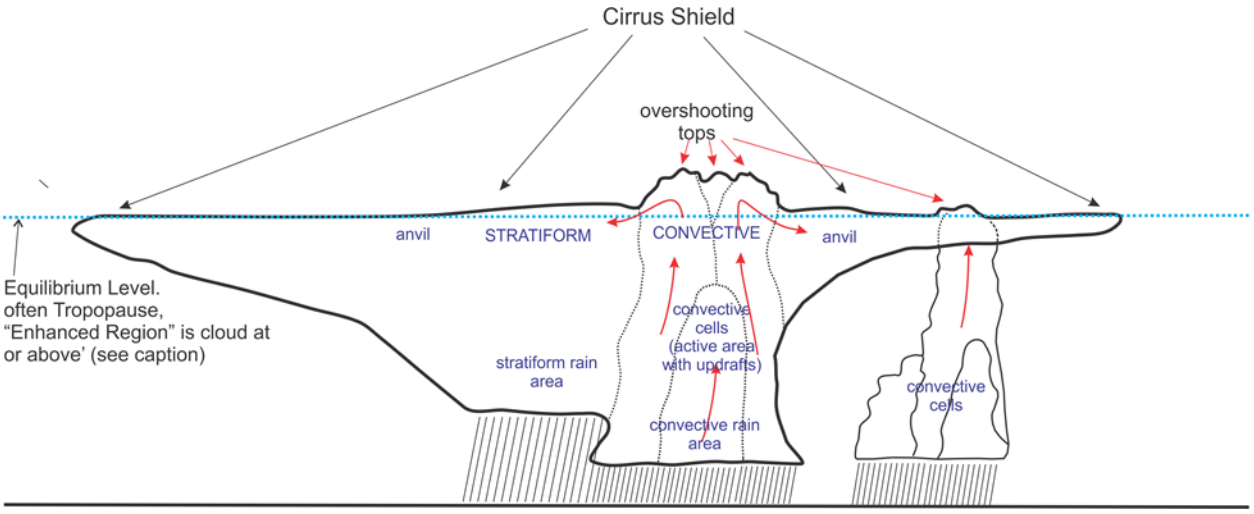

Figure 3. Simplified cross-section of a cloud with concepts shown (see Figure 2 example)

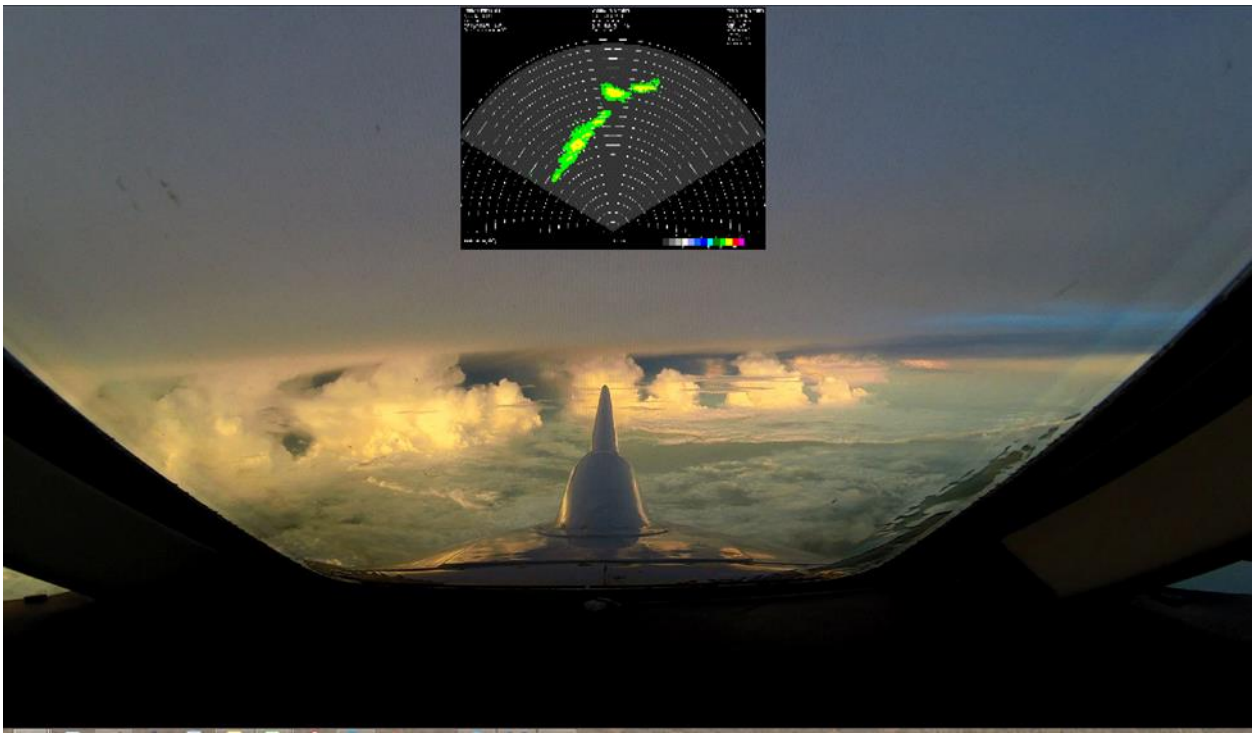

Figure 4. Video frame of an approach toward a small line of convective cells with pilot's radar screen superimposed at top-center

Figure 5 shows a radar cross section of a relatively small cumulonimbus cloud near Darwin Australia, with Doppler-derived winds to illustrate the vertical lift in such a cloud. Convergence of air is observed on the right side of this cloud with a vertical lift that can be traced from near the surface to almost 14 km. Near the surface, the summer monsoon air mass near Darwin typically contains about 18 g of water per kg of air. By 14 km, due to the decrease in saturation vapor pressure with temperature, almost all of that 18 g/kg must condense out into hydrometeors. For a typical Darwin summer monsoon air mass, this, in theory, could lead to local "adiabatic"

concentrations in updrafts reaching a maximum TWC of the order of 8 gm^{-3} at a pressure altitude of approximately 25,000', eventually lowering to about 5 gm^{-3} at 40,000' due to air parcel expansion effects eventually dominating over the condensation rate. The evolution of the condensed water from liquid water to ice particles is a complicated path that is not fully understood, and is the subject of focused research within the HAIC-HIWC Science team. However, as measured in this study, deep convective clouds with cloud top temperatures usually colder than -60 C and sometimes reaching down to -90 C, are almost entirely composed of ice particles within the temperature range sampled in this study (-10 C to -50 C).

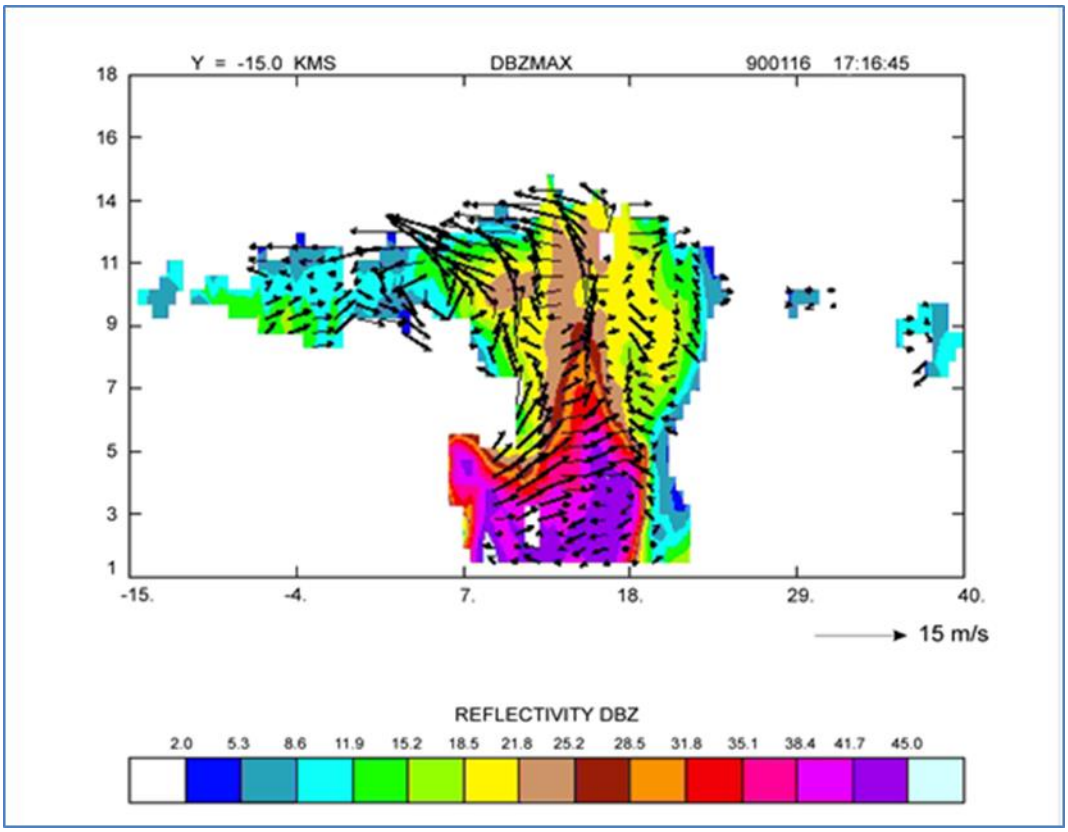

Figure 5. Cross-section of a monsoon convective cell within the range of Darwin weather radars, with radar reflectivity and wind fields shown ([31])

Based on pilot observations and meteorological study of engine-event cases, the environment that causes engine events was proposed by [18], namely broad cirrus regions encompassing convective storms of scale varying from isolated cumulonimbus, to mesoscale complexes, to tropical storms. Temperatures at event level varied between 0 and -50 C, with events occurring in an atmosphere warmer than an international standard atmosphere (ISA) by as much as 25 C. The environment was reported to be "dominated by ice crystals with very little supercooled LWC," and with "mass concentrated at sub-200 μm sizes" [18]. The small ice particle sizes were hypothesized to account for the low radar reflectivity. Meteorologists and the aviation community have long known that deep convective clouds can be hazardous to aircraft, with possible heavy turbulence, airframe icing, lightning, and hail, but such conditions have for the most part been avoidable using the on-board pilot's radar. But there is indeed a wide spectrum of conditions that can be expected in deep convective clouds. Researchers have noted that deep convective clouds over the ocean ("oceanic

convection") generally have much less lightning, lower updraft velocities, and lower radar reflectivity at jet flight-altitudes than deep convective clouds forming over land masses ("continental convection"). In one study [32], vertical profiles of radar reflectivity in oceanic convective cores near Darwin, Australia showed a much lower reflectivity above the freezing level than tropical continental convection in the same region, which, in turn, had lower reflectivity above the freezing level than mid-latitude continental clouds, while all had comparable radar reflectivity below the freezing level. In fact, the median oceanic radar reflectivity, over the volume scale of the ground-based radar, was below detection on the pilot's radar (< 20 dBZ) above about 23,000' pressure altitude. This was a central observation supporting the hypothesis of how engine-event pilots were encountering high IWC conditions and not detecting them on their radars. The observations during engine events of TAT anomalies and "rain on the windscreen" (both now confirmed to be a result of melting ice particles at high concentrations) were strongly suspected to be indicators of flight into high IWC. The concurrent pilot observations of low radar reflectivity, with confirmation from meteorological event analysis when ground radar information was available, strongly indicated that high IWC could exist in low-radar reflectivity conditions. The observations [32] suggested that aircraft could be flying through core updraft areas of oceanic convection without encountering high reflectivity or vigorous updrafts, lightning, and hail, but the potential for high IWC from deep lift was still present. This required ice particle mass to be concentrated at small sizes, an unconventional conclusion given the general understanding within the cloud physics research community; however, supporting microphysical hypotheses have been developed and are contained in the HIWC Science Plan [1]. The measurements from this project are in fact unique, and provide a significant potential for scientific discovery related to the evolution of ice particles in deep convection.

The meteorology of engine events continued to be studied after the initial investigations of the EHWG [30,33]. Ref. [33] described the cloud types, which caused 62 engine events on Boeing aircraft, suitable for meteorological analysis at the time of the study. As it was a major influence on the selection of clouds for the flight campaigns, a brief review of their results follows. Most events were observed in large MCSs. Thirty-eight percent were in relatively benign *Oceanic MCSs*, "with little to no radar returns at cruise flight level anywhere in the system, but (where) large regions of moderate to heavy rainfall will exist below the freezing level." Thirty-four percent were in *Strong Tropical MCSs*, similar to the former but "with regions of high radar reflectivity at cruise flight level associated with strong updraft cores," although the aircraft were not flying in the high-reflectivity regions. Both would typically have formed in tropical or sub-tropical air masses, and have a "large round or oval cirrus anvil shield of the order of 185 km in diameter or greater." Eight percent of events were found in *Tropical Multi-cell Clouds*, "a group or cluster of individual convective cells with deep anvil regions on the order of 56 km in diameter or smaller." A further eight percent were in *Continental MCS*, "a convective system that forms in mid-latitude regions in a relatively drier and more wind sheared environment as compared to Oceanic and Strong Tropical MCS." These systems have cirrus anvil shields "on the order of 185 km in diameter and often much larger." Six percent were found in *Classic Continental Anvils*, usually occurring "in mid-latitudes over land regions," and often forming in the afternoon due to solar heating. An additional 6% of cases were classified as *Other*, and were associated with frontal convection, lake-effect convection, and developing continental convection. The typical atmospheric sounding had tropical characteristics, with weak to moderate instability and high precipitable water. The authors suggested that the associated long cirrus traverses in the MCSs noted above may be an important factor affecting engine events.

Further updates provided new and mostly consistent information on the meteorology of engine events. Events in 11 case studies in the Japan/Southeast Asia oceanic region [24] were linked to the proximity in space and time to a local active cell, and not necessarily to the period of maximum activity within the overall lifecycle of the MCS. Figure 6 shows the aircraft traverse for one of these 11 engine-event cases. The white cloud area represents the temperatures at or colder than the equilibrium level. The red cloud area is at least 10 degrees colder than the convective equilibrium level, termed by the authors an "equilibrium level overshoot" (ELO), and is indicative of the region where updrafts would be found. In Figure 2, the ELO would likely be the more textured area on the right side of the cloud image. In Figure 6, the aircraft passed within 27 Nm of the center of an ELO that peaked in an area about 15 minutes before the aircraft traverse. In 8 of the 11 cases, including that shown in Figure 6, the aircraft penetrated the cloud below this ELO, strongly suggesting that high IWC was associated with proximity to updraft. Furthermore, consistent with the findings of [34], these engine events occurred in relatively large clouds, where the average length of traverse through what [34] termed the "enhanced region" (the white area in Figure 6), was 105 Nm.

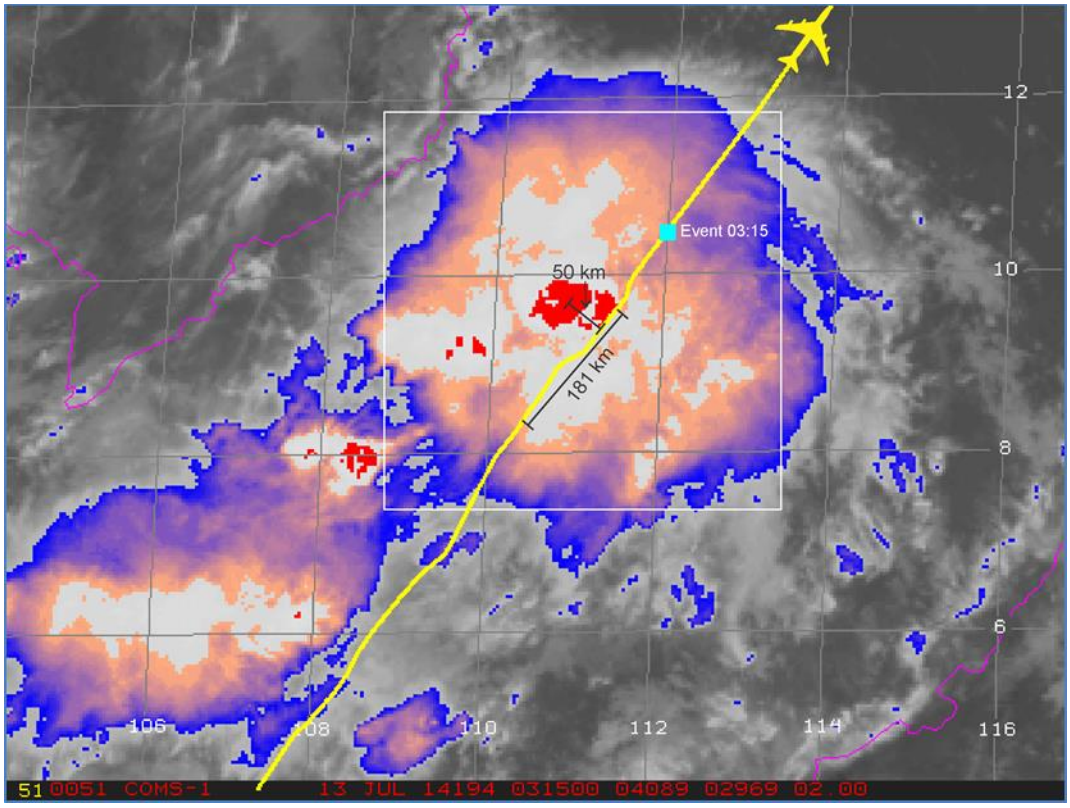

Figure 6. Engine-event case study in a typical event-causing oceanic MCS ([24])

In summary, the elements of the hypothesis of the meteorological environment causing engine events, from the EHWG investigations and later studies previously noted, are summarized next. The early conclusions were used in the design of the flight strategies outlined in section 2.5, and the later studies either have led to refinements that were instituted before the flight programs, or have generally supported the strategies undertaken.

- Engine events occur in high TWC areas of deep convective clouds.
- The high TWC environment is dominated by ice crystals with little or no liquid water (i.e., high IWC).
- The high IWC results from deep lift in these clouds, and is located within or near the associated updraft areas.
- Events usually occur in conditions of low radar reflectivity (green or no echo on the pilot's radar), little lightning, and low-moderate turbulence levels at flight levels, especially in oceanic clouds. It is hypothesized that commercial aircraft may be directly penetrating the high IWC updraft areas in such clouds. The low radar reflectivity is thought to be associated with small ice crystal sizes.
- Events also occur in more vigorous systems producing updraft cores with high reflectivity at altitude, lightning, and high turbulence levels. It is hypothesized that such systems have sufficiently high IWC levels to produce engine events at the typical safe distance commercial aircraft use to pass by these cores[5].
- The most common engine-event cloud is a tropical MCS or tropical storm, over ocean or over land, with a cirrus shield with a characteristic size of 100 Nm or larger at or colder than the convective equilibrium level. The cloud of Figure 6 represents a good example of a typical engine-event cloud. Other examples can be found in Figure 8 [18], and Figure 2 and Figure 3 [34].
- Engine events may be linked to longer IWC exposures (i.e., larger MCSs may be more conducive to events). In contrast, it has been suggested that air data probe events may be linked to shorter exposures to more extreme high IWC values.
- Engine events in the event-rich Southeast Asia/Japan region show no favored time of day, but are rather closely linked in time and space to the peak of a local cloud top overshoot, a signature of the updraft region in such a cloud.

Although the hypothesis for the meteorology of engine-event clouds had been modified since the first discussions of the EHWG, the original assumption that zones of high IWC are linked to deep lift in convective updrafts is unchanged. The Appendix D/P TWC envelope, which is based on estimates of maximum condensed water content in such updrafts, is described in the following section.

1.2.3 A Review of Appendix D/P

The interim ice crystal envelope is based on observations of the environment encountered during engine events, and provides a temperature-altitude envelope, estimates of the 99th percentile TWC (hereinafter TWC_{99}) for different flight-level temperatures and altitudes, and an estimate of particle size. The envelope was developed to address flight into deep convective cloud in which the TWC is dominated by ice crystals.

The temperature-altitude and TWC_{99} envelope of Appendix D/P was developed based on discussions within the EHWG; details of the derivation can be found in [27]. Figure 7 shows the inventory of engine-event points used to establish the Appendix D/P temperature-altitude envelope. Figure 8 shows the new Appendix D/P temperature-altitude envelope in more detail,

[5] The FAA Official Guide to Basic Flight Information and ATC Procedures [35] recommends avoiding "by at least 20 miles any thunderstorm identified as severe or giving intense radar echo. This is especially true under the anvil of a large cumulonimbus."

defined by the inflection points A-B-D-E-F-G-H-A. Also shown are the FAR Appendix C [10] temperature-altitude envelopes for continuous max icing (blue line) and intermittent max icing (red line). The Appendix D/P envelope extends Appendix C intermittent max boundaries to -40 C (C-D-E-F), and adds a new warm atmosphere extension bounded on the right by a linear approximation of the Military Standard 210A hot-day[6][23] (G-H), while extending the Appendix C warm boundary (H-I, -3.33 C) and the new cold extension of -60 C (F-G). An updated figure from [33] showing engine events up to and including 2014 is shown in Figure 9. The different symbol types represent different engine types. Note that there have been some events outside the envelope, including a cluster of points near 37,000' reaching up to about 5 degrees warmer than the Appendix D/P ISA+20 C boundary. Some air data probe events also have been shown to occur a little outside the Appendix D/P envelope, for example, at temperatures colder than -60 C [25]. The EUROCAE Working Group 89 qualification standards for pitot and pitot-static probes extends the temperature-altitude envelope to -70 C, based on consideration of in service events [33].

[6] The G-H part of the Appendix D temperature-altitude envelope appears to be a linear approximation of the MIL 201A hot-day [23] from -3.33 to -40 C, linearly extended to -60 C, that is approximately, but not exactly ISA +20. Altitude-temperature end points, estimated from Figure 2 of [27] for points H and G are approximately (19870',-3.33 C) and (47380',-60 C), respectively.

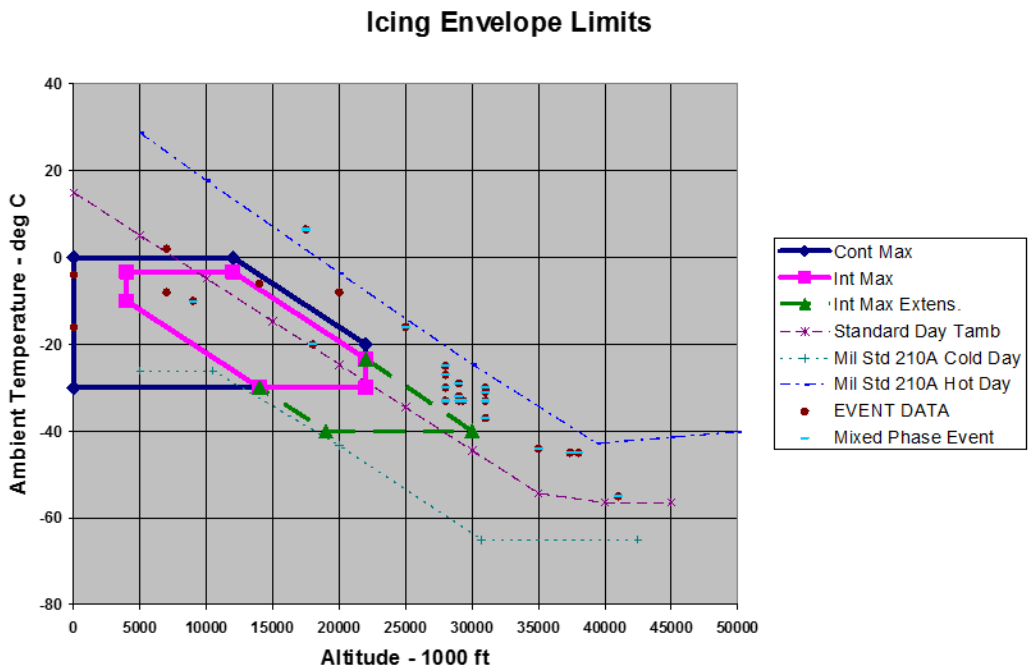

Figure 7. Inventory of altitude and temperatures of engine events used to establish the Appendix D/P temperature-altitude envelope ([27, 22])

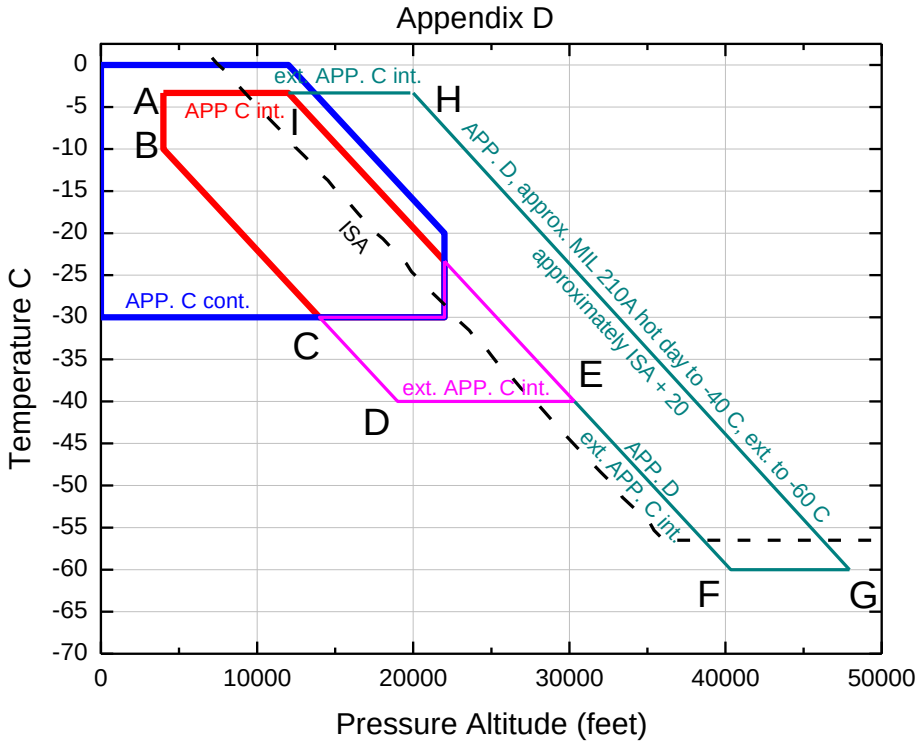

Figure 8. Appendix D/P temperature-altitude envelope in greater detail, defined by points A-B-D-E-F-G-H-A (adapted from [27])

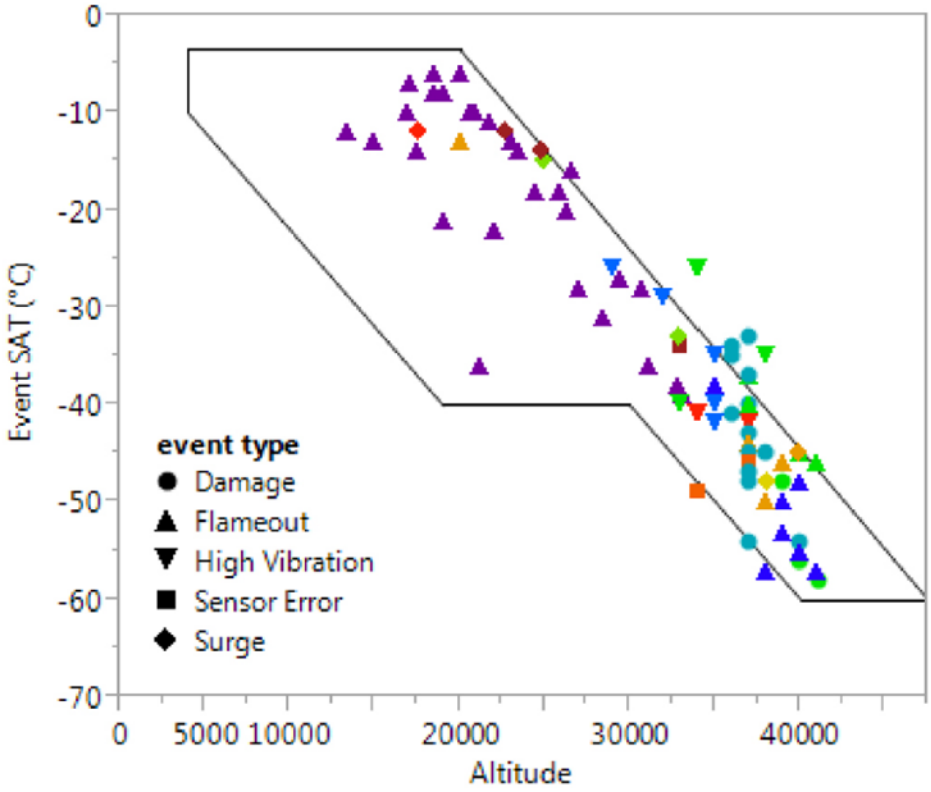

Figure 9. Inventory of 84 Boeing engine events with available static air temperature (SAT) and pressure altitude (feet); comparison to Appendix D/P temperature-altitude envelope (adapted from [33])

Based on the hypothesis that engine events occur in high TWC regions of deep convective clouds, in updraft regions with low radar reflectivity, the starting point for the Appendix D/P TWC envelope was the calculation of the maximum condensed water contents ("adiabatic water contents") in deep undiluted updrafts [27]. Note that calculation of true adiabatic water contents requires knowledge of the actual cloud base, which can vary greatly with time and location. For the purpose of estimating upper limits on the expected TWC values, a conservative assumption was made that the cloud base reflected a 90% relative humidity at the ground. For example, for an average January-March Darwin atmospheric sounding with a surface temperature of 25 C, the lifting of surface air with a relative humidity of 90% would produce a cloud base approximately 215 m above ground, with a water vapor mixing ratio of approximately 18 g/kg at cloud base. There is no information in the atmospheric science literature on the frequency, length scales, or even the confirmed existence of adiabatic updrafts in the type of deep convective clouds that cause engine events. Also, the processes that diminish the TWC in updrafts (e.g., precipitation fallout, entrainment of out-of-cloud sub-saturated air) are thought to be quite efficient. Thus, the use of adiabatic TWCs for Appendix D/P was considered to be overly conservative, especially over distance scales much larger than the suspected widths of the updrafts themselves, and it was recognized that the values would need to be scaled down.

The EHWG deliberated on the appropriate distance scale to use as a reference for Appendix D/P TWC values. It was agreed that an appropriate length scale should reflect what was known about the time of exposure to high IWC prior to an engine event. An informal analysis of the time from the onset of a TAT anomaly (assumed to roughly estimate the start of high IWC exposure) to the first symptoms of an engine event was performed, with the approximate distance scale estimated at 20 Nm. The decision was then made to further adjust the TWC reference distance scale for Appendix D/P to 17.4 Nm, to be compatible with CFR Part 25, Appendix C.

In order to scale down the Appendix D/P maximum condensed water content estimates to more realistic values, the RAE data set from the 1950s, the only available extensive in-situ data set in high IWC conditions, was used. The RAE and the UK Met Office collected a large in-situ data set of TWC values in large convective clouds out of Darwin, Entebbe, and Singapore between 1956 and 1958, and included an appendix of the TWC values in their summary report [9]. The data were analyzed by the EHWG to derive the TWC_{99} values as a function of distance scale. At the 17.4 Nm distance scale, the ratio of TWC_{99} to the calculated maximum condensed water content value at the median pressure altitude and temperature of the data set was found to be 0.65. A matrix of TWC values for pressure altitude-temperature pairs was then derived from calculations of the vertical profile of maximum condensed water content for a variety of surface temperatures. The entire matrix was then scaled down by a factor of 0.65 to force the values to equal the RAE reference data set at its average temperature and pressure altitude. Figure 10 shows the resulting figure of TWC versus pressure altitude for a series of temperature curves [27]. The distance factor *df*, the ratio of the 99^{th} percentile RAE TWC to that at 17.4 Nm, also was computed from the McNaughton data set, and was estimated at $df=1.263-0.213\ log10(d(Nm))$ over a range of about 4.35 to 300 Nm [27]. For example, distance factors at 5, 17.4, 30, 50, and 100 Nm from this expression are 1.11, 1.00, 0.95, 0.90, and 0.84, respectively.

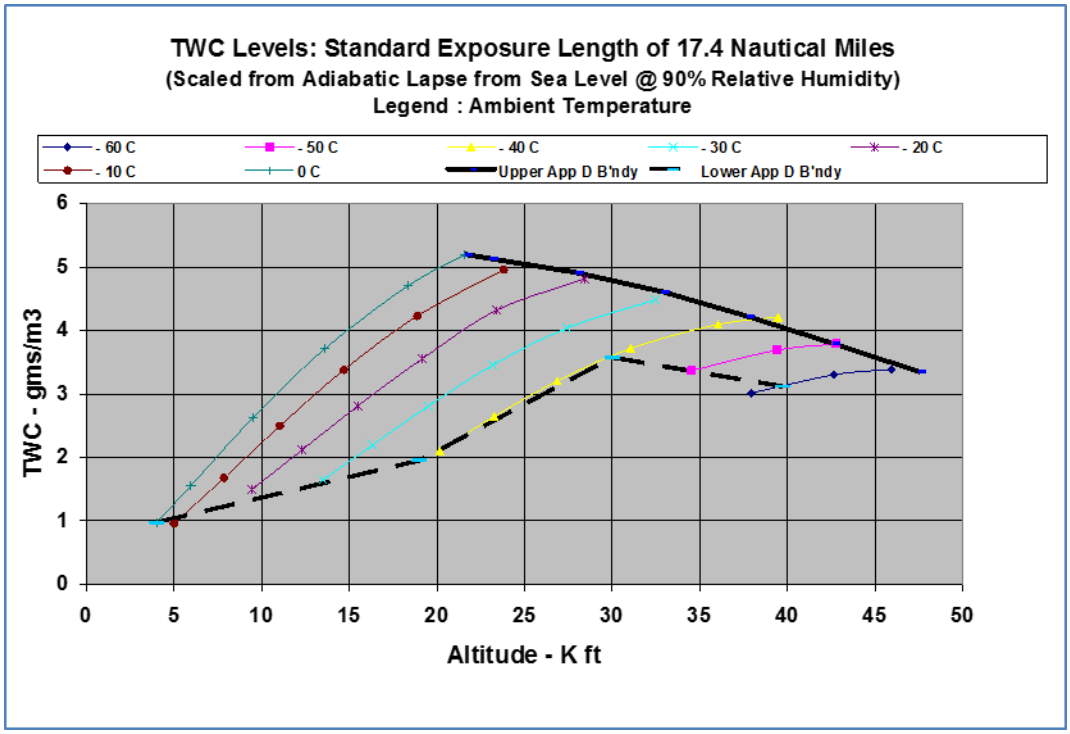

Figure 10. Appendix D/P TWC envelope representing the estimated 99th percentile TWC for 17.4 Nm exposure ([27])

Appendix D/P also contains a table defining the supercooled liquid portion of the Appendix D/P TWC. This table is replicated in Table 1 below. These are the same LWC levels recommended in ice crystal conditions in the FAA ADS-4 guidelines [36].

Table 1. Guidelines for LWC in ice crystal conditions (FAA ADS-4 [36] and [7])

Temperature Range – deg. C	Horizontal Cloud Length (Nm)	LWC – g/m^3
0 to -20	≤ 50	≤ 1.0
0 to -20	Indefinite	≤ 0.5
< -20		0

The EHWG concluded that "ice particle characteristic size may be a key parameter affecting engine ice accretion" [27]. From the sparse information available at the time on particle size in such conditions, some of it being contradictory and having been taken with instrumentation with suspected errors and biases, the EHWG concluded that "median mass diameters (MMDs) lower than 200 µm might be expected," but that "further measurements were required with improved instrumentation to provide more confidence" [27]. The current Appendix D/P rule states that "ice crystal size median mass dimension range is 50-200 µm (equivalent spherical size) based on measurements near convective storms" [7].

1.2.4 The Engine Harmonization Working Group Technical Plan and Recommendations

In addition to proposing the new Appendix D/P ice crystal environment envelope (section 1.2.4), the EHWG proposed a Technical Plan to increase understanding of the atmospheric environment and ice accretion physics, and to develop test facilities, with the following tasks:

1. Evaluation and development of instrumentation for the measurement of high IWC conditions
2. Flight test research for characterization of high ice water content environments
3. Experimental testing in support of ice accretion model development and validation for high ice water content environments
4. Development of test facility requirements for demonstrating engine compliance with the new ice crystal environmental envelope

Of special interest to this report are the first two tasks. The EHWG recognized that the Appendix D/P TWC limits were based on theory and scaled to measurements taken with outdated instruments with questionable accuracy[7], and only at intermediate altitudes up to about 28000'. The estimate of ice crystal characteristic size was likewise uncertain, due to known or suspected shortcomings of instrumentation used to make the rather small number of measurements available at the time of the Appendix D/P development. The first two tasks of the EHWG Technical Plan address the need to collect a new in-situ microphysical dataset, in the kind of clouds that cause engine events. The dataset would be used to: (a) assess the new Appendix D/P environmental envelope; (b) support engineering studies related to EHWG Technical Plan items (3) and (4) above; and (c) support fundamental and applied scientific research in the areas of cloud microphysics, cloud modeling, high IWC nowcasting, and radar and satellite remote sensing of the high IWC environment. To address the scientific research application of the data, an international science team composed of collaborators from government research agencies, universities, and the aviation industry was eventually assembled. Their objectives are outlined in detail in the HIWC Science Plan [1] and augmented by HAIC partners, and will not be repeated here. The next sections describe the efforts related to the collection of this data set.

After the completion of its ARAC tasks, the EHWG continued to meet as the EIWG, and refined a strategy for the collection of the dataset, providing the following recommendations:

a. Upgrade instrumentation as required to make defensible in-situ measurements (section 2.1) in high IWC areas of deep convective clouds in a future flight program (section 2.3).
b. Perform a flight program to collect in-situ data in the same kind of clouds that cause engine events, based on information available in publications on engine-event meteorology. The recommended location of the first flight program was Darwin, Australia, where abundant suitable weather is experienced in the rainy season. Flights should follow idealized flight plans developed within the EHWG and EIWG. Details of the above are contained in the HIWC Science Plan [1], and in sections 2.3 through 2.5.

[7] The RAE TWC instrument collected bulk measurements during flight for weighing and subsequent TWC calculation. It was mounted in an overconcentration zone close to the top fuselage of the aircraft [37]. The accuracy can not be convincingy traced. The RAE TWC_{99} measurements that scale Appendix D at about -10 C are almost a factor of 2 higher than those of this report for -10 C (section 3.5.1).

c. The data results should include TWC_{99} levels, estimation of the occurrence mixed-phase and LWC levels, and estimates of the ice crystal MMD, although details on the latter were only specified after the completion of the three flight programs.
d. At least 100 data points, as defined in section 2.5 , should be collected at the 17.4 Nm distance scale at each temperature level defined below, based on statistical sampling uncertainty estimated by the EHWG for the RAE data set.
e. Data should be provided over a range of distance scales, up to at least 17.4 N, from which the distance factor (TWC_{99} (d) / TWC_{99} (17.4 Nm)) should be estimated. If the flight program provided sufficient data, TWC_{99} estimates at longer distance scales also should be provided.
f. Initial temperature levels were modified by the EIWG for practical reasons after the first of three flight programs to final selections of -50, -40, -30, and -10 C, ±5 C (in order of priority).
g. Other recommendations were made to exploit the unique data set to be collected in the flight campaigns. They are not central to this report and will not be listed here.

The choice of the number of points to be collected in the flight campaigns was discussed with the EHWG in 2007. A Pratt and Whitney statistician performed an analysis of the RAE data set [9]. Using 17.4 Nm distance-averaged data, the uncertainty of TWC_{99} estimates due to sampling statistics dropped below 16% (two standard deviations) of the mean value for sample sizes larger than 100 points, and low- biases in the 99^{th} percentile values increased in magnitude quickly for sample sizes smaller than 50 points. One hundred points, therefore, was recommended as a prudent target to remain within a 20% sampling uncertainty. A similar analysis will be presented in Appendix B to estimate the statistical sampling bias and uncertainty of the data set of this report.

Based largely on [29] (see section 1.2.2), the EHWG recommended that 85% of the sampling time in the flight campaigns be devoted to large tropical MCSs, 60% in oceanic MCS (assumed to be less vigorous), and 25% in overland MCS (assumed to be more vigorous like the *Strong Tropical MCS* of [29]). The remaining 15% of sampling time was to be devoted to vigorous smaller scale afternoon isolated continental convection producing *Classic Continental Anvils*, also of [29]. The larger fraction of flights would be devoted to the less vigorous MCS, because of the possibility of penetrating updraft cores, which could not be safely done in more vigorous MCSs. Data from within updraft cores were necessary to fulfill many of the HAIC-HIWC science objectives.

2. COLLECTION OF FLIGHT CAMPAIGN DATA SETS

2.1 INSTRUMENTATION UPGRADES AND NEW INSTRUMENT DEVELOPMENTS FOR FLIGHT CAMPAIGNS

The EHWG concluded that some improvements to airborne cloud measuring probes would be necessary to ensure reliable and defensible in-situ cloud measurements. The primary measurements of interest were the hydrometeor liquid and ice bulk water contents, and the ice crystal characteristic size. The team responsible for the instrumentation was composed of scientists and engineers, with decades of individual experience in making airborne cloud measurements using modern instrumentation. The team reviewed the significant amount of existing research within the atmospheric science airborne research community. Although a wide set of issues was identified for instrument investigation, many of which were pursued and are listed in the HIWC

Science Plan [1], there were three main topics that required attention to ensure optimum flight measurements of the primary cloud parameters. First, it was concluded that existing instrumentation for the measurement of bulk TWC in the high IWC environment was either unreliable in such harsh conditions, or the level of accuracy was unknown or indefensible. A new instrument was required. Second, it was concluded that the class of instrumentation that would be used to provide particle characteristic size suffered from a number of issues degrading accuracy, especially for small particle measurements. One major issue was contamination from debris caused by particles shattering and bouncing from the probe tips ahead of the sample volume. This issue was already a matter of significant debate and research in the atmospheric science community. Third, it was concluded that the separation of the liquid and solid components in the mixed-phase environment was a particularly challenging problem, one that even now has not been fully resolved. Fortunately, the impact of this issue will prove to be minor for regulatory objectives, as the data collected for this report have shown that regions of mixed phase are infrequent in the regions sampled in these deep convective clouds. When observed, the LWC is quite low (section 3.4). The most important special efforts to improve instrumentation for the flight campaigns are summarized in Appendix A, with a condensed version provided next.

A prototype isokinetic evaporator probe (IKP-1) was initially designed for the flight campaigns by the National Research Council of Canada (NRC) and Environment and Climate Change Canada (ECCC) to measure cloud bulk TWC, with a design goal of 0.1-10 gm^{-3} at 200 ms^{-1} true air speed, 20 KPa, and -40 C static air temperature (SAT), and with an accuracy of 20%. A newer downsized and improved version of the probe (IKP-2) was developed by SEA and NRC for use on the first flight campaign airborne platform, the Service des Avions Français Instrumentés pour la Recherche en Environnement (SAFIRE) Falcon-20 aircraft. The IKP-2 underwent extensive wind tunnel performance and accuracy testing prior to the flight campaigns, as described in Appendix B. Figure 11 shows the probe installed on the Falcon-20 aircraft. The probe measures the total ambient background vapor plus hydrometeor water content (TWC). The estimate of TWC requires the subtraction of an independently measured ambient background humidity value. Although the ambient value is negligible at the coldest flight campaign levels, it rises exponentially with temperature and is of the order of 2 gm^{-3} at -10 C. To date, this has limited the practical use of the probe in turbulent tropical conditions to about -10 C and colder, due to the associated errors in the measurement and synchronization of the ambient vapor. Appendix B discusses the errors associated with the estimation of ambient background vapor.

Figure 11. Isokinetic evaporator (IKP-2) under the wing of the Falcon-20 aircraft ([38])

Appendix A also describes the modifications to the cloud particle spectrometers for this program, mostly accomplished by ECCC in collaboration with manufacturers. The efforts were mainly focused on the improvement of ice PSD measurements by mitigating the effects of the ice crystal shattering issue previously noted. ECCC developed a set of probe-leading edge tips designed to deflect spurious impacting particles away from the sample volume, and performed research on the use of software algorithms to further eliminate artifacts. ECCC also worked with Droplet Measurement Technologies (DMT) to create a new version of their Cloud Droplet Probe (the CDP-2) to mitigate shattering effects. The manufacturer of the Two-Dimensional Stereo Optical Array Spectrometer (2D-S) probe also incorporated anti-shattering tips, similar to those developed by ECCC for other probes. 2D-S anti-shattering tips, with the most up-to-date design at the time, were installed on the 2D-S probes used during the three flight campaigns. Much of ECCC's effort was used to improve probes installed on the Convair-580 research aircraft, which carried a much larger complement of particle-measuring probes than the other aircraft used during the campaigns.

Although some efforts were launched to improve the measurement of mixed phase in high IWC conditions (Appendix A, section A.3), the results of these efforts were limited, and were not implemented within the flight campaigns, with the exception of some testing of a new Artium High Speed Imager (HSI) on the Convair-580 during Cayenne-15 flight campaign. The HSI data provided valuable experimental testing of a new cutting-edge instrument, but were not used in this report.

The development and performance testing of flight campaign probes required extensive use of wind tunnel facilities. The team used North American facilities such as the NASA Icing Research Tunnel (IRT), the Cox and Co. LeClerc Icing Wind Tunnel, the NRC M7 wind tunnel, and the NRC Research Altitude Test Facility (RATFac), the last three of which at the time included ice cloud simulations with varying levels of control, but all with limited calibration of IWC levels. Although estimation of absolute LWC in wind tunnels is relatively well developed and accepted, the same was not the case for ice cloud simulations. The team examined reference methods for

absolute calibration of IWC in simulated ice clouds, in order to compare to the airborne cloud measurement probes in the NRC M7 wind tunnel. Overall, these wind tunnel tests were a critical part of ensuring the success of these measurements, and have been further discussed with respect to the accuracy estimates of the IKP-2 TWC in Appendix B. Further wind tunnel testing of cloud instrumentation was performed within the HAIC experiment (not reported here).

2.2 PRIMARY IN-SITU INSTRUMENTS USED FOR COMPARISONS TO APPENDIX D/P

Comparisons of flight campaign in-situ-measurements to the interim Appendix D/P will be presented in this report for the following parameters/conditions:

- Total Water Content (TWC)
- Ice crystal MMD
- Occurrence and best estimate of levels of LWC in mixed phase

Table 2 lists the primary instruments used to make the measurements that will support the comparisons of this report. The research aircraft used in the flight campaigns are the SAFIRE Falcon-20 (Figure 12), the NRC Convair-580 (Figure 13), and the NASA DC-8 (Figure 14). Full research instrumentation lists for each aircraft are provided in Table 3 through Table 8. Details on NAWX and pilot's radar listed in Table 5 and Table 6 for NRC Convair-580 are provided in [39,40]. SAT measurements, used in defining the temperature-altitude envelope, and in partitioning Appendix D/P data points into the discrete temperature intervals, were collected on the Falcon-20 and the DC-8 using TAT probes commonly used on commercial aircraft[8]. The Convair-580 SAT measurements were derived from an Aventech Aircraft Integrated Meteorological Measurements System (AIMMS-20) probe. Pressure measurements for the three aircraft were derived from standard total and static pressure ports and corrected to accurate values using standard procedures.

[8] These probes did not experience TAT anomalies such as have been observed during many engine events, although a particular Rosemount TAT probe installed on the DC-8 as a secondary research probe for two flights did.

Table 2. Primary instrumentation used in this report for comparisons to Appendix D/P

Measurement	SAFIRE Falcon-20	NRC Convair-580	NASA DC-8
Static Air Temperature	Rosemount 102	Aventech AIMMS-20	Rosemount 102
Total Water Content	Isokinetic Evaporator IKP-2	Isokinetic Evaporator IKP-2	Isokinetic Evaporator IKP-2
Ice Particle Median Mass Diameters (MMDs) and Particle Size Distributions (PSDs)	Stratton Park Engineering (SPEC) 2D-S optical array spectrometer	Stratton Park Engineering (SPEC) 2D-S optical array spectrometer	Stratton Park Engineering (SPEC) 2D-S optical array spectrometer
	DMT Precipitation Imaging Probe (PIP)	DMT Precipitation Imaging Probe (PIP)	DMT Precipitation Imaging Probe (PIP)
Mixed-phase/liquid water content (LWC) assessment	Goodrich Ice Detector	Rosemount Ice Detector	Goodrich Ice Detector (when available)
	Droplet Measurement Technologies (DMT) Cloud Droplet Probe (CDP-2)	Particle Measuring Systems Forward Scattering Spectrometer Probe (FSSP-100)	DMT CDP-2
	Science Engineering Associates (SEA) WCM-2000 with hot-wire LWC sensor (when available)	Nevzorov LWC/TWC hot-wire sensors	

SEA = Science Engineering Associates, SPEC = Stratton Park Engineering

Table 3. SAFIRE Falcon-20 instrument list for HAIC-HIWC field campaigns Darwin-14 and Cayenne-15 (only one of instruments (6), (7), or (8) was flown at a time)

	Cloud In-Situ Microphysics	Comments		State parameters & thermodynamics	Comments
1	DMT Cloud Droplet Probe (CDP-2)	2-50 µm	14	Rosemount 858 5-hole pressure probe and transducers	Static pressure, airspeed, attitude, 3D wind vector
2	Stratton Park Engineering Co. (SPEC) 2D Stereo Probe (2D-S)	10-1280 µm imaging	15	Rosemount 102 BW air temperature sensors	
3	DMT Precipitation Imaging Probe (PIP)	100-6400 µm imaging	16	General Eastern 1011B chilled mirror dewpoint	
4	Science Engineering Associates (SEA) Isokinetic TWC Evaporator (IKP-2), s.n. 1	~0.1-10 gm^{-3} at 200ms^{-1}	17	Buck Research CR-2 chilled mirror dewpoint	
5	SEA Robust Hot-Wire TWC Probe	Under-wing on CDP-2 pod	18	SpectraSystems WVSSII TDL hygrometer	Background water vapor
6	SEA Water Content Measuring System WCM-2000: Darwin-14 0.53 or 2.1 mm cylindrical sensors; Cayenne-15 0.53 mm cylindrical sensor	bottom fuselage mount	19	Licor 840A hygrometer	Background water vapor
7	SEA Water Content Measuring System WCM-2000 with second Robust Probe	bottom fuselage mount	20	Aerodata relative humidity	
8	SEA Ice Crystal Detector (ICD)	bottom fuselage mount	21	Purging system for hygrometer air lines (Cayenne-15 only)	

Table 4. SAFIRE Falcon-20 instrumentation list during the HAIC-HIWC field campaigns in Darwin-14 and Cayenne-15 (only one of items (6), (7), or (8) was flown at a time) (continued)

	Cloud In-Situ Microphysics	Comments		State parameters & thermodynamics	Comments
9	Rosemount Icing Detector model 871LM5			Navigation	
			22	Litton 90-100 Inertial Reference System	
			23	Trimble Global Positioning System (GPS)	
			24	Rockwell Collins ADC-80 Air Data Computer	
			25	Rockwell Collins ADC-80 Air Data Computer	
	Cloud Remote sensing			Miscellaneous	
10	RASTA (RAdar SysTem Airborne) W-band multi-beam Doppler cloud radar	95 GHz	26	Mako video camera of pilot's instruments	
11	Atmospheric Measurement of Potential and ElectRic field of Aircraft (AMPERA)	Fuselage/under-wing mounted field mills	27	GoPro camera, windshield view, for some flights	
12	Primus 660 pilot's radar	9343.85 MHz	28	Atmosphere PLANET flight mission guidance system	
13	L3Com WX-500 stormscope (lighning)	Cayenne-15 only			

For more details on SAFIRE standard instrumentation, see http://www.safire.fr/web/index.php?option=com_content&view=article&id=3&Itemid=9&lang=en. Details on RASTA are provided in [41-42].

Table 5. NRC Convair-580 instrumentation during the HAIC-HIWC field campaign in Cayenne, May 2015

	Cloud In-Situ Microphysics	Comments		State parameters & thermodynamics	Comments
1	Droplet Measurement Technologies (DMT) Ultra High Sensitivity Aerosol (UHSAS)	0.06-1µm	23	Aventech Aircraft Integrated Meteorological System (AIMMS-20)	Temperature, humidity, static pressure, airspeed, position, heading, attitude, 3D wind vector
2	Particle Measuring Systems (PMS) Forward Scattering Spectrometer Probe (FSSP-100)	2-32 µm or 2-47 µm	24	Rosemount 858 5-hole pressure probe and transducers	Static pressure, airspeed, attitude, 3D wind vector
3	DMT Cloud Droplet Probe (CDP-2)	2-50 µm	25	Licor 6262 hygrometer	Quantity 2
4	PMS cloud Optical Array Probe OAP-2DC	50-1600 µm imaging	26	Licor 840A hygrometer	
5	PMS precipitation OAP-2DP	200-6400 µm imaging	27	Buck Research CR-2 chilled mirror dewpoint	
6	DMT Cloud Imaging Probe (CIP)	25-1600 µm imaging	28	Reverse flow air temperature	NRC design
7	DMT Precipitation Imaging Probe (PIP)	100-6400 µm imaging	29	Rosemount air temperature sensors	Quantity 2
8	Stratton Park Engineering Co. (SPEC) 2D Stereo Probe (2D-S)	10-1280 µm imaging	30	Static air pressure sensors	Quantity 2
9	SPEC Cloud Particle Imager (CPI)	2.3 µm pixel res. imager	31	Honeywell Radio Altimeter	
10	Artium Technologies High Speed Imager (HSI)	7 µm pixel res. imager		Navigation	
11	Science Engineering Associates (SEA) Isokinetic TWC Evaporator (IKP-2) s.n. 2	~0.1-10 gm^{-3} at 200ms^{-1}	32	Honeywell Inertial Measurement Unit (IMU)	Quantity 2

Table 6. NRC Convair-580 instrumentation during the HAIC-HIWC field campaign in Cayenne, May 2015 (continued)

	Cloud In-Situ Microphysics	Comments		State parameters & thermodynamics	Comments
12	SEA Robust Hot-Wire TWC Probe		33	Litton Inertial Reference System (IRS)	
13	SPT Nevzorov Hot-Wire Probe		34	NovAtel Global Positioning System (GPS)	Quantity 2
14	Rosemount Icing Detector		35	GoPro camera, cockpit mounted	Cockpit mounted
15	Environment and Climate Change Canada (ECCC) Bulk Cloud Extinction Probe	0.2-200 km^{-1}			
	Cloud Remote sensing			Miscellaneous	
16	ProSensing G-band Water Vapour Radiometer (GVR)	183.31 ± 1, 3, 7 and 14 GHz	36	Purging system for hygrometer air lines	
17	Alpenglow Elastic Cloud Lidar (AECL) Zenith	355 nm	37	Atmosphere PLANET flight mission guidance system	
18	Alpenglow Elastic Cloud Lidar (AECL) Nadir	355 nm			
19	SEA Ka-band cloud radar	35 GHz			
20	ProSensing NRC Airborne W and X Band (NAWX) radar	9.41 GHz, 94.05 GHz			
21	Rockwell Collins RTA-858 pilot's radar	9343.85 MHz			
22	Garmin AT MX20 Storm Scope	Lightning detector			

FSSP = Forward Scattering Spectrometer Probe, OAP - Optical Array Probe

Table 7. NASA DC-8 instrument list for the NASA/FAA HIWC-RADAR field campaign Florida-15 (only one of items (5) or (6) was flown at a time)

	Cloud In-Situ Microphysics	Comments		State parameters & thermodynamics	Comments
1	DMT Cloud Droplet Probe (CDP-2)	2-50 µm Left-wing pylon	11	Aventech ARIM200 Digital Air Data Probe	Temperature, relative humidity, static pressure, airspeed, angle of attack, sideslip
2	Stratton Park Engineering Co. (SPEC) 2D Stereo Probe (2D-S)	10-1280 µm Imaging Right-wing pylon	12	Rosemount model 102 AH2AG air temperature sensors	Ship system (Quantity 2)
3	DMT Precipitation Imaging Probe (PIP)	100-6400 µm Imaging Right-wing pylon	13	Goodrich model 102LA2AG or 102LJ2AG total air temperature sensors	Mounted in front of windscreen, special for project
4	Science Engineering Associates (SEA) Isokinetic TWC Evaporator (IKP-2), s.n. 2	~0.1-10 gm^{-3} at 200ms^{-1}	14	Weston Instruments LM-5-11-1 Solid Wire temperature probe	Window blank mounted
5	SEA Robust Hot-Wire TWC Probe	Mounted in front of windscreen	15	Edgetech Vigilant Model 137	Ship system, Inlet on window blank
6	SEA Ice Crystal Detector (ICD)	Mounted in front of windscreen	16	Licor 840A hygrometer	Background water vapor, inlet and vent on window blank
7	Goodrich Icing Detector model 871LM5	Last 4 flights only	17	Purging system for hygrometer air lines	
	Cloud Remote sensing			Miscellaneous	
8	Honeywell RDR-4000 modified pilot's radar	9.375 GHz	18	Video camera of pilot's instruments and pilot's radar screen	

Table 8. NASA DC-8 instrument list for the NASA/FAA HIWC-RADAR field campaign Florida-15 (only one of items (5) or (6) was flown at a time (continued)

	Cloud In-Situ Microphysics	Comments		State parameters & thermodynamics	Comments
9	L3 Com WX-1000E Storm Scope (lighning)	recorded	19	GoPro camera, windshield view	
			20	NASA flight mission guidance system	
	Navigation				
10	LTN92 Ring Laser Gyro Inertial Navigation System	GPS and INS			

Figure 12. SAFIRE Falcon-20 aircraft used in the Darwin-14 and Cayenne-15 HAIC-HIWC flight campaigns

Figure 13. NRC Convair-580 aircraft used in the HAIC-HIWC Cayenne-15 flight campaign

Figure 14. NASA DC-8 aircraft used in the NASA/FAA HIWC-RADAR Florida-15 flight campaign

TWC was measured on all three aircraft using the isokinetic evaporator (IKP-2, Table 2, Figure 11) that was specially developed for this program (section 2.1, and Appendix A) to provide TWC measurements in the high-speed, high-altitude, high IWC environment with a target accuracy of 20%. Two copies of the probe were manufactured, with IKP-2 serial # 1 being flown on the Falcon-20, and IKP-2 serial # 2 being flown on the DC-8 and Convair-580[9]. The under-wing mounting locations for the IKP2 and particle probes were considered by the instrument specialists to be very good, and probably the best practical choice given the desire for uncontaminated free-stream measurements. The inlets were forward of the leading edge of the wing, and therefore unlikely affected by any ice crystal debris bouncing from the wing or nose of the aircraft.

There is no probe that can directly measure MMD, or the distribution of mass versus size (mass size distribution (MSD)) of an ice crystal population, from which MMD can be deduced. Such

[9] The two copies of the IKP2 are essentially identical, and provide measurements with high precision Appendix B, section B.2).

information must be derived from probes that measure the PSDs (number concentrations), followed by an estimation of the MSDs using additional information and assumptions. For this project, ice crystal PSD measurements were primarily made with two commercially available optical array probes (OAPs) with overlapping size ranges, both in common use in the atmospheric research community—the Stratton Park Engineering Co. (SPEC) 2D-Stereo (hereinafter 2D-S)[43] and the DMT Precipitation Imaging Probe (PIP) [44] spectrometers (Table 2, Figure 15). Both probes produce two dimensional monochromatic shadow images created by particles crossing a laser beam, from which particle size, shape, and concentration can be derived. The 2D-S and PIP probes measure particles nominally in the 10-1280 µm size range at 10 µm pixel resolution, and 100-6400 µm at 100 µm pixel resolution, respectively, although software reconstruction of partial images is used to extend the upper size limit of the latter to 12800 µm. A composite PSD is calculated from 10-12800 µm using the data from both probes (Appendix C). The same types of probes, and the same software techniques were applied for all aircraft PSD data sets in order to minimize any inter data set bias. The effort included an optical array probe software intercomparison between ECCC and the Laboratoire de Météorologie Physique (LaMP) to identify and rectify any software issues. The DMT CDP-2, and its predecessor the Particle Measuring Systems Forward Scattering Spectrometer Probe (FSSP-100), are non-imaging probes that have been commonly used to measure cloud droplets in the 2-50 µm size range. Photographs of the CDP-2 and FSSP-100 are shown in Figure 16 and Figure 17. Particles are individually sized by measuring the amount of light forward-scattered as they pass through a focused laser. The probe output is a size distribution in a user-defined number of size channels (typically 20, for the CDP-2, 15 for the FSSP-100). More information on the CDP-2 principal of operation is available in [45]. The probes are intended for measurement of small liquid droplets, and were not used in this study to cover the smallest range of the ice crystal PSDs, due to uncertainty and problems with their responses to ice crystals. CDP-2 measurements during the flight programs were, in fact, often found to be erroneous in the presence of significant concentrations of ice crystals [46] (also see example in Appendix D, Figure D-4). Since it is shown in section 3.6 that less than 10% of the PSD ice mass resides in particles smaller than 100 µm, the use of the 2D-S to estimate the sub-50 µm part of the MSD rather than a scattering probe like the CDP-2 was considered acceptable for this study. The FSSP-100 and CDP-2 were, however, used in the mixed-phase analysis (section 3.4), where the Convair-580 FSSP-100 in particular provided primary mixed-phase LWC results.

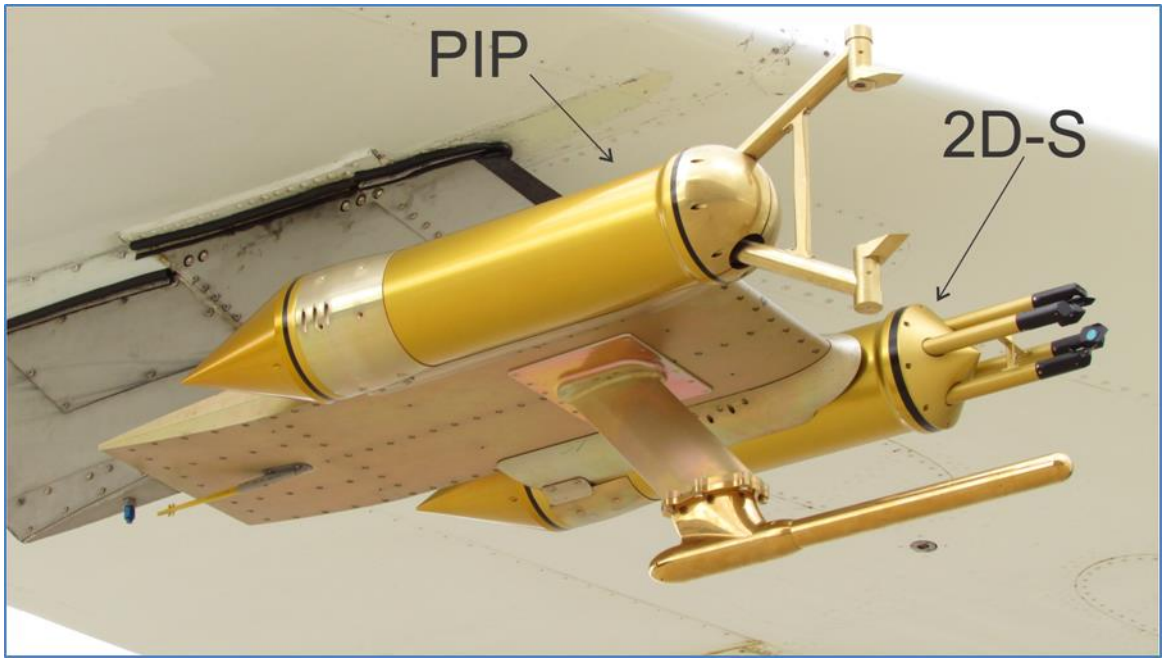

Figure 15. DMT PIP and SPEC 2D-S optical array spectrometers under the wing of the NASA DC-8 aircraft during the HIWC RADAR flight campaign

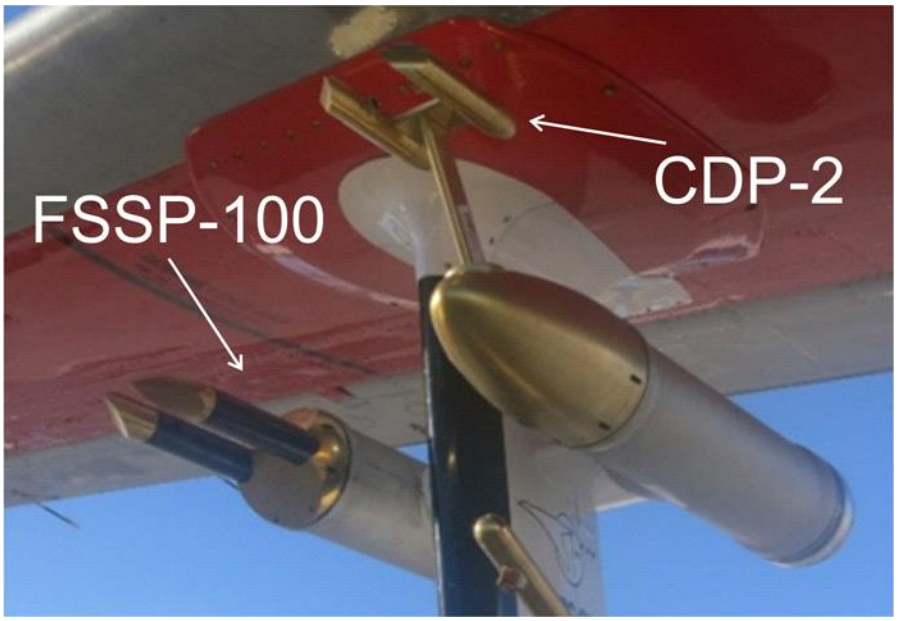

Figure 16. FSSP-100 and CDP-2 probes under the wing of the NRC Convair-580 during the Cayenne-2015 HAIC-HIWC flight campaign

Figure 17. DMT CDP-2 under the wing of the NASA DC-8 aircraft during the HIWC RADAR flight campaign

The 2D-S probe is arguably the most advanced cloud imaging spectrometer of its kind currently in routine use for cloud in-situ measurements in its size range. The probe actually includes two imaging systems that provide independent views of cloud particles in orthogonal directions, usually vertically and horizontally in a perpendicular direction to the aircraft motion. The second imaging system also provides a backup in case of failure of the first. A photograph of the forward section of the 2D-S from [43] is given in Figure 18, where a simulated projection of the laser sample area has been artificially added. A more detailed depiction of the sample volume of a generic OAP is provided in Appendix C, Figure C-1. In actual fact, the sensitive sample area decreases to a smaller and smaller central area between the probe arms as the optical depth of field becomes smaller with decreasing particle size, (see [47] for a more detailed discussion). The PIP OAP probe (Figure 15) similarly provides two-dimensional monochromatic images, but covers the larger particle size range, with one imaging channel rather than the two used by the 2D-S. The PIP is a modern probe in common use within the atmospheric research community for measurements in this size range.

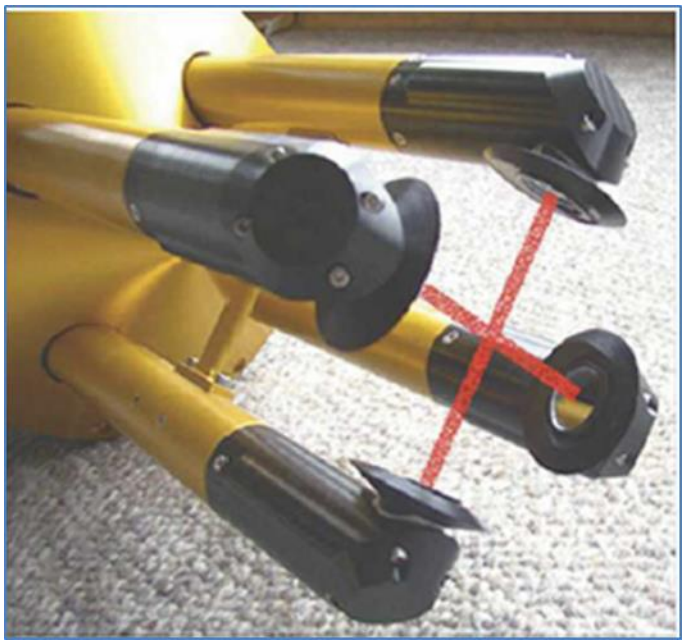

Figure 18. Forward sampling arms of the SPEC 2D-S probe with simulated projection of the laser sample volume of the two independent probes ([43])

Selected 2D-S images of ice crystals, many with identifiable crystal habits, and some of which are large semi-transparent dendritic crystals, are shown in Figure 19, upper panel. The selected PIP images in the lower panel include some identifiable dendrites and two heavily rimed particles, perhaps graupel, on the far right of the panel. However, in the flight program data, 2DS and PIP images with common identifiable shapes were more the exception than the rule. The highest fraction of ice crystals sampled during the flight programs, not unlike from other flight programs reported by the general atmospheric science literature, tended to be mixtures of irregular particles, aggregates, partially rimed particles, or from particle habits not recognizable by a non-expert. Typical 2D-S and PIP images in high IWC regions from the NASA/FAA HIWC-RADAR flight program are shown in Figure 20 and Figure 21, respectively. The vertical bar visible next to each image is coded auxiliary information embedded in the image buffer. The bars also provide a convenient scale reference indicating the 1.28 mm and 6.4 mm widths of the 2D-S and PIP diode arrays. Appendix C provides details on how PSDs and MSDs are calculated from the probe two-dimensional imagery, as well as details on the merging of the data from the two probes.

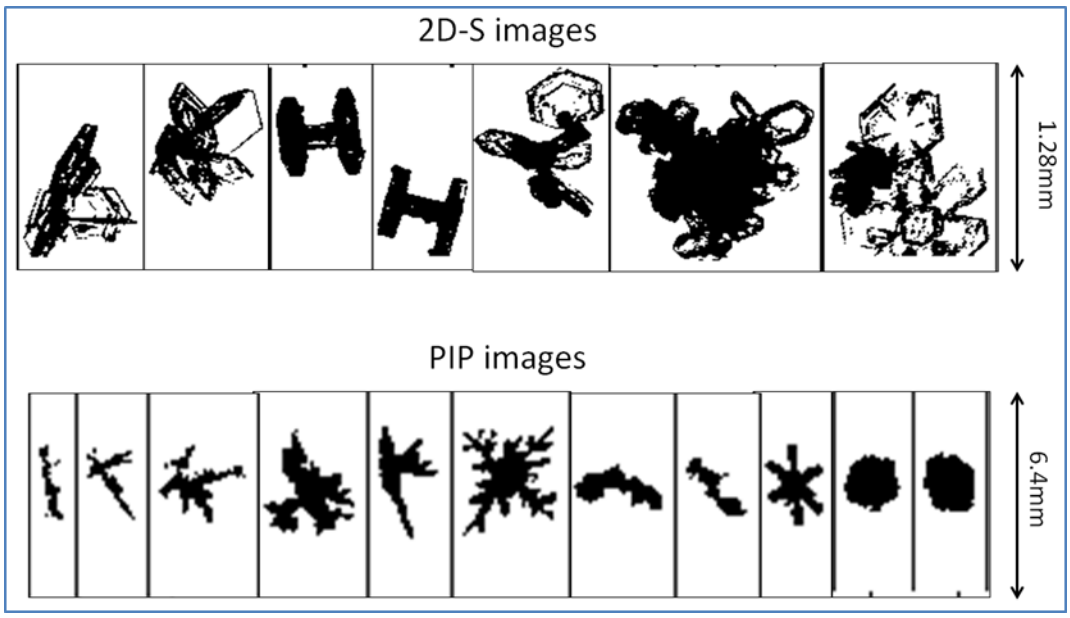

Figure 19. Images of pristine ice crystals sampled by 2D-S probe and PIP probes during the HAIC-HIWC campaigns—vertical bars provide image scale and extent of the diode array

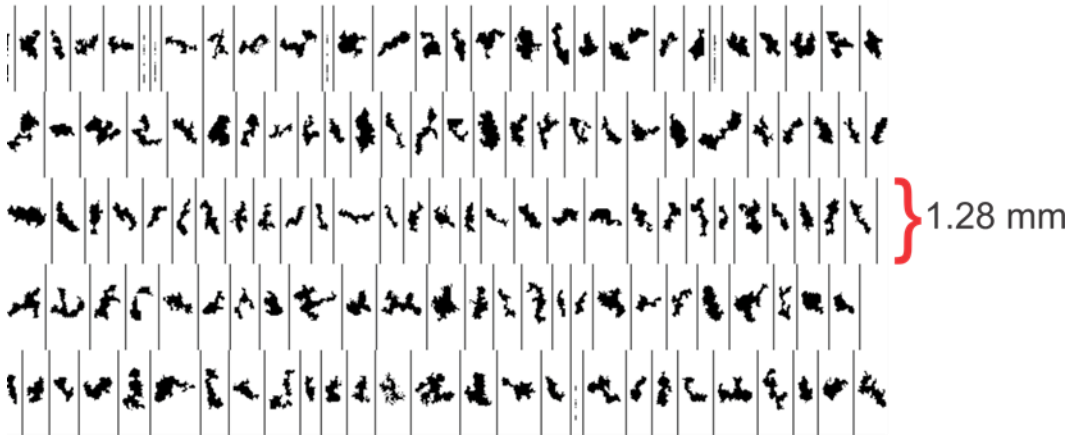

Figure 20. Actual 2DS images sampled in a high IWC region during the HIWC-RADAR flight program—1.28 mm is the extent of the diode array

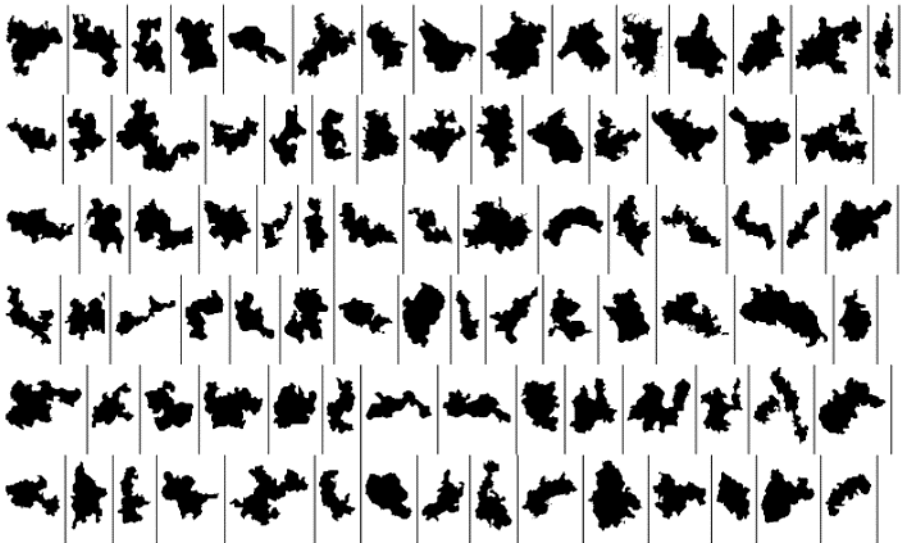

Figure 21. Actual PIP images sampled in a high IWC region during the HIWC-RADAR flight program—data from a different period than Figure 17

Measurement of the occurrence and amount of LWC in high IWC mixed-phase cloud is a challenging problem. In brief, results of this report will show that mixed-phase cloud in the flight programs was relatively rare. When encountered, LWC amounts were low and difficult to quantify due to contaminating effects of ice crystals on the probes that estimate LWC, especially in high IWC situations. The strategy for identification and estimation of LWC was similar to that which was used by [48] for more conventional stratiform mixed-phase clouds, and entailed careful examination of a combination of instruments listed in Table 2, including an Icing Rate Detector (Figure 22), a cloud droplet scattering probe, and occasionally a hot wire LWC sensor. See section 3.4 and Appendix D for details on the mixed-phase analysis.

Figure 22. Goodrich Ice Detector under the wing of the NRC Convair-580 aircraft

The locations of the primary instruments on the Falcon-20, Convair-580, and DC-8 aircraft are shown in Figure 23 through Figure 26, respectively.

Figure 23. Location of primary probes on the Falcon-20 during the HAIC-HIWC Darwin-14 and Cayenne-15 flight campaigns

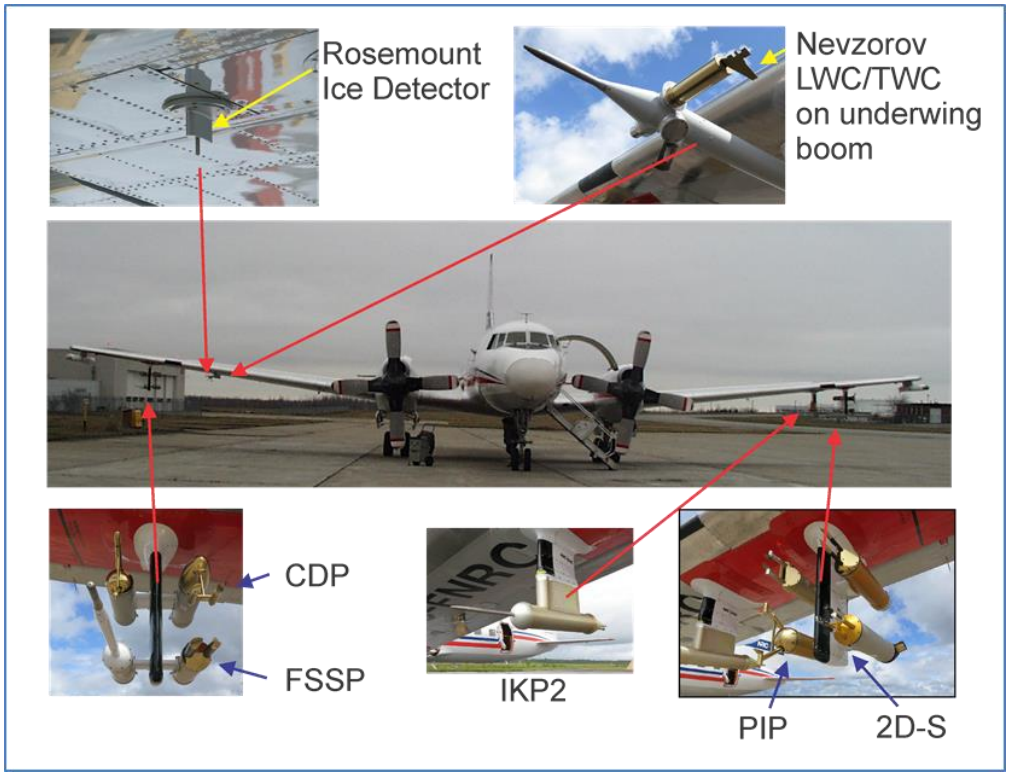

Figure 24. Location of primary probes on the NRC Convair-580 during the HAIC-HIWC Cayenne-15 flight campaign

Figure 25. Location of primary probes on the DC-8 during the HIWC-RADAR Florida-15 flight campaign (DC-8 photo courtesy of Suresh Atapattu)

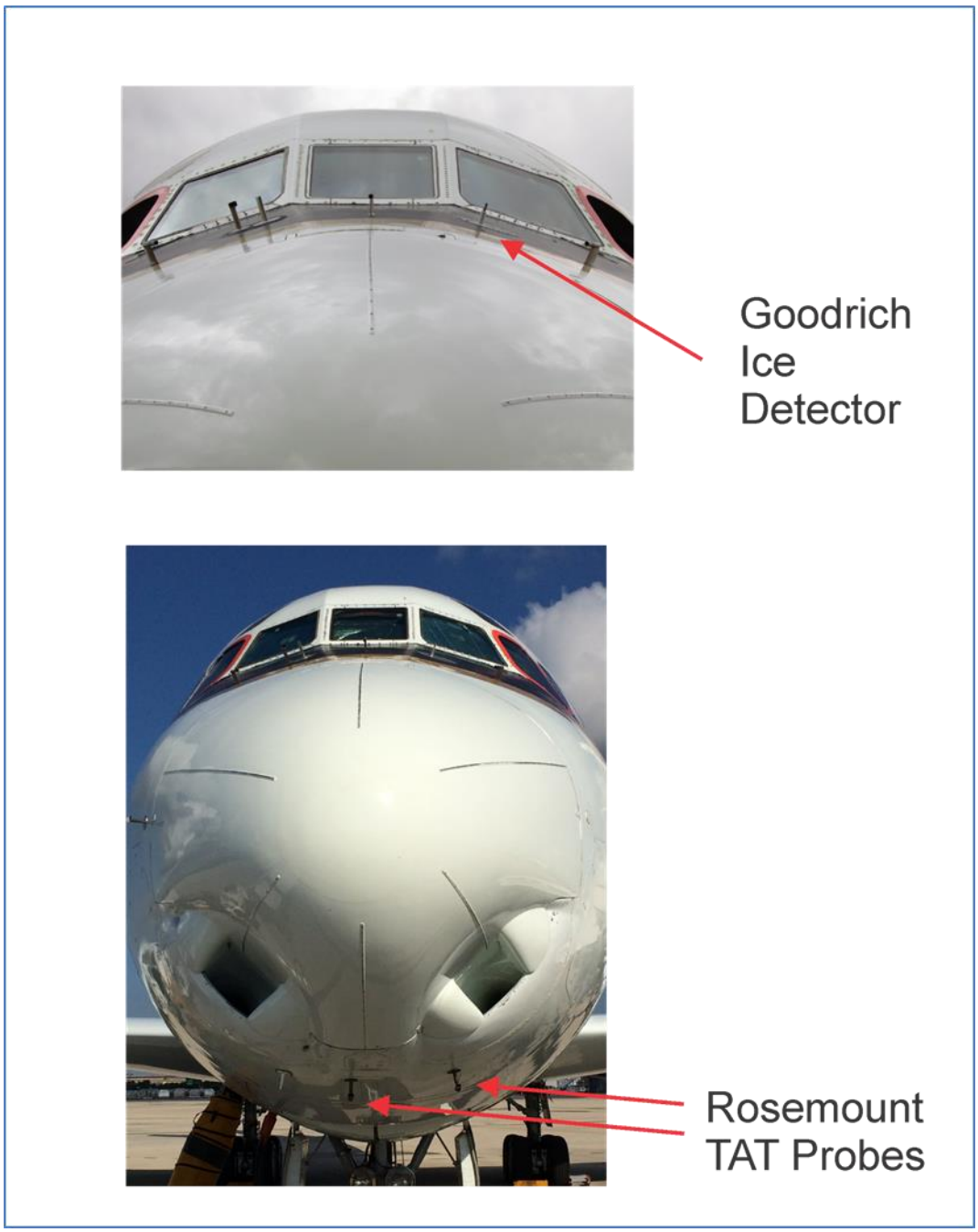

Figure 26. Location of probes on the DC-8 during the HIWC-RADAR Florida-15 flight campaign

2.3 FLIGHT CAMPAIGNS

Three flight campaigns have provided all the data used in this report's comparisons to Appendix D/P. The first two, the Darwin-14 (16 January – 18 February 2014) and Cayenne-15 (5-29 May 2015) flight campaigns, were performed as part of the HAIC-HIWC partnership. The third Florida-15 flight campaign (12-29 August 2015) was conducted independently by NASA and FAA out of Fort Lauderdale, Florida as part of its NASA/FAA HIWC-RADAR project. Florida-15

focused on pilot radar development, but it collected data compatible with the objectives of this report. Deep convective clouds were sampled in all three of these locations.

Table 9 demonstrates that the weather at the field campaign locations was generally representative of tropical oceanic conditions at other locations throughout the world. The campaigns were conducted during or near peak months of convection, and the weather during the flight campaigns was climatologically normal or indicative of abundant convection. Table 9 contains bases of operations for the three flight programs in the first three rows. Darwin values are from http://www.bom.gov.au/climate/extreme/records.shtml. Table 9 also contains peak monthly and annual precipitation amounts for a collection of stations in the tropical latitude belt. Since most of the precipitation in these locations is from convective weather, these amounts also reflect the relative activity of convective clouds in the regions. The first three rows list bases of operations for the flight campaigns providing data for this report. Singapore and Entebbe, along with Darwin, were included because they were the bases from which the 1950s RAE data sets were collected, which supported the legacy guidance of FAA ADS-4 [36]. Pohnei, Micronesia, was specifically chosen for inclusion in the table because it is within a regional maximum of yearly precipitation within the Tropical Warm Pool over the western Pacific and eastern Indian oceans, the region of warmest sea surface temperatures in the world, with accompanying high atmospheric water vapor content, vigorous convection, and heavy precipitation [49]. This location is expected to be particularly favored for oceanic convective cloud. Overall, the yearly precipitation amounts of Table 9 vary by about a factor of 3. The monthly maximum values vary between 202 and 579 mm. The values for the three flight locations range from the lower to the higher end of those in Table 9. Table 10 contains data from http://www.bom.gov.au/climate/averages/tables/cw_014015.shtml, http://www.usclimatedata.com/climate.php?location=USFL0149, http://www.meteofrance.com/climat/outremer/matoury/97307001/normales. Table 10 shows the climatological average precipitation amounts by month for Darwin, Cayenne, and Fort Lauderdale. The three campaigns were conducted either during or near the month(s) of climatological peak precipitation. Table 10 also includes the actual precipitation experienced during the months of the flight programs. The 2014 totals for January and February in Darwin are similar to the climatological values. The May 2015 total for Cayenne is about 54% of the climatological precipitation, but is still substantial at 314 mm. The Fort Lauderdale total indicates a fairly normal year. There is, therefore, nothing particularly unusual about the weather experienced during the flight campaigns. Their times and locations were not chosen based on climatological precipitation alone. Practical considerations such as airspace access, political stability, ground facilities, budget cycles, and the schedules of the research aircraft were also important factors. Each location selection, however, was based on the desire to collect data in tropical clouds similar to those that cause engine events. The most common clouds are large MCSs or tropical storms with a cirrus shield characteristic size of 100 Nm or larger, with very cold tops approaching the tropopause, as discussed in the next section.

Table 9. Precipitation amounts at tropical locations from various internet sources (some undocumented)

Location	Peak month	Precip. in peak month (mm)	Annual precip. (mm)	Comments
Darwin	Jan.	424	1723	HAIC-HIWC Darwin-14, Airbus 2010, HAIC-2016, and 1950s RAE flight campaigns
Cayenne	May	579	3516	HAIC-HIWC Cayenne 2015, and Airbus 2010 flight campaigns
Fort Lauderdale	Jun.	202	1688	NASA/FAA HIWC-RADAR flight campaign
Singapore	Dec.	288	2331	1950s RAE flight campaign
Entebbe	May	279	1574	1950s RAE flight campaign
Taipei	Jun.	322	2100	
Panama City	Nov.	401	2565	
La Reunion	Jan.	379	2172	HAIC-2016
Colombo, Sri Lanka	Oct.	303	1497	
Guam	Aug.	356	2278	
Pohnei, Micronesia	May	496	4825	In regional precipitation maximum in Tropical Warm Pool.

Table 10. Monthly precipitation amounts in mm for Darwin, Cayenne, and Fort Lauderdale

	Darwin		Cayenne		Fort Lauderdale	
	Climatology	2014	Climatology	2015	Climatology	2015
Jan	423.7	474.7	451.2		67.1	
Feb	371.3	252.5	309.4		82.0	
Mar	315.2		334.3		90.9	
Apr	100.4		448.4		88.9	
May	21.6		579.4	314.4	157.0	
Jun	1.8		411.4		248.9	
Jul	1.1		245.7		188.0	
Aug	4.8		143.6		202.9	188.9
Sep	15.8		55.7		240.0	
Oct	70.3		63.3		163.1	
Nov	142.2		133.4		99.1	
Dec	254.3		340.5		61.0	
Sum	1722.5		3516.3		1688.8	

One of the important considerations for the first flight campaign out of Darwin was the proximity to the Tropical Warm Pool. The atmospheric science community has conducted a number of flight programs in the area due to high frequency of convective weather and its importance to the global large-scale atmospheric circulation. The Darwin-14 campaign was conducted with the SAFIRE Falcon-20 aircraft during the months of January and February, to maximize the probability of capturing at least one monsoon incursion during which the most common engine-event cloud type was expected to be abundant. Figure 27 shows the tracks of the 23 Darwin-14 flights in different colors. Almost all flights were in oceanic deep convection within approximately 200 Nm of the coastline, roughly 600 Nm to the east and west of Darwin. Excluding transit and calibration flights, 17 flights provide data used in this report. It was often possible to sample the updraft regions and the source of high IWC at altitude, and it was the consensus of the HAIC-HIWC Science team that the large MCSs sampled were generally representative of the tropical oceanic environment (see section 4.). The program was terminated early with only about half the intended data collection, due to an engine failure unrelated to ice crystal icing, and waning weather.

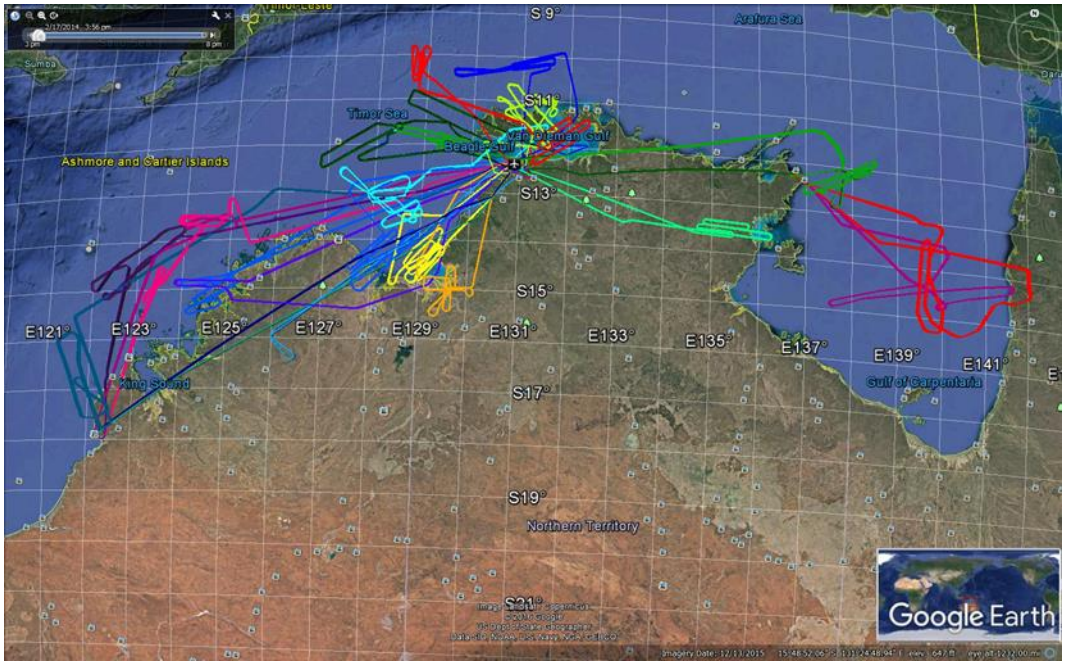

Figure 27. Individual flight tracks of Falcon-20 aircraft during the Darwin-14 flight campaign

The Cayenne-15 flight campaign was then organized to collect the remaining required data. In addition to the Falcon-20 aircraft, two additional aircraft were employed: the NRC Convair-580, highly instrumented for cloud in-situ and remote measurements; and a Honeywell Boeing 757, instrumented for a pilot radar development project, but with no in-situ cloud data collection. Only the Falcon-20 and the Convair-580 provide Cayenne-15 data for this report, for which flight tracks in separate colors are highlighted in Figure 28 and Figure 29, respectively. The flights were conducted within about 150 Nm of the coastline from about 300 Nm east to 300 Nm west of Cayenne. A total of 17 Falcon-20 and 10 Convair-580 flights from the Cayenne-15 campaign provided data for this report. There was a larger fraction of flights over land than during Darwin-14 flights. The MCS studied in Cayenne tended to be smaller and with warmer cloud tops than those in Darwin. Updraft regions were often penetrated during oceanic flights, but less so in continental convection due to lightning and more frequent high reflectivity at altitude.

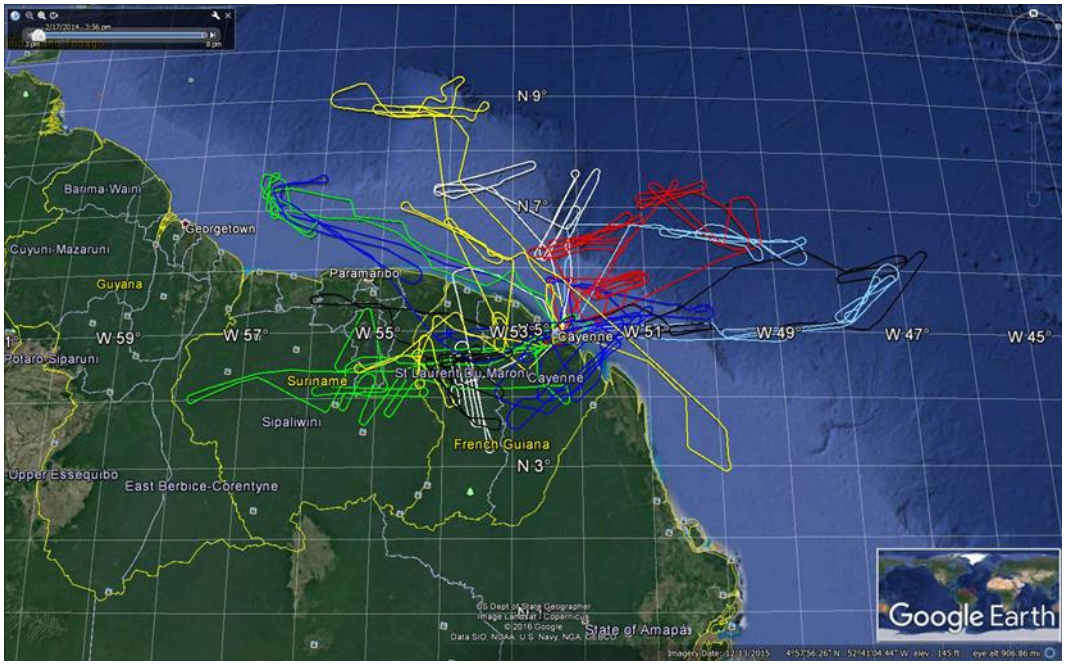

Figure 28. Individual flight tracks of Falcon-20 aircraft during the Cayenne-15 flight campaign

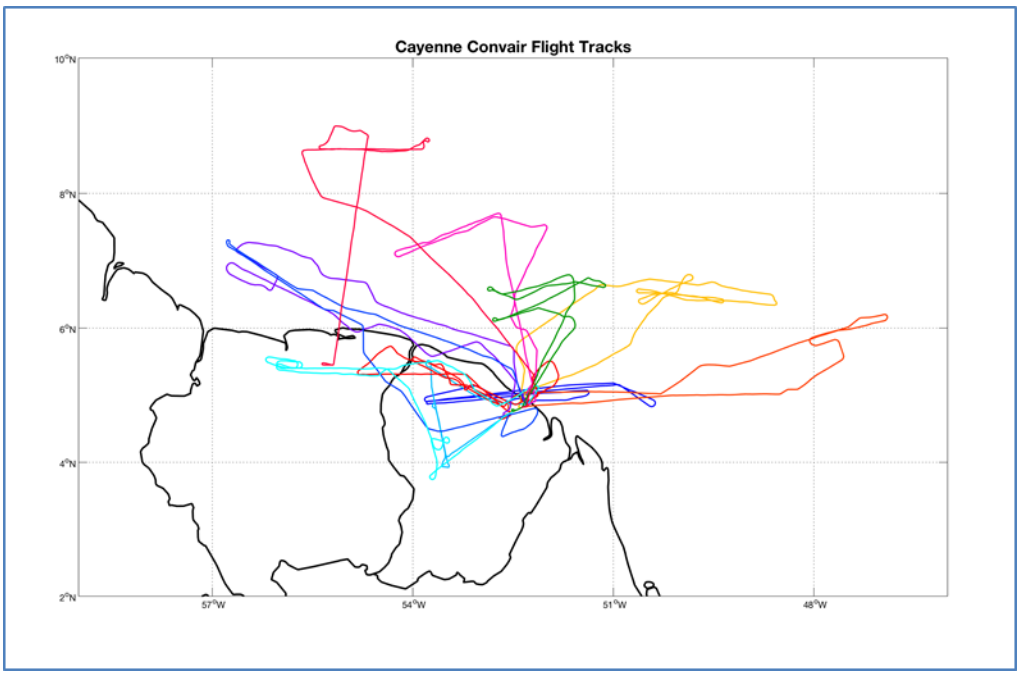

Figure 29. Individual flight tracks of Convair-580 aircraft during the Cayenne-15 flight campaign

The Florida-15 flight campaign was conducted out of Fort Lauderdale, Florida with the NASA DC-8 research aircraft in August 2015. August was chosen more because of aircraft scheduling than due to climatological considerations. Nevertheless, there was no difficulty in locating suitable

MCS clouds. Figure 30 shows the flight tracks in separate colors for the 10 NASA/FAA HIWC-RADAR flights. The long range of the DC-8 permitted targeting clouds at a longer distance from the base of operations, thereby providing more flexibility. The clouds sampled in the first three weeks of the project were primarily medium to large oceanic convective systems or large coastal systems, the latter of which tended to be quite electrically active. In addition, two tropical storms were sampled over the four final flights, providing an excellent data set of high IWC over relatively long distance scales.

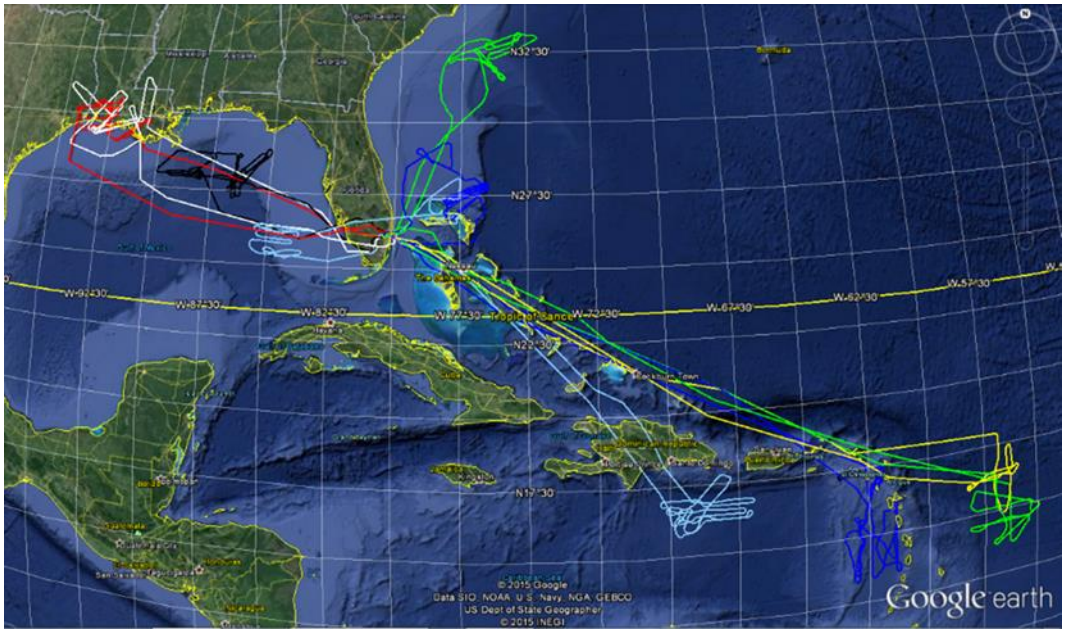

Figure 30. Individual flight tracks of NASA DC-8 research aircraft during the HIWC-RADAR Florida-15 flight campaign

2.4 TYPE OF CLOUDS SAMPLED AND COMPARISON TO ENGINE-EVENT CLOUDS

Due to the choice of tropical locations for the flight measurements, not all of the cloud types noted by [33] could be sampled. In particular, *Continental MCS*, being defined by the authors as occurring in a mid-latitude, drier atmosphere, could not be sampled. It was decided that smaller-scale, afternoon, isolated continental convection observed in Darwin during break periods between monsoons, and frequently during May in Cayenne, were similar enough to be categorized as *Classic Continental Anvils* of [29], and simply called here *Continental Anvils*. For this report, tropical MCS are further sub-classified into Offshore MCS, Coastal MCS, Overland MCS, and Tropical Storms for project documentation. However, there was no attempt to partition the data between the *Oceanic* (less vigorous) and *Strong Tropical* (more vigorous) MCS, since such a determination somewhat depended on when in the evolution of the cloud system it was sampled, and how exactly one would define *Strong Tropical*. In some flights (e.g., Darwin-14 flights 14 and 15), the clouds were offshore but arguably more *Strong Tropical* than *Oceanic*, because red echo on the pilot's radar at flight altitude was prevalent and such cells could only be sampled from a safe distance. In many other offshore MCS cases sampled, growing cells were avoided due to lightning rather than high reflectivity on the pilot's radar. However, more benign cells were

sampled elsewhere in the system, so it is unclear how to label such a system. Furthermore, more vigorous cells were sometimes sampled later in their lifecycle once electrical activity had subsided.

Table 11 through Table 14 contain information on the individual flights that provided the Appendix D/P comparison data during the three flight campaigns, including a column identifying the cloud type. The Size column in each table is a rough approximation. The north-south (dns) and east-west (dew) distances across cloud colder than -50C were visually estimated from infrared satellite images, and a characteristic size then estimated by (.5)x(dns)x(dew). Table 15 provides a summary of the distances in nautical miles sampled according to cloud type. Clouds not used in the Appendix D/P analysis (e.g., non-targeted clouds sampled in transit) are excluded from Table 11 through Table 15. Overall, for the three projects: 55.8% of the data sampling was in offshore oceanic MCSs, 14.5% in coastal MCSs, 4.8% in overland MCSs originating over the ocean, 17.3% in tropical storms, and 7.4% in small-scale afternoon continental convection (also see Figure 31). The sum of the first four categories above, representing all tropical oceanic systems, was about 92%, compared to the 85% recommendation of the EHWG. Small to mid-sized afternoon continental systems, sampled only in Cayenne, represented only about 7% of the totals, compared to the 15% recommended by the EHWG for such a cloud type.

Table 11. General information on HAIC-HIWC Falcon-20 flights out of Darwin, Australia

UTC Date (Takeoff)	flt	Origin-destination	Takeoff	Landing	Area of Operation	Cloud Type	Size (Nm)
16-Jan-14	2	DRW-BME	21:24	00:25	Kimberly Coast	Offshore MCS	180
17-Jan-14	3	BME-DRW	02:31	05:10	Kimberly Coast	Offshore MCS	110
18-Jan-14	4	DRW-DRW	21:51	00:46	Kimberly Coast	coastal MCS, offshore sampling	210
23-Jan-14	6	DRW-DRW	20:12	23:20	Joseph Bonaparte Gulf	coastal MCS, mostly offshore sampling	170
24-Jan-14	7	DRW-DRW	bef 20:09	22:34	Kimberly Plateau	Overland MCS	230
27-Jan-14	8	DRW-DRW	20:42	23:53	Northern Joseph Bonaparte Gulf	Offshore MCS	150
28-Jan-14	9	DRW-DRW	21:08	23:44	Top end, Arnhem Land	Overland MCS	170
29-Jan-14	10	DRW-GOV	20:06	23:22	Offshore Gove, northern Gulf of Carpentaria	Offshore MCS	160
2-Feb-14	12	DRW-DRW	20:35	23:45	Joseph Bonaparte Gulf	Tropical storm (unnamed)	210
3-Feb-14	13	DRW-DRW	04:05	06:32	Joseph Bonaparte Gulf	Tropical storm (unnamed), sampled just inland	150
4-Feb-14	14	GOV-GOV	20:34	23:50	Gulf of Carpentaria	Offshore MCS	310
5-Feb-14	15	GOV-GOV	23:28	02:31	Gulf of Carpentaria	Offshore MCS	310
7-Feb-14	16	DRW-BME	21:02	00:18	North/northeast of Broome	Offshore MCS	260
8-Feb-14	18	DRW-DRW	20:48	00:01	Kimberly Coast	Offshore MCS	270
9-Feb-14	19	DRW-BME	20:48	00:14	North/northwest of Broome	Offshore MCS	260
17-Feb-14	22	DRW-DRW	21:43	01:02	West of Darwin	Offshore MCS	260
18-Feb-14	23	DRW-DRW	21:37	00:47	North of Darwin	Offshore MCS	160
						Median	210
						Min	110
						Max	310

Table 12. General information on HAIC-HIWC Falcon-20 and Convair-580 flights out of Cayenne, French Guiana

Date	F-20 flt #	F-20 takeoff UTC	F-20 landing UTC	CV580 flt #	CV580 takeoff UTC	CV580 landing UTC	Coordinated flts?	Area of Operation	Cloud Type	Size Oceanic MCS (Nm)	Size Continental (Nm)
10-May-15	10	19:03	21:22				no	West French Guiana	Continental daytime convection		80
12-May-15	11	20:02	22:27	8	19:19	21:25	no	French Guiana and Suriname	F20: Continental daytime convection CV580: offshore shallow cells		60
14-May-15	12	14:17	17:15				yes	Northeast of Cayenne	Coastal MCS	60.0	
15-May-15	13	8:35	12:10				yes	Northeast of Cayenne	Offshore MCS	100.0	
16-May-15	14	8:23	11:54	11	8:29	12:10	yes	East/northeast of Cayenne	Offshore MCS	70.0	
16-May-15	15	15:59	18:33	12	16:18	18:12	yes	West French Guiana	Oceanic advected over land, daytime	60.0	
18-May-15	16	19:27	22:41					Northeast of Cayenne	Offshore MCS	90.0	
19-May-15	17	14:19	17:28					North of Brazil Coast, then northwest of Cayenne	Offshore MCS	60.0	
20-May-15				13	9:04	12:20	no	Just inland along west coast of French Guiana	Coastal MCS		
23-May-15	18	9:14	12:45	14	8:58	12:39	yes	North of Suriname coast	Offshore MCS	80.0	
23-May-15	19	15:24	19:00	15	15:53	19:26	yes	North of Suriname coast, and overland French Guiana	Offshore MCS, and overland	100.0	
24-May-15	20	8:52	12:08					East/northeast of Cayenne	Offshore MCS	130.0	
25-May-15	21	19:08	22:41	16	18:36	22:15	yes	French Guiana and Suriname	Continental daytime convection		50
26-May-15	22	8:33	11:59	17	9:34	12:26	yes	North/northwest of Cayenne	Offshore MCS	170.0	
26-May-15	23	13:10	15:52	18	14:05	17:04	yes	North/northeast of Cayenne	Offshore MCS	100.0	
27-May-15	24	8:27	12:06	19	8:48	12:28	yes	North of Suriname, well offshore	Offshore MCS	100.0	

Table 13. General information on HAIC-HIWC Falcon-20 and Convair-580 flights out of Cayenne, French Guiana (continued)

Date	F-20 flt #	F-20 takeoff UTC	F-20 landing UTC	CV580 flt #	CV580 takeoff UTC	CV580 landing UTC	Coordinated flts?	Area of Operation	Cloud Type	Size Oceanic MCS (Nm)	Size Continental (Nm)
28-May-15	25	19:27	22:54					Suriname and French Guiana	Continental daytime convection		40
29-May-15	26	8:48	12:06					Coastal area and inland of east French Guiana coast	Coastal MCS	210.0	
									Median	100	55
									Min	60	40
									Max	210	80

Table 14. General information on NASA/FAA HIWC-RADAR Florida-15 flights out of Fort Lauderdale, Florida—all flights initiated and terminated in Fort Lauderdale

UTC Date	flt	Takeoff	Landing	Area of Operation	Cloud Type	Size Nm
12-Aug-15	1	14:28	19:46	Atlantic	Offshore MCS	130
13-Aug-15	2	14:52	19:31	Atlantic	Offshore MCS	110
14-Aug-15	3	13:01	18:40	Gulf of Mexico	Offshore MCS	90
16-Aug-15	4	13:15	20:28	Gulf of Mexico	Offshore MCS and individual cells	90
19-Aug-15	5	12:06	19:27	Gulf of Mexico	Coastal MCS	220
21-Aug-15	6	13:56	21:04	Gulf of Mexico	Coastal MCS	140
23-Aug-15	7	11:20	19:41	East Caribbean Sea	Tropical Storm Danny	190
26-Aug-15	8	11:06	20:55	East Caribbean Sea	Tropical Storm Erika	210
27-Aug-15	9	12:03	22:01	East Caribbean Sea	Tropical Storm Erika	190
28-Aug-15	10	13:20	21:07	East Caribbean Sea	Tropical Storm Erika	180
					Median	160
					Min	90
					Max	220

Table 15. Distance sampled in different cloud types for the HAIC-HIWC and HIWC-RADAR Falcon-20, Convair-580, and DC-8 flights out of Darwin, Cayenne, and Fort Lauderdale

Cloud Type (this report)	Cloud Type Mason and Grzych (2011)	HAIC-HIWC Darwin-14 Nm	HAIC-HIWC Cayenne-15 Nm	HIWC-RADAR Florida-15 Nm	Total by cloud type Nm	Total by cloud type %
Offshore-MCS	Oceanic or Strong Tropical MCS	5271	7883	3413	16567	55.8
Coastal-MCS	Oceanic or Strong Tropical MCS	658	1467	2166	4291	14.5
Overland-MCS (oceanic origin)	Oceanic or Strong Tropical MCS	835	578	0	1413	4.8
Tropical Storm	Oceanic or Strong Tropical MCS	1014	0	4132	5146	17.3
Small-Mid Size Afternoon Continental Anvils	Classic Continental Anvil (similar)	0	2191	0	2191	7.4
Afternoon initiated Continental MCS	Continental MCS	0	0	0	0	0
Other	Other		75.6			0.3
Total by project (Nm)		7778	12119	9711	29608	
Total by project %		26.2	41.1	32.7		

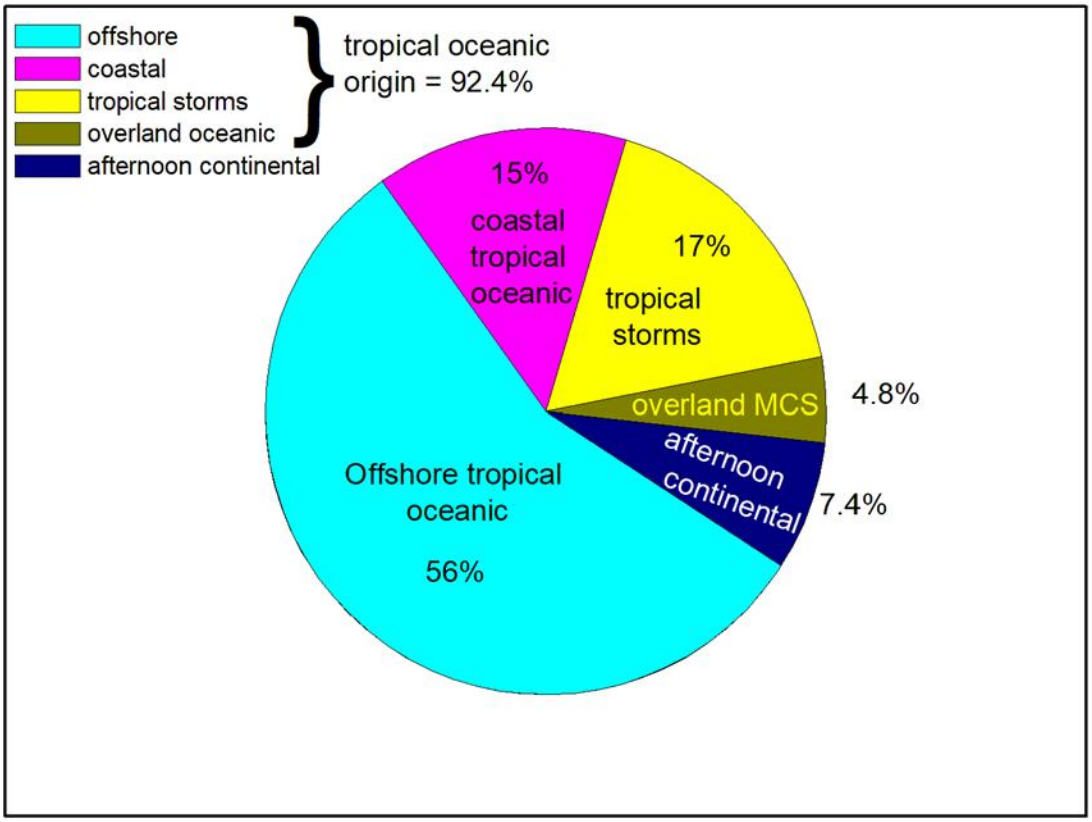

Figure 31. Percentage of clouds in different categories for the combined HAIC-HIWC and HIWC-RADAR data sets

The assumption of the HIWC Science Plan that benign and vigorous MCS, or perhaps more precisely *less* and *more* vigorous MCS, would be distinctly associated with oceanic and overland convection, respectively, and sampled in a straightforward manner as such, has proven to be an oversimplification. Large MCSs forming over land were either not observed during the projects, or formed late in the day, complicating sampling due to the daytime flight restrictions. However, because offshore convection was found to be of varying vigor and so to require the use of both sampling strategies addressed in section 2.5, it is contended that the objective of collecting data in weaker *Oceanic* MCS and *Stronger Tropical* MCS has been fulfilled at least partially, albeit mostly over the oceans.

Table 16 contains a comparison of cloud-related parameters for engine event and flight campaign clouds. The engine event data are from the following: 46 events in [32]; 52 events in [35]; and 11 events in Southeast Asia in [24]. These studies do not report unique events in each case, but are rather updated analyses of the evolving Boeing engine-event database containing common events. One of the notable differences in the data is the median cloud top temperature. Cayenne-15 and Florida-15 have similar median values to the 46 events data set of [33], all around -60 C. The Darwin-14 clouds have much colder tops, and are similar to values for Southeast Asia [24], at around -80 C. The main significance of this difference may simply be related to the probability of an aircraft at cruise penetrating a sustained, continuous portion of cloud well below its top.

Precipitable Water[10] (PW) values, a measure of the integrated water vapor in the atmosphere, were all indicative of a moist tropical atmosphere, with Florida-15 medians being the lowest at 51 mm, Southeast Asia engine events the highest at 64 mm.

In Table 16, the flight program "Cirrus Size" columns are rough approximations of characteristic size, where the north-south (dns) and east-west (dew) distances across cloud colder than 50 C were visually estimated from infrared satellite images at the midpoint of the sampling time, and characteristic size was then estimated as (dnsdew)0.5. Boeing engine-event statistics for "enhanced regions" are: ! from [33], 46 events; # from [24], 11 southeast Asia events; + from [35], 52 MCS events. For more details, see section 2.4.

Table 16. General cloud and atmospheric properties during project sampling and comparison to engine events

	HAIC-HIWC Darwin-14	HAIC-HIWC Cayenne-1	HIWC-RADAR Florida-1	Boeing engine events[!+]	Boeing engine events south-east Asia [#]
Cloud Characteristic Cirrus Size, MCS , defined by ≤-50 C IR area (median Nm)	210	100	160	n/a	n/a
Cloud Characteristic Cirrus Size, MCS , defined by length across "enhanced region" (median Nm)	105[+]	n/a	n/a	130[+]	137
Cloud Characteristic Cirrus Size, Classic Continental Anvil , defined by ≤-50 C IR area (median Nm)	n/a	55	n/a	n/a	n/a
Cloud Characteristic Cirrus Size, Classic Continental Anvil, defined by length across "enhanced region" (median Nm)	n/a	n/a	n/a	n/a	n/a
Median of cloud segment minimum Cloud Top Effective Temperature (C)	-80	-62	-61	-63[!]	-84
Median Atmospheric Precipitable Water (mm)	60	58	51	58[!]	64

IR = infrared

For the three flight campaigns, a simple rough estimate of cloud size was obtained from the size of the cloud cirrus shield colder than -50 C in order to be consistent for campaign-to-campaign

[10] Defined as the depth of water in the vertical column of the atmosphere if all water vapor were condensed

comparisons. The north-south (d_{ns}) and east-west (d_{ew}) distances across sampled cloud areas defined by IR (11.9 μm) temperatures colder than -50 C were measured by manual inspection of GOES and MTSAT IR images, and the effective diameter was estimated as $(d_{ns}\ d_{ew})^{0.5}$. This size represents a characteristic value of the length of cloud that an aircraft at a -50 C cruise might cross. Table 16 also includes values for the three campaigns. The largest MCSs so defined were observed in Darwin-14, with a median size of 210 Nm. Florida-15 and Cayenne-15 sizes were 160 and 100 Nm. Sampled only in Cayenne-15, the classic continental anvils were substantially smaller with a median size of 55 Nm.

Due to different definitions, the comparison of event and flight campaign cloud characteristic size is more difficult. The engine-event cloud sizes were defined as the distance the event aircraft crossed through cloud that was at or colder than the convective equilibrium or tropopause level (see Figure 3), the "enhanced distance." The Boeing authors argued that a long traverse through a cloud area defined this way was a consistent event characteristic and more pertinent to event statistics than, for example, the length across the -50 C boundaries. Unfortunately, this characteristic size definition is sensitive to the choice of the equilibrium/tropopause level, and may be open to a certain degree of subjective interpretation. Consequently, estimates of enhanced distance have not yet been produced for all the flight campaign data for this report, although Table 16 contains some comparisons available for Darwin-14 from [35]. The median enhanced distance for Darwin-14 clouds and 52 Boeing event clouds were estimated from figure 2.13 of [35] to be about 105 and 130 Nm, respectively. The median enhanced distances for 11 engine-event case studies in Southeast Asia was 137 Nm. Engine-event clouds tended to be a little larger than Darwin-14 clouds, but not by a wide margin. A more comprehensive comparison to Cayenne-15 and Florida-15 clouds may be possible in the near future, using objective techniques currently being developed for both the event and campaign data.

2.5 FLIGHT PLANS AND DATA COLLECTION METHODOLOGIES

Flight plans for the collection of data for comparison to Appendix D/P TWC and particle size were developed in discussions with the EHWG, and are detailed in the HIWC Science Plan. The plans were developed based on the hypotheses of the cloud environment that causes engine events, as summarized at the end of section 1.2.4, with a typical engine-event cloud depicted in Figure 6.

The flight plans were developed to collect data in level traverses across clouds in conditions similar to those of engine events, as summarized in section 1.2.2. Yellow and red echo regions on the pilot's radar were not to be intentionally penetrated at altitude, and lightning and heavy turbulence were to be avoided. The campaigns were to collect data from cloud areas that would normally be traversed by commercial aircraft, but while passing near or in active cells. Tracks were chosen to pass within 20 Nm of low-level rain area associated with such cells if possible. Due to safety concerns, cloud sampling was to be done only in daylight hours for the HAIC-HIWC flights in Darwin and Cayenne. For the NASA/FAA HIWC-RADAR flights, there was no such restriction, but nighttime flights were not conducted for operational simplicity, and due to an ample number of suitable daytime targets for the primary radar objectives of the flight campaign.

Simple flight plans were developed for both benign *Oceanic* and more vigorous *Strong Tropical* MCS (defined in section 2.4), the latter expected to be observed predominantly over land. In the end, the flight programs revealed that oceanic systems could contain both benign cells and

vigorous active cells with high IWC, the latter with lightning and/or high radar reflectivity at altitude, particularly at the beginning of their lifecycle. Such vigorous cells were typically avoided, sampled from a safe distance, or sampled later in their life cycle. Late afternoon continental systems initiated by the daytime solar forcing typically had copious lightning, requiring sampling from a safe distance, but often formed too late in the day for daytime sampling.

Figure 32 shows a proposed idealized flight plan for data sampling in a typical engine-event oceanic MCS. The background cloud for this and Figure 33 is a large MCS observed over the Gulf of Carpentaria in January 2010. The left panel shows a Japanese MTSAT IR image, color enhanced to highlight, in white, cloud top temperature colder than the approximate convective equilibrium level (corresponding to the "enhanced region" of [33]). The right panel shows the coincident low-level precipitation field from the Tropical Rainfall Measurement Mission (TRMM) satellite-based radar. The flight plan is a simple survey pattern of the region expected to contain active cells, over or within 20 Nm of the low-level heavy rain area. The flight plan was designed to collect long transects of high IWC if found. Ideally, the onboard flight director would terminate flight legs if the IWC fell below 0.1 gm^{-3} and there were no other indications of increasing IWC ahead. However, the HIWC Science Plan also included the option to focus on active cells with shorter legs. For the most part, Figure 32 contains the basic plan most used for sampling most oceanic MCSs. Although the survey pattern would be performed ideally at the four temperature intervals outlined in section 1.2.4, most storms were sampled at a subset of those intervals.

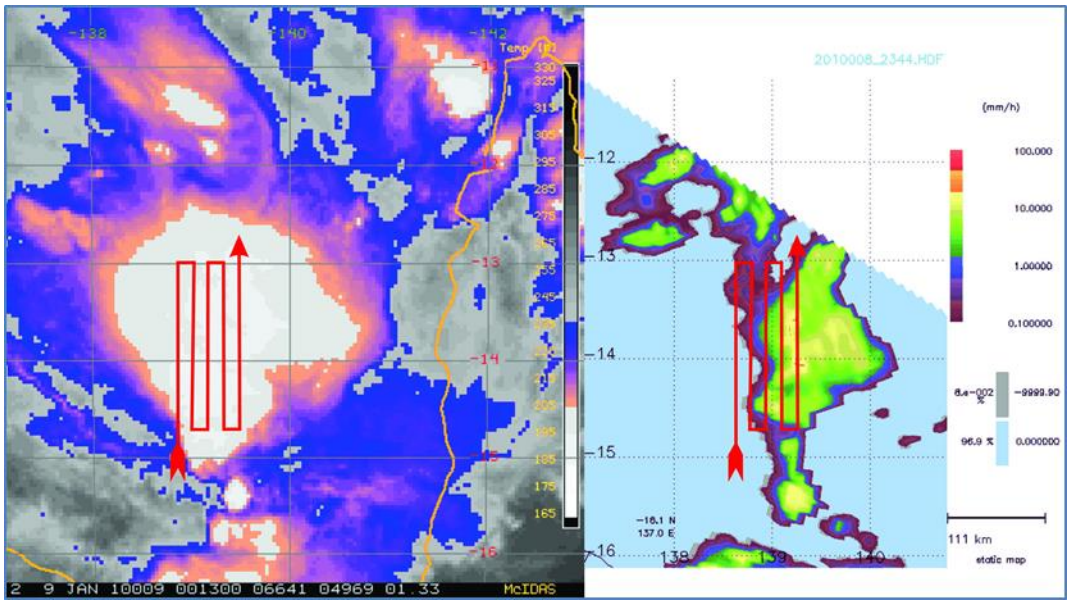

Figure 32. Sample flight plan for survey of high IWC region of typical engine-event oceanic MCS showing a satellite IR of a large MCS (left) and the same track over the TRMM low-level precipitation field (right) (Plot from the HIWC Science Plan [1])

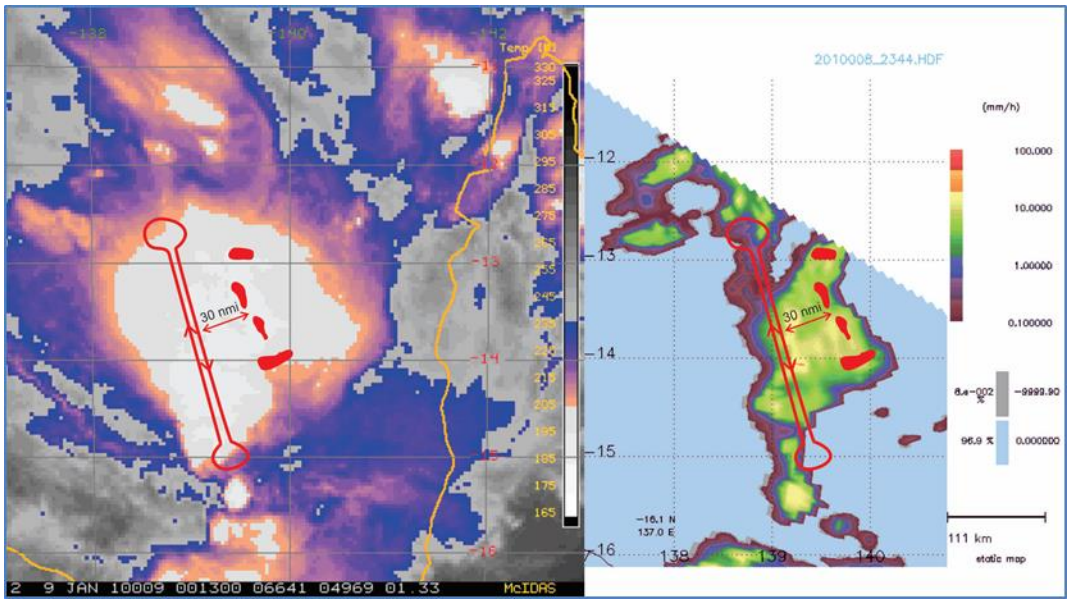

Figure 33. A strong tropical MCS with vigorous cells per Figure 32 ([1])

Figure 33 shows the corresponding idealized flight plan for a hypothetical *Strong Tropical* MCS with vigorous cells added here for illustration as red regions on satellite and radar pictures. In this case, an aircraft track a safe distance from vigorous cells would be chosen by the pilot, depicted in this figure as 30 Nm from the red echo on the pilot's radar, preferably downwind if safety permitted. With increasing pilot experience, this clearance was often reduced, but was normally not less than 10 Nm to the red-echo boundary.

Common methods were used in all three flight programs to select clouds for data collection and guide the aircraft during the cloud sampling. In Darwin-14, for example, the HAIC-HIWC team had office space at the Northern Territories Regional Weather Office, taking advantage of its general forecasting services while conducting its own specialized flight program forecasting and nowcasting. Due to the tendency for oceanic convection to diminish in the late morning, especially in Darwin, the HAIC-HIWC team started watching for suitable MCSs at about 1 a.m. local time. The objective was usually to plan for in-cloud sampling in daylight as early in the morning as possible, typically corresponding to an approximate 6:00 a.m. takeoff. Due to the time required to file and activate a flight plan, it was necessary to decide whether to conduct flight operations, and where to conduct them, about three hours before takeoff (i.e., ~ 3:00 a.m.). After takeoff, a team of scientists and forecasters on the ground provided real-time flight guidance to the pilots and scientists on board the aircraft. In Darwin, the main tools used for this were: (1) the MTSAT satellite imagery, provided in special rapid-scan format at ten-minute resolution by the Japan Meteorological Agency; (2) the Australian Bureau of Meteorology meteorological radar network (when the aircraft was within its coverage); and (3) the Global Position and Tracking Systems Pty. Ltd. (GPATS) lightning network. As the aircraft approached a target cloud, the ground team suggested start and end coordinates for first run through the cloud. If the run appeared to be impassable due to high reflectivity at altitude, the pilots adjusted the run so as to sample near the active cells from a safe distance (e.g., Figure 33). If the run did not have high reflectivity at altitude, it was then recommended to the pilots to use their onboard radar to optimize the run as follows: (1) on approach, tilt the radar down to identify any regions of heavy rain below the aircraft, and

adjust the start point to overfly the region; (2) set the tilt to zero degrees and change the radar to maximum gain to try to identify the region of maximum reflectivity at flight altitude ahead, and further adjust the run start and end points to fly through this region; and (3) after the first run, set up a survey pattern with parallel runs to the first, with a spacing to be determined according to the conditions, but typically 5-10 Nm apart (Figure 32). Survey runs were typically performed until the area under investigation was no longer active and TWCs had diminished, or if another more attractive target had developed within or near the current MCS. While the aircraft was busy performing a set of survey runs, the ground team provided feedback, and identified the target for the next cloud survey. This basic strategy of general guidance from the ground and onboard decision-making was practiced in all three flight programs and overseen by one or more of the same HAIC and HIWC scientists to ensure a level of consistency in the data collection.

In practice, the idealized flight plans were modified to return the best data for actual conditions, and could even combine the patterns of Figure 32 and Figure 33 depending on what was observed at flight altitude on the pilot's radar, and how the storm evolved. Figure 34 shows an example of an actual flight track for which the aircraft was able to penetrate active cells. The data are from an unnamed tropical storm sampled during Darwin-14 flight 12. Figure 35 shows time histories of IKP-2 TWC, updraft velocity, and satellite IR cloud top effective temperature (T_{eff}) along the aircraft track, for a northeast to southwest straight-and-level FL340 run at approximately -36 C. Note that in this example, the aircraft penetrated five distinct updraft areas where high IWC was found, the strongest of which reached almost 20 ms^{-1} and contained the highest maximum TWC of approximately 3.5 gm^{-3} for the run. The coldest satellite IR cloud top temperatures reached about -84 C in approximately the same location.

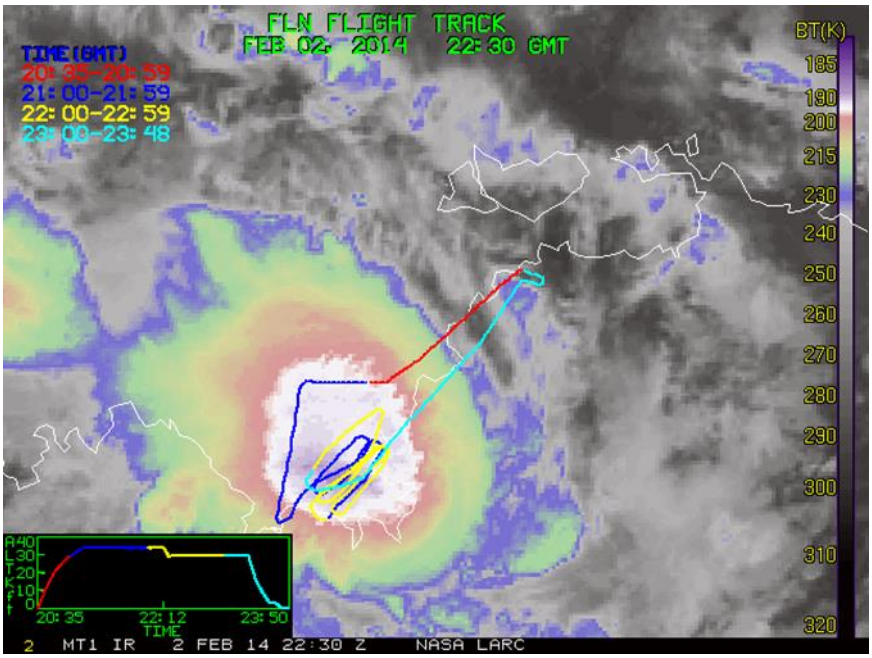

Figure 34. Actual flight plan for Darwin-14 flight 12 on 2 Feb 2014 in an unnamed tropical storm, showing the survey pattern used in an oceanic cloud system without vigorous cells at altitude (Courtesy of NASA Langley)

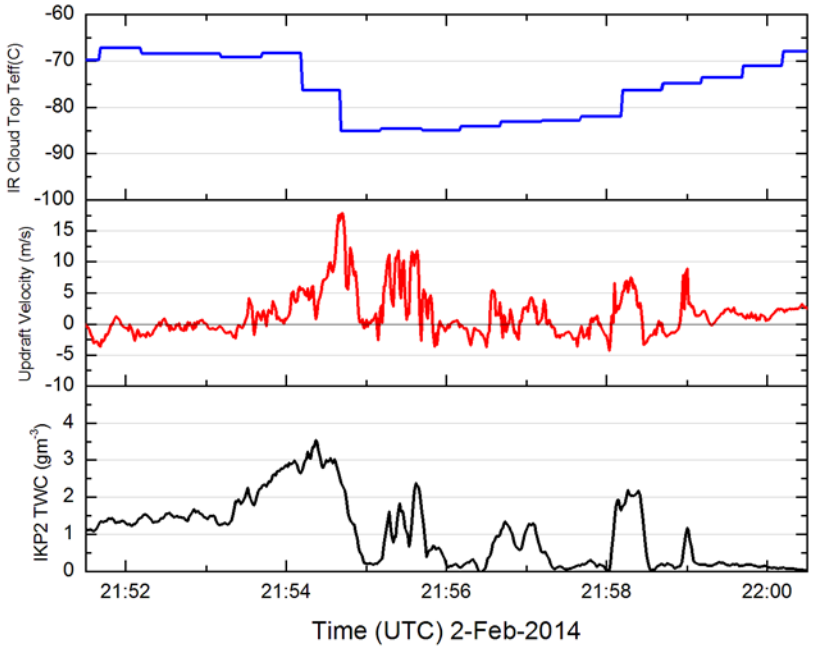

Figure 35. Sample time history of cloud parameters for a straight and level run from Darwin-14 Flight 12 (also see Figure 34). Average in-cloud temperature and pressure altitude were -35.6 and 33960 feet, respectively

Figure 36 shows a second example from the first run of Darwin-14 flight 16 through an MCS north of Broome. In this case, the lightning detection network observed a significant number of strikes to the north of the flight track (shown as orange "+" symbols on the figure). The run was chosen to cross the length of the MCS in deep cloud, but south of the most electrically active areas. In general, the pilots did not note the presence of high reflectivity at altitude in this storm, and the more vigorous cells were identified and avoided according to the occurrence of lightning. Along the first run itself, the pilots noted no issues with vigorous cells; however, on the next reciprocal run offset to the north, an area of graupel was encountered and a course change was made for further avoidance. Figure 37 displays cloud parameters along the first run. Several updraft areas were penetrated, the most significant near 22:28 UTC reaching about 10 ms^{-1}, and collocated with the peak TWC of about 2.5 gm^{-3} for the run. Satellite IR cloud top Teff estimates along the aircraft track were as cold at -84 C. This example illustrates how many of the flights were conducted. The aircraft worked in the area of cold cloud tops where active cells and high TWC could be expected. Vigorous cells with high reflectivity at altitude or lightning were avoided, while more benign adjacent cells were sampled in the same system. This run also is notable for the very long exposure to high TWC. The average TWC over the entire 105 Nm run is 1.49 gm^{-3}, the TWC peaks at about 2.5 gm^{-3} and rarely drops below 1 gm^{-3}.

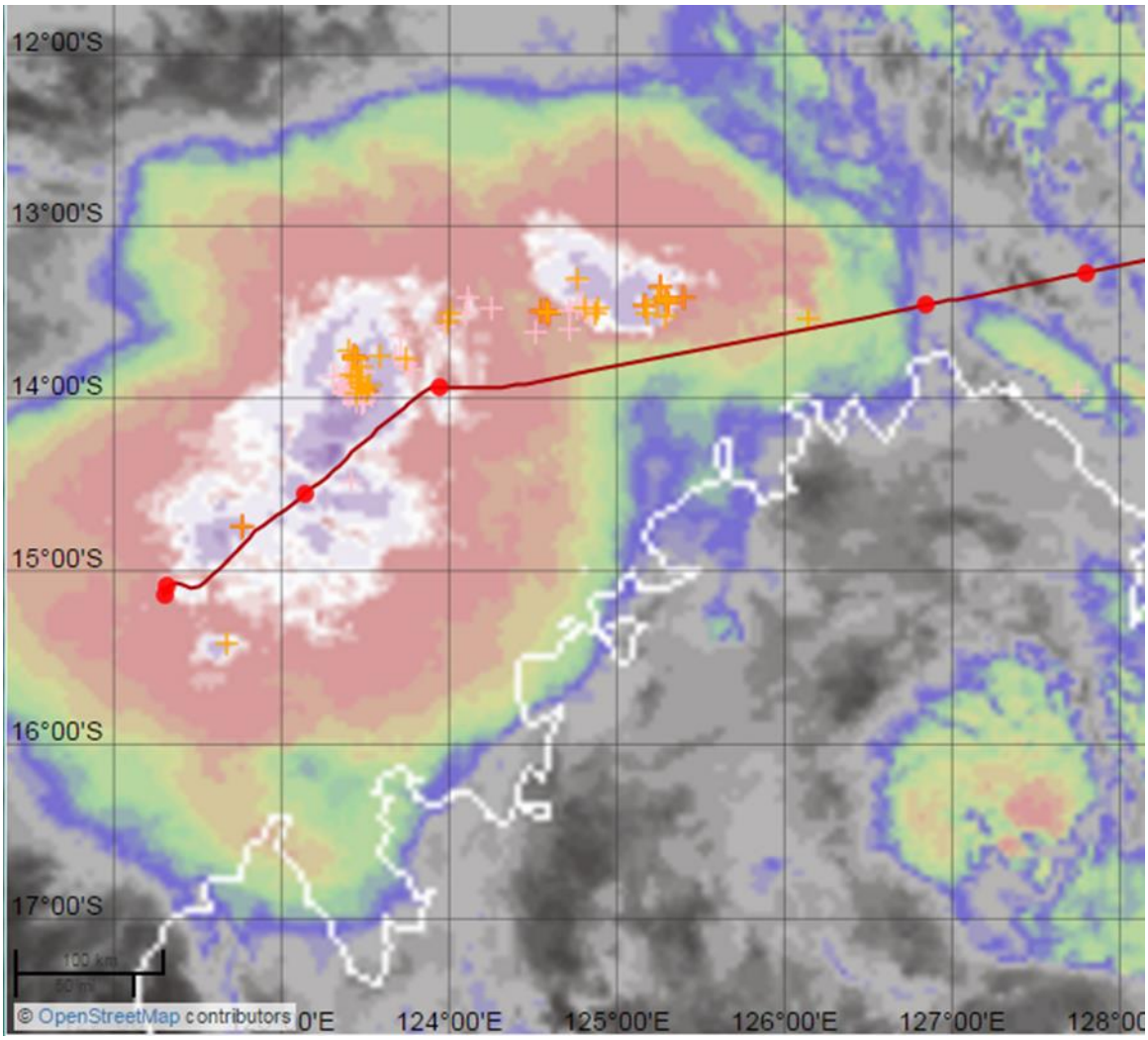

Figure 36. Falcon-20 track for first run during Darwin-14 flight 16, on 7 Feb 2014 ending at ~ 22:40 UTC (Courtesy of the National Center for Atmospheric Research Earth Observing Laboratory HAIC-HIWC Field Catalog. Lightning data courtesy of GPATS lightning network)

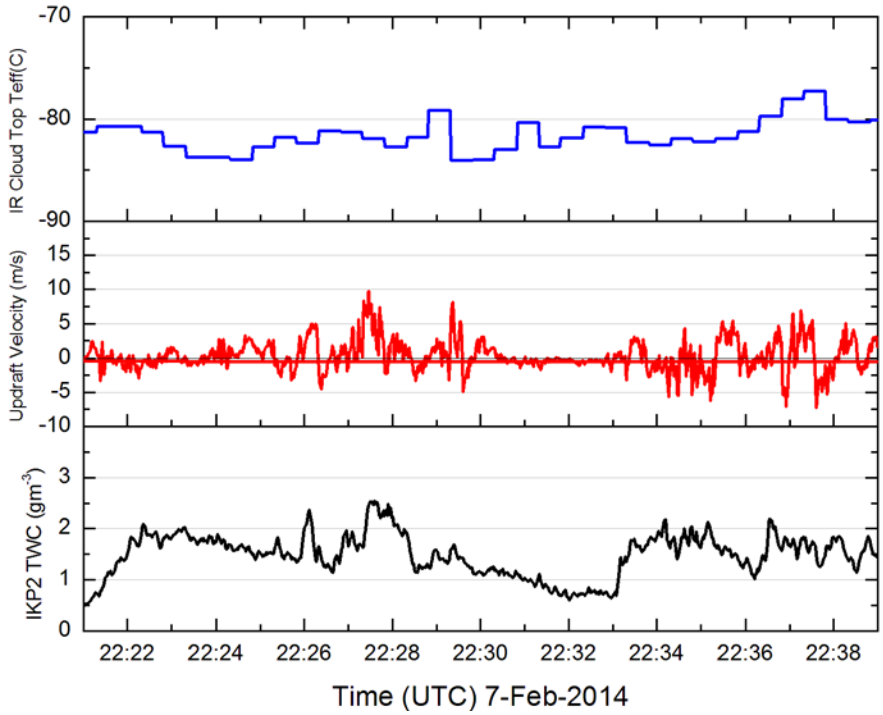

Figure 37. Sample time history of cloud parameters for a straight and level run from Darwin-14 Flight 16 (also see Figure 36). Average in-cloud temperature and pressure altitude were -37.0 and 33,998 feet, respectively

There is a possibility that the lightning avoidance methods used in the project may have somewhat biased the data set relative to conditions a commercial aircraft might encounter. Lightning strikes on commercial aircraft are not uncommon. It has been estimated that globally an aircraft is struck by lightning every 1000 flight hours [50][11]. It stands to reason that aircraft that commonly traverse regions of deep convective clouds such as those studied in this report would exceed this rate. For the flight campaigns, lightning strikes could damage the cloud-measuring equipment and cause major downtime for servicing that could threaten the data collection targets, particularly in Darwin and Cayenne, which were remote to home laboratories and manufacturers' facilities. Therefore, it was decided to avoid, as much as possible, cloud regions with significant electrical activity. The high level of lightning information used for flight guidance during the flight campaigns afforded much more efficient identification than on commercial flights, and thus more efficient avoidance. The above discussion related to Figure 36 illustrates how lightning avoidance affected the locations of cloud traverses. Such lightning areas were usually associated with the most recently formed active cells, and likely contained high IWC. In some cases, these cells contained high reflectivity at altitude, and therefore would not have been sampled according to the sampling strategy. In more radar-benign lightning areas, the cells were sometimes sampled once the lightning had subsided. How TWC levels in the data set may have been affected is unclear.

[11] The source of the strike rate in this article is cited without reference as provided by the French Office National d'Etudes et Recherches Aerospatiales (ONERA)

As an aside, only one lightning strike struck a project aircraft during the three flight campaigns, namely to the Falcon-20 during flight 10 of the Darwin-14 campaign, at approximately 22:54 UTC on 29 January 2014. Although the storm system did contain cells with concentrated lightning strikes, the strike to the aircraft occurred in a region well away from these cells. The aircraft was at -30 C and passing within 11 Nm of a cell with red echo at flight altitude, but with no lightning detected. Shortly after the strike, the pilot elected to land at nearby Gove Airport to inspect the aircraft, where no damage to the aircraft or research instrumentation was found.

3. RESULTS

3.1 DEFINITION OF DATA POINTS FOR APPENDIX D/P TWC COMPARISONS

The data from each of the three flight campaigns were analyzed to produce a set of data points for comparison of TWC_{99} values to the FAA Title 14 Code of Federal Regulations Part 33 Appendix D and the identical EASA CS-25 Appendix P TWC envelope (termed earlier as Appendix D/P). As recommended by the EHWG and EIWG and summarized in section 1.2.4, a total of at least 100 data points over a reference distance scale of 17.4 Nm, collected in deep convective clouds of the types described in section 2.4, were to be collected at each of the four reference temperature levels of -50, -40, -30, and -10 ±5 C (in order of priority). See section 1.2.4 for the rationale on the choice of a total number of 100 or more points.

The data points defined in this report will hereinafter be called "Type 1" data points, to distinguish them from other possible definitions[12]. Figure 38 shows a hypothetical depiction of Type 1 data points for a single cloud run, and for an arbitrary reference distance scale. The red circles mark the start and end points of non-overlapping distance-strips of equal length along the flight track. Each data point for this analysis is the average IKP-2 TWC value along the flight track within the circle. More precisely, each Type 1 data point average is computed for the narrow strip along the flight track from one end of the circle to the other, rather than within the total area of the circle. For this example, if the length of the run in Figure 38 were 130 Nm, the 13 non-overlapping points depicted in the figure would represent 10-Nm Appendix D/P TWC data points. For this report, non-overlapping Type 1 data points were computed in this manner for 13 distance scales from 0.5 Nm to 100 Nm. Although the definition of data points was not discussed in any great detail by the EHWG, the use of the Type 1 data point in this analysis was perhaps due to its similarity to what was provided by the icing cylinder measurements used for the FAR Part 25 Appendix C envelope [10].

[12] At least one other data point definition is being investigated by a HAIC-HIWC team partner and may be reported separately in the future.

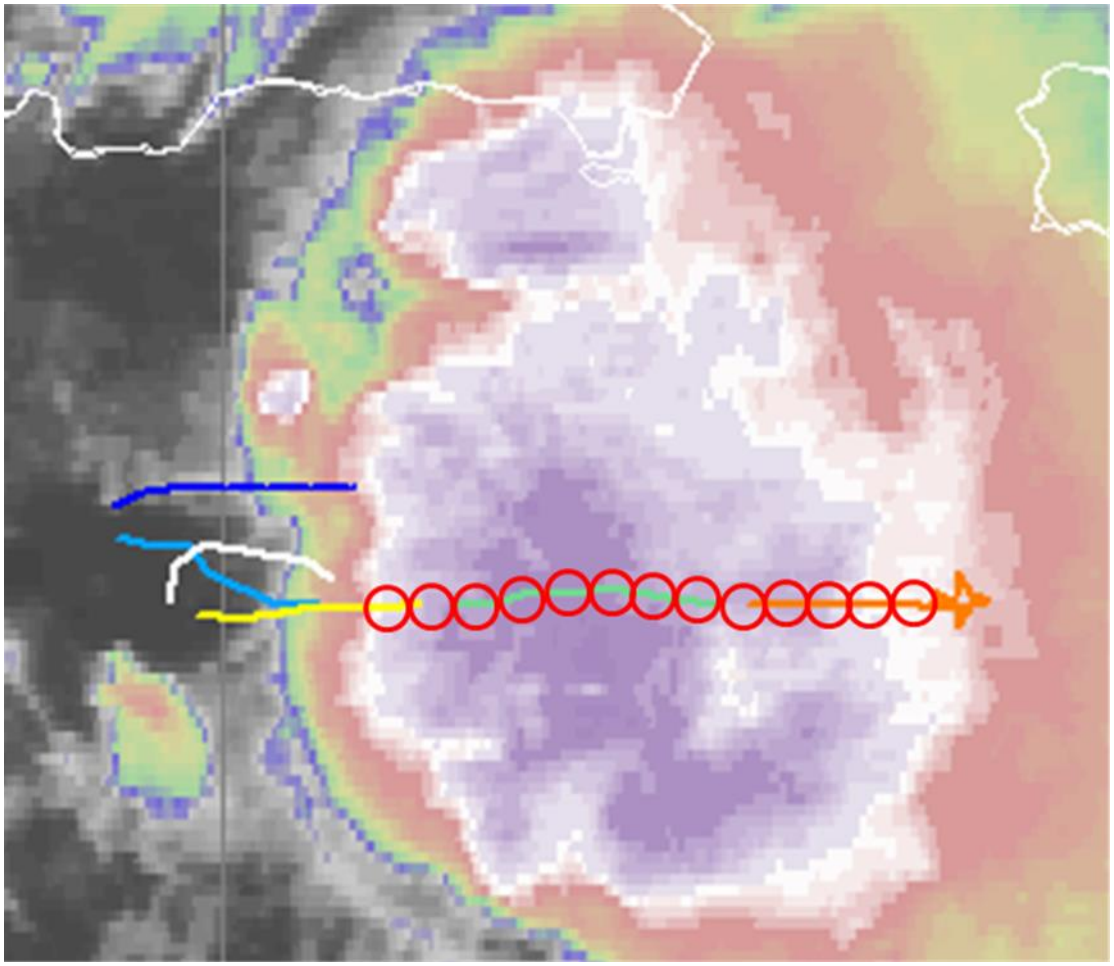

Figure 38. Sample time history of cloud parameters for a straight and level run from Darwin-14 Flight 16 (also see Figure 36). Average in-cloud temperature and pressure altitude were -37.0 and 33,998 feet, respectively

The procedure for this report was to first examine the cloud flight track data visually and then identify all the in-cloud level runs. All data in climbs or descents were excluded. A run was defined as a traverse across a cloud, similar to that which might be performed by a commercial aircraft. Overall, if the heading of a segment changed by more than 90 degrees, it was assumed that a repositioning in the cloud for a reciprocal run was underway, a new run was started, and at least part of the turn was usually excluded from the data set. In order to accurately define data points for averaging to different distance scales, the IKP-2 time series was transformed from one-second interval data to 0.01 Nm data by interpolation using the true airspeed measurements. An inventory of the data sets collected according to this procedure is described in the following section.

3.2 GENERAL INVENTORY OF DATA

Table 17 provides an inventory of the cloud runs for each flight program data set, and some basic information on the runs. Each flight data set contributes significantly to the final composite data set. Of the total 472 level flight runs from 52 project flights, 47 provided suitable data. The average length of the flight runs, by project, varies from 45.7 to 76.8 Nm, with an overall average of 63.4

Nm. Run lengths vary between 2.5 Nm and 236.1 Nm. The averages of the run-average TWCs vary from 0.62 to 0.79 gm^{-3}, with an average of 0.70 gm^{-3}. Note that these are averages, and not 99th percentile TWCs. The average run lengths and TWCs were similar for each project.

Table 17. Summary of cloud run properties from each flight program data set

	Darwin-14 Falcon-20	Cayenne-15 Falcon-20	Cayenne-15 Convair-580	Florida-15 NASA DC-8	All Projects
Number of flights with Appendix D/P cloud measurements:	16	17	10	9	52
Number of cloud runs	119	150	76	127	472
Avg. length of runs (Nm):	66.6	58.6	45.7	76.8	63.4
Min. length of run (Nm):	3.4	4.3	2.5	7.8	2.5
Max. length of run (Nm):	236.1	235.7	175.8	159.9	236.1
Avg. TWC (gm^{-3}) (avg. of run avgs.)	0.79	0.62	0.78	0.66	0.70

Table 18 shows the number of 17.4 Nm data points collected by project and temperature interval. Note that the -20 C interval was not requested by the EHWG but was occasionally sampled. Due to the small number of points (44), the -20 C interval will not be discussed in detail in this report. For all other temperature intervals, the target of 100 17.4 Nm points was exceeded by at least a factor of 2.5, and in fact 100 points were obtained at -50, -40, -30, and -10 C out to the 40, 50, 50, and 30 Nm distance scales respectively (not shown). The "all temperature intervals" row includes a few additional points for > -5 C for the Convair-580. Figure 39 shows the distribution of data points by project location in pie charts. In the -40 and -30 C intervals, there is a roughly equal contribution from the Darwin-14, Cayenne-15, and Florida-15 data sets. In the -50 C interval, the Florida-15 project is the main contributor. In the -10 C interval, almost all data are provided from the Cayenne-15 project by the Falcon-20 and the Convair-580. There were practical reasons for these proportions. After the Darwin-14 project, it was recognized that the campaign was lacking in -50 and -10 C data points, which were made priorities during the next Cayenne-15 project. The Convair-580, due to its ceiling, did almost all of its sampling within the -10 C level, with the Falcon-20 also providing substantial -10 C data in Cayenne-15. In general, the Falcon-20 was unable to reach to -50 C level until after about 1.5 hours of its three-hour flight time, limiting its opportunity to collect at -50 C. After the Cayenne-15 project, -50 C data were still lacking to reach the target of 100 points. The DC-8, with its ten-plus hours of flight time, had more flexibility in reaching the -50 C level, and the project made this temperature interval a high priority.

Table 18. Number of 17.4 Nm Type-1 data points collected at each temperature level by project

	Darwin-14 Falcon-20	Cayenne-15 Falcon-20	Cayenne-15 Convair-580	Florida-15 NASA DC-8	All Projects
-10 C (-15 < T ≤ -5)	12	101	153	5	271
-20 C (-25 < T ≤ -15)	17	26	1	0	44
-30 C (-35 < T ≤ -25)	141	130	0	174	445
- 40 C (-45 < T ≤ -35)	187	111	0	136	434
-50 C (-55 < T ≤ -45)	30	55	0	178	263
All temperature intervals	387	423	158	493	1461

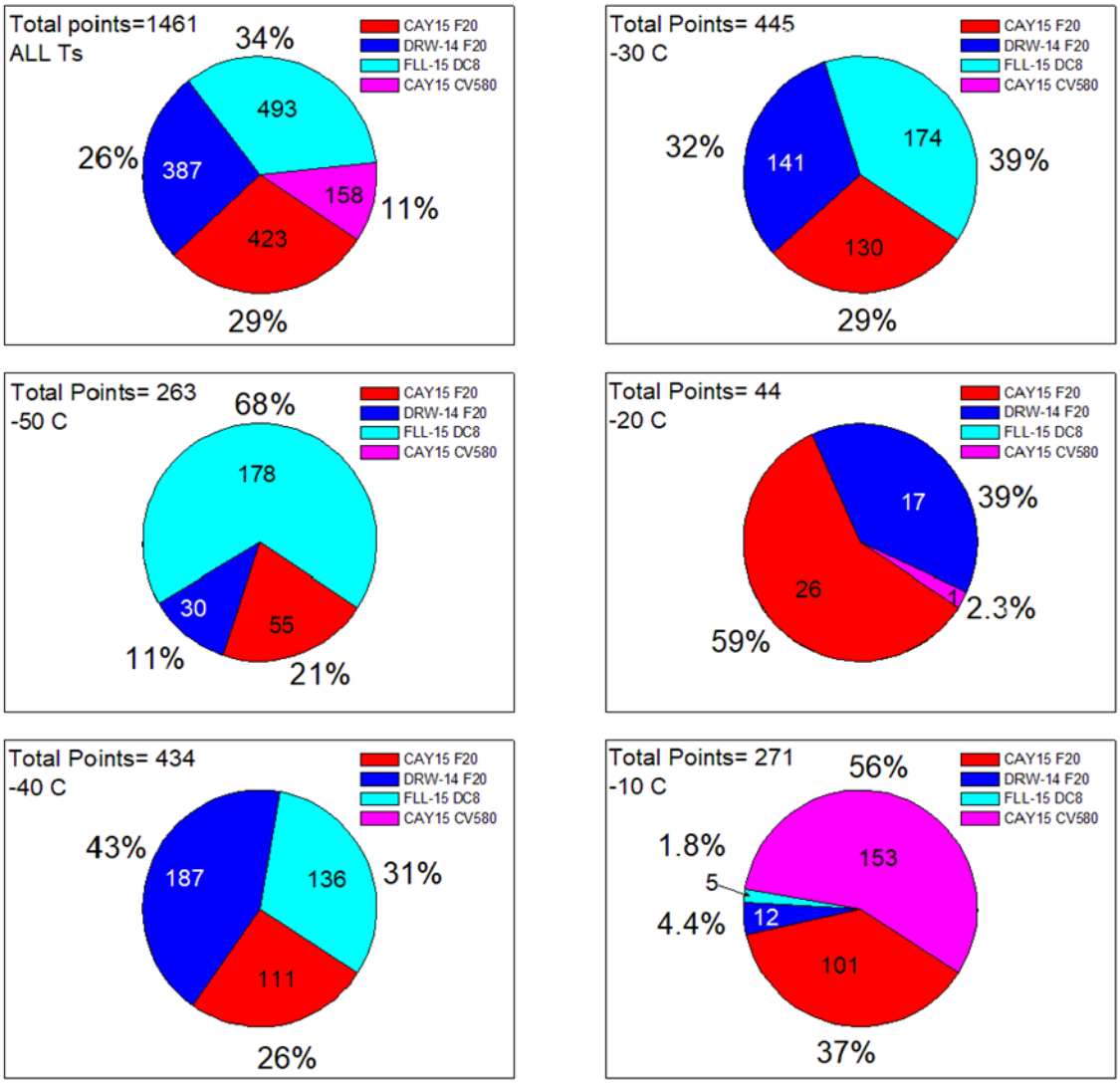

Figure 39. Number of 17.4 Nm Type 1 data points collected by data set at each temperature interval

3.3 TEMPERATURE-ALTITUDE ENVELOPE SAMPLED DURING FLIGHTS

Figure 9 shows the most recently published engine-event, temperature-altitude envelope. In this section, the corresponding data from the flight programs will be presented for comparison to the engine-event data.

Note that many of the engine events in Figure 9 experienced TAT anomalies, erroneous temperature readings caused by ice-particle icing in the sensor housing (also see section 1.2.2). The likelihood of occurrence of a TAT anomaly differs between aircraft types [33], an observation that these authors attributed to installation location of the probe. At least one Boeing aircraft has not experienced TAT anomalies at all. The probes used for temperature measurements in this study did not suffer from TAT anomalies, and the temperature measurements that follow are reliable. However, it is important to note that one auxiliary Rosemount temperature sensor installed on the

nose of the DC-8 aircraft for two flights experienced frequent TAT anomalies in high IWC conditions, while another Rosemount temperature probe installed for the other eight flights in the same location did not. This confirmed that the specific probe design was an additional factor to installation location. The observation of the TAT anomalies in the one probe also provided an important link to engine-event conditions, and confirmed that one could not infer a difference from engine event conditions from the lack of TAT anomalies in the bulk of the project's TAT data. A further link to engine events was the frequent observation of water of the windscreen in high IWC (melting ice particles), presumably equivalent to the "rain on the windscreen" noted by many engine-event pilots.

Figure 40 shows the average radiosonde temperature profiles during the periods of the Darwin-14, Cayenne-15, and Florida-15 flight campaigns, superimposed on the Appendix D/P temperature-altitude envelope. The profiles are similar, with Darwin being the warmest, Cayenne next, and finally Florida being the coolest profile. Departures of the Cayenne line from ISA are shown for reference on the figure for three of the targeted temperature intervals, varying between ISA +16.8 at -10 C and ISA + 10.7 at -40 C. All profiles suggest that the flight campaign in-cloud data points will be distributed within the warm extension of the Appendix D/P envelope.

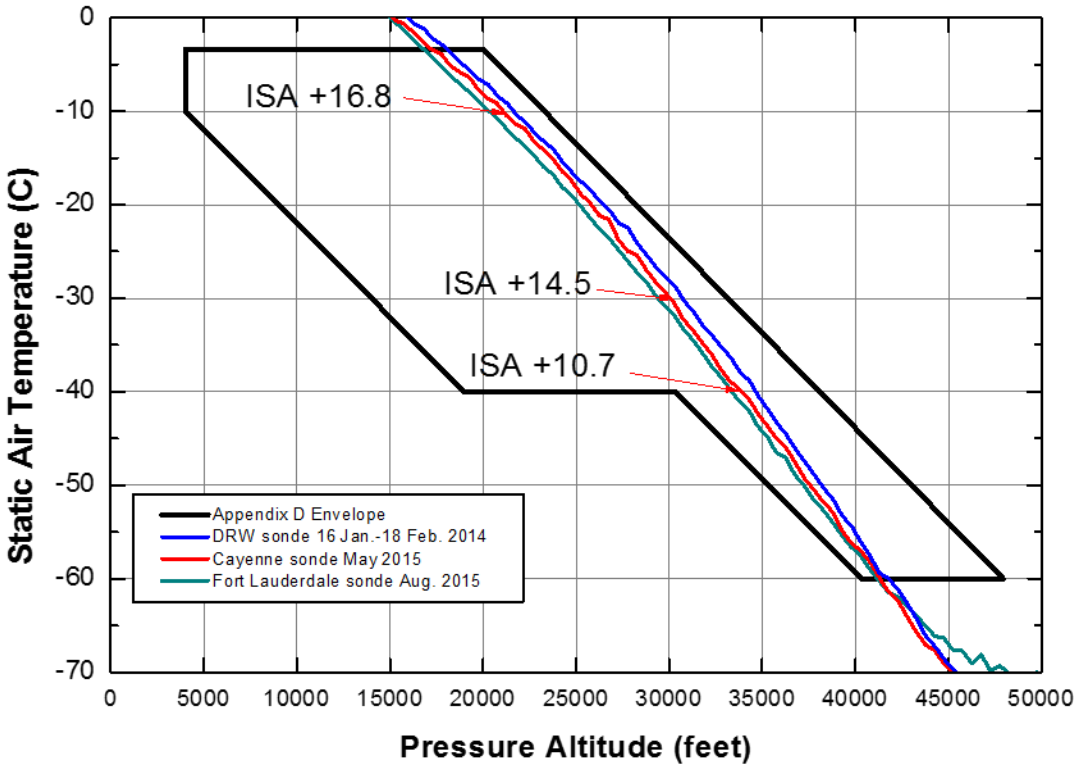

Figure 40. Average radiosonde measurements for three campaigns including departures from ISA values for the Cayenne May 2015 line

Figure 41 shows the in-cloud, temperature-altitude data from three flight campaigns, with each point representing the average pressure altitude and SAT for a single cloud traverse. The Darwin-14 (blue) data points tend to be the warmest, followed by the Cayenne Falcon-20 (red)

and finally the Florida DC-8 points (dark cyan), as suggested by the temperature profiles ofFigure 40. Deviations of the points from the average radiosonde profiles are expected due to individual daily temperature departures from the average profile, differences in location from the radiosonde station, and the effect of the cloud on the temperature profile. Overall, the cloud segments are within the warm extension of the Appendix D/P envelope. Comparing to the corresponding engine-event, data-point distribution in Figure 9, the flight program data are similar, although there are no data near -60 C due to the ceiling limitations of the aircraft, and there are more engine-event data towards the right-most (warm atmosphere) Appendix D/P boundary.

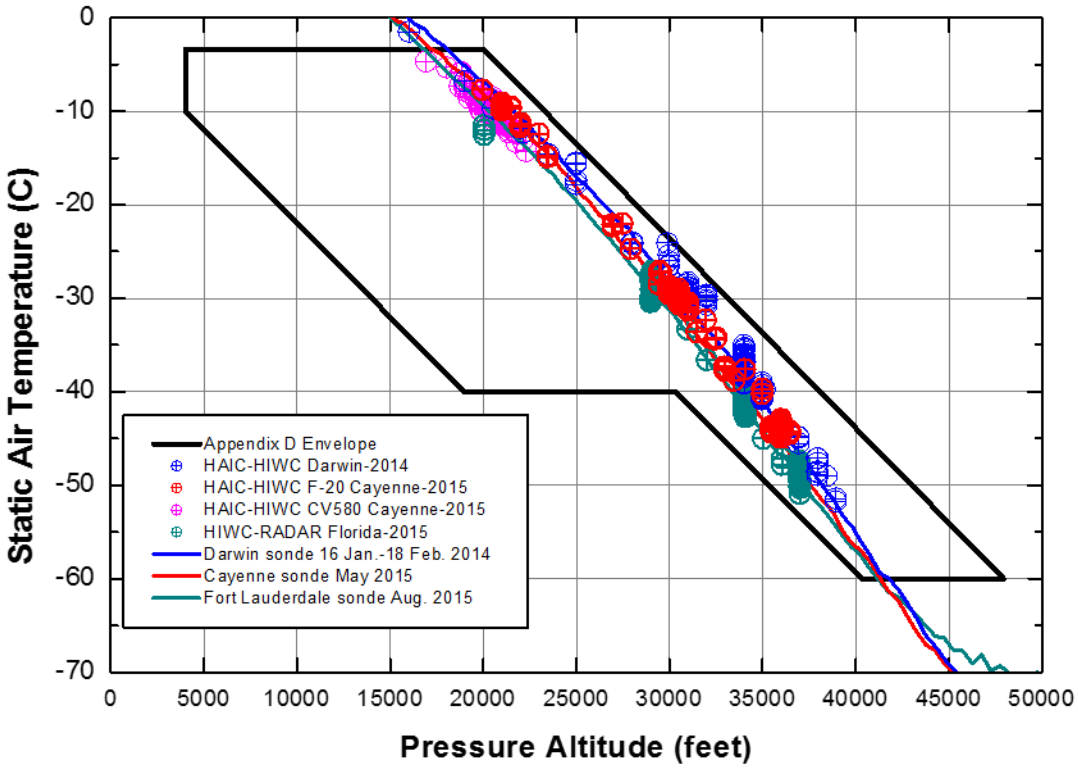

Figure 41. Temperature-altitude envelope data points for Darwin-14 and Cayenne-15 projects (Falcon-20 and Convair-580) and Florida-15 DC-8 project, with average radiosonde measurements from Figure 40

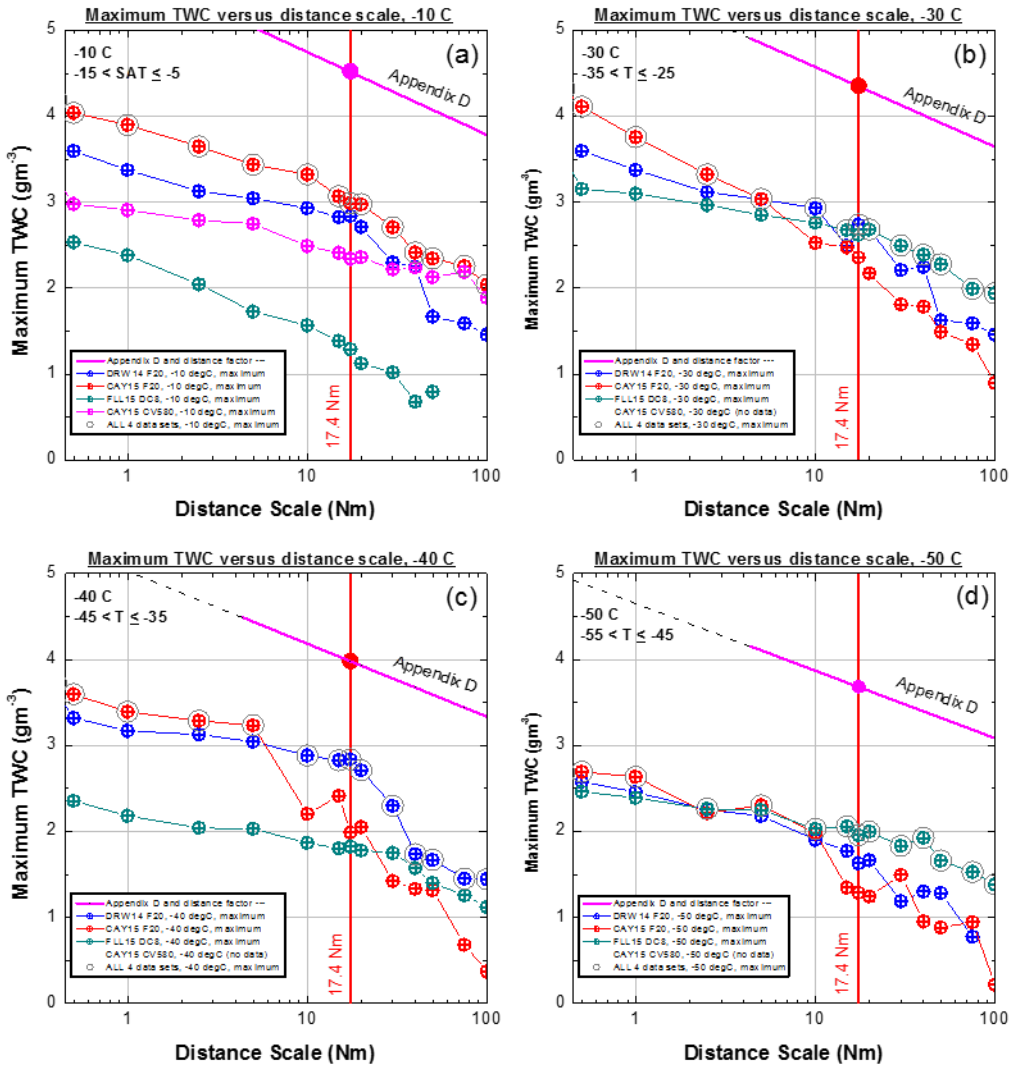

Figure 42. Maximum TWCs measured for four different project data sets at temperature intervals (a) -10 C, (b) -30 C, (c) -40 C, and (d) -50 C (overall max TWC in gray circle)

3.4 OCCURRENCE OF AND LWC LEVELS IN MIXED-PHASE

The current state of knowledge on mixed-phase clouds has been recently reviewed and reported [51]. These authors point out that although significant progress has been made over the past decades, there are still considerable gaps in our understanding. Although there is a significant body of information in the atmospheric literature on the occurrence of mixed phase in stratiform clouds and shallow convective clouds, there is little such information for mature deep convective clouds like those studied in these flight programs. High levels of LWC have been reported in one study in updrafts at the tops of convective clouds rising through the -40 C level [52]. However, the clouds studied during the HAIC-HIWC and HIWC-RADAR flight programs were typically mature MCSs with tops that had already reached -60 C or colder, and therefore already possessing abundant concentrations of ice that would influence the liquid content of any embedded updraft. Calculations have shown that the fraction of liquid in a mixed-phase cloud results from interplay between the rate of liquid depletion by vapor transfer to existing ice particles due to the difference

between saturation values with respect to liquid and ice, and the rate of production of condensate that is a function of the updraft velocity [53]. In the absence of any updraft, existing ice particles will eventually glaciate a mixed-phase cloud. The limited number of past in-situ measurements in mature, deep convective storms have found glaciated conditions in stratiform regions, and LWC only in core updraft areas [12, 54, 55], and then only at temperatures warmer than about -12 C [54]. In general, these studies indicate a rapid glaciation above the freezing level. In spite of this information, at the outset of the first HAIC-HIWC flight campaign, there was concern about the possibility of encountering heavy airframe icing, particularly at the -10 C level. In the end, such conditions were not observed during any of the three flight campaigns. In fact, supercooled LWC in cloud was infrequent, and airframe icing, at most, moderate. It is, however, important to keep in mind that the measurements of this campaign are from deep mature MCSs, and there is no claim here that they are generally valid for other cloud situations.

The IKP-2 probe measures both LWC from cloud droplets, and IWC from ice particles (TWC=IWC+LWC), and therefore does not provide direct mixed-phase information. The assessment of mixed-phase conditions requires experience in interpreting the idiosyncratic behavior of cloud in-situ instrumentation, which is typically performed using a combination of instruments ([48]). In the case of this report's data sets, the task is made more challenging by the generally low levels of LWC observed, and the high level of IWCs that have contaminating effects on instruments normally used to measure or infer LWC. Due to the technical nature of the discussion, details of the mixed-phase analysis are contained in Appendix D. Only results will be presented in this section.

The Convair-580 carried the most extensive set of cloud instrumentation, enabling a more quantitative estimate of the mixed-phase conditions. The Convair-580 mixed-phase analysis was performed by ECCC. The ten Convair-580 flights in Cayenne-15 that provide Appendix D/P assessment data were performed mostly within the 0 to -15 C temperature interval. Inspection of the instrument response revealed that hot-wires, normally used for LWC estimation in conventional clouds with a low-moderate IWC, suffered from a false response to ice crystals that was too large to permit an accurate estimation of LWC in this data set. However, the PMS FSSP-100 probe, measuring in the 2-47 µm cloud droplet size range, and equipped with anti-shattering tips (Appendix A) to reduce artifacts, displayed almost no ice crystal contamination and provided the aircraft's best estimate of the cloud LWC in high IWC conditions. The analysis revealed that mixed-phase regions in cloud were usually less than a few nautical miles wide. The liquid component was usually less than 0.1 gm^{-3} and never exceeded 0.25 gm^{-3}. The liquid fraction was usually less than 20% of the TWC. Spatially, the fraction of in-cloud distance with LWC > 0.1 gm^{-3} was estimated at about 5%. LWC regions identified by the FSSP-100 were highly correlated to negative excursions in the Ice Detector vibration frequency (called hereinafter an ice detector "deflection").

A similar analysis was performed for the Darwin-14 and Cayenne-15 Falcon-20 data sets, but with less instrumentation from which mixed-phase could be inferred. As in the case of the Convair-580 analysis, hot-wire probes were found to possess too large of a false response to ice crystals to be used accurately, possibly exacerbated by a suspected but uncharacterized concentration enhancement at the hot-wire LWC probe location on the lower fuselage of the aircraft. The assessment was done primarily based on the Goodrich Ice Detector, with additional information provided by the DMT CDP-2 probe, the latter similar to the FSSP-100 noted previously, but found

by ECCC to be more prone to contamination on the Convair-580 in high IWC situations. The data sets were visually inspected to identify all periods when there was a significant ice detector deflection indicating ice accretion on its vibrating rod, and thus the presence of supercooled LWC. The average LWC over the period was computed from the slope of the ice detector deflection, an estimate claimed here to be no better than a factor of 2 in accuracy. Although this instrument is not commonly used for LWC estimation, for this report, it was decided that it would provide less ambiguous measurements given the response problems of the hot-wires and CDP-2 in high IWC clouds. As it turned out, CDP-2 and ice detector LWC estimates were quite similar. The spatial fraction of liquid zones defined in this way decreased with decreasing temperature as expected, from about 2.8% to 0.36% to 0.20 % in the -10, -20, and -30 ±5 C intervals. No LWC zones were colder than -35 C. Even if the definition of a LWC zone was broadened to include zones with CDP-2 number concentrations greater than 10 cm^{-3} (an arbitrary concentration threshold that would usually identify the boundaries of a conventional liquid-droplet cloud), but with no discernible contamination due to ice crystals, the spatial fractions increase only slightly to 3.0, 0.8, and 0.7%, respectively. The median and maximum LWC exposure distances and event average LWCs were 0.7 and 6.2 Nm and 0.08 and 0.32 gm^{-3}, respectively. Overall, the results from the Falcon-20 are similar to those from the Convair-580 at -10 C, and would not have greatly changed had the CDP-2 LWC been substituted. However, the following shortcomings of the results are noted for project documentation. At temperatures near or warmer than a TAT of 0 C, the ice detector response can be unreliable. Erosion of accreted ice by impacting ice particles that would reduce ice-detector-derived LWCs is also suspected, although little is known about this effect.

The Florida-15 DC-8 data set had the least information from which mixed-phase information could be deduced. Ice detector data were available for only three flights, during which there were no deflection events. Using the CDP-2 concentration greater than 10 cm^{-3}, again, as a surrogate for possible LWC zones, only short distances were observed, and no major differences were revealed relative to the other data sets. Due to the uncertainty in the results, no quantitative information is provided here, but some information is included in Appendix D. Since the most significant contribution from the DC-8 is to the -50 C data set, and very little data was collected at -10 C, the lack of mixed-phase information from the DC-8 is not considered a significant issue.

In summary, mixed-phase regions in the four data sets were most common in the -10 C temperature interval, where the best estimate of spatial extent and levels of LWC (~5% of distance containing LWC > 0.1 gm^{-3}, and maximum LWC of about 0.25 gm^{-3}) were provided by the Convair-580 analysis. At -30 C, the Falcon-20 data revealed a spatial fraction of about 0.2-0.7%, depending on how LWC zones were defined. The median and maximum LWCs of the only seven ice-detector events were 0.10 and 0.12 gm^{-3}, respectively. The coldest temperature at which an ice detector deflection was observed was -34.8 C.

3.5 IN-SITU TWC RESULTS

3.5.1 TWC_{99} Uncertainty Summary

Appendix B describes the efforts to estimate the uncertainty in IKP-2 TWC_{99} estimates and percentiles. This effort has been undertaken to support the legitimacy of the TWC measurements, and is considerably more detailed than what is usually produced for TWC uncertainty estimates

within the atmospheric science community. Combining the component estimates into a single error term is not straightforward. The results are summarized in point-form below.

- System accuracy estimates [56] reveal that uncertainty is temperature-dependent due to the importance of background water vapor (BWV) subtraction, and, in relative terms, is highest at low TWC and warm temperatures. Although TWC errors are predicted to be up to 50% at 0.1 gm^{-3} and -10 C, they are small at the high levels that determine the TWC_{99} values. These idealized uncertainties are estimated to be about 3.5%, 2.2%, 2.1%, and 2.1% at the levels of the 17.4 Nm TWC_{99} values at -10, -30, -40, and -50 C.
- Direct comparisons were made to two LWC references: a field calibration cart developed specifically for this project, and the NASA IRT. In the first case, the slope of the best-fit lines for multiple calibrations was found to be ±1.05, with no systematic difference. In the second case, a systematic scale factor difference was observed, with the IKP-2 being about 11% higher than the NASA IRT. The IRT staff claims the accuracy of their reference to be about10%. This scale factor difference would suggest a conservative error (overestimate) in TWC if applied solely to the IKP-2.
- Precision of the two IKP-2 probes used in the flight campaigns, estimated by independent testing of the same test points at the IRT, is very high, at approximately 1%.
- IWC references in wind tunnels are less developed and poorly documented. The team performed its own comparisons at the NRC M7 test cell using ice capture tubes (ICTs), a method that has been used in other tunnels, but with no accuracy estimates that we could find. The ICT method was found to be problematic and prone to underestimation [38]. The IKP-2 measured systematically higher TWC values, on the average by 20%. The discrepancy is believed to be largely due to the underestimation of the ICTs. Nevertheless the 20% agreement was taken as a positive and unique result for IWC measurements, at least suggesting that there were no gross errors specifically related to the IKP-2's ability to melt and evaporate ice particles.
- A possible IKP-2 systematic overestimate of up to 11% is acknowledged based on the IRT test results above, but it is recommended to revisit this if and when further information becomes available. The ICT results are not considered accurate enough to provide a sound reference comparison.
- Due to troubles with the BWV measurements on the aircraft during the flight programs, it was necessary to assume BWV at ice saturation values in clouds for all flight campaign data. ECCC has provided the first estimates of the error incurred at -10 C using the only four flights with reliable BWV measurements (Appendix B, section B.4.1). Although ECCC found that errors could be substantial in relative terms at low TWC, they were small at the high levels that determine the TWC_{99} values, typically less than 2%. A comparison of the two independent IKP2 calculation algorithms using ice saturation BWV (one for the Convair 580 and the other for the Falcon-20 and DC-8) to the "truth" value computed for the four flights with good BWV measurements yielded overall TWC_{99} overestimation at -10 C of less than about 4%, and less than 1% at the reference distance of 17.4 Nm. On the average, the two calculation algorithms were found to differ from each other by less than 3% for TWCs greater than 1.5 gm^{-3}.
- The effect of the ice-saturation BWV assumption in the temperature intervals other than -10 C was estimated using a Monte Carlo simulation of the IKP-2 TWC calculation, using input TWC frequency distributions from the composite data sets, and BWV error

distributions provided by the four Convair-580 reference flights at -10 C (Appendix B, section B.4). Simulations predicted decreasing error with decreasing temperature. Taking into account the small underestimate of the errors by the Monte Carlo simulations for the four reference flights, results yielded an overestimate of TWC_{99} in the -10, -30, -40, and -50 C intervals of up to roughly 6%, 5%, 1%, and 0.1% respectively. The relatively small effect of the ice saturation BWV assumption is a result of the observation that, on the average, BWV values only slightly exceeded ice saturation during the four Convair-580 reference flights, particularly at the high IWC values.

- Statistical uncertainty in TWC_{99} values due to sampling was estimated using a random data set re-sampling procedure (Appendix B, section B.5). Effects include an increasing low-bias in the TWC_{99} mean value as sample size decreased, and variation in the TWC_{99} estimates during random re-sampling. Above a distance scale of about 30 Nm, there is a concern that uncertainty estimates become increasingly unreliable due to reduction in the data set diversity (fewer clouds and fewer runs).
- Final adjustments and assignment of uncertainties to the IKP-2 TWC_{99} values and other percentiles, that take into account both errors due to ice saturation BWV assumption, and sampling effects, have been provided by random resampling of the Monte Carlo simulations noted above (Appendix B, section B.6). These estimates and uncertainties are included in section 3 in the plots of TWC_{99} versus distance (Figure 43 through Figure 47), and the cumulative frequency distribution plots (Figure 48 through Figure 57). Appendix F and Table F-1 through Table F-14 provide these values for all the data set subsets, and temperature intervals when sufficient numbers of data points are available. Bias due to sampling uncertainties and errors due to the assumption of ice saturation BWV work in opposite directions. Ice saturation assumption errors generally dominate at the warmer temperatures and shorter distance scales. Sampling bias generally dominates at the longer distance scales. At the 17.4 Nm distance scale, the adjustments of the TWC_{99} values for the composite data sets are less ± 2% over all temperature intervals, and sampling uncertainty ($\pm 2\sigma$) varies between about 8 and 12%. Further insights may be provided by a statistician's review.

3.5.2 Maximum and Ninety Ninth Percentiles

The in-situ measurements of the IKP-2 maximum and TWC_{99} values for Type 1 data points (section 3.1) will be summarized here. The results will be displayed for the four different temperature intervals, and as a function of distance scale, from 0.5 Nm to the maximum distance scale for which 100 points are available. In this section, data for Darwin-14 Falcon-20, Cayenne-15 Falcon-20, Cayenne-15 Convair-580, and Florida-15 DC-8 data are shown as blue, red, magenta, and dark cyan symbols, respectively. The shortest distance scale presented is 0.5 Nm. IKP-2 readings on shorter distance scales are considered unreliable due to an observed overshoot/undershoot problem with the IKP-2 LI-COR 840A hygrometer that is not discernable with 5-second (~ 0.5 Nm) or longer averaging.

Figure 42(a-d) displays the maximum IKP-2 TWC values measured in the four data sets. The maxima for the combined four data set values are circled with open gray symbols. As distance scale increases, all maximum TWC values decrease due to averaging over the longer distances. At short distance scales, the maximum values were observed in the Falcon-20 Cayenne-15 data set for all four temperature intervals. Other data sets have higher maximum values at longer distance

scales except at -10 C, where the Falcon-20 Cayenne-15 data set has consistently higher maximum TWC values. The project maximum TWCs at the shortest distance scale of 0.5 Nm, and at17.4 Nm were 4.1 and 3.0 gm^{-3}, both measured by the Falcon-20 in Cayenne-15 at -30 C and -10 C, respectively. The project maximum TWCs at the highest priority -50 C temperature interval at 0.5 and 17.4 Nm were 2.7 and 2.0 gm^{-3}, measured by the Falcon-20 in Cayenne-15 and the DC-8 in Florida-15, respectively.

Percentiles were calculated by ranking all data points in order of TWC, defining a percentile value for each of the ranked values, and then estimating the TWC percentiles at discrete levels (e.g., 99^{th} percentile) by linear interpolation. The particular method for calculating the percentile of each point is described in [57-58] as method 7, where a total of nine methods are discussed. Some small variations in the 99^{th} percentile can be expected according to the definition used. Definition 7 yields identical results to the "percentile" function in MicroSoft Excel 2010. Note that the 99^{th} percentile value is determined by this method by the highest 1% of the data points, and thus can be quite insensitive to the lower TWC values in the frequency distribution. If the TWC points are evenly distributed, the resolution of these percentiles is at best 1/n, where n is the number of data points, so 100 points provide in rough terms a 1% resolution of the 99^{th} percentile. Accordingly, in the following graphs, TWC_{99} values will be displayed only up to distance scales with at least 100 data points unless otherwise noted. Differences between the four data sets are discussed in section 3.5.4.

Figure 43 through Figure 47 display the IKP-2 TWC_{99} values from the flight campaigns for each temperature interval as a function of distance scale. Separate plots are provided for each data subset (i.e., Darwin-14 Falcon-20, Cayenne-15 Falcon-20, Cayenne-15 Convair-580, Florida-15 DC-8, and all subsets combined for a composite TWC_{99}). The composite results for all four data sets combined are shown as open black squares. The straight TWC_{99} value calculated directly from the data subsets are shown as the open symbols. Open circles represent the TWC_{99} values calculated directly from the individual project data sets, with embedded small symbols representing the values corrected for sampling bias and ice saturation assumption, and error bars estimating the 2-sigma statistical sampling uncertainty. The corrected TWC_{99} values and uncertainties, estimated from the Monte Carlo simulations described in section 3.5.1 and Appendix B, are shown as small solid circles with $\pm 2\sigma$ uncertainty bars, and are arbitrarily shown for up to one distance scale higher than the straight TWC_{99} values. The project subset values are deliberately displaced slightly on the X axis from each other for visual separation, with the composite data set centered on the actual distance scale. Note that in Appendix B the uncertainties for distance scales greater than 30 Nm appear to decrease due to decreasing data set diversity, and though they are included in these figures, they have been flagged as questionable. A vertical red dotted line identifies the Appendix D/P 17.4 Nm reference distance scale, and an inset expansion window is provided in each plot to permit more accurate comparisons of the data sets near this reference distance. The red solid symbol near the top of each diagram shows the Appendix D/P TWC at 17.4 Nm for the average pressure altitude and SAT of the data sets in the temperature interval, and the sloped magenta line shows the corresponding Appendix D/P TWC as a function of distance scale after applying the Appendix D/P distance factor. The ratio of the combined results to Appendix D/P at 17.4 Nm is 58.2%.

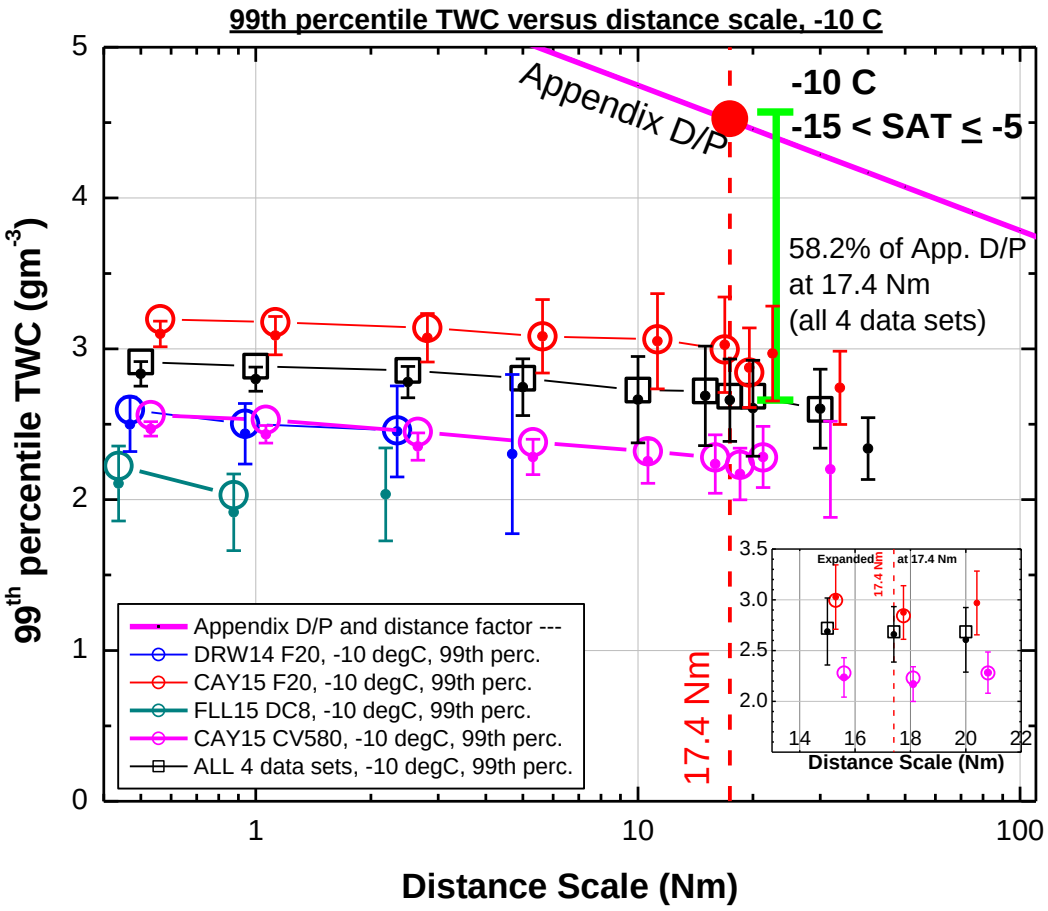

Figure 43. Comparison of 99th percentile TWC values as a function of distance scale for temperature interval -10 C (± 5 C) for the four data sets. Open symbols plotted for points with > 100 samples bias-corrected and error bars extended one distance scale

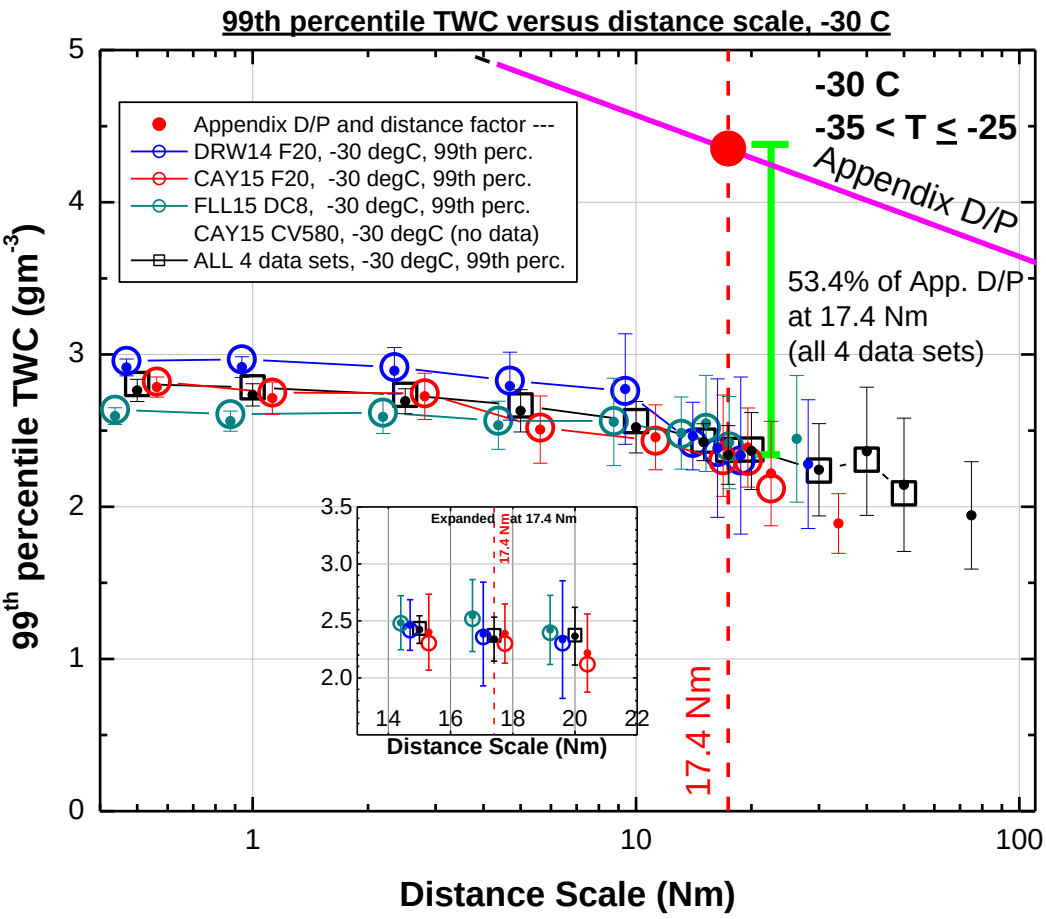

Figure 44. -30 C (± 5 C) temperature interval per Figure 43

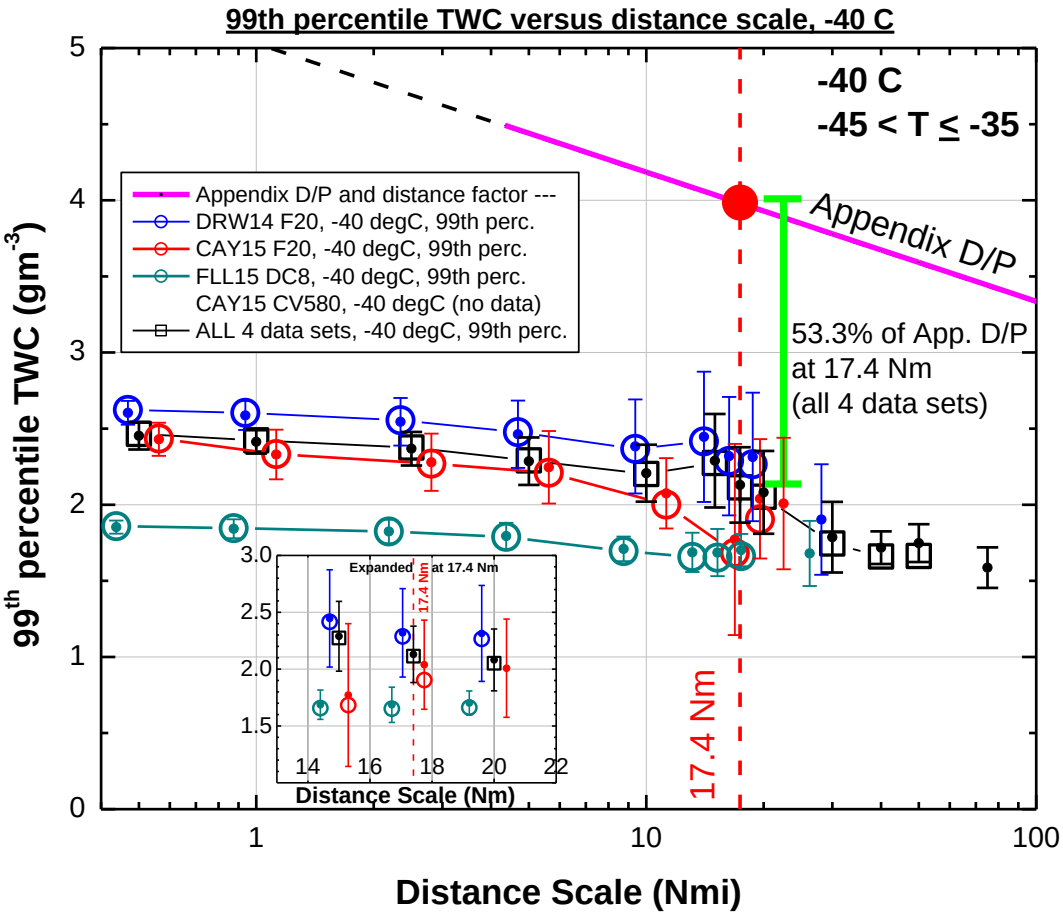

Figure 45. -40 C (± 5 C) temperature interval per Figure 43

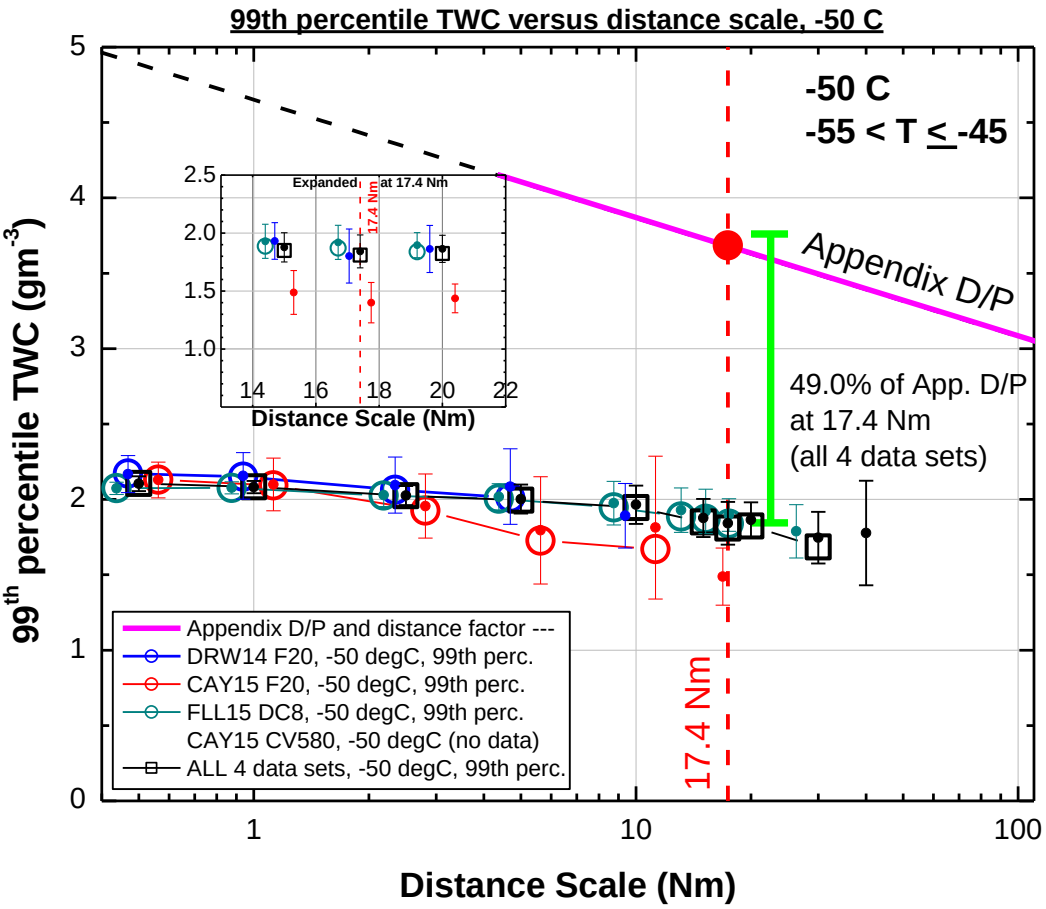

Figure 46. -50 C (± 5 C) temperature interval per Figure 43

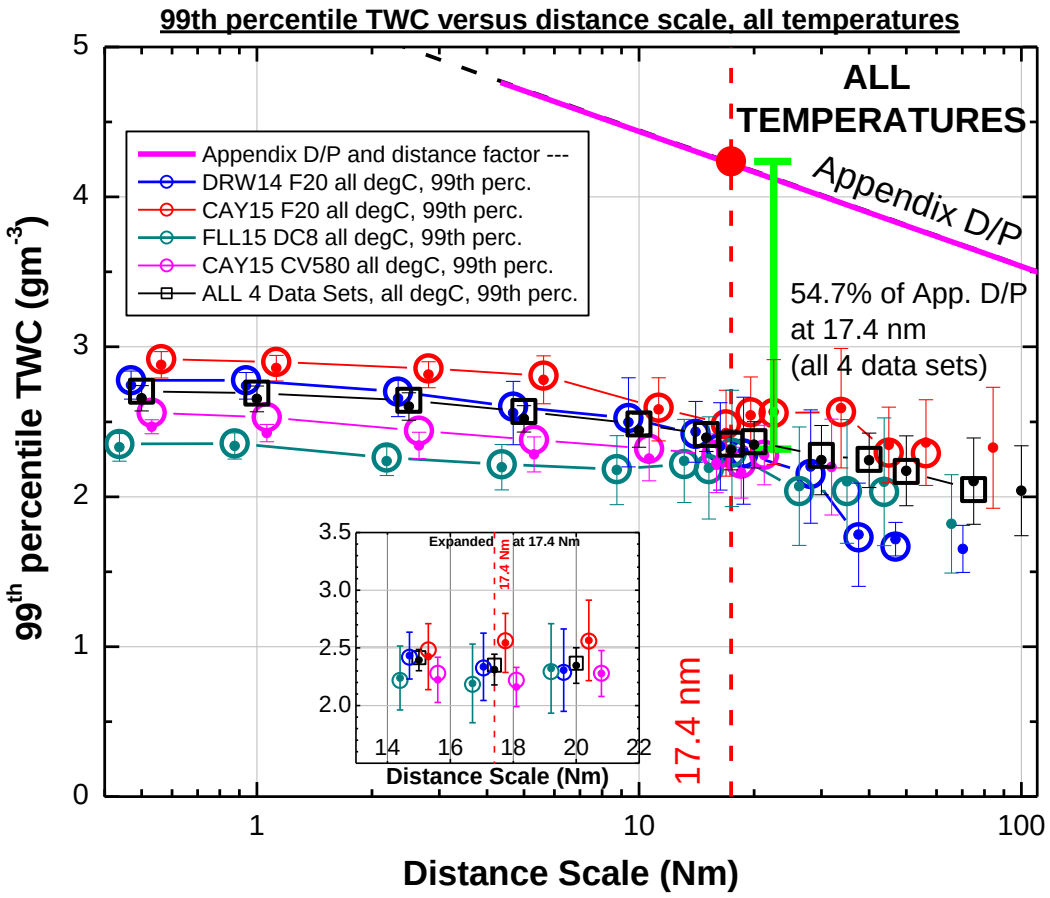

Figure 47. All temperature intervals per Figure 43

Figure 43 displays the TWC_{99} results for -10 C (± 5 C), by project, as a function of distance scale. As discussed earlier, almost all of the data points described in this figure (93%) come from the Cayenne-15 Falcon-20 and Convair-580 data sets (section 3.2, and Figure 39). Note that at short distance scales all TWC_{99} values are significantly lower than the maximum value in Figure 42(a). This is simply due to the fact that at the lower distance scales, there are a very large number of points. For example, at 0.5 Nm and -10 C, combining the data sets there are 11524 data points, so the maximum value shown in Figure 42(a) represents something closer to a (1-1/11507)*100 percentile, or approximately the 99.99th percentile.

The combination of all four project -10 C data sets yields a final corrected TWC_{99} value (small solid black circles) of 2.66 gm^{-3} at 17.4 Nm from 273 data points, with a ±2σ uncertainty of about ±0.27 gm^{-3}. One hundred data points are available out to 30 Nm, where the TWC_{99} has dropped marginally to 2.62 gm^{-3}. The change in the 99th percentile TWC with distance scale will be discussed later in section 3.5.6. The difference relative to Appendix D/P is illustrated by the vertical green span line from the Appendix D/P point to the combined data set point at 17.4 Nm, with the 58.2% percentage of Appendix D/P shown in text to the right of this span line.

Figure 44 shows the corresponding results for the -30 C (± 5 C) temperature interval. The ceiling limit of the Convair-580 prevented it from contributing any data to the -30, -40, or -50 C intervals.

In the -30 C interval, there are approximately equal contributions of points from the three remaining data sets (Figure 39). There are only small differences between the TWC_{99} values of the three locations, although the Florida-15 DC-8 data set tends to be the lowest except at the longest distance scales. The combined data set yields a TWC_{99} value at 17.4 Nm of 2.34 ±0.20 gm^{-3}, 53.4% of Appendix D/P. One hundred data points are available out to 50 Nm.

Figure 45 shows results for the -40 C (± 5 C) temperature interval. Again, there are nearly equal contributions of points from the Darwin-14, Cayenne-15, and Florida-15 campaigns (Figure 39). At 17.4 Nm, the Florida-15 data set yields the lowest TWC_{99} values, about 30% lower than the highest values (from Darwin-14). The combined data set TWC99 at 17.4 Nm is 2.14 ±0.25 gm^{-3}, 53.3% of Appendix D/P.

Figure 46 shows results for the -50 C (± 5 C) temperature interval. In this case, the majority of the data points (68%) are contributed by the Florida-15 campaign. The TWC_{99} values are very similar for all three projects. The TWC_{99} value of the combined data set at 17.4 Nm is 1.84 ± 0.14 gm^{-3}, 49.0% of Appendix D/P.

Figure 47 summarizes the TWC_{99} results where all the temperature intervals from each data set are combined. The figure also contains a curve for a complete composite of all projects and temperature intervals. Due to the uneven distribution by temperature of data points from each project, and the change in TWC_{99} with temperature revealed above, combining the data sets this way may be of limited value. Nevertheless, the results are provided for completeness. At 17.4 Nm, the composite TWC_{99} value is 2.32 ± 0.13 gm^{-3}, 54.7% of the estimated Appendix D/P value.

For additional project documentation, Table F-1 through Table F-14 contain maximum TWC, unadjusted TWC_{99}, 50^{th} and 99^{th} percentile corrected TWC_{99} and uncertainty, and SAT and pressure altitude for a series of distance scales, by data set and by temperature interval.

Note that when progressing from the warmest to the coldest temperature interval, the Appendix D/P TWC at 17.4 Nm decreases with each temperature change, from 4.53 gm^{-3} at -10 C, to 3.70 gm^{-3} at -50 C. The flight campaign TWC_{99} values at 17.4 Nm also decrease with each temperature change, from 2.66 gm^{-3} at -10 C, to 1.84 gm^{-3} at -50 C. In fact, the Appendix D/P and observed TWC_{99} values decrease with decreasing temperatures at roughly the same rate, with the composite ratio of observed to Appendix D/P at 17.4 Nm being about 54.7% (58.2%, 53.4%, 53.3%, and 49.0% at -10, -30, -40, and -50 C, respectively). This is an interesting result that indicates there is support in the data set for the underlying assumption that is the basis for Appendix D/P TWC values, i.e., that peak values of TWC should be linked to core updraft areas and associated adiabatic TWC estimates. This, in turn, provides some support for the continued use of the form of Appendix D/P (Figure 10). Regarding the development of that figure, recall that it is based on calculations of adiabatic (theoretical maximum condensed) TWC for deep lift, scaled down by a factor of 0.65 based on calculation of 17.4 Nm TWC_{99} values for the 1950s RAE data set [27]. If one had started the exercise of ref. [27] with the all-temperature data set (Figure 47) of this report rather than the RAE data set, one would simply have calculated a scale factor of about 0.36 (0.547 * 0.65) rather than 0.65 to derive the Appendix D/P TWC figure (Figure 10). Adopting a new scale factor for Appendix D/P TWCs may be an option if it is so decided that a change is appropriate.

3.5.3 TWC Cumulative Frequency Distributions (CFDs)

Figure 48 and Figure 49 show the TWC cumulative frequency distributions by data set for the 0.5 and 17.4 Nm distance scales in the -10 C interval. Symbols estimate values corrected for the assumption of ice saturation, background water vapor, and statistical sampling low bias (Appendix B). Error bars represent ±2 standard deviation uncertainties estimated for sampling statistics and background water vapor uncertainty combined. If fewer than 100 data points were collected, lines are dotted, and symbols and uncertainty bars are not plotted. The lower figure covers the entire percentile range, and the upper figure is a magnified view of the 0.9-1.0 percentile range. Data are for the reference 0.5 Nm distance scale.

Figure 50 through Figure 58 contain the corresponding TWC CFDs for the -30, -40, and -50 C intervals, and the combined data sets containing all data from these intervals. While providing information additional to the TWC99 values, these figures also better illustrate differences between the individual data sets, as discussed in the next section. In each figure, the directly measured TWC CFDs are given by the solid lines, or dotted if the data set contained less than 100 points, and corrected percentiles with $\pm 2\sigma$ uncertainties from the Monte Carlo simulations of section B.6 (incorporating both ice saturation BWV errors and sampling uncertainties) are provided as open symbols with horizontal error bars at selected intervals. The number of flight campaign data points for each data set is contained in the legend.

Figure 58 displays the ratio of 99.9th to 99th percentile IKP-2 TWC by data set and as a composite data set for: (a) all temperatures combined , (b) -50 C, (c) -40 C, (d) -30 C, and (e) -10 C. Panel (f) contains the composite four data set results by temperature interval. Ratios are shown only for distance scales at which at least 500 points were collected. Uncertainty bars define 95% confidence intervals, determined using the Monte Carlo simulation described in Appendix B, section B.6.

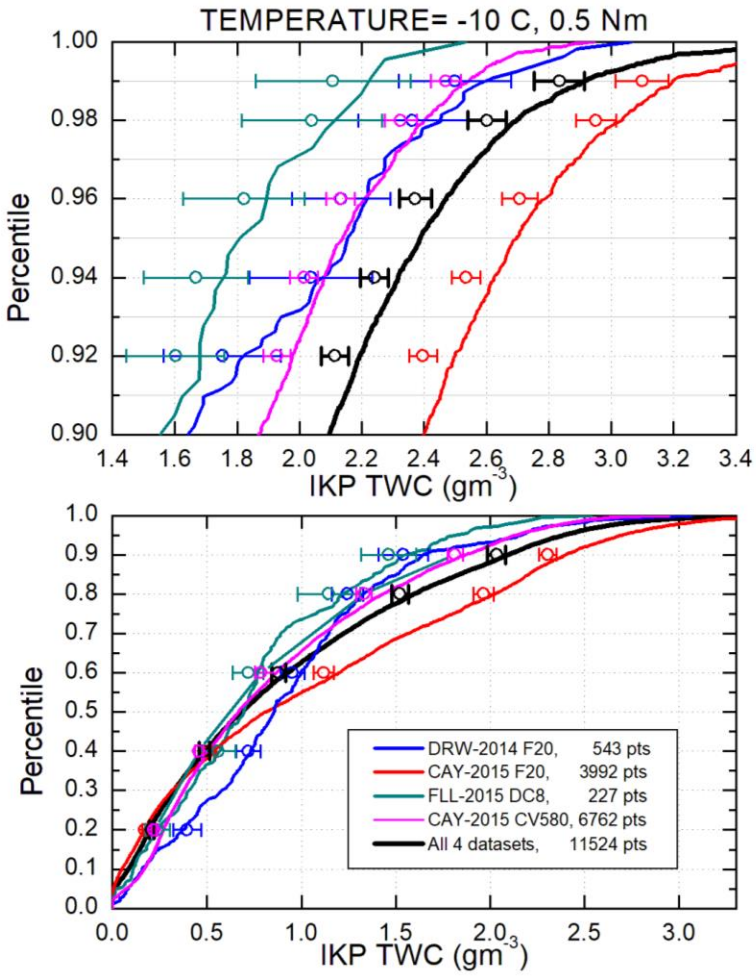

Figure 48. Cumulative frequency distributions for each data set and the combined four data sets (black) for the -10 C interval

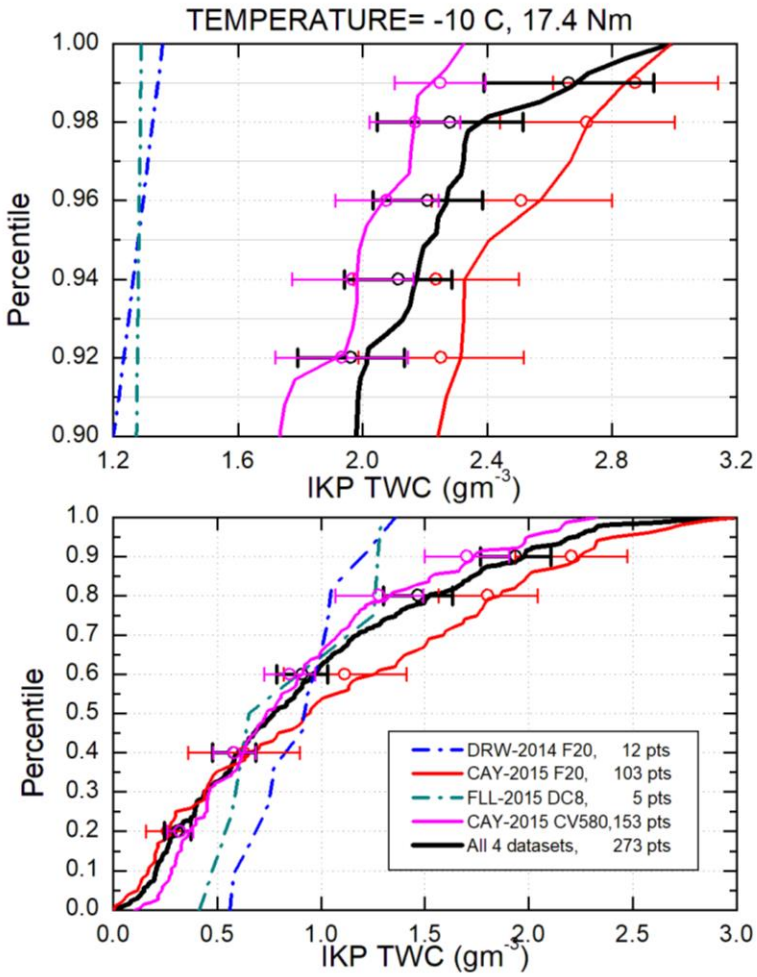

Figure 49. -10 C interval and 17.4 Nm distance scale per Figure 48

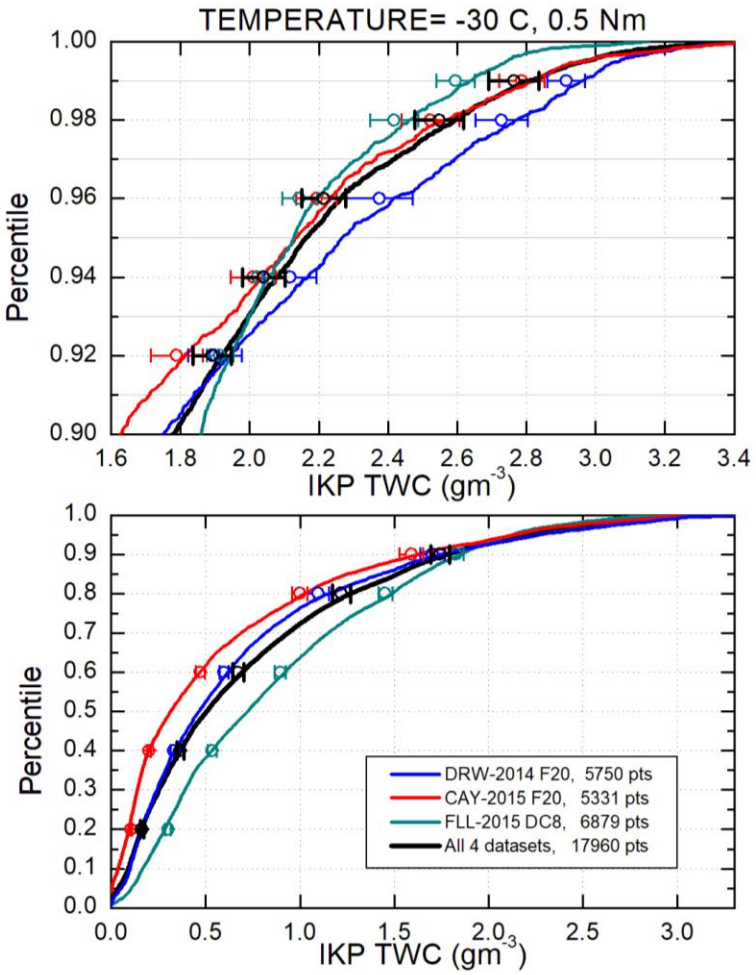

Figure 50. -30 C interval and 0.5 Nm distance scale per Figure 48

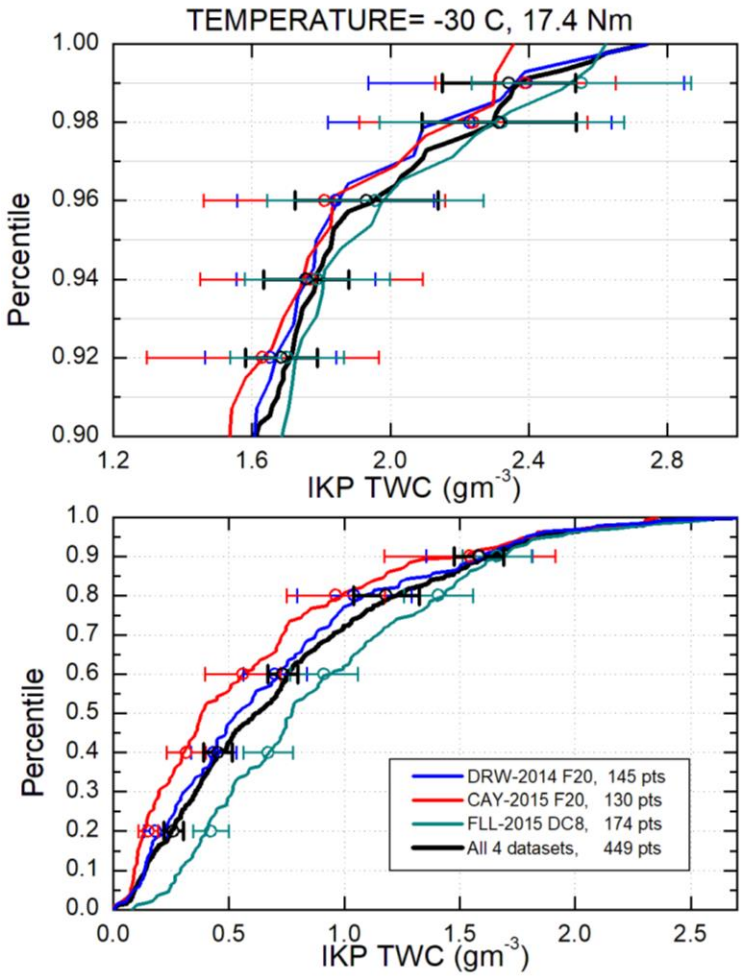

Figure 51. -30 C interval and 17.4 Nm distance scale per Figure 48

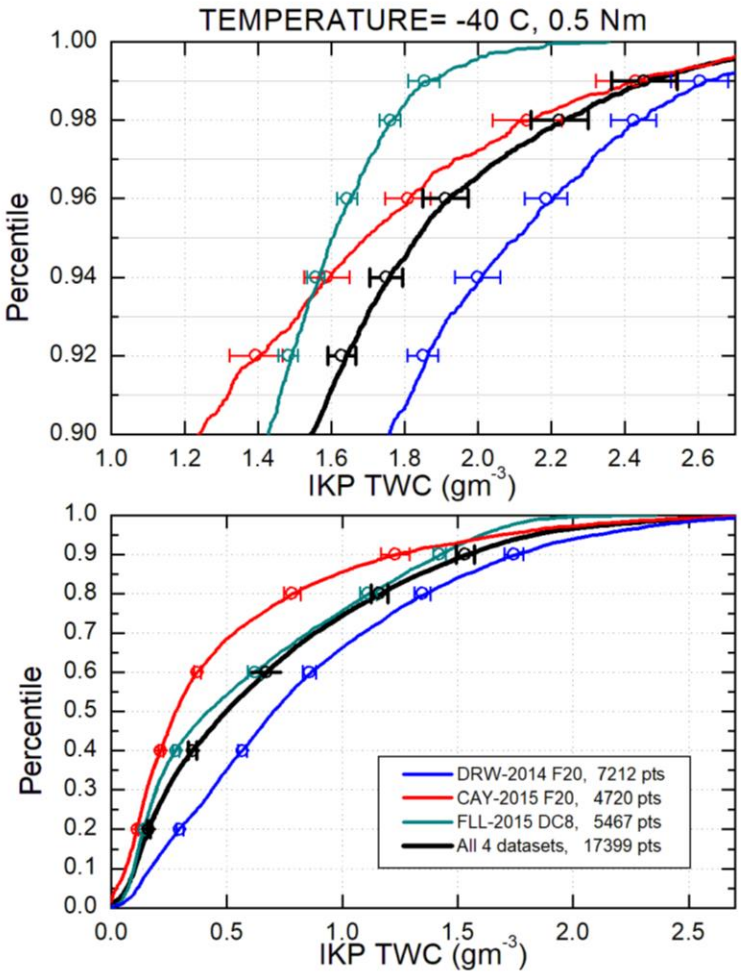

Figure 52. -40 C interval and 0.5 Nm distance scale per Figure 48

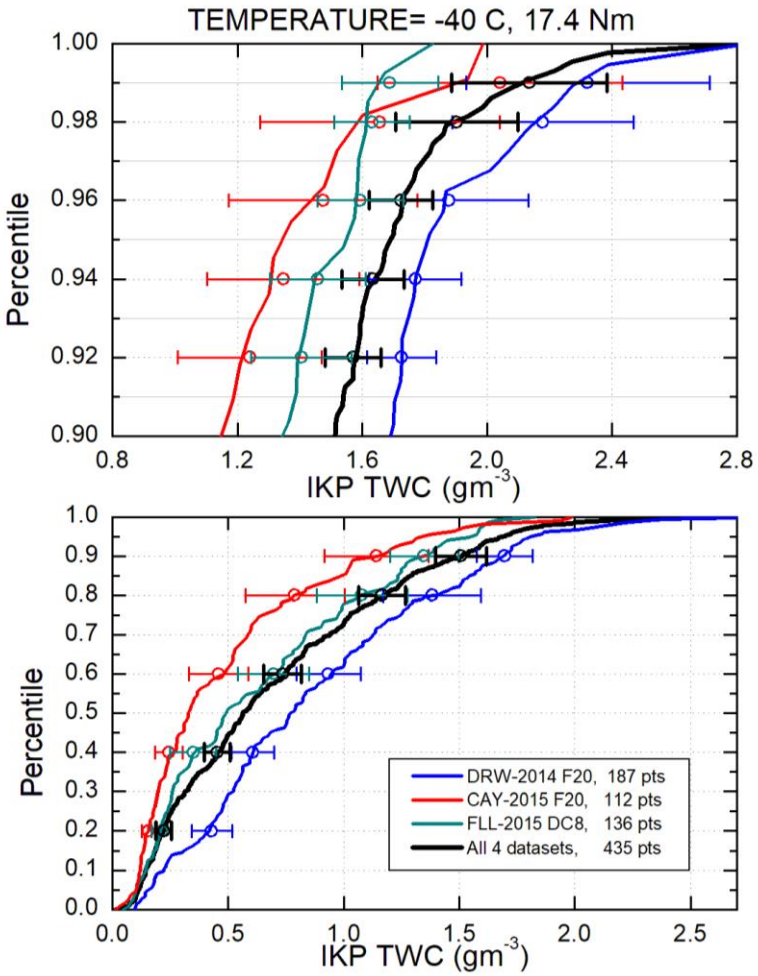

Figure 53. -40 C interval and 17.4 Nm distance scale per Figure 48

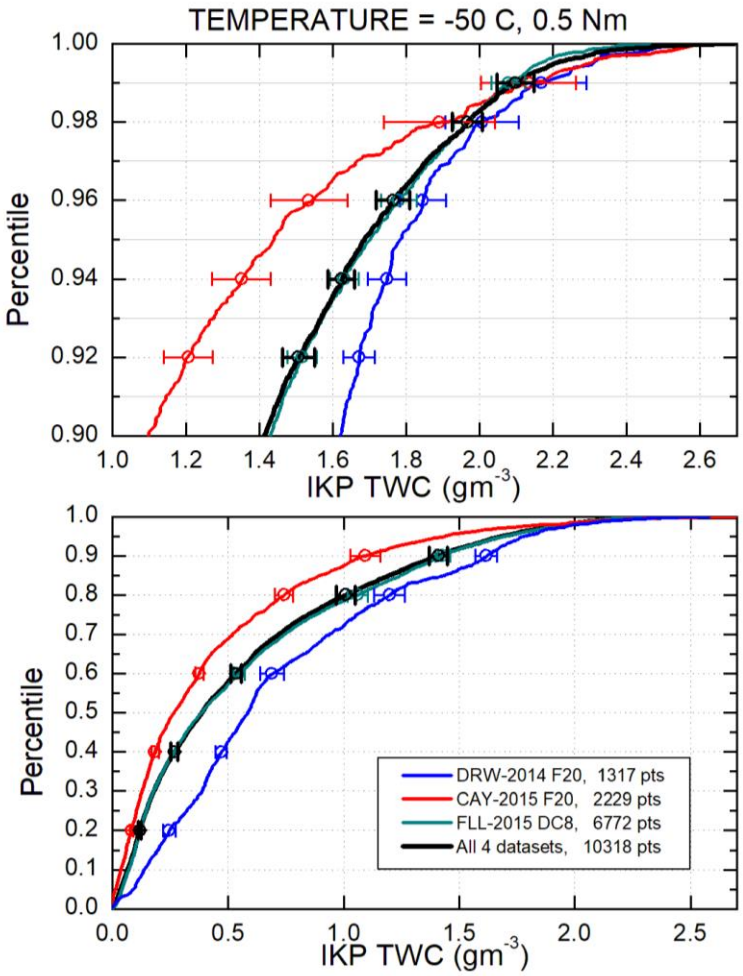

Figure 54. -50 C interval and 0.5 Nm distance scale per Figure 48

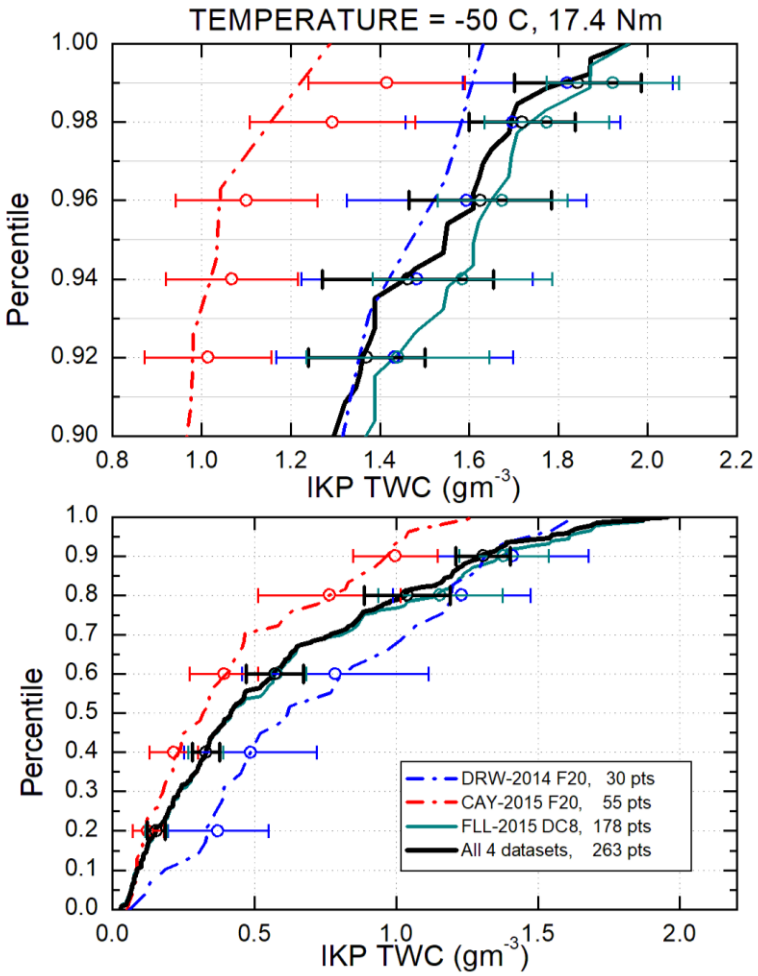

Figure 55. -50 C interval and 17.4 Nm distance scale per Figure 48

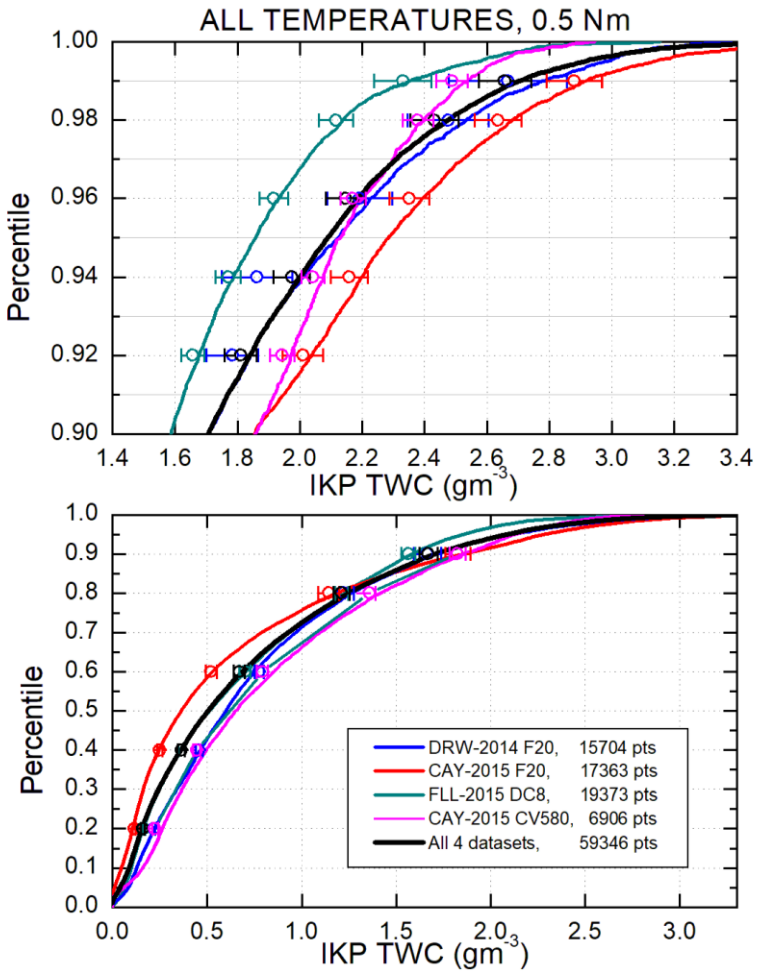

Figure 56. All temperature intervals and 0.5 Nm distance scale per Figure 48

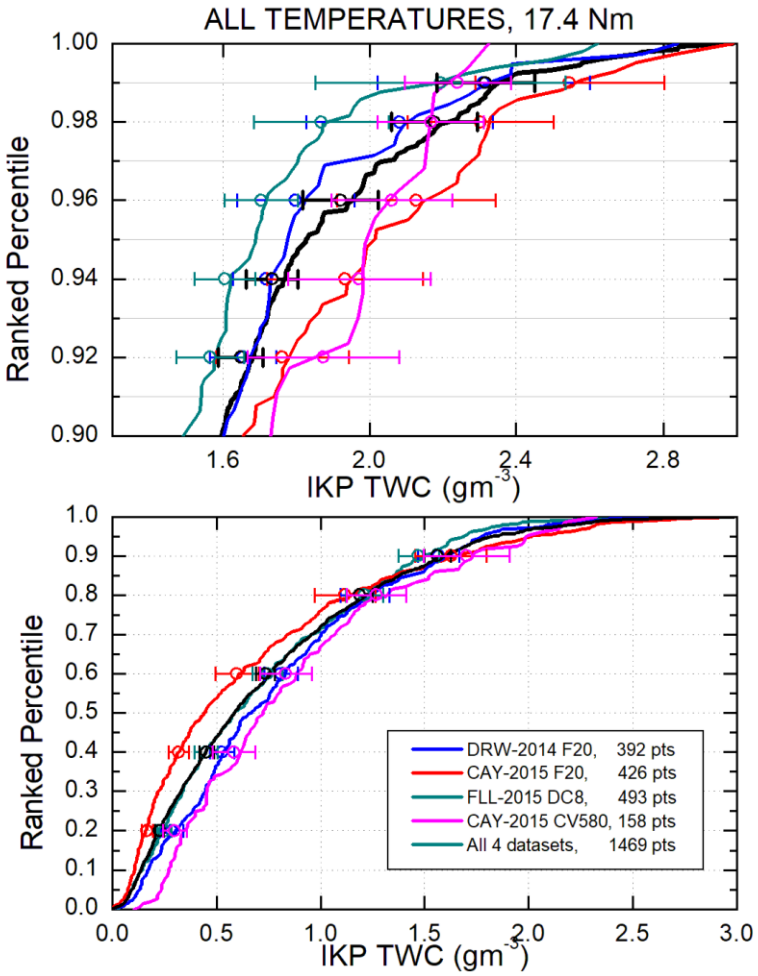

Figure 57. All temperature intervals and 17.4 Nm distance scale per Figure 48

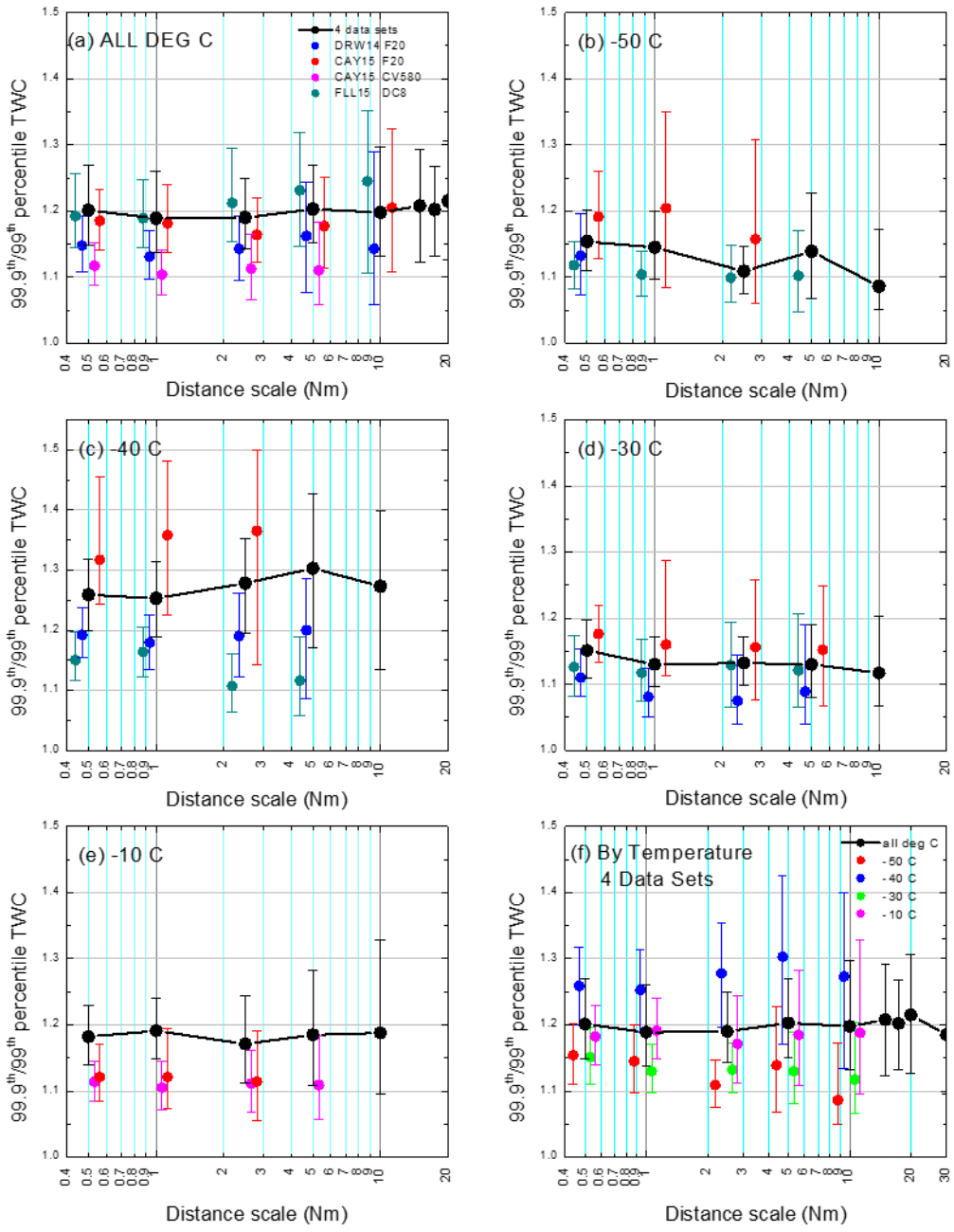

Figure 58. Ratio of 99.9th to 99th percentile IKP-2 TWC by data set and as composite data set (f)

3.5.4 Data Set Differences

At the outset of the Cayenne-15 measurement campaign, it was decided that all IKP-2 data collected in deep convective clouds within the primary temperature levels would be used in the Appendix D/P TWC assessment. Data sets from the different locations would be combined and the assessment would be performed on this combined data set, and their differences noted. In this section, such data set differences and other issues related to combining the data are discussed.

The TWC CFDs of Figure 48 through Figure 58 reveal some differences in the way TWC values were distributed within a data set. The Falcon-20 Cayenne-15 data set tended to have more low TWC data points at -30, -40, and -50 C relative to the other campaigns, as indicated by the higher percentiles at low TWC values. This is clear from the 0.5 Nm distance scale plots (Figure 50, Figure 52, Figure 54, Figure 56, and Figure 58(a), all lower plots), where the Cayenne-15 Falcon-20 line is always to the left of the other plots for percentiles lower than about the 90th percentile. The uncertainty bars do not overlap those of the other data sets at this distance scale. In spite of this larger number of low TWC points, the Falcon-20 Cayenne-15 TWC maxima were higher (Figure 42), particularly at the shorter distance scales. It is these uppermost values of the TWC distribution that are the most important to the TWC_{99} value, which is determined by only the highest ~1% of the points. In the 17.4 Nm distance scale data sets shown in Figure 51 through Figure 58(b), which are, of course, derived by averaging contiguous data points from the lowest distance scale data sets, the same behavior is observed, although the uncertainty bars are wider and overlap other data sets due to sampling uncertainty created by the smaller number of points. The Florida-15 and Darwin-14 TWC CFDs showed no consistent behavior relative to one another. One must look through all these plots and their overlaps individually to estimate the significance of the data set differences at each percentile. This topic will not be discussed at length here, other than for the discussion of the 17.4 Nm TWC_{99} values later in this section.

Table 19 contains TWC_{99} values at 0.5 and 17.4 Nm (upper and lower tables, respectively). TWC_{99} values are only shown if more than 100 data points were collected. There are some distinct differences between the TWC_{99} estimates of the 4 data sets within common temperature intervals. Project maximum differences, expressed as ratios of the maximum to minimum TWC99, with uncertainties, are provided in the last two columns. There is a consistent difference between Falcon-20 and Convair-580 TWC_{99} values at all distance scales in the -10 C interval, with the Convair-580 values being approximately 25-30% lower (also see Figure 43, inset). At 0.5 and 17.4 Nm, the Falcon-20/Convair-580 TWC ratios are 1.26 ± 0.04 and 1.33 ± 0.16, respectively. These data sets were collected in the same approximate geographical location over the same time period, in many cases on the same day and in the same cloud area, typically with the Falcon-20 collecting a little earlier than the Convair-580. One would, therefore, expect approximately the same statistics from the two data sets. It is unlikely that there was a bias between the two IKP-2 probes used to collect the measurements. In wind tunnel tests, the precision of the two same IKP-2 probes, processed with the same software, was found to be of the order of 1% (Appendix B, Figure B-3). Furthermore, a comparison was performed between the two different algorithms used to process the Convair-580 and Falcon-20 IKP2 probes, using data from 4 Convair-580 flights with diverse characteristics during the Cayenne-15 project (Appendix B, section B.4). The two algorithms produced approximately the same TWC_{99} values[13]. It also seems unlikely that the clouds were systematically different due to chance. The following are two speculative explanations: the Falcon-20 pilots consistently chose tracks through more intense precipitation areas, or the Falcon-20 pilot's radar displayed lower reflectivity than that of the Convair-580 for the same weather, which would yield the same result. This explanation also is consistent with the lower MMD values measured by the Convair-580 (section 3.6). Darwin-14 and Florida-15 differences at -10 C are perhaps insignificant due to the very small number of samples.

[13] A software comparison for four selected Convair-580 flights in the Cayenne-15 campaign, using the Convair and Falcon-20 IKP2 software algorithms, yielded TWC_{99} differences of < 1% at 17.4 Nm, and ~2% at 0.5 Nm distance scales, the Falcon-20 algorithm being higher in both cases. Also see Appendix B.

Table 19. TWC99 values and uncertainties by project, at the 0.5 Nm distance scale (upper table) and 17.4 Nm (lower table)

TWC_{99} (gm^{-3}) ± 2σ at 0.5 Nm						
	Darwin-14	Cayenne-2015, (1) F20 and (2) CV580	Florida-15	Combined 4 data sets	Max TWC_{99}/ Min TWC_{99}	F20/CV580
-10 ± 5 C	2.50 ± 0.18	(1) 3.10 ± 0.09 (2) 2.47 ± 0.05	2.11 ± 0.25	2.83 ± 0.08	1.47 ± 0.18	1.26 ± 0.04
-30 ± 5 C	2.92 ± 0.06	(1) 2.79 ± 0.07 (2) no data	2.60 ± 0.06	2.76 ± 0.07	1.12 ± 0.03	
-40 ± 5 C	2.60 ± 0.08	(1) 2.43 ± 0.11 (2) no data	1.85 ± 0.04	2.45 ± 0.09	1.41 ± 0.05	
-50 ± 5 C	2.17 ± 0.12	(1) 2.13 ± 0.12 (2) no data	2.07 ± 0.04	2.10 ± 0.05	1.05 ± 0.06	

TWC_{99} (gm^{-3}) ± 2σ at 17.4 Nm						
	Darwin-14	Cayenne-2015, (1) F20 and (2) CV580	Florida-15	Combined 4 data sets	Max TWC_{99}/ Min TWC_{99}	F20/CV580
-10 ± 5 C	Insufficient data	(1) 2.88 ± 0.26 (2) 2.17 ± 0.17	Insufficient data	2.66 ± 0.27	1.32 ± 0.16	1.32 ± 0.16
-30 ± 5 C	2.39 ± 0.46	(1) 2.39 ± 0.26 (2) no data	2.55 ± 0.32	2.34 ± 0.19	1.07 ± 0.24	
-40 ± 5 C	2.32 ± 0.39	(1) 2.04 ± 0.39 (2) no data	1.69 ± 0.16	2.13 ± 0.25	1.38 ± 0.26	
-50 ± 5 C	Insufficient data	(1) Insufficient data (2) no data	1.92 ± 0.15	1.84 ± 0.14	Insufficient data	

In the -30 C interval (also see Figure 44), all data sets provide similar TWC_{99} values at 17.4 Nm. However, at shorter distance scales, the Florida-15, Cayenne-15, and Darwin-14 data sets provide the lowest, intermediate, and highest values, respectively. At 0.5 Nm, for example, the ratio of the highest (Darwin-14) to lowest (Florida-15) value is 1.13 ± 0.03 (Table 19). In the -40 C interval, a similar consistent trend is observed (also see Figure 45), but the ratio at 0.5 Nm between the highest (Darwin-14) and lowest (Florida-15) increases to 1.40 ± 0.05. This difference could be explained if Florida-15 clouds simply had lower TWC_{99} values. However, again pilot decisions on tracks across clouds and different pilot radar response should again be considered[14]. There may be enough overlapping information in the Convair-580, Falcon-20, and Honeywell 757 (also equipped with an RDR-4000 radar like that of the DC-8) pilot radar records to determine whether

[14] The HIWC-RADAR scientists formed the subjective impression that the Florida campaign clouds produced more red-echo at high altitude on the DC-8 RDR-4000 radar than observed in Darwin and Cayenne on the Falcon-20 Primus, and more maneuvering around cells was required. This has not been confirmed by a rigorous study but is noted here for future reference.

such a radar difference existed. However, this is a non-trivial task, and this investigation was not undertaken.

In the -50 C interval (Figure 46), all data sets provide similar TWC_{99} values across the full range of distance scales. This appears to be inconsistent with the arguments of the previous paragraph. However, there are at least two possible explanations. First, due to the general decrease of reflectivity with altitude, perhaps all pilots during the three campaigns were able to sample more freely at -50 C, less influenced by their own decisions or different pilot-radar response. Second, there was a systematic bias in the Falcon-20 data to collect -50 C data later in the flight, both in Darwin-14 and in Cayenne-15; the Falcon-20 was typically unable to reach the -50 C level until 90 minutes after takeoff. Since oceanic systems were often observed to be decaying during flights, particularly in Darwin-14 (section 4.2), the -50 C TWC values may have been reduced relative to what might have been measured at the beginning of these flights, and this could have possibly lowered the Falcon-20 TWC_{99} values to be similar to those of the DC-8. In Florida-15, the -50 C level was the highest priority, and the performance characteristics of the DC-8 aircraft permitted longer transits to systems with abundant and active cloud at -50 C, and no delay before climbing to -50 C. Consequently, the Florida-15 -50 C data was collected with no particular time-of-flight bias.

In summary, there are some distinct differences between TWC CFDs and TWC_{99} values of the different data sets. The Cayenne-15 data set contained more low-TWC data but nevertheless adequate high IWC regions to generate similar TWC_{99} values, at least at the short- to middle-distance scales. Some data set differences may be a result of the way the different aircraft sampled a system, perhaps due to pilot decisions or different pilot radar response for the same weather. Pilot radar response could be the topic of future work, relying on an international cross-comparison of the different weather radars to assess any differences. The -10 C level data is location-biased, with almost all of the data coming from Cayenne-15. Similarly, the -50 C level data is dominated by the Florida-15 data set. Up to 50% differences were observed in the TWC_{99} values from data set to data set within a common temperature interval, perhaps due to the above-noted factors. This report combines the data sets to derive the composite TWC_{99} values and their percentages of Appendix D/P (Figure 43 through Figure 47). It can be argued that the use of the maximum TWC_{99} of the three locations may be a more conservative approach if sufficient data points are available. Therefore, it should be noted that all of the data required for such a modified Appendix D/P comparison are provided graphically in Figure 43 through Figure 47, and numerically, in Appendix F, Table F-1 through Table F-14. The overall flight campaign result, that observed TWC_{99} values were roughly 50% of Appendix D/P values, is not expected to be greatly changed. This can be concluded in a simple manner by visually inspecting Figure 43 through Figure 46, and re-assigning the TWC_{99} value to the maximum data subset value rather than the composite value.

3.5.5 Higher Percentiles

The availability of well over 100 data points at the shorter distance scales offers the opportunity to examine higher TWC percentiles. Following the logic of approximately a 1/n resolution in ranked percentiles, the 99.9^{th} percentile TWC ($TWC_{99.9}$) can be reasonably estimated for distance scales at which at least 1000 points were collected. The median $TWC_{99.9}/TWC_{99}$ ratios are shown by data set and by temperature in Figure 58(a-e), where one additional distance scale below the 1000 point threshold was included for illustration, due to the typical maximum distance scale of

only 5 Nm having at least 1000 points for individual data sets. The ninety five percent confidence intervals were generated using the Monte Carlo bootstrap estimates described in Appendix B, section B.6. Overall, the median ratios span from about 1.1 to 1.3, and within a given temperature interval, there are consistent differences in the medians from data set to data set, presumably due to CFD differences at the highest TWCs. In only a few cases do the uncertainty bars not overlap at all (e.g., -40 C, 0.5 and 1 Nm distance scales, Cayenne-15 Falcon-20 versus Florida-15 DC-8). In Figure 58(e), the combined data set ratios exceed the two individual data set ratios that make up the great majority of the data points. This perhaps unexpected behavior is likely the result of combining the distinctly different TWC CFDs of the Falcon-20 and Convair-580 at -10 C (see Figure 48), and points out that the ratios of composite data sets should be viewed with caution. The last panel (Figure 58(f)) shows the median ratios of the composite data set by temperature interval. Although there are some consistent ratio differences according to temperature, the trend with temperature is not monotonic. This figure also contains the ratios for the composite data set for all temperature levels (black), the largest data grouping available. The ratios are relatively constant at about 1.2 from 0.4-20 Nm. Therefore, if a statement can be made about the median ratio of $TWC_{99.9}$ to TWC_{99}, it is roughly about 1.2 ± 0.1 for individual temperature intervals out to 5 Nm, and possibly out to 20 Nm for all temperature intervals combined.

An analysis was also performed for the ratio of the 99.99th percentile to the 99th percentile TWC ($TWC_{99.99}/TWC_{99}$) for distance scales having more than 10000 points. Sufficient numbers were available only at the 0.5 Nm distance scale for the individual data sets, and for 0.5, 1.0, and 2.5 Nm for the 4 combined data sets. The results are similar to those above. The median $TWC_{99.99}/TWC_{99}$ ratio can be estimated at about 1.3 ± 0.1 out to at most the 2.5 Nm distance scale. Extension of these ratios to higher distance scales would be highly speculative.

3.5.6 Distance Factor

Appendix D/P includes a multiplication factor to be applied to estimate the TWC_{99} at distance scales other than 17.4 Nm. This "distance factor" was estimated from the 1950s RAE data set [27, 9]. With little knowledge of the actual RAE flight paths, the data were simply concatenated in order to derive the distance factor. It was acknowledged that the distance factor thus calculated would be conservative, especially at long distance scales, since the actual frequency of long distance scale clouds was expected to be less than this simple concatenation procedure would produce.

Figure 59 displays the combined four-data set TWC_{99} values versus distance scale, as in Figure 43 through Figure 47, but now the Appendix D/P distance factor is applied relative to the *observed* TWC_{99} at 17.4 Nm rather than the Appendix D/P TWC envelope value.

Appendix D displays distance factor comparisons, and the new proposed distance factor. TWC_{99} versus distance is displayed with black symbols (combined four data sets only, with $\pm 2\sigma$ uncertainties) as in Figure 42 through Figure 46; App. D/P distance factor (df) multiplied by the observed TWC_{99} at 17.4 Nm is displayed in magenta; new df is displayed in magenta from fit to the all temperature data: (a) all temperatures, (b) -50 C interval, (c) -40 C interval, (d) -30 C interval, and (e) -10 C interval.

Note that the Appendix D/P distance factor (dashed magenta line) actually fits the observed data (black symbols) fairly well except at distance scales below about 5 Nm, where it is an extrapolation of the data fit[15], and where it results in significant overestimation of the measured TWC_{99} values.

Examination of Figure 59(b-e) reveals that this is also the case for each individual temperature interval. Consequently, it was decided that a polynomial fit was required to account for the non-linear tendency of the TWC_{99} versus log-distance across the 0.5-100 Nm range. The fit for the all-temperature data set is included as the "new poly fit df" line (violet) in Figure 59(a). The new proposed distance factor derived from the flight campaign data is as follows:

$$df = 1.145 - 0.0674 * \log_{10}(dNm) - 0.0366 * (\log_{10}(dNm))^2 \quad (1)$$

where dNm= distance scale in Nm.

[15] The Appendix D distance factor [27] was derived from a dataset with a minimum distance scale of about 4.5 Nm.

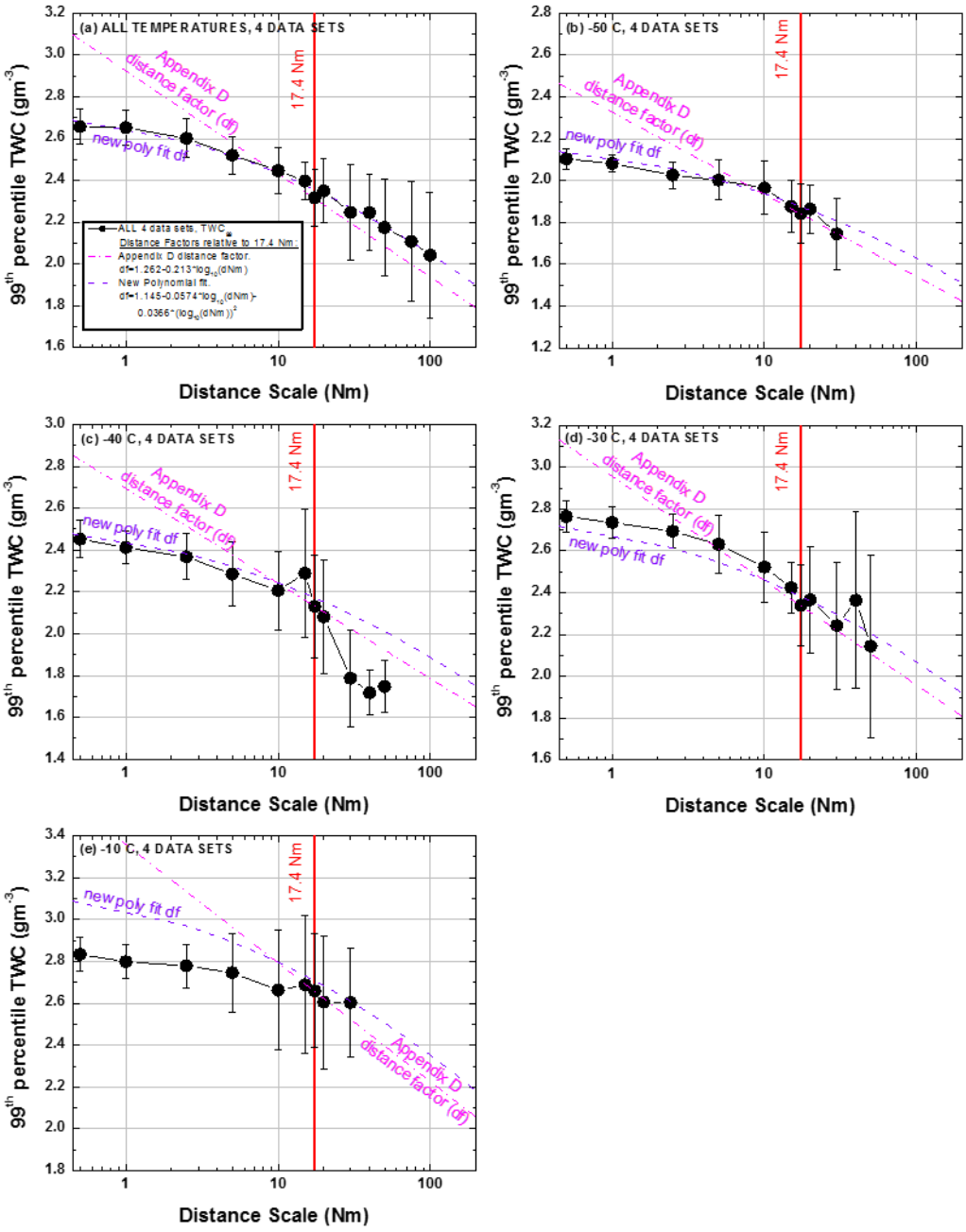

Figure 59. Appendix D distance factor comparisons and new proposed distance factor

The distance factor again represents a multiplication factor relative to the TWC_{99} value at 17.4 Nm. The same distance factor is next applied to the discrete temperature interval data in Figure 59(b-e). At -50 C (Figure 59(b)), the new distance factor fits the data quite well over the entire distance range. At -40 C (Figure 59(c)), the new fit is good out to about 17.4 Nm, above which it overestimates significantly (e.g. ~20% at 40 Nm). At -30 C Figure 59(d), the fit underestimates TWC_{99} a little at the lowest distance scales, but is good for distance scales greater than or equal to about 15 Nm. Finally, at -10 C (Figure 59(e), the fit overestimates TWC_{99} at the lowest distance scales, but is good for distance scales greater than or equal to about 10 Nm. Note that the decrease

in the observed TWC_{99} (d) values in Figure 59(a-e) from 0.5 to 10 Nm is relatively small for all temperature levels, and is always less than 11%. Within this distance range, the predicted TWC_{99} (d) using the new distance factor is within about 10% of observed in the four temperature intervals. Most of the change in TWC_{99} versus distance is at larger distance scales, where either the fit is quite reasonable, or the fit overestimates the TWC_{99} values, and is thus conservative. The importance of deviations of the original Appendix D or the new polynomial distance factors from the observed data can only be assessed by those that will apply these measurements. If using the new distance factor, one should also note that its fit range is 0.5-100 Nm, and application outside this range involves extrapolation with the accompanying risks. The distance factor is only applicable only to TWC_{99} values from the Type 1 data points used in this study, and as defined in section 3.1.

3.6 IN-SITU PSD AND MMD

Information of the properties of cloud particles was deduced from the detailed analysis of two-dimensional images recorded during flights by optical array probes such as the 2D-S and PIP, the primary instruments used for the PSD analysis of this report as described in section 2.2. Visual inspection of images collected during the flight programs revealed that ice particles were most often composed of irregular-shaped particles and aggregates. Graupel or otherwise heavily rimed particles were only occasionally observed. No hail was observed. Figure 17 and Figure 18 contain sample 2D images in high IWC cloud from the flight campaigns. In this section, and in Appendix C, the methodology for calculation of PSDs, Mass Size Distributions (MSDs), and MMDs are described. The methodology is reviewed below, and flight campaign ice particle size statistics are summarized.

The computer analysis of OAP imagery provides the number of hydrometeors (cloud droplets and ice crystals) per volume of air as a function of the size of the hydrometeors (i.e., the PSD). During these flight campaigns, mixed-phase regions were infrequent (section 3.4), comprising less than ~5% of the in-cloud measurement distance. In order to simplify the calculation of PSDs, MSDs and MMDs, mixed-phase regions have been manually excluded from the analysis of the PSD data set, so that the PSDs of this report are representative of ice-crystal populations only.

Post processing of the OAP images is complex. It requires rejection of all images resulting from measurement artifacts as fully described in [46] and also reviewed in Appendix C of this report. Various parameters can be extracted from the analysis of the recorded image: maximum hydrometeor length parallel and perpendicular to the flow direction, area equivalent diameter, maximum dimension, area, and perimeter, as general examples. The size distributions presented in this section rely on the "area equivalent diameter," which is derived from the total number of shaded pixels (i.e., the area of a single OAP image) assuming a circular shape: $D_{eq} = 2\sqrt{Area/\pi}$. In ice-cloud conditions, the relationship between the size D of ice particles and their mass m is usually parameterized using a power law relationship: $m = \alpha D^{\beta}$. Various constant values for α and β have been reported in the literature, depending on temperature, ice crystals habit, cloud type, etc. For this study, β is deduced from the analysis of ice particles images, as described in [59, 46]. Subsequently, α is constrained so that the total mass calculated from the PSDs equals the TWC that has been measured by the IKP-2 probe (the reference measurement for TWC). This method produces time-varying α and β, reflecting changes in the ice crystal morphology along the flight

track. Once α and β are known, the PSD can be converted into a MSD with an associated MMD, defined as the diameter below and above which there are equal mass fractions.

PSDs, cumulative MSDs and MMDs presented in this section were derived from SAFIRE Falcon-20 Darwin-14 and Cayenne-15 data sets, NRC Convair-580 Cayenne 2015 data set, and the NASA DC-8 Florida-15 data set. Periods of aircraft climbs and descents have been excluded. First, data were sorted into the same temperature intervals as for the TWC_{99} analysis: -10, -30, -40, and -50 ± 5 C. Then, periods of data during which selected TWC thresholds have been reached or exceeded over selected distance thresholds were identified. Overall, three TWC thresholds (0.7, 1.0 and 1.5 gm^{-3}) and three distance scales (0.5, 17.4 and 30 Nm) were used. Taking MMD values from the 1 gm^{-3} TWC threshold and 0.5 Nm distance scale are taken as "reference," extensive sensitivity tests have demonstrated that other MMD values in a given temperature interval fall within +/-10% of that reference. In the following discussion, only results for the 1 gm^{-3} / 0.5 Nm reference condition are presented. The 1 gm^{-3} threshold ensures a focus on high IWC regions, whereas the distance scale of 0.5 Nm maximizes the number of data points. Results for other TWC thresholds and distance scales are presented in Appendix C.

Figure 60 presents the cumulative mass distribution as a function of size for different temperatures, separately for the Falcon-20, Convair-580, and DC-8 data sets. Table 20 summarizes the corresponding MMD values. The figure and table demonstrate that MMD decreased with decreasing temperature, meaning that the relative contribution of small ice crystals to the total mass increased with altitude. For the -40 and -50 C temperature intervals, particles smaller than 400 µm accounted for more than 50% of the total mass, whereas within the -10 C interval, such small ice crystals only accounted for roughly 25% of the total mass. Sensitivity tests presented in Appendix C also demonstrated that the average MMD was much more a function of temperature than of any other parameter. The MMD increase with temperature was almost identical for all TWC thresholds and distance scales. Note also that the results from each of the project locations and aircraft were quite similar.

Table 20. MMDs per Deq (in microns) deduced from the different curves in Figure 60

Distance scale: 0.5 Nm TWC from IKP-2: ≥1 gm^{-3}	Temperature			
	-50°C	-40°C	-30°C	-10°C
F20 data set	316	401	476	747
DC8 data set	329	381	493	-
Convair-580 data set	-	-	-	630

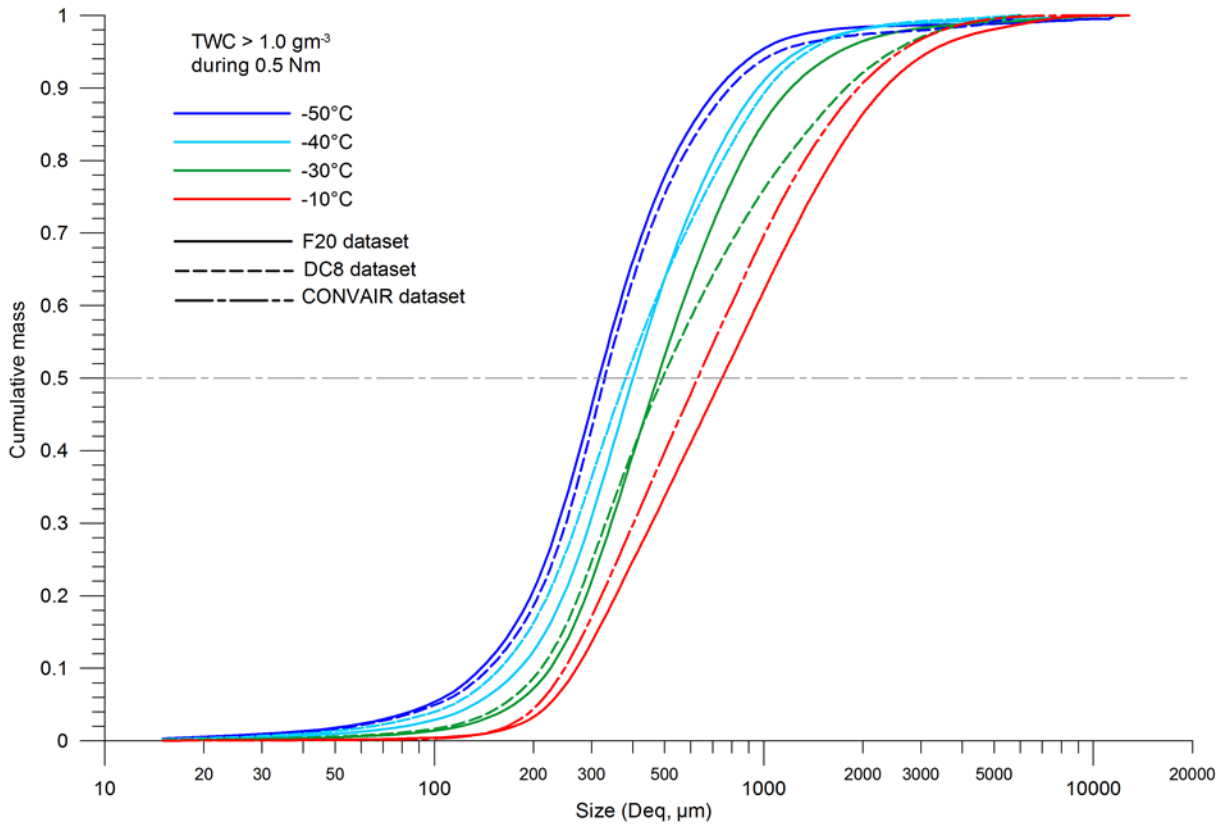

Figure 60. Cumulative mass distributions as a function of Deq

Figure 61 shows the corresponding PSDs. Both the number of small (below 200 µm) and large (larger than 1 mm) particles changed with temperature in high IWC regions. As temperature increased, the number concentration of small ice crystals decreased, whereas the number of large ice crystals increased. Below 100 µm, the number concentrations at cold temperatures (-50 C) were a factor of 10 higher than those at warm temperatures (-10 C), where above 1.5 mm this ratio was reversed.

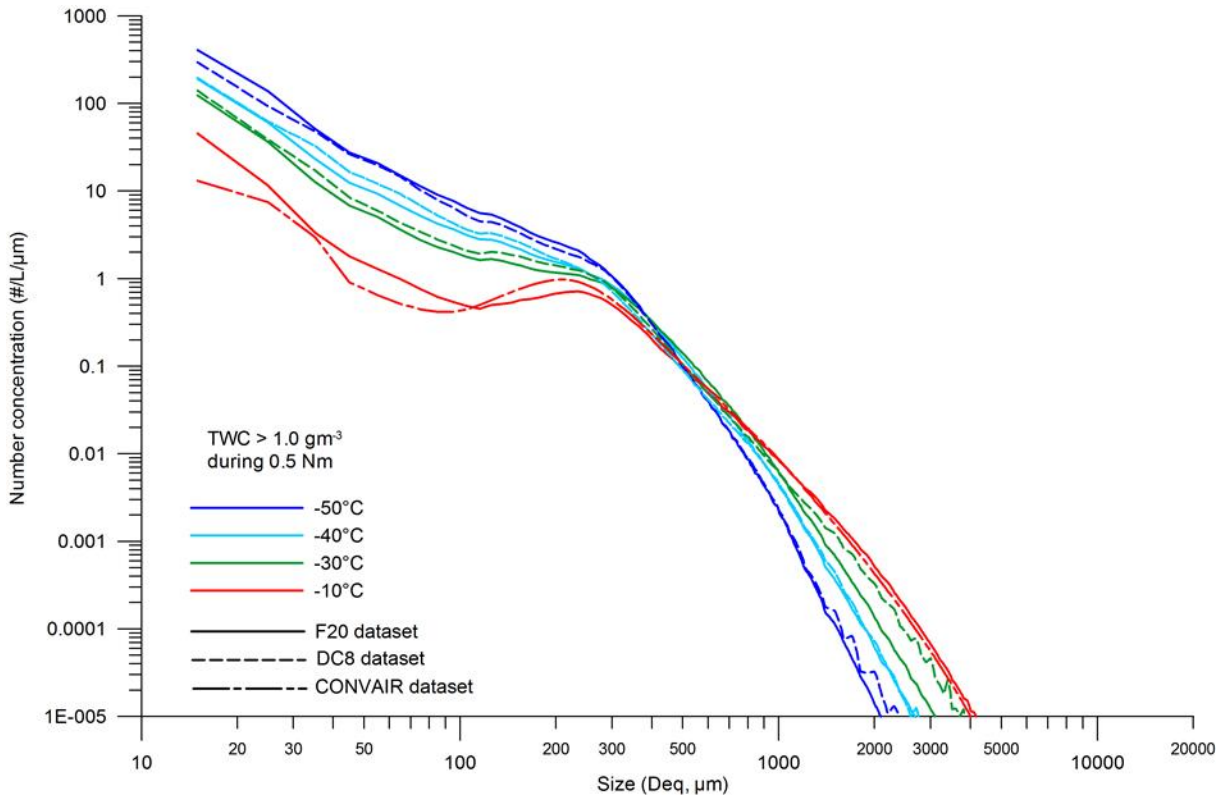

Figure 61. PSDs: line-types and colors per Figure 60

In summary, in high IWC conditions, the number of small ice crystals increased with decreasing temperature, while the number of large crystals decreased. Roughly speaking, MMD increased approximately 100 µm for each 10 C temperature increase from -50 to -10 C (Table 20).

4. REPRESENTATIVENESS OF DATA SET IN DESCRIBING GLOBAL AVIATION EXPOSURE TO HIGH IWC

The data set that was used to establish the FAR Part 25 Appendix C envelope [10] for conventional supercooled LWC was initially collected in the late 1940s over the continental USA [60]. A total of 1038 icing cylinder measurements were collected during 252 icing encounters, all of which were used in the statistical analysis. The report notes that "the results are only applicable to the Unites States," but the report methods "should provide a framework for placing the data on a statistical basis that is not limited in scope to the United States." In this way, those authors acknowledged that their results might not be globally representative, and might be amended using their techniques if future data became available. During a 1969 FAA Aircraft Ice Protection Symposium, the originating lead author summarized additional measurements taken in the 20 years since the original data set [61]. The new data had been taken on commercial and military North American continental and trans-Atlantic flights, on icing research flights by the Canadian NRC, and by the Russian Meteorological Service over several Russian sites. Although there were difficulties in interpreting some of the almost 6000 additional measurements, the author concluded that the standards developed from the original data, still in force today, were "generally consistent with the data that have become available since their adoption," and that the criteria had stood the "test of use," the experience of aircraft being "more comprehensive than any data collection

program." As in the case of the Appendix C data collection, the data sets reported herein are also limited due to the practical constraints of collecting such expensive and technically challenging data. The results also can be reviewed as future data sets become available, and as commercial aircraft experience accumulates.

Decisions determining the nature of the flight campaign data set (e.g., location of measurements, types of clouds studied, and flight sampling strategies) were specifically driven by meteorological conditions experienced during engine power-loss events. However, in the future, the data set may be more generally used to globally characterize the high-altitude, high TWC environment to which commercial aviation is exposed. During the HAIC-HIWC Science Team meeting on December 8, 2016 in Capua, Italy, a special discussion was held to solicit the opinions of the team on limitations of the data set in globally representing this environment. The meeting was announced in advance to allow members to prepare their opinions and make any presentations thought to be relevant. The HAIC-HIWC Science team was composed of cloud microphysicists, cloud modelers, nowcasting specialists, satellite and radar remote-sensing specialists, meteorologists, aeronautical engineers, and other aviation industry specialists, representing government regulatory and research agencies, universities, and airframe manufacturers, based in Australia, Canada, France, Italy, and USA. The sub-sections below summarize and expound on the possibly noteworthy issues relative to global representativeness and bias of the data set. These issues are in addition to location differences noted in the data sets already discussed in section 3.5.3, and the avoidance of lightning, discussed in section 2.5.

4.1 LOCATIONS OF THE THREE CAMPAIGNS

The data sets of this report were collected mostly in MCS clouds in two tropical locations in the month of their climatological maximum rainfall (Darwin, Australia, 16 January – 18 February 2014; Cayenne, French Guiana 5-29 May 2015) and in a third subtropical location (Florida, 12-28 August 2015) during a convectively active period. The data include six flights in tropical storms, two during Darwin-14 and four during Florida-15. Figure 1 displays the locations of these flight campaigns relative to 162 Boeing engine events documented by 2015. The clustering of these events is likely highly influenced by the density of air traffic and a number of other non-meteorological factors, and is not an indicator of a lack of suitable clouds at the flight campaign locations. It also may be influenced by idiosyncratic sensitivity of particular engine type/airframe combinations to ice crystal icing, and the specifics of where and when such aircraft fly. Figure 62 displays satellite 11 μm IR observations of clouds with effective cloud top temperatures colder than -63 C, and an area greater than 10^5 km^2 (corresponding to equivalent circular diameter of about 193 Nm), for the period of 1998-2004, from [62]. This reveals where on the earth aircraft at cruise altitude are most likely to encounter large and deep MCSs. Note the similarity between the engine-event locations and the locations of large MCSs. Some of the clusters of points in Figure 62 are related to strong *continental* MCSs (e.g., over continental Africa, southeast South America), discussed further in section 4.4. The largest concentration of points that can be associated with *oceanic* MCSs, the primary target for the measurements of the three flight campaigns, spans from about 20 S to 20 N, and from about India on the west to the central Pacific on the east. This is the location of the Tropical Warm Pool, the region of the highest global sea surface temperatures (see Figure 63, from [63]), fueling high atmospheric water vapor concentrations, and deep convective clouds that develop heavy precipitation. The Darwin-14 campaign location is within the Tropical Warm Pool, and the associated region of large MCSs with cold cloud tops (Figure 62). The HAIC-

HIWC Science team thus concluded that, of the three locations, Darwin was probably the most representative of the many areas of tropical oceans that have experienced engine events. In fact, many of the atmospheric and cloud properties noted by [24] for their case studies of event-rich oceanic Southeast Asia are very similar to those experienced during the Darwin-14 campaign (e.g., cirrus shield size, cold point tropopause, convective parcel equilibrium level, and atmospheric PW). The Cayenne-15 project experienced weaker and shallower convection with less-broad cirrus shields, as expected from Figure 62, but the campaign nevertheless provided good complementary data from these smaller systems, with short distance scale (peak) TWC values that, in fact, exceeded Darwin-14 values. Almost all data for the -10 C temperature interval was collected in Cayenne-15. The data from the Florida-15 campaign provided yet another somewhat different data set, again in shallower MCS than those sampled in Darwin-14. The initial flights in oceanic MCS were more prone to lightning and high reflectivity at flight altitude, and the final four tropical storm flights displayed similarities to the two Darwin-14 tropical storm flights of 2 and 3 February 2014. The majority of the -50 C data comes from the Florida-15 campaign. Each data set provided somewhat different but complementary data. No data set by itself provided sufficient data to provide the TWC_{99} statistics requested by the EHWG. In spite of the observed location differences as large as 40% in TWC_{99} at 17.4 Nm for specific temperature intervals (Table 19), perhaps due to unintended sampling decision differences rather than location (section 3.5.3), there is a strong advantage to having collected data in three different locations. If all data had been collected only in Darwin as originally intended, a location bias would probably have been the largest question with no information for assessment.

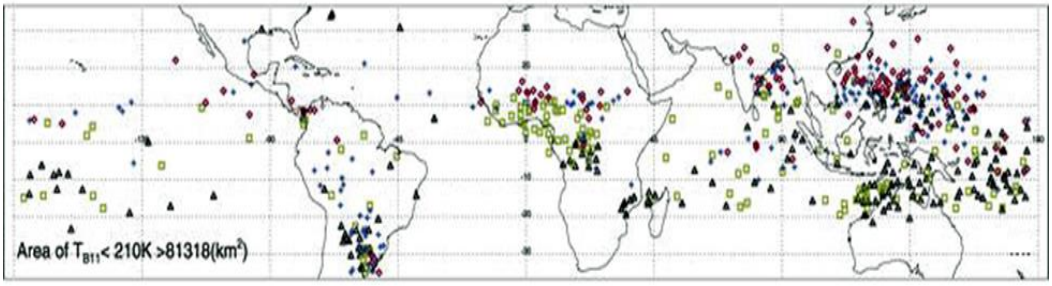

Figure 62. Satellite IR-derived locations of large clouds with cold tops [62]. Symbol colors by three-month periods: DJF=black, MAM=green, JJA=red, SON=blue

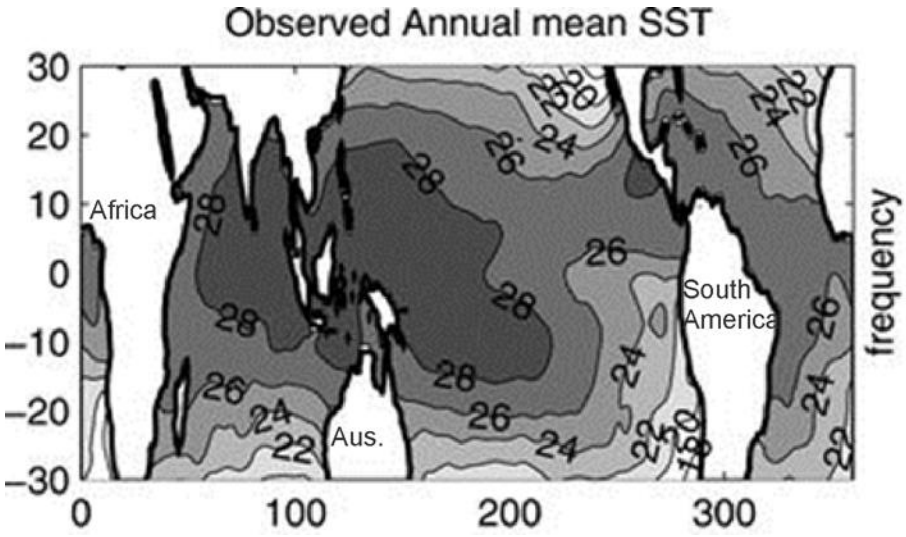

Figure 63. Geographical distribution of average global sea surface temperature [63]

4.2 DIURNAL VARIATIONS IN OCEANIC MCSS

As discussed in earlier sections, the HAIC-HIWC flight campaigns targeted oceanic convection, in particular large oceanic MCS with circular or oval cirrus shields with scales of the order of 100 Nm or larger. A number of studies have shown that there is a global nighttime maximum in oceanic convective activity leading to an early morning maximum in precipitation (e.g., [64, 65]). The area of tropical cloud cluster tops colder than -65 C (indicative of the area of deep convective cloud) over the Pacific Ocean has been shown to be highest between 1:00 a.m. and 5:00 a.m. local time, after which time it decreased markedly [66]. Similarly, Tropical Rainfall Measurement Mission (a precipitation radar measuring from space) measurements have shown that the area of radar returns greater than or equal to 20 dBZ maximizes between about 3:00 a.m. and 6:00 a.m. local time in oceanic regions between 20º S and 20º N [65]. The nighttime maximum is possibly due to diurnal differences in radiative cooling and heating that destabilize the atmosphere during nighttime [67]. A wide variety of specific local influences also may affect both oceanic and continental convection cycles. In the Darwin area, it is likely that land-sea breezes influence convection on a large scale over the top end of Australia, supporting enhancement of coastal oceanic convection at night, and suppressing it during the day. During all three flight campaigns, there was a general impression that oceanic convection was strongest in the early morning hours, with the deepest cloud dissipating by late morning. There were notable exceptions, particularly in the case of the tropical storms.

Before the Darwin-14 flight program, project partners at the Australian Bureau of Meteorology emphasized that flights should be conducted as early as possible in the day due to the expected overnight oceanic maximum. An analysis of the occurrence of deep convection in the Darwin monsoon season confirmed the existence of two local time-of-day maxima in rainfall: the first in the early morning associated with oceanic systems, and the second in the late afternoon associated with more vigorous overland systems [68]. Due to reasons of safety-of-flight, the project management decided that cloud sampling would be performed only in daylight hours, precluding the possibility of flight measurements during the suspected period of peak oceanic activity. Similarly, the Convair-580 was restricted to daytime flights in Cayenne-15. In order to optimize

the daytime sampling, the general mode of operation during Darwin-14 and Cayenne-15 was to start preparations as early as 1:00 a.m. local time to allow for the earliest possible cloud sampling after daybreak. For the Florida-15 campaign, no such daytime restriction was imposed on the DC-8 flight operations; however, ample cloud systems were available during daytime hours to achieve the campaign's primary radar objectives. Due to the added complexity of nighttime operations, only daytime flights were conducted, again often starting in the morning after daybreak. The question, therefore, arises as to whether the data sets of this report are biased relative to what commercial aircraft flying twenty-four hours a day would experience. Possible diurnal influences at the flight campaign locations are examined in detail in Appendix E, and in an abbreviated summary on this section, to determine if there were indicators of enhanced cloud conditions during the nighttime hours.

For this investigation, the area of the coldest satellite IR cloud tops is used as an indicator of the potential for high IWC in convective clouds. Although Ref. [24] found no diurnal preference in the time of day of engine events, such events generally were linked to large areas of cold convective cloud [29], and, in fact, correlated to the vicinity and time of maximum area of the coldest cloud tops [24], which are likely regions of overshooting tops. Ref. [69] found a supporting reverse-correlation between flight campaign in-situ TWC and the distance to overshooting tops identified from satellite imagery. Therefore, there is reason to believe that the time with the greatest area of the deepest cloud would coincide with the most convectively active period, therefore, marking the period with the highest potential for high IWC[16]. The simplest practical method for assessing cloud diurnal variations in deep cloud amount is through analysis of regular geostationary satellite IR images.

In Appendix E, the relative IR satellite cloud-top areas at selected temperature thresholds are presented by time of day, in both a climatological analysis and a storm-specific analysis. These analyses endeavor to address two questions: (1) were the flight campaign measurements collected at the time of day that the IR climatology suggests is best, and (2) in the particular storms studied, were the measurements made at the optimum time during the cloud lifetime. For item (1), fixed geographical regions were defined for Cayenne and Florida, and 20-year climatological averages specifically for the months of the flight campaigns were produced. A similar analysis for Darwin may be undertaken in the future if resources permit. For (2), the evolution of individual cloud systems sampled during Darwin-14 was studied. Each cloud system was tracked for a 24-hour period, and the flight measurements were put in context of the lifecycle of the system. A corresponding Cayenne-15 analysis is underway and will be reported separately at a later date. There are no plans to perform such an analysis for the Florida-15 storms.

The 20-year climatological analysis (1996-2015, May only) for Cayenne was performed in six fixed geographical boxes (Figure E-1). The continental box displayed the expected late afternoon maximum due to daytime convection. Two coastal boxes showed traits of both oceanic and continental clouds, as expected due to the boxes covering both oceanic and ocean regions. For the four oceanic boxes, individual and composite results were obtained. The results display a distinct nighttime maximum between 00:00-06:00 solar time at the coldest cloud top temperatures, with a second mode appearing later in the morning (Figure E-5). The period between 06:00 and 09:00 is climatologically a period of rapid decrease in cloud area $\leq$ -65 C, while cloud area $\leq$ -40 C increases

[16] Note that other potentially correlated factors such as lightning and high radar reflectivity also should be considered in assessing whether pilots would avoid such cold cloud.

until it reaches its maximum at about 14:00, thereafter decreasing rapidly. The results for the single month of 2015 revealed the same features, although somewhat noisier due to less data.

The 20-year August climatological analysis for Florida was performed for three fixed oceanic geographical boxes that spanned the regions of the DC-8 flights (Figure E-9). For this project, time-of-day animations of the 20-year climatology of images of anvil area, produced for an independent project, revealed important information on specific regional influences within each box, including land-sea breeze convective initiation, coastal suppression of daytime offshore convection, and perhaps the influence of easterly waves. These boxes exhibited the same two modes as observed for Cayenne, although the nighttime mode was somewhat weaker, especially for box 2, where it was visible only for cloud areas ≤ -75 C, and the mid-day mode was more dominant (Figure E-11). Box 3, the closest to Cayenne, displayed the diurnal behavior closest to that of Cayenne. The Florida results for 2015 are a little different than the 20-year climatological results, in that the nighttime mode is even less apparent.

One interesting result from the above climatological analyses is that the differences between the individual oceanic geographical boxes in Cayenne and Florida are actually larger than the Cayenne-versus-Florida differences (Figure E-16). This is likely a consequence of the box-specific regional influences within a campaign's domains, as revealed for the Florida domain in the diurnal anvil animations previously discussed. The non-uniform behavior of different boxes within the campaign domains, including different diurnal signals, complicates any general statements that might be made based on any domain-average climatology.

To date, storm-specific diurnal investigations have been performed only for the Darwin-14 campaign. Each MCS sampled during the project was studied for an 18-hour period bracketing the flight, starting from midnight. The areas of satellite IR cloud-top temperatures colder than a series of temperature thresholds between -40 and -90 C were calculated by time of day. Differences between the time of the maximum cold cloud area and the flight sampling midpoint times of the Falcon-20 sampling were computed. Due to the frequency of lightning during the period of the coldest cloud area maxima, time differences were calculated with respect to the ≤ -70 C IR area maximum, since this often corresponded to the time of decrease in lightning activity, and perhaps represented the time at which flight sampling would have been optimum. As suspected, the ≤ -70 C area maxima usually occurred before daylight (median 04:40 solar time), and the Falcon-20 sampled after the maxima in 14 out of the 17 flights, an average of 2.6 hours later. The median ratio of the ≤ -70 C area at the flight time relative to that at the maximum was 0.58. If the time of the ≤ -80 C IR area maximum had been alternatively chosen as reference, the time difference increased to 3.2 hours. There is only one day during the Darwin-14 campaign in which the same cloud at different lifecycle stages was sampled, in two separate flights about 7 hours apart. The cloud system was a tropical storm, and had an unusually long lifetime relative to the more common MCS sampled in Darwin-14. Flights 12 and 13 were conducted about 1.9 hours after the morning ≤ -70 C maximum, and about 5.8 hours before the second maximum associated with a storm regeneration, respectively. During both periods, active convection was sampled. The bottom of Figure E-18 shows thumbnails of IR images illustrating the decay and regeneration of the cloud, and IR cloud areas colder than selected threshold temperatures. Cloud traverses for flights 12 and 13 at about -36 C revealed nearly equal average TWC values, although these comparisons were not ideal due to the way the clouds were sampled. More convincing was the comparison of peak 0.5 Nm TWC values collected in the active cells, which were nearly the same during each flight

(Table E-3). Thus, the results suggested that if active cells were present and sampled during a flight, peaks' TWC values for the day might not be greatly affected by when the sampling was done, and that the more likely lifecycle influence would be on the distance scale over which high TWC values might be encountered. Moreover, the ultimate effect of late sampling would be the eventual absence of active cells, and a general decrease in the TWC levels as the cloud dissipated without new generation of high TWC from active cell updrafts. Active cells were normally present when starting flight sampling, but the breakup of such cells often marked the decision to end the sampling of a cloud system.

Although the results of the climatological and storm-specific analyses provide context to the flight sampling during the three campaigns, they do not provide any solid quantitative information on how this report's TWC_{99} statistics may have been affected. No corrections have been applied to the data as a result of this diurnal analysis. However, it is the consensus of opinion of the HAIC-HIWC Science team that due to the daytime-only sampling, it is possible that TWC_{99} statistics of the three flight campaigns may be lower, and peak TWC levels may be sustained over shorter distances relative to what might have been measured during the period of the clouds' maximum activity. The latter effect seems clear: if the area of deep cloud is larger, the hypothesis of high TWC over a longer distance scale is intuitively reasonable. However, the effect on the data set's maximum shorter scale TWC values is not clear. The flights very often tracked close to local overshooting tops, the region where the flight data suggests the highest TWCs are found, and the region highly correlated to engine events [24]. There is no obvious reason why flight-level maximum TWC values in daytime overshoots would be lower than those in nighttime overshoots, which is supported at least in the one available comparison noted above for Darwin-14 flights 12 and 13. As space-borne measurements and techniques improve, the quantification of diurnal effects may become more realistic. As an example, the CloudSat W-band radar-in-space has provided approximately ten years of global, vertical, cross-section swaths of radar reflectivity, which may in the future be processed into global climatological profiles of IWC using improved reflectivity-IWC relationships for high IWC regions obtained from the HAIC-HIWC flight campaigns ([70]). However, the uncertainty created by diurnal effects is not likely to be resolved in the short term, and in the event of a future flight campaign, collection of nighttime and daytime data should be considered to reduce this uncertainty.

4.3 LOW AEROSOL CONCENTRATION ENVIRONMENT OF FLIGHT CAMPAIGN LOCATIONS

The locations of the three flight campaigns were all in what are considered to be relatively low aerosol concentration environments, especially Darwin and Cayenne, due to their remoteness from concentrated human population areas, industrial centers, bio-mass burning during the periods of the flight programs, and other sources of anthropogenic aerosol. This issue of "cloud-aerosol" interaction has been the subject of considerable research in the atmospheric science community over the last couple of decades, primarily due to its influence on the radiative properties of cloud tops and, in turn, the earth's radiation balance. It is considered to be a potentially important feedback in global climate change studies. Increased aerosol concentration has been linked to an increased number of cloud droplets with a smaller average size [71], and in shallow clouds to the suppression of drizzle by reducing "warm rain" precipitation formation [72], a process that is more efficient when larger droplets are present. Tropical clouds in a pristine environment have been argued to develop rain efficiently by the warm-rain process, whereas warm-rain precipitation can

be effectively suppressed in similar clouds injected with high aerosol from industrial emissions and bio-mass burning, presumably due to the nucleation of more numerous but smaller droplets [73-75]. There has been limited discussion in the literature specifically on the impact of increased aerosol on TWC levels in deep convective clouds. Cloud-aerosol interactions are admittedly complex, and have been postulated to affect storm dynamics as well as microphysics, which, in turn, can affect TWC. There is some evidence of an aerosol effect on the properties of thunderstorm tops. In one study, the effective diameter of ice particles at cloud top, estimated from satellite measurements, was found to be smaller in higher aerosol versus lower aerosol environments [76]. Although this study supports a microphysical modification in the types of clouds studied in this report as a result of increased aerosol, there is no clear conclusion how TWC itself might be affected. In another study, ice particles were found to form higher in clouds in a polluted atmosphere due to the suppression of ice multiplication processes [77]. Here we provide a speculative, first-order hypothesis on the aerosol effect on TWC of the deep convective clouds described in this report. In a high-aerosol environment, the suppression of warm rain and delay in the formation of ice likely leads to retention of more condensed water as the cloud grows beyond the freezing level. It therefore may be more likely to maintain a higher TWC aloft.

A variety of aerosol types produced naturally in the atmosphere can act as cloud droplet-forming nuclei, or cloud condensation nuclei (CCN). Certain regions of the world are known or suspected to have greatly increased CCN concentrations from industrial emissions, biomass burning, and other human activities. SO_2 emissions are generally a good surrogate for industrial activity. SO_2 is converted in the atmosphere to sulfate particles, which are quite efficient CCN. Figure 64 shows a 2010 land-based global SO_2 emissions inventory [78]. North America, Europe, India, and Southeast Asia are all major emitters, with Southeast Asia being the most important. While emissions in North America and Europe have decreased markedly over the last two decades, emissions in Asia and other developing countries are rising [79]. Based on Figure 64, one might therefore expect that the ocean regions in tropical and subtropical Southeast Asia, and particularly to the east of China, would experience higher sulfate aerosol concentrations than elsewhere in the world, and for those concentrations to increase relative to other regions in the foreseeable future. There also is a local maximum in engine events in this region [18, 24]. While a high frequency of MCS clouds, congested air traffic, and perhaps less flexibility for pilots to execute weather-related course changes are likely important factors contributing to this local maximum, there also is the interesting possibility that higher-TWC cloud caused by air pollution might also be a factor. If so, the TWC_{99} statistics of this report may be biased low relative to such geographical locations due to the relatively clean environments in which they were collected.

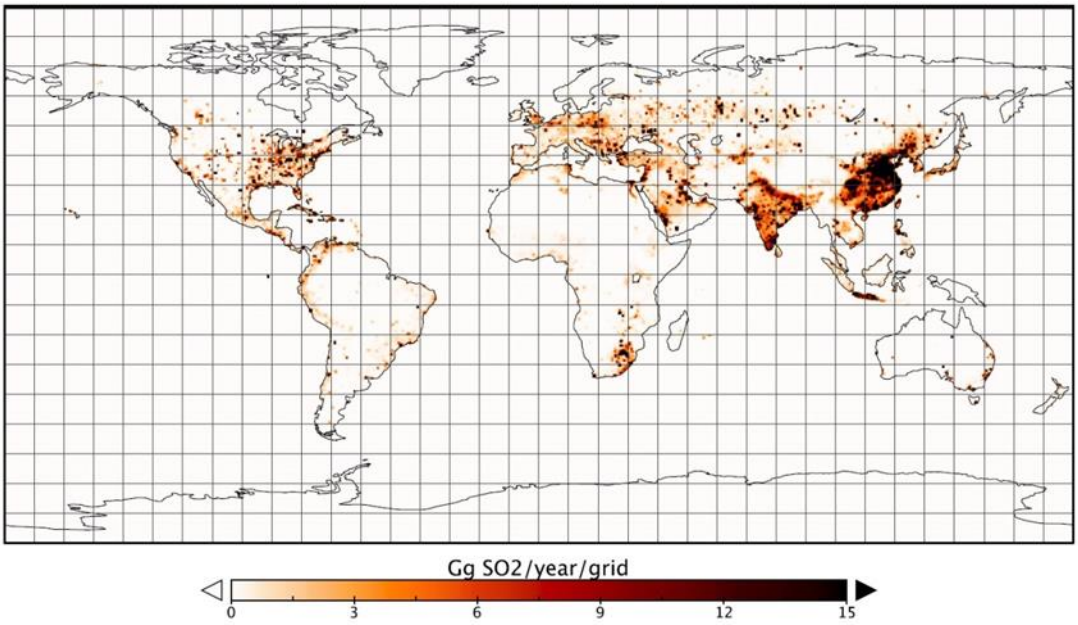

Figure 64. Global map of 2010 land-based emissions of S02 [78]

4.4 LARGE AND VIGOROUS CONTINENTAL MCSS

The types of clouds sampled in the three flight campaigns were guided by the weather analyses of engine events [29], where 80% were in a tropical air mass, roughly half of which were in more benign systems over the ocean, and the other half in stronger systems over the land. Only 8% were from mid-latitude continental MCSs, which were reported by these authors to generally form in a drier and more wind-sheared environment, and could be considerably more vigorous than tropical oceanic and even tropical overland MCSs. With the occurrence of more events of this type over central equatorial Africa as noted below, it is probably now appropriate to excise the "mid-latitude" term and refer to these simply as "continental MCSs." Continental systems over North America can form along frontal boundaries with embedded linear squall line features than can span from southern Canada down to the Gulf of Mexico. Such systems may produce high TWC on unusually long distance scales that would not be found in the types of oceanic MCSs studied in the flight campaigns. They also can form from multiple thunderstorms into a circular shield of cold cloud tops with an area much larger than individual thunderstorms. A particular form that meets certain objective criteria, including a cloud-top area colder than -52 C greater than 50,000 km^2 (circular equivalent diameter 136 Nm) for at least six hours, is called a Mesoscale Convective Complex. All of these systems tend to have strong updrafts, copious lightning, and high reflectivity regions at flight altitude. Some sampling of tropical overland late-afternoon systems was accomplished during the Cayenne-15 campaign, but these were typically smaller and shorter-lived systems. Sampling of the largest of such systems would have required sampling after sunset. The Cayenne-15 cases included in the data set are not representative of the "continental" category according to the definition of [29].

The locations of the earth's most intense convective storms have been studied using seven years of TRMM satellite-based radar measurements commencing in late 1994 [80]. The intensity-defining parameters included lightning flash rate, the maximum height of the 40 dBZ echo, and

microwave brightness temperature at frequencies sensitive to ice water path. For illustration, Figure 65 displays the geographical distribution of lightning flash rate. For the most part, intense storms so defined occur over land, most notably over the USA, equatorial Africa, and southeast South America. They are more visible to the pilot due to their lightning and high reflectivity at altitude. Presumably, core updraft regions with high TWC are therefore effectively avoided by normal use of the pilot's radar and other visual cues. An especially severe form called a supercell has a rotating and quasi-continuous updraft that can be sustained for hours. In general, the higher flight-level reflectivity and lightning of continental versus oceanic MCS are evidence of the differences in the microphysics of their core regions. The stronger updrafts of continental MCS likely preserve small liquid cloud droplets to higher levels in the storm, conducive to production of high reflectivity graupel or hail and lightning. The question is then whether these systems could produce TWC levels sufficiently high to induce an ice crystal icing event at a conventionally safe distance from the core (e.g., 20 Nm). There also is speculation that small liquid droplets in continental updraft cores may sometimes reach the level of homogenous freezing, forming a zone of very small frozen cloud droplets with very high TWC and low reflectivity. In this scenario, high TWC at altitude could be as undetectable on the pilot's radar as in oceanic MCSs. Note also that higher aerosol concentrations are likely in continental cases, and they are thus possibly subject to this additional influence on their microphysical properties, as hypothesized in the previous section.

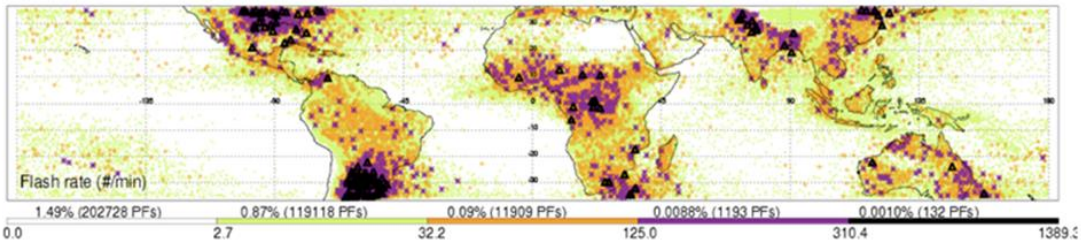

Figure 65. Geographic distribution of lightning flash rates [80]. Purple and black symbols are > 125 and > 310 flashes per minute

The most recent inventory of engine events [24] does display evidence of more overland cases than in the previous inventories [18, 33], possibly "continental" according to our updated definition of [29]. These are in two of the intense storm locations of [80]—southeast South America and equatorial Africa. The African cases noted in [24] are all nighttime events, and probably linked to a regional MCS formation phenomenon that has been previously noted and extensively researched by others. Some microphysical data have been collected in these clouds, but not specifically focused on the measurement of high IWC. Late afternoon convection forms along an interior continental range of mountains, and clouds grow overnight into large MCSs that propagate through the night towards the west, often past the African Atlantic coast [81]. The nature of the South America events was not discussed in detail in [24], other than that they predominantly occur overnight and into the morning. Certainly, the largest and deepest MCSs in the world have been observed in northern Argentina-southern Brazil. A more detailed investigation of these African and South American cases could help determine whether these engine events are associated with such severe cases, and whether in general the frequency of continental cases is now increasing to the point that the data set examined in this report is lacking an important cloud type.

The EIWG has been made aware of the occurrence of pitot anomalies in large continental convective clouds, for which an up-to-date inventory of date, time, and location is not publicly available. In this regard, it is prudent to note that the overall ice crystal icing threat may not be fully described by engine event clouds. Large, long-lived continental MCSs may become more important with further examination of current ice crystal icing issues, or if new issues develop. The current data set is void of such continental measurements.

5. SUMMARY AND CONCLUSIONS

Three successful flight campaigns have provided a modern, high-quality data set of the in-situ properties of deep convective clouds for the assessment of the FAA Title 14 Code of Federal Regulations Part 33 Appendix D mixed-phase/glaciated ice crystal envelope [7], and its EASA identical equivalent Appendix P [8] (hereinafter "Appendix D/P"). Airborne radar remote-sensing measurements may provide additional assessment data [5], but were not considered in this report. The basic objectives and strategies for the Appendix D/P assessment were formulated and updated during discussions of the Engine Harmonization Working Group (EHWG) and its successor the Engine Icing Working Group between 2004 and 2015. The first two campaigns were international collaborations between the European High Altitude Ice Crystals (HAIC) project and the North American High Ice Water Content (HIWC) project, and the third was the independent NASA/FAA HIWC-RADAR project. The HAIC-HIWC campaigns were conducted in Darwin, Australia with the SAFIRE Falcon-20 (Darwin-14), and in Cayenne, French Guiana with the Falcon-20 and the NRC Convair-580 (Cayenne-15). The NASA/FAA HIWC-RADAR campaign was conducted with the NASA DC-8 aircraft out of Fort Lauderdale, Florida (Florida-15). All aircraft were instrumented for in-situ cloud measurements, and the same instrument types have for the most part been used to provide the measurements described in this report. Before the flight campaign, modifications were made to existing instrumentation to improve performance in the harsh conditions, and a new isokinetic evaporator (IKP-2) was developed to make reliable and defensible TWC measurements. The IKP-2 provided all TWC measurements used in the Appendix D/P comparisons in this report. The same analysis methods were used for computation of cloud parameters when possible, or are otherwise reported and compared in this report.

The data were collected during 45 flight missions (multi-aircraft coordinated flights counted as one) on 40 different days, in 472 runs in or across approximately 115 clouds, and consists of about 29,600 Nm of in-cloud data. The data set is extensive and unique, with no current equivalent from the aviation industry of the atmospheric science community. All of the clouds sampled were in a warm, moist tropical atmosphere, with in-cloud points distributed exclusively in the warm extension of the Appendix D/P temperature-altitude envelope, not unlike the distribution observed for engine events.

The prime cloud type that was targeted was an oceanic Mesoscale Convective System (MCS) with an anvil and associated cirrus shield, at or near the equilibrium temperature level, of 100 Nm or larger. Large MCSs have been identified as the most common cloud type observed during engine events. Such clouds pump the high moisture content of the tropical boundary layer high into the atmosphere, where it must condense out to cloud hydrometeors. The clouds sampled in the flight programs had tops typically between about -60 and -90 C. In total, 92% of the in-cloud data was collected in such clouds, 18.7% of which was from six flights in three tropical storms. About 7% was collected in overland anvils of afternoon convection. The objective was to sample the clouds

in the vicinity of active cells, using satellite to identify the deepest cloud, and tilt-down on the pilot's radar to identify heavy rain below the aircraft as an indicator of high IWC aloft, but avoid vigorous cells and lightning as per commercial aircraft recommended procedures. The oceanic MCSs sampled were at times relatively benign, with no high reflectivity at altitude on the pilot's radar, and at other times more vigorous, with lightning and high reflectivity at altitude. High IWC was found to be associated with updrafts in both the benign and more vigorous cells, as expected. In the more benign cloud cases, the updraft cores were directly sampled, and in the more vigorous cases, either less-active neighboring cells were directly sampled within the MCS if possible, or the vigorous cells would be sampled at a safe distance. In some cases, the aircraft sampled only a stratiform area of the MCS after convective activity had ceased.

By temperature interval, the percentages of data by in-cloud distance are 19.5%, 3.3%, 30.2%, 29.5%, and 17.5% for -10, -20, -30, -40, and -50 ±5 C, respectively. The -20 C interval was not a target interval; due to the low data collection, it is not discussed in detail in this report. The project was tasked to collect at least 100 17.4 Nm-average "Type 1" non-overlapping data points (see section 3.1 for definition) to compute 99th percentile TWC statistics (TWC_{99}) at the four remaining temperature intervals. In this task, the projects were successful, collecting 271, 445, 434, and 263 points in the -10, -30, -40, and -50 C intervals. Naturally, many more points were collected at shorter distance scales. Data processing at different distance scales permitted the assessment of the Appendix D/P TWC_{99} "distance factor." A series of 13 distance scales between 0.5 and 100 Nm were analyzed, with 17.4 Nm being the "reference" scale for the TWC_{99} comparison to Appendix D/P.

The data set was evaluated for the occurrence of mixed phase, and levels of LWC. Mixed-phase cloud was found to be quite rare in the data set, and its occurrence diminished with decreasing temperature. The best estimates were made in Cayenne-15 by the Convair-580 aircraft, flying mostly within the -10 C temperature interval. Mixed-phase regions were usually less than a few nautical miles wide, and the average LWC never exceeded 0.25 gm^{-3}. Spatially, the fraction of in-cloud distance with LWC > 0.1 gm^{-3} was estimated at about 5%. A similar analysis was performed using the Darwin-14 and Cayenne-15 Falcon-20 data. The spatial fraction of mixed-phase zones was about 2.8% and 0.20 % in the -10 and -30 C intervals. There were no mixed-phase zones colder than -35 C. The median and maximum LWC exposure distances and event-average LWCs were 0.7 and 6.2 Nm and 0.08 and 0.32 gm^{-3}, respectively. The TWC data described in this report contain both liquid and ice components, but are clearly highly dominated by glaciated cloud. The Appendix D/P mixed-phase guidelines include a table specifying the supercooled portion of TWC, where, for example, in the 0 to -20 C range, the LWC is specified as ≤ 1.0 gm^{-3} for a cloud length of ≤ 50 Nm. The measurements of this report suggest that the guideline is excessive relative to the flight campaign data set. However, it is important to note that the tops of the flight campaign clouds had already grown to -60 C or colder, with high ice concentrations that would influence the liquid content of any embedded updraft. Shallower clouds may well contain more significant mixed-phase regions.

The maximum TWC observed at the shortest reported distance scale of 0.5 Nm was 4.1 gm^{-3}, measured in the -30 C temperature interval. At -50 C, the 0.5 Nm maximum was 2.7 gm^{-3}. At the 50 Nm distance scale, the all-temperature and -50 C maxima were 2.4 gm^{-3} and 1.7 gm^{-3}. Data from the three flight campaigns were combined for an overall 17.4 Nm TWC_{99} comparison to Appendix D/P (Figure 43 through Figure 47). The flight campaign TWC_{99} (17.4 Nm) values were

consistently lower than Appendix D/P values. In the -10, -30, -40, and -50 C intervals they were 2.7, 2.4, 2.1, and 1.8 gm^{-3}, respectively, about 58%, 53%, 53%, and 49% of Appendix D/P (overall 54.7%). Both Appendix D/P and flight campaign values decreased with decreasing temperature (increasing altitude) at about the same rate, providing some support for the physical basis of the appendix. The Appendix D/P TWCs are calculated values based on deep adiabatic lift for a span of low-level dewpoint temperatures, and scaled down by a factor of 0.65 to match the 17.4 Nm TWC_{99} calculated by the EHWG from the 1950s RAE deep convective cloud data set. Using the same procedure, the data of the current flight programs would have yielded a scale factor of about 0.36 (54.7% of 0.65) rather than 0.65.

The data sets display some location differences, and perhaps even aircraft bias or sampling strategy bias. Lightning areas, likely to be high TWC areas, were avoided using information from ground-based lightning detection networks, probably more efficiently than they would have been on a commercial aircraft. Ninety three percent of the -10 C data was collected during Cayenne-15. Sixty eight percent of the -50 C data was collected during Florida-15 (Figure 39). The uneven distribution of data at these temperatures is related to what had been accomplished in the previous flight program, and to the performance characteristics of the aircraft, as discussed in more detail in the main body of this report. The Cayenne-15 -10 C data set is comprised of both Falcon-20 and Convair-580 data, the former measuring TWC_{99} values a factor of 1.26 ± 0.04 and 1.32 ± 0.16 (± 2σ) higher at 0.5 and 17.4 Nm, respectively (Figure 43, Table 19). Further work is required to determine the cause of this discrepancy (e.g., did the Convair-580 consistently fly farther from precipitation cores than the Falcon-20, etc.), as the difference does not appear to be related to instrument bias or data processing. The Cayenne-15 data set contains the highest proportion of low TWC points for -30 C and colder (Figure 48). In spite of this, it contains the highest peak TWC values, which have the most influence on 99th percentiles. The largest location-to-location ratio of TWC_{99} (17.4 Nm) values was 1.38 ± 0.26 for Darwin-14 to Florida-15 at -40 C (Table 19, lower panel).

The Appendix D/P TWC_{99} distance factor was found to be reasonable for scale distances greater than or equal to 5 Nm, the approximate minimum distance scale from which it was developed, but it increasingly overestimated when extrapolated to shorter distance scales. A new polynomial distance factor expression was fit to the all-temperatures data set, and then evaluated for each specific temperature interval (Figure 59(a-e)). It was concluded that values from the new expression are either conservative, or within a few percent when predicting lower than observed.

For the analysis of the PSDs, cumulative mass distributions and MMD, the infrequent mixed-phase cloud periods were removed to provide ice-only particle distributions. The raw probe data are two-dimensional images of crystals, revealing mostly irregular ice particles grown by vapor diffusion and aggregation, with only occasional brief occurrences of higher density graupel particles. No hail was encountered. From the particle images, PSDs were produced by computer analysis. The approach taken to supply PSD data for the regulatory application is different than the 99th percentile approach for the TWC data. Since the primary driver for ice crystal icing events is likely the TWC level, it would not be meaningful to report the 99th percentile mass diameter, or the 99th percentile of the MMDs, since it is the MMDs during high IWC events that are of interest. PSDs were selected only when the IKP-2 TWC exceeded a selected IWC threshold value over a minimum distance threshold, providing a large number of data points only at high IWC for MMD calculation. Three distance and TWC thresholds were examined, and the results presented here are

for thresholds of 1 gm^{-3} and 0.5 Nm. The most important factor affecting MMDs was found to be the ambient temperature. MMDs increased with temperature (decreasing altitude). Average MMD values at -10, -30, -40, and -50 C were approximately 690, 480, 390, and 320 μm, respectively (Table 20). MMD differences between the Falcon-20 and DC-8 data sets were small: about 4 % at -50 C (DC-8 versus Falcon-20), 5% at -40 C (DC-8 versus Falcon-20), and 3 % at -30 C (DC-8 versus Falcon-20). At -10 C, where data were provided almost exclusively from the Cayenne-15 Convair-580 and Falcon-20 data sets, the differences were somewhat larger, with the Falcon-20 MMD being about 18% higher than that of the Convair-580. A sensitivity test was performed using alternate TWC thresholds of 0.7 and 1.5 gm^{-3}, and reference distances of 17.4 and 30 Nm, and MMDs changed by at most 14% (Table B-11 and Table B-12). Figure 60 shows cumulative mass distributions.

The HAIC-HIWC Science team discussed the representativeness of the data set in describing aviation global exposure to high IWC conditions. In general, the clouds sampled in the Darwin-14 campaign best represented the published properties of the large tropical MCS associated with engine events, especially those in the oceanic regions of Southeast Asia. The Cayenne-14 and Florida-15 MCSs, although smaller and shallower, provided complementary data and were important in completing the data set at four temperature levels. Moreover, there was a definite advantage to having collected the data in three locations. If all data had been collected in a single location, location bias would be possibly the largest open question. Nevertheless, the science team identified three primary shortcomings in the data set.

First, only daytime measurements were made, in Darwin-14 and Cayenne-15 for reasons of flight safety, and in Florida-15, due to other project scientific and operational priorities. The deepest oceanic clouds are known to have their peak intensities in the early morning hours and to diminish after daylight. To some degree, this was observed during all three campaigns, but the impression was that the effect was strongest in Darwin-14. Twenty-year satellite climatologies for fixed oceanic geographical boxes near Cayenne and Florida for the months of the respective flight campaigns revealed two modes in the diurnal distribution of cold cloud top area between -40 C and -80 C—one in the early morning that was dominant for the coldest cloud tops, and a second in the late morning to early afternoon dominant for the warmer cloud tops. Within each campaign area, geographical variations in the diurnal results were in fact larger than the inter-campaign area differences, illustrating the importance of regional influences such as coastal interactions, tropical waves, etc., and underscoring the difficulty in generalizing the results of these satellite studies. For Darwin, instead of a long-term climatology, the diurnal variations in individual storms sampled by the aircraft were studied. Although every attempt was made to sample as early as possible after daybreak, Darwin-14 satellite infrared cold cloud-top imagery revealed that the Falcon-20 sampled on the average about 2.6 hours after what was surmised to have been the optimum sampling time for high TWC. Although the above studies provide some context to the flight measurements at each location, they provide no solid quantitative information on how TWC_{99} statistics of this report may have been affected. There is some reason to believe that elevated TWCs would have been sampled over longer distance scales if sampled at the optimum time when the coldest cloud-top areas were larger, but whether higher absolute TWC values would have been sampled is an open question. Further storm-specific analyses are underway from Cayenne, and will be reported at a later date.

Second, most flights were conducted in regions associated with relatively clean air and low aerosol concentrations. These regions contrast greatly with oceanic regions off the coast of Southeast Asia (e.g., China), where the highest concentration of aerosol-producing, industrial gas emissions on earth are found, resulting in high air-pollution levels with high aerosol loadings and low visibilities. The link to TWC levels is speculative. Tropical clouds growing in a clean environment efficiently produce rain by a "warm rain" process even before they reach the freezing level, reducing the amount of condensate that could be lifted to flight altitudes. In a high aerosol environment, there is evidence that the efficiency of this warm rain process is reduced or even cut off. Furthermore, there is some evidence that the development of precipitation by the growth of ice particles in an updraft may be delayed in high aerosol conditions. Although the microphysical evolution of clouds is rife with interactions and complexities, the first-order hypothesis put forth here is that a high aerosol environment may produce higher TWCs aloft. The high frequency of engine events in oceanic Southeast Asia is undoubtedly influenced by factors such as high-traffic density and the frequency of suitable clouds, but the proximity to large pollution sources creates a certain level of curiosity as to the influence of aerosol.

Third, the data set is completely void of data from large vigorous continental MCSs, such as those observed over the continental USA in the spring and summer. This cloud type includes the strongest storms observed on the earth, and as such, they are likely to be efficiently avoided by pilots using conventional in-flight detection techniques. In early studies, only a small fraction of engine events were observed in this cloud type (~8%); however, in a more recent study they appear to be increasing in frequency, especially over continental Africa and southeastern South America. Is it possible that such storms may produce sufficiently high TWCs at a conventional safe distance from core regions to induce ice crystal icing events at a significant frequency? A more detailed examination of these engine-event cases might help determine whether the assessment of this report is lacking an important cloud type.

It is prudent to recognize that the results of this report, although unique in breadth and quality, come from limited measurements in a domain much smaller than that charted by commercial aircraft. Using a modified quote from the report outlining the data set collected in the 1940s for FAR Part 25 Appendix C envelope [10], the data from this study are *applicable only to the regions in which they were collected*, and may be augmented according to the techniques of this report if future data analysis and/or raw data become available.

6. REFERENCES

1. Strapp, J. W., G. A. Isaac. A. Korolev, T. Ratvasky, R. Potts, P. May, A. Protat, P. Minnis, A. Ackerman, A. Fridlind, J. Haggerty, and J. Riley, "The High Ice Water Content (HIWC) Study of deep convective clouds: Science and technical plan.", 2016, FAA Rep. DOT/FAA/TC-14/31, available at http://www.tc.faa.gov/its/worldpac/techrpt/tc14-31.pdf. 105 pps.

2. Dezitter, F., A. Grandin, J.-L. Brenguier, F. Hervy, H. Schlager, P. Villedieu, and G. Zalamansky, 2013: HAIC - High Altitude Ice Crystals. *5th AIAA Atmospheric and Space Environments Conference*, American Institute of Aeronautics and Astronautics http://arc.aiaa.org/doi/abs/10.2514/6.2013-2674 (Accessed February 9, 2015).

3. Schwarzenboeck, A., and co-authors, 2018: Analysis method used to provide all in situ TWC, IWC, LWC, and corresponding PSD (as a function of maximum and surface equivalent cloud particle diameters) data. *EASA Technical Report EASA.2013.FC.27.SC003 EASA HighIWC D3.18 R2.0*

4. Schwarzenboeck, A., and co-authors, 2018: Characterization of in-situ measured microphysical properties in high IWC regions during the 2014 and 2015 HAIC/HIWC international field campaigns. *EASA Technical Report EASA.2013.FC.27.SC003 EASA HighIWC D3.19 R2.0.*

5. Protat, A., and co-authors 2018: Retrieval of microphysical properties from cloud radar RASTA remote sensing data and closure analysis. *EASA Technical Report EASA.2013.FC.27.SC003 EASA HighIWC D3.20 R2.0.*

6. Huet, F., and co-authors, 2018: Intermediate report and assessment of the CS-25 Appendix P. *EASA Technical Report EASA.2013.FC.27.SC003 EASA HighIWC D3.21 R2.0.*

7. Title 14 Code of Federal Regulations, Part 25 and 33 Appendix D. Airplane and Engine Certification Requirements in Supercooled Large Drop, Mixed Phase, and Ice Crystal Icing Conditions. Docket No. FAA–2010–0636; Amendment Nos. 25–140 and 33–34, published by the Office of the Federal Register, National Archives and Records Administration, Washington, DC. Effective November 4, 2014.

8. EASA CS 25 Book 1 Appendix P, annex to Executive Director Decision 2015/008/R of 12 March 2015 amending Certification Specifications and Acceptable Means of Compliance for Large Aeroplanes CS-25 at Amendment 16. Available from https://www.easa.europa.eu/document-library/certification-specifications/cs-25-amendment-16.

9. McNaughton, I.I., "The analysis of measurements of free ice and ice/water concentrations in the atmosphere of the equatorial zone.",1959, *Royal Aircraft Establishment (Farnborough) Technical Note No. : Mech. Eng. 283.*

10. Title 14 Code of Federal Regulations, Part 25 Airworthiness Standards: Transport Category Airplanes, Section C25.1: Appendix C; published by the Office of the Federal Register, National Archives and Records Administration, Washington, D.C., Amdt. 25-140, Effective 5-Jan-2015.

11. Riley, J.T., 1998: Mixed-Phase Icing Conditions: A Review. FAA Technical Report DOT/FAA/AR-98/76. Available from http://www.tc.faa.gov/its/worldpac/techrpt/ar98-76.pdf.

12. Lawson, R.P., Angus, L.J., and Heymsfield, A..J., "Cloud Particle Measurements in Thunderstorm anvils and Possible Threat to Aviation," *J. Aircraft, Vol. 35, No. 1*, 1998, pp. 113-121.

13. FAA Docket No. 96-NM-162-AD; Amendment 39-9694; AD 96-14-09. Airworthiness Directives: British Aerospace Model Bae 146-100A, -200A, and -300A Series Airplanes.
14. FAA Docket No. 96-NM-162-AD; Amendment 39-9694; AD 96-14-09. Cancellation. Available from http://rgl.faa.gov/Regulatory_and_Guidance_Library/rgad.nsf/0/0FC9B18C4E49D19886256A0A00736F22?OpenDocument.
15. FAA Docket No. 98-ANE-42-AD; Amendment 39-11225; AD 99-15-06. Available from http://rgl.faa.gov/Regulatory_and_Guidance_Library/rgad.nsf/0/61A90814DF61966686256862007440B8?OpenDocument&Highlight=96-14-09.
16. FAA Docket No. 98-ANE-42-AD; Amendment 39-11225; AD 99-15-06. Available from http://rgl.faa.gov/Regulatory_and_Guidance_Library/rgad.nsf/0/61A90814DF61966686256862007440B8?OpenDocument&Highlight=94-07-09 .
17. FAA Docket No. 98-ANE-42-AD; Amendment 39-11225; AD 99-15-06. Available from http://rgl.faa.gov/Regulatory_and_Guidance_Library/rgad.nsf/0/61A90814DF61966686256862007440B8?OpenDocument&Highlight=99-15-06.
18. Mason, J., Strapp J.W. and Chow P., 2006. "The Ice Particle Threat to Engines in Flight." *44th AIAA Aerospace Sciences meeting and Exhibit*, Reno, Nevada AIAA 2006-206.
19. In-flight Icing Encounter and Loss of Control Simmons Airlines, d.b.a. American Eagle Flight 4184 Avions de Transport Regional (ATR) Model 72-212, N401AM, Roselawn, Indiana October 31, 1994; Volume 1: (NTSB/AAR-96-01)
20. In-flight Icing Encounter and Loss of Control Simmons Airlines, d.b.a. American Eagle Flight 4184 Avions de Transport Regional (ATR) Model 72-212, N401AM, Roselawn, Indiana October 31, 1994; Volume II (NTSB/AAR-96-02)
21. National Transportation Safety Board Safety Recommendation A-96-54. August 15, 1996.
22. Mazzawy, R. S., 2009, "Technical Compendium from Meetings of the Engine Harmonization Working Group," DOT/FAA/AR-09/13.
23. Climatic Extremes For Military Equipment. MIL-STD-210A, U.S. Government Printing Office,Washington 25, D.C., 2 August 1957.
24. Bravin, M., Strapp, J.W., and Mason, J.G., "An Investigation into Location and Convective Lifecycle Trends in an Ice Crystal Icing Engine Event Database," 2015, *SAE Technical paper 2015-01-2130.*
25. Duviver, E., 2010: "High Altitude Icing Environment," *Intl. Air Safety and Climate Change Conf.*, 8-9 Sep. 2010, Cologne, Germany, available from http://www.easa.europa.eu/conferences/iascc/doc/ Workshop%201%20Presentations/Workshop1_DAY%202/1_Duvivier_EASA/IASCC_E%20Duvivier.pdf
26. Ice and Rain Minimum Qualification Standards for Pitot and Pitot-static Probes, 2015. SAE AS5562, Society of Automotive Engineers, 17 pp.

27. Mazzawy, Robert S., and Strapp J. Walter, “Appendix D – An Interim Icing Envelope : High Ice Crystal Concentrations and Glaciated Conditions”. 2007, *SAE Transactions, Journal of Aerospace*, 116, 634-642.

28. Grandin, A., Merle, J-M, Weber, M., Strapp, J.W., Protat, A., and King, P. "AIRBUS Flight Tests in High Total Water Content Regions", 6th AIAA Atmospheric and Space Environments Conference, AIAA AVIATION Forum, (AIAA 2014-2753)http://dx.doi.org/10.2514/6.2014-2753

29. Mason, J.G., and M. Grzych, 2011: The challenges identifying weather associated with jet engine ice crystal icing. *SAE Transactions, Journal of Aerospace*, doi:10.4271/2011-38-0094.

30. American Meteorological Society, "Mesoscale Convective System". Glossary of Meteorology 2014.

31. May, P., C. Jakob, and J.H. Mather, 2004: Tropical Warm Pool International Cloud Experiment (TWP-ICE): Cloud and Rain Characteristics in the Australian Monsoon. DOE Report DOE/ER/ARM-0401. 33 pp.

32. Zipser, E.J., and K.R. Lutz, 1994: The vertical profile of radar reflectivity of convective cells: A strong indicator of storm intensity and lightning probability? *Mon. Wea. Rev.*, 122, 1751–1759.

33. Gryzch, M. and J. Mason, 2010: Weather conditions associated with jet engine power loss and damage due to ingestion of ice particles: What we’ve learned through 2009. *14th Conference on Aviation, Range and Aerospace Meteorology, AMS*, Atlanta, GA, 17-21 January 2010.

34. FAA Aeronautical Information Manual. Official Guide to Basic Flight Information and ATC Procedures. 2015. U.S. Department of Transportation, Federal Aviation Administration. Available from https://www.faa.gov/air_traffic/publications/media/aim.pdf.

35. Grzych, M., Tritz, T., Mason, J., Bravin, M., and Sharpsten, A., “Studies of Cloud Characteristics Related to Jet Engine Ice Crystal Icing Utilizing Infrared Satellite Imagery,” SAE Technical Paper, 2015-01-2086, 2015, doi:10.4271/2015-01-2086.

36. Bowden, D.t., Gensemer, A.E., and Speen, C.A., 1965: Engineering Summary of Airframe Icing Technical Data. FAA Technical Report ADS-4. Available from http://www.dtic.mil/dtic/tr/fulltext/u2/608865.pdf.

37. McNaughtan, I..I. and F. J. Bigg, 1959: Development and calibration of the pitot type ice concentration meter. *Royal Aircraft Establishment (Farnborough) Technical Note No. : Mech. Eng. 281*.

38. Strapp, J.W., Lilie, L.E., Ratvasky, T.P., Davison, C.R., and C. Dumont, 2016. Isokinetic TWC Evaporator Probe: Development of the IKP2 and Performance Testing

for the HAIC-HIWC Darwin 2014 and Cayenne Field Campaigns, *8th AIAA Atmospheric and Space Environments Conference, AIAA Aviation*, AIAA 2016-4059. http://dx.doi.org/10.2514/6.2016-4059

39. Protat, A., D. Bouniol, J. Delanoë, P. May, A. Plana-Fattori, A. Hasson, E. O'Connor, U. Görsdorf, and A. J. Heymsfield, 2009: Assessment of CloudSat reflectivity measurements and ice cloud properties using ground-based and airborne cloud radar observations. J. Atmos. Oceanic Technol., 26 (9), 1717-1741.

40. Delanoë, J. A. Protat, O. Jourdan, J. Pelon, M. Papazzoni, R. Dupuy, J.-F. Gayet, and C. Jouan, 2013 : Retrieval of polar ice cloud properties using RALI platform during POLARCAT campaign. Atmospheric Chemistry and Physics. J. Atmos. Oceanic Technol., 30, 57–73.

41. Wolde, M. and Pazmany, A., 2005, NRC Dual-Frequency Airborne Radar For Atmospheric Research, Proceedings 32nd Conference on Radar Meteorology, American Meteorological Society, 24-29 October 2005, Albuquerque, NM, USA, P1R.9.

42. Wolde, M., Nguyen, C., Korolev, A.V., and Bastian, M., 2016. "Characterization of the Pilot X-band radar responses to the HIWC environment during the Cayenne HAIC-HIWC 2015 Campaign", 8th AIAA Atmospheric and Space Environments Conference, AIAA Aviation Forum, (AIAA 2016-4201).

43. Lawson, R. P., D. O'Connor, P. Zmarzly, K. Weaver, B. A. Baker, Q. Mo, and H. Jonsson, 2006: The 2D-S (Stereo) probe: Design and preliminary tests of a new airborne, high speed, high-resolution particle imaging probe, *J. of Atmos. Oceanic Technol.*, 23, 1462-1477.

44. Baumgardner, D., and Coauthors, 2011: Airborne instruments to measure atmospheric aerosol particles, clouds and radiation: A cook's tour of mature and emerging technology. Atmospheric Res., 102, 10–29, doi:10.1016/j.atmosres.2011.06.021

45. Lance, S., Brock, C. A., Rogers, D., and Gordon, J. A.: Water droplet calibration of the Cloud Droplet Probe (CDP) and in-flight performance in liquid, ice and mixed-phase clouds during ARCPAC, Atmos. Meas. Tech., 3, 1683-1706, doi:10.5194/amt-3-1683-2010, 2010.

46. Leroy, D., E. Fontaine, A. Schwarzenboeck, and J. W. Strapp, 2016: Ice Crystal Sizes in High Ice Water Content Clouds. Part I: On the Computation of Median Mass Diameter from In Situ Measurements. *J. Atmospheric Ocean. Technol.*, 33, 2461–2476, doi:10.1175/JTECH-D-15-0151.1.

47. Korolev, A.V., J.W. Strapp, and G.A. Isaac, 1998b: Evaluation of the accuracy of PMS optical array probes. *J. Atmos. Oceanic Technol.*, 15, 708-720.

48. Cober, S. G., G. A. Isaac, A. V. Korolev, and J. W. Strapp, 2001: Assessing cloud-phase conditions. *J. Appl. Meteor.*, 40, 1967–1983, doi:10.1175/1520-0450(2001)040<1967:ACPC>2.0.CO;2.

49. Webster, P.J., and R. Lukas, 1992: TOGA COARE: The Coupled Ocean–Atmosphere Response Experiment. *Bull. Amer. Meteor. Soc.*,73, 1377–1416

50. Rash, C.F., When Lightning Strikes, 2010, AeroSafety World, June, 2010. https://flightsafety.org/asw-article/when-lightning-strikes/

51. Korolev, A., G. McFarquhar, P.R. Field, C. Franklin, P. Lawson, Z. Wang, E. Williams, S.J. Abel, D. Axisa, S. Borrmann, J. Crosier, J. Fugal, M. Krämer, U. Lohmann, O. Schlenczek, M. Schnaiter, and M. Wendisch, 2017: Mixed-Phase Clouds: Progress and Challenges. *Meteorological Monographs*, **58**, 5.1–5.50, https://doi.org/10.1175/AMSMONOGRAPHS-D-17-0001.1

52. Rosenfeld, D., W.L. Woodley, T.W. Krauss, and V. Makitov, 2006: Aircraft microphysical documentation from cloud base to anvils of hailstorm feeder clouds in Argentina. *J. Appl. Meteor. Climatol.*, 45, 1261–1281.

53. Korolev, A. V. Rates of phase transformations in mixed-phase clouds.2008. Q.J.R. Meteorol. Soc., 134: 595–608. doi:10.1002/qj.230

54. Stith, J. L., J. E. Dye, A. Bansemer, A. Heymsfield, C. Grainger, W.W. Petersen, and R. Berticelli, 2002: Microphysical observations of tropical clouds. *J. Appl. Meteor.*,41, 97-117.

55. Black, R. and J. Hallett, 1986: Observations of the ice distributions in hurricanes, *J. Atmos. Sci.*, 43, 802-822

56. Davison, C. R., Strapp, J. W., Lilie, L., Ratvasky, T. P., and Dumont, C., " Isokinetic TWC Evaporator Probe: Calculations and Systemic Error Analysis", 2016, *8th AIAA Atmospheric and Space Environments Conference*, June 17, 2016, Washington, DC. AIAA-4060. http://dx.doi.org/10.2514/6.2016-4060

57. Hyndman, R.J. and Fan, Y. (November 1996). "*Sample Quantiles in Statistical Packages*", The American Statistician 50 (4): pp. 361–365.

58. NIST/SEMATECH e-Handbook of Statistical Methods. http://www.itl.nist.gov.div898/handbook/, section 7.2.6.2, April 2012.

59. Fontaine, E., A. Schwarzenboeck, J. Delanoë, W. Wobrock, D. Leroy, R. Dupuy, C. Gourbeyre, and A. Protat, 2014: Constraining mass–diameter relations from hydrometeor images and cloud radar reflectivities in tropical continental and oceanic convective anvils. *Atmos Chem Phys*, 14, 11367–11392, doi:10.5194/acp-14-11367-2014.

60. Lewis, W., and N.R. Bergrum, 1951: A Probability Analysis of the Meteorological Factors Conducive to Aircraft Icing in the United States. NACA Tech. Note 2738, 99 pp.

61. Aircraft Ice Protection: Report of Symposium April 28-30, 1969. Federal Aviation Administration, Washington, DC Flight Standards Service. Available from

http://www.dtic.mil/cgi-bin/GetTRDoc?Location=U2&doc=GetTRDoc.pdf&AD=AD0690469

62. Liu, C., E.J. Zipser, and S.W. Nesbitt, 2007: Global Distribution of Tropical Deep Convection: Different Perspectives from TRMM Infrared and Radar Data. *J. Climate*, 20,489–503, doi: 10.1175/JCLI4023.1.

63. Levitus, S., and T.P. Boyer, 1994. "Temperature Vol. 4, World Ocean Atlas 1994", NOAA Atlas NESDIS 4.

64. Allbright, M.D., E.R. Recker, R.J. Reed, and R. Dang. 1985. "The Diurnal Variation of Deep Convection and Inferred Precipitation in the Central Tropical Pacific During January-February 1979." *Mon. Wea. Rev. 113* 1663-1680

65. Liu, C., E.J. Zipser, 2008: Diurnal cycles of precipitation, clouds, and lightning in the tropics from 9 years of TRMM observations. Geophys. Res. Letters, 35, L04819, doi:10.1029/2007GL032437

66. Chen, S. S., and R. A. Houze, Jr., 1997: Diurnal variation and life cycle of deep convective systems over the tropical Pacific warm pool. *Quart. J. Roy. Meteor. Soc.,* 123, 357-388.

67. Randall, D.A., Harshvardhan, and D.A. Dazlich, 1991: Diurnal variability of the hydrological cycle in a GCM. J. Atmos. Sci., 48, 40-62.

68. Protat, A., S. Rauniyar, V. V. Kumar, and J. W. Strapp, 2014: Optimizing the Probability of Flying in High Ice Water Content Conditions in the Tropics Using a Regional-Scale Climatology of Convective Cell Properties. *J. Appl. Meteorol. Climatol.*, 53, 2438–2456, doi:10.1175/JAMC-D-14-0002.1.

69. Yost, C. R., Bedka, K. M., Minnis, P., Nguyen, L., Strapp, J. W., Palikonda, R., Khlopenkov, K., Spangenberg, D., Smith Jr., W. L., Protat, A., and Delanoe, J.: A prototype method for diagnosing high ice water content probability using satellite imager data, Atmos. Meas. Tech., 11, 1615-1637, https://doi.org/10.5194/amt-11-1615-2018, 2018.

70. Protat, A.A., J.J. Delanoë, J.W. Strapp, E.E. Fontaine, D.D. Leroy, A.A. Schwarzenboeck, L.L. Lilie, C.C. Davison, F.F. Dezitter, A.A. Grandin, and M.M. Weber, 2016: The Measured Relationship between Ice Water Content and Cloud Radar Reflectivity in Tropical Convective Clouds. *J. Appl. Meteor. Climatol.*, 55, 1707–1729, doi: 10.1175/JAMC-D-15-0248.1.

71. Twomey, S.A., 1977: The influence of pollution on the shortwave albedo of clouds. *J. Atmos. Sci*., 34, 1149–1152.

72. Albrecht, B. A., 1989: Aerosols, cloud microphysics, and fractional cloudiness, *Science*, 245, 1227-1230.

73. Rosenfeld, D., 2000: Suppression of rain and snow by urban and industrial air pollution, *Science*, 287, 1793-1796.

74. Rosenfeld, D., Lohmann, U., Raga, G., O'Dowd, C, Kulmala, M, Fuzzi, S., Reissell, A, and Andreae, M., 2008: Flood or Drought: How Do Aerosols Affect Precipitation? *Science* 321, 1309-1313. doi: 10.1126/science.1160606

75. Wendisch, M., and Coauthors, 2016: The ACRIDICON–CHUVA campaign: Studying tropical deep convective clouds and precipitation over Amazonia using the new German research aircraft HALO. *Bull. Amer. Meteor. Soc.*, 97, 1885–1908, doi:https://doi.org/10.1175/BAMS-D-14-00255.1.

76. Sherwood, S.C. Aerosols and ice particle size in tropical cumulonimbus. *Journal of Climate*, Vol. 15, No. 9, 2002, pp 1051-1063

77. Braga, R. C., Rosenfeld, D., Weigel, R., Jurkat, T., Andreae, M. O., Wendisch, M., Pöschl, U., Voigt, C., Mahnke, C., Borrmann, S., Albrecht, R. I., Molleker, S., Vila, D. A., Machado, L. A. T., and Grulich, L.: Further evidence for CCN aerosol concentrations determining the height of warm rain and ice initiation in convective clouds over the Amazon basin, Atmos. Chem. Phys., 17, 14433-14456, https://doi.org/10.5194/acp-17-14433-2017, 2017.

78. Klimont, Z. , S. J. Smith, and J. Cofala , 2013: The last decade of global anthropogenic sulfur dioxide: 2000–2011 emissions. Environ. Res. Lett. 8 (2013) 014003 (6pp), doi:10.1088/1748-9326/8/1/014003

79. Forster, P., V. Ramaswamy, P. Artaxo, T. Berntsen, R. Betts, D.W. Fahey, J. Haywood, J. Lean, D.C. Lowe, G. Myhre, J. Nganga, R. Prinn, G.Raga, M. Schulz, and R.V. Dorland, 2007: Changes in Atmospheric Constituents and in Radiative Forcing, in Climate Change 2007: The Physical Science Basis. Contribution of Working Group I to the Fourth Assessment Report of the Intergovernmental Panel on Climate Change, edited by S. Solomon, D. Qin, M. Manning, Z. Chen, M. Marquis, K.B. Averyt, M.Tignor, and H.L. Miller, Cambridge University Press, United Kingdom and New York, NY, USA.

80. Zipser, E.J., C. Liu, D.J. Cecil, S.W. Nesbitt, and D.P. Yorty, 2006: Where are the most intense thinderstorms on earth?, *Bull. Amer. Meteor. Soc.*, 87,1057–1071, doi: 10.1175/BAMS-87-8-1057.

81. Laing, A.G., Carbone, R., Levizzani, W., and Tuttle, J. 2008. The Propagation and Diurnal Cycles of Deep Convection in Northern Tropical Africa. *Q. J. R. Meteorol. Soc.*, 134, 93-109.

82. Brenguier J.-L., W. D. Bachalo, P. Y. Chuang, B. M. Esposito, J. Fugal, T. Garrett, J.-F. Gayet, H. Gerber, A. Heymsfield, A. Kokhanovsky, A. Korolev, R. P. Lawson, D. R. Rogers, R. A. Shaw, W. Strapp and M. Wendish, 2013: In Situ Measurements of Cloud and Precipitation Particles. In Airborne Measurements for Environmental Research: Methods and Instruments, first edition by M. Wendish and J.-L. Brenguier. 2013. Wiley-VCH Verlag GmbH & Co. KGaA.

83. Korolev. A.V., Isaac, G.A., Cober, S.G., Strapp, J.W., and Hallett, J., 2002. Microphysical characterization of mixed-phase clouds. *Q. J. R. Meteorol. Soc.* (2003), 129, pp. 39–65

84. Strapp, J.W., J. MacLeod, and L.E. Lilie, 2008: Calibration of Ice Water Content in a Wind Tunnel / Engine Test Cell Facility. *15th Inter. Conf. On Clouds and Precipitation*, Cancun, Mexico, 7-11 July 2008.

85. Davison, C. R., MacLeod, J. D., Strapp, J. W., and Buttsworth, D. R., 'Isokinetic Total Water Content Probe in a Naturally Aspirating Configuration: Initial Aerodynamic Design and Testing", *46th AIAA Aerospace Sciences Meeting and Exhibit*, Jan. 10, 2008, Reno, Nevada, AIAA-2008-0435.

86. Davison, C.R., MacLeod, J.D., and Strapp, J.W., "Naturally Aspirating Isokinetic Total Water Content Probe: Evaporator Design and Testing," *1st AIAA Atmospheric and Space Environments Conference,* 25 June 2009, San Antonio, Texas, AIAA-2009-3861.

87. Davison, C. R., Landreville, C., and MacLeod, J. D., "Initial Development and Testing of Isokinetic Probe to Measure Total Water Content During Ground and Airborne Testing," NRC, LTR-GTL-2010-0002, Ottawa, Mar. 2010.

88. Davison, C.R., MacLeod, J.D., and Ratvasky, T.P., "Naturally Aspirating Isokinetic Total Water Content Probe: Preliminary Test Results and Design Modifications," *2nd AIAA Atmospheric and Space Environments Conference,* 2-5 August 2010, Toronto, Ontario, AIAA-2010-7530.

89. Davison, C.R., Ratvasky, T.P., and Lilie, L.E., "Naturally Aspirating Isokinetic Total Water Content Probe: Wind Tunnel Test Results and Design Modifications," *SAE 2011 International Conference on Aircraft and Engine Icing and Ground Deicing*, 13-17 June 2011, Chicago, Illinois, SAE 2011-38-0036.

90. Field, P. R., R. Wood, P. R. A. Brown, P. H. Kaye, E. Hirst, R. Greenaway, and J. A. Smith, 2003: Ice Particle Interarrival Times Measured with a Fast FSSP. *J. Atmospheric Ocean. Technol.*, 20, 249–261, doi:10.1175/1520-0426(2003)020<0249:IPITMW>2.0.CO;2.

91. Korolev, A., and G. A. Isaac, 2005: Shattering during Sampling by OAPs and HVPS. Part I: Snow Particles. *J. Atmospheric Ocean. Technol.*, 22, 528–542, doi:10.1175/JTECH1720.1.

92. Heymsfield, A. J., 2007: On measurements of small ice particles in clouds. *Geophys. Res. Lett.*, 34, L23812, doi:10.1029/2007GL030951.

93. Korolev, A., E. Emery, and K. Creelman, 2013: Modification and Tests of Particle Probe Tips to Mitigate Effects of Ice Shattering. J. Atmos. Oceanic Technol., 30, 690–708,https://doi.org/10.1175/JTECH-D-12-00142.1

94. Korolev, A.V., E. F. Emery, J. W. Strapp, S. G. Cober, G. A. Isaac, M. Wasey, D. Marcotte, 2011: Small ice particles in tropospheric clouds: fact or artifact? Airborne Icing Instrumentation Evaluation Experiment. . *Bull. Amer. Met. Soc*., 92, 967-973.

95. Field, P. R., A. J. Heymsfield, and A. Bansemer, 2006: Shattering and Particle Interarrival Times Measured by Optical Array Probes in Ice Clouds. *J. Atmospheric Ocean. Technol.*, 23, 1357–1371, doi:10.1175/JTECH1922.1.

96. Baker, B., Q. Mo, R. P. Lawson, D. O'Connor, and A. Korolev, 2009: The Effects of Precipitation on Cloud Droplet Measurement Devices. *J. Atmospheric Ocean. Technol.*, 26, 1404–1409, doi:10.1175/2009JTECHA1191.1.

97. Lawson, R.P., 2011: Effects of ice particles shattering on the 2D-S probe. *Atmos. Meas. Tech*., 4, 1361-1381.

98. Korolev, A.V., and P. R. Field, 2015: Assessment of the performance of the inter-arrival time algorithm to identify ice shattering artifacts in cloud particle probe measurements. *Atmos Meas Tech*, 8, 761–777, doi:10.5194/amt-8-761-2015.

99. Korolev, A., 2011a: *Probe Tips for Airborne Instruments Used to Measure Cloud Microphysical Parameters*. *United States Patent No. 7,861,584*, Issued: January 4, 2011, Owner: Her Majesty the Queen in Right of Canada, as Represented by The Minister of Environment.

100. Lilie, L., Emery, E., Strapp, J. W., and Emery, J. "A Multiwire Hot-Wire Device for Measurement of Icing Severity, Total Water Content, Liquid Water Content, and Droplet Diameter " 43rd AIAA Aerospace Sciences Meeting and Exhibit, AIAA-2005-859, 2005.

101. Lilie and SEA co-authors, "HAIC/HIWC 2014 Darwin and 2015 Cayenne Flight Campaigns Update I
Presentation: Description and Results for a Simple Ice Crystal Detection System for Airborne Applications," *8th AIAA Atmospheric and Space Environments Conference*, June 17, 2016, Washington, DC. (AIAA 2016-4058). http://dx.doi.org/10.2514/6.2016-4058

102. Stallabrass, J. R., 1978: An appraisal of the single rotating cylinder method of liquid water content measurement. National Research Council Canada, Rep. LTR-LT-92, 26 pp.

103. Strapp, J.W., J. Oldenburg, R. Ide, L. Lilie, S. Bacic, Z, Vukovic, M. Oleskiw, D. Miller, E. Emery, and G. Leone, 2002: Wind tunnel measurements of the response of hot-wire liquid water content instruments to large droplets. *J. Atmos. and Oceanic Technol.* Strapp, 20, 791-806.

104. R Core Team. R: A language and environment for statistical computing. R Foundation for Statistical Computing, Vienna, Austria. 2013. URL http://www.R-project.org/.

105. Wu, W., and G. M. McFarquhar, 2016: On the Impacts of Different Definitions of Maximum Dimension for Nonspherical Particles Recorded by 2D Imaging Probes. *J. Atmospheric Ocean. Technol.*, 33, 1057–1072, doi:10.1175/JTECH-D-15-0177.1.

106. Korolev, A., and B. Sussman, 2000: A Technique for Habit Classification of Cloud Particles. *J. Atmospheric Ocean. Technol.*, 17, 1048–1057, doi:10.1175/1520-0426(2000)017<1048:ATFHCO>2.0.CO;2.

107. Korolev, A.V., 2007b: Limitations of the Wegener-Bergeron-Findeisen mechanism in the evolution of mixed-phase clouds. *J. Atmos. Sci.*, 64, 3372-3375

108. Heymsfield, A. J., and J. L. Parrish, 1978: A Computational Technique for Increasing the Effective Sampling Volume of the PMS Two-Dimensional Particle Size Spectrometer. *J. Appl. Meteorol.*, 17, 1566–1572, doi:10.1175/1520-0450(1978)017<1566:ACTFIT>2.0.CO;2.

109. Locatelli, J. D., and P. V. Hobbs, 1974: Fall speeds and masses of solid precipitation particles. *J. Geophys. Res.*, 79, 2185–2197, doi:10.1029/JC079i015p02185.

110. Brown, P. R. A., and P. N. Francis, 1995: Improved Measurements of the Ice Water Content in Cirrus Using a Total-Water Probe. *J. Atmospheric Ocean. Technol.*, 12, 410–414, doi:10.1175/1520-0426(1995)012<0410:IMOTIW>2.0.CO;2.

111. Mitchell, D. L., 1996: Use of Mass- and Area-Dimensional Power Laws for Determining Precipitation Particle Terminal Velocities. *J. Atmospheric Sci.*, 53, 1710–1723, doi:10.1175/1520-0469(1996)053<1710:UOMAAD>2.0.CO;2.

112. McFarquhar, G. M., M. S. Timlin, R. M. Rauber, B. F. Jewett, J. A. Grim, and D. P. Jorgensen, 2007: Vertical Variability of Cloud Hydrometeors in the Stratiform Region of Mesoscale Convective Systems and Bow Echoes. *Mon. Weather Rev.*, 135, 3405–3428, doi:10.1175/MWR3444.1.

113. Heymsfield, A. J., C. Schmitt, A. Bansemer, and C. H. Twohy, 2010: Improved Representation of Ice Particle Masses Based on Observations in Natural Clouds. *J. Atmospheric Sci.*, 67, 3303–3318, doi:10.1175/2010JAS3507.1.

114. Cotton, R. J., and Coauthors, 2013: The effective density of small ice particles obtained from *in situ* aircraft observations of mid-latitude cirrus: Effective Density of Small Ice Particles. *Q. J. R. Meteorol. Soc.*, 139, 1923–1934, doi:10.1002/qj.2058.

115. Duroure, C., H. R. Larsen, H. Isaka, and P. Personne, 1994: 2D image population analysis. *Atmospheric Res.*, 34, 195–205, doi:10.1016/0169-8095(94)90091-4.

116. Baumgardner, D., and A. Rodi, 1989: Laboratory and wind tunnel evaluations of the Rosemount icing detector. *J. Atmos. Oceanic Technol.*,6, 971–979.

117. Cober, S.G., G.A. Isaac, and A.V. Korolev, 2001: Assessing the Rosemount Icing Detector with In Situ Measurements. *J. Atmos. Oceanic Technol.*, 18, 515–528, doi: 10.1175/1520-0426(2001)018<0515:ATRIDW>2.0.CO;2.

APPENDIX A—INSTRUMENT DEVELOPMENT EFFORTS TO SUPPORT AIRBORNE MEASUREMENTS FOR THE FLIGHT CAMPAIGNS

A.1. DEVELOPMENT OF ISOKINETIC EVAPORATOR PROBE (IKP, IKP-2) TO PROVIDE PRIMARY BULK IN-SITU TWC MEASUREMENTS

Airborne bulk in-situ estimates of TWC in clouds have been collected within the atmospheric sciences community over the years using three primary methods: (1) integration of mass size distributions (MSDs) after conversion from Particle Size Distributions (PSDs), and direct measurements from (2) hot-wire devices, and (3) flow-through evaporators. The integration of MSDs can be problematic, due to various shortcomings in the optical array probes providing the PSDs, and perhaps more importantly, the lack of applicable information on the density of ice particles versus size, which varies according to the particle morphology and growth history. Estimation of uncertainty in mass estimates is difficult, and may vary with time due to local changes in particle densities. A review of the available bulk in-situ TWC hot-wire and flow-through evaporator technologies at the time has been provided in [A-1]. There is no one technology that is superior over the full range of conditions in cloud. Hot wires offer an attractive package for installation on an aircraft due to their small size, but it is necessary to have two elements of different geometry in order to estimate TWC in mixed-phase conditions, due to the near unity efficiency of most elements for most liquid water content (LWC) conditions, and the relatively low efficiency (< 50%) for ice particles (e.g., [A-1]). Due to the lack of information on the efficiency over the wide variety of flight and cloud conditions, it was decided that hot wires posed too large a risk for use as the new high ice water content (IWC) reference instrument, and that a technology providing a near unity collection efficiency for both LWC and IWC was required. A new hot wire developed by SEA, described in section A.3, was however very useful in developing tunnel ice-cloud simulations and in performing exploratory measurements in high IWC clouds before the HAIC-HIWC and HIWC-RADAR flight programs [A-2, A-3].

Flow-through evaporators have been used since the 1960s, although there is little documentation of their use in high IWC conditions. Air and hydrometeors enter an inlet, after which the hydrometeors are evaporated, increasing the humidity of the air in the flow path. The TWC is then deduced from this increase in the humidity. The hydrometeor collection efficiency has the potential to be near unity if the flow is regulated to be isokinetic, an issue that becomes important if there is significant mass at small sizes, such as in liquid or mixed-phase conditions. Flow-through evaporators have been used to provide accurate measurements of very low IWC conditions in high altitude clouds [A-1], but have been subject to saturation problems in high IWC. They also tend to be relatively large probes.

In 2006, the HIWC team concluded that a new instrument was required for the measurement of the high-speed, high-altitude, and high-TWC environment. The design would require measurement of TWC in harsh high-IWC conditions up to 10 gm^{-3} at 200 ms^{-1} TAS, with a near unit efficiency over a wide range of hydrometeor sizes. National Research Council of Canada (NRC) and Environment And Climate Change Canada (ECCC) discussed various designs, and concluded that an isokinetic flow-through evaporator was the best option. The first probe (IKP-1) was developed by NRC and ECCC with contributions from SEA. Design and specific performance predictions of the various subsystems have been detailed in numerous publications [4-7]. The probe was designed to fit in an under-wing canister of a Gulfstream G-II aircraft, at the time the

intended primary flight campaign aircraft. In 2012, the modification of this aircraft for flight test was cancelled, and the primary data collection effort was transferred to the Service des Avions Français Instrumentés Pour la Recherche en Environnement Falcon-20 research aircraft, contributed by the High Altitude Ice Crystals (HAIC) project. The IKP-1 was too large, too heavy, and consumed too much electrical power to be used on the Falcon-20. Consequently, a new effort funded by the FAA and NASA was started in February 2013 to develop a smaller probe (IKP-2) in anticipation of the first flight deployment 12 months ahead. The effort was led by SEA, with NRC performing the necessary evaporator and flow path modifications. Although the principles of operation and component systems are essentially the same for IKP-1 and IKP-2, the downsizing effort was challenging. Changes included a new evaporator, flow path, and canister. Some redesign of the control system was required to reduce wing wiring requirements. The hygrometer was changed to a commercially available unit for reliability and serviceability. Upon completion of the manufacturing, the probe performance was assessed in four test entries at three different wind tunnel facilities (Cox and Co. LeClerc Icing Research Laboratory, NASA Icing Research Tunnel (IRT), and NRC RATFac). After observing a saturation problem in high IWC, modifications were performed on the evaporator. The probe was then retested in the NRC RATFac at IWC values up to 15 gm^{-3} under realistic flight conditions of 200 ms^{-1} and 20 HPa, and deemed ready for flight. The probe was then used successfully in its first deployment during the HAIC-HIWC flight campaign in Darwin in January 2014. Figure 11 shows the IKP-2 installed on the Falcon-20 aircraft.

Details of the principle of operation follow. Air and hydrometeors enter a 6.8 mm diameter inlet at the end of a 45 cm long boom, and flow through a spiral evaporator where the hydrometeors are forced to the heated wall. The inlet and boom are also well heated to prevent ice buildup. Anti-icing has been extensively tested in high LWC conditions in the wind tunnels. Some evaporation of particle is predicted before even entering the evaporator section. Calculations predict that particles larger than about 25 μm impact the evaporator wall early into its ten spiral turns, while smaller particles have enough residence time to fully evaporate before exhaust [A-8]. Impacting the wall slows the particles' progress through the flow path, enhancing heat exchange for melting and evaporation while minimizing potential of hydrometeor accumulation that could lead to saturation before the air exhausts the back of the probe. Flow path air is maintained at 80 C. A hygrometer embedded in the probe then measures the humidity of the ambient air plus that added by the evaporation of the hydrometeors, and TWC is deduced from this increase in humidity. The probe was designed to produce a slightly super-isokinetic flow at the inlet by creating a pressure drop at the exhaust. Flow is automatically throttled back in real time to a calculated isokinetic value by adjustment of a restricting butterfly valve. The measurements of the flight program have now shown that the mass of high IWC clouds is concentrated at ballistic sizes. The collection efficiency of the probe can be assumed to be near unity even without the isokinetic flow regulation.

The IKP-2 measures the sum of the ambient background water vapor (BWV) plus the evaporated hydrometeors. It requires the subtraction of an independently measured BWV value to obtain hydrometeor TWC. This requirement imposes a practical limit on the use of this probe in its current configuration to measurements at roughly 0 C or colder in turbulent tropical conditions due to the high BWV levels at warmer temperatures. The formulae used in the IKP-2 TWC calculation, the BWV subtraction, and TWC comparisons are discussed further in appendix B. Saturation testing, isokinetic flow performance, and de-icing performance have been detailed in in [A-9], and system accuracy is detailed in [A-10].

A.2 IMPROVEMENTS OF PSD MEASUREMENTS BY MITIGATION OF SHATTERING AND BOUNCING ARTIFACTS

By the mid-2000s, the atmospheric science community had compiled a convincing body of evidence that PSD measurements from optical array and scattering probes contained artifacts due to shattering of particles that impacted the leading edge of probe tips or sample tubes, or the breakup of delicate particles in the aerodynamic disturbance around the probe [A-11 through A-13]. Figure A-1 shows a conceptual view of impact shattering for an optical array probe (OAP), from [A-14]. It was later shown that the number concentration of small ice particles measured by OAPs could be overestimated by as much as two orders of magnitude [A-15], which would have a major impact on cloud microphysics research. The effect on higher moments of the PSDs such as mass or extinction was much smaller, but still significant for the regulatory objectives of this report. Shattered particles had been shown to generally have shorter inter-arrival times than particles from the natural population, and algorithms were developed to reject shattered particles based on this observation (e.g., [A-11, A-16 through A-19]). However, such algorithms were found to be only partially effective because a significant fraction of real particles still had short inter-arrival times, and some shattered particles had long inter-arrival times [A-19]. These authors suggested the additional use of special patented probe tips [A-15] designed by ECCC to deflect debris from shattered particles away from the probe sample volume. Although the impetus for this substantial ECCC effort was the improvement of ice particle measurements for the future HIWC flight programs, such probe tip modifications have now been broadly accepted within the atmospheric science community, and applied by manufacturers to most new cloud particle measurement probes.

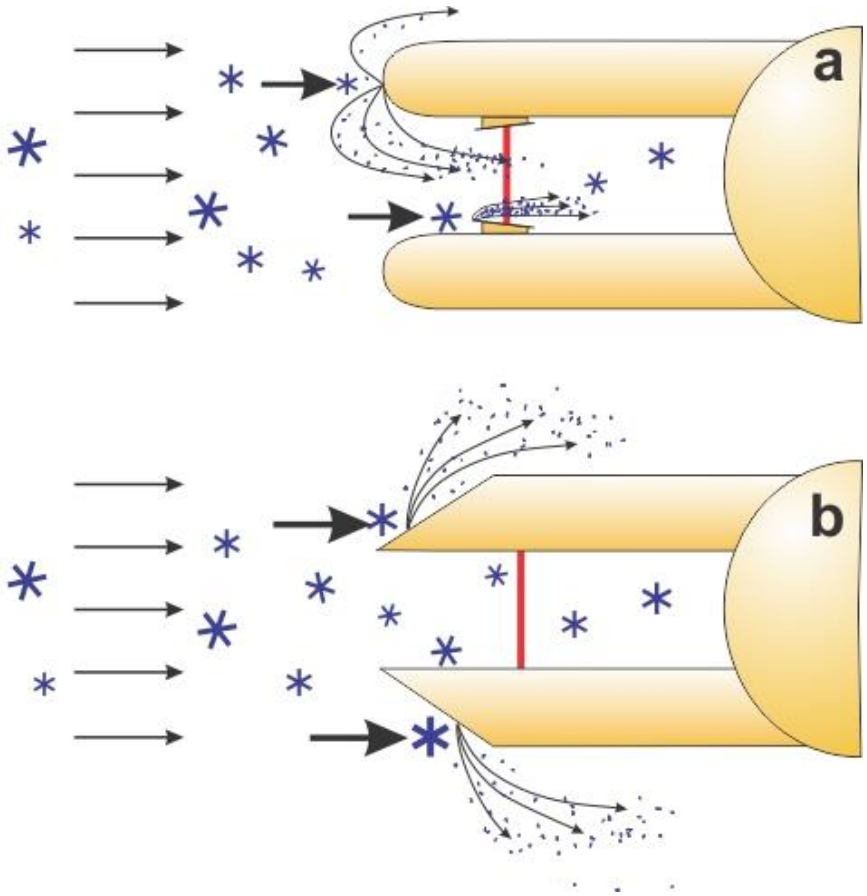

Figure A-1. Conceptual depiction of (a) ice particle shattering on OAP tips and debris bouncing into probe sample volume (red) and (b) same as (a) with special tip probe [A-14]

The ECCC effort included in-house design and testing of probe tips for an extensive array of particle probes that were to be used on the original aircraft planned for the HIWC flight campaign. In addition to developing new anti-shattering tips for the legacy PMS 2D-C probe and the PMS Forward Scattering Spectrometer (FSSP) probe, ECCC developed similar modifications for the Droplet Measurement Technologies (DMT) CDP, CIP, and Precipitation Imaging Probe (PIP) probes. These included not only new anti-shattering tips, but also modifications for improved shedding of liquid water from optical windows and enhanced de-icing protection. The efficacy of the anti-shattering tips was tested using high-speed video at the Cox and Co. LeClerc Icing Research Laboratory wind tunnel, and then on the Convair-580 during a dedicated instrumentation flight test project. The most successful anti-shattering tip designs for the CDP, CIP, and PIP were then provided to DMT, who adapted them for their commercial instruments. The tips were used extensively on the probes installed on the Convair-580 during the Cayenne-15 flight program. The Falcon-20 and DC-8 flight campaign aircraft each had a capacity for only three particle-measuring probes, the DMT CDP-2, the DMT PIP, and the SPEC 2D-S probes (Table 3, Table 4, Table 7, and Table 8). Both carried CDP-2 probes with the ECCC/DMT modifications. The DC-8 PIP also was equipped with these modifications, but not the Falcon-20 PIP. However, the effect of shattering on the data provided by this probe for the PSD analysis (Appendix C) is likely negligible, given that only PIP data > 800 μm are used. Finally, the most recently available anti-shattering probe tips provided by SPEC at the time were used on all 2D-S probes.

A.3 OTHER MISCELLANEOUS INSTRUMENTATION IMPROVEMENTS FOR THE MEASUREMENT OF HIGH IWC

Before the development of the IKP-2, there was an immediate need for a reliable TWC estimate in high-IWC/high-speed situations, with a first application of mapping the spatial distribution of IWC in the NRC M7 wind tunnel [A-2]. The application required a small instrument such as a hot-wire device that could be easily moved through the tunnel. The available hot-wire TWC probes at the time were subject to mechanical breakage due to the high speed impacts of solid ice particles. To address the issue, in 2007 SEA developed the first new probe contributing to the efforts of the HIWC project partners. SEA used a TWC wire element with a particle trapping geometry as a sensor. TWC was estimated by measuring the amount of power required to keep the wire at constant temperature during ice particle melting and evaporation. However, unlike other TWC sensors available at the time, SEA imbedded a solid element TWC sensor in the leading edge of a strong narrow strut to provide mechanical strength. This was recognized as a requirement to withstand ice particle impacts at jet aircraft speeds, and accordingly, the instrument became known as the "Robust" probe (see Figure A-2). The Robust probe sense element has a near-unity collection efficiency for 20 μm water droplets, but a collection efficiency of only about 40% for the ice particles generated at the NRC M7 wind tunnel. Consequently a separate LWC estimate and accurate efficiencies are required to derive IWC in mixed-phase conditions. The unknown risk of resolving these efficiencies was a deciding factor in moving forward with the IKP as the primary TWC instrument for the flight campaign Appendix D/P measurements. Notwithstanding the efficiency uncertainty, the Robust probe was found to provide reliable surrogate measurements of IWC in glaciated conditions at the NRC M7 tunnel, and was also used successfully to collect early IWC measurements in exploratory Airbus flight campaigns in Darwin and Cayenne in 2010, and in Chile in 2012 [A-3]. It was also flown on the Falcon-20, Convair-580, and DC-8 during the HAIC-HIWC and NASA/FAA HIWC-RADAR flight programs, and comparisons to the IKP-2 have yielded better information on the IWC collection efficiency [A-20]. SEA has since combined design aspects of the Robust probe and its multi-element probe [A-21] into an ice crystal detector for commercial aircraft [A-22].

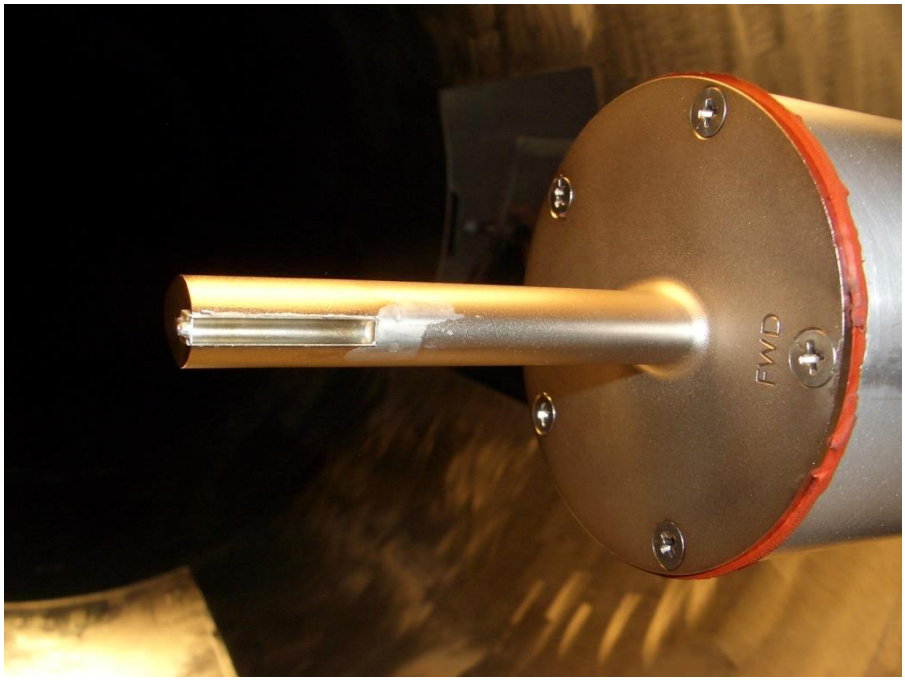

Figure A-2. Robust hot-wire probe (Science Engineering Associates [A-2])

The flight programs addressed the characteristics of the mixed-phase components of the high IWC environment as well as possible, given the capabilities of the instrumentation. The separation of the liquid and ice components in mixed-phase clouds was known to be a very challenging instrumentation problem, with likely no complete short-term, achievable solutions. But as discussed in section 3.4 and Appendix D, mixed-phase conditions were encountered infrequently in the flight campaign data sets, and when encountered, LWC levels were generally low or below background detection levels elevated by false response due to ice crystals. The next several paragraphs briefly explain the limitations of the current instrumentation and list some efforts to improve measurements.

Hot-wire sensors have been used extensively to date to estimate LWC and IWC in mixed-phase clouds [A-21]. However, the accuracy of the separation is strongly dependent on how well the collection efficiency of the TWC sensor for ice (typically 30-50%) and false response of the LWC sensor to ice (~5-10%) are known. Since the IKP-2 can, in theory, be substituted for the TWC measurement, the main uncertainty is then in the LWC measurement, caused mainly by ~5-10% false response of the LWC sensor to IWC. In high IWC and low LWC conditions, the false response can overwhelm the LWC signal, rendering it undetectable. Such was the case for the flight campaign data. Although wind tunnel testing predicted a possible reduction in the false response of the LWC sensor to ice to about 3-4% using a smooth solid-element SEA LWC sensor rather than a wound wire, due to the limited possible aircraft mounting locations for the sensor, it was installed in a region of an estimated factor of 2 over-concentration of ice, counteracting any benefits due to the smooth sensor.

Bulk LWC and IWC measurements, in theory, also can be extracted from integration of PSD measurements, although this method has its own complications. Since the LWC component of a mixed-phase cloud is often concentrated in cloud droplets smaller than 50 μm, estimation would

usually require the use of a DMT CDP-2 or PMS FSSP-100 probe to cover the liquid part of the size range, but the response of these probes is not fully understood when ice particles are also present, and can be dubious. These probes do not discriminate between ice and water hydrometeors. ECCC has now shown with Cayenne-15 flight campaign data that CDP-2 modifications to mitigate contamination by ice particle shattering were only partially successful, but the FSSP-100 modifications virtually eliminated such contamination (see Appendix D). Consequently, the most defensible assessment of the mixed-phase conditions of the flight campaigns was provided using the FSSP-100 measurements from the Convair-580 (section 3.4). There also were several initiatives within the HAIC project to improve PSD phase discrimination in the mixed-phase environment. The UBP/LaMP provided a special DMT scattering probe with a depolarization feature, the Cloud Particle Spectrometer with Polarization Detection, to discriminate ice from liquid particles in the 2-50 μm size range. The phase discrimination feature was considered experimental, and the intention was to fly it occasionally on the Falcon-20 in place of the CDP-2 to assess the technology. Unfortunately, the schedule did not permit changing to this probe in either the Darwin-14 or Cayenne-15 campaigns. Perhaps the most significant new instrument was the High Speed Imager (HSI), developed by Artium Technologies, with HAIC supporting the assessment of the probe in wind tunnel testing and in airborne measurements on the Convair-580 during the Cayenne-15 experiment. This probe provides high-resolution images of cloud particles, and unlike other imaging probes, is designed to accept only those that are nominally in focus (see Appendix C for discussion of out-of-focus particles). This simplifies issues related to the proper sizing of cloud particles, and may help in providing a better separation of liquid and ice PSDs through better image identification (e.g., circular liquid versus non-circular ice). Also, the sample volume of this probe is forward of the leading edge of the probe tips, possibly eliminating probe-induced shattering artifacts discussed in section A.2. The analysis of the HSI probe data is ongoing. Currently, the probe appears to be a significant step forward that may be particularly important in mixed-phase identification.

During early flight tests in high IWC conditions, temporary but complete failures of certain legacy particle probes were observed. The HIWC team recognized this issue as an unknown risk to measurements during the future flight campaigns, and undertook an assessment of all of the probes intended for use on the flight campaign aircraft. A series of tests was performed at the Cox and Co. LeClerc Icing Research Laboratory wind tunnel, and the NRC M7 high-speed tunnel in high IWC conditions. A number of the probes were found to experience failures of this type, and the problem was isolated to electrostatic charging, inadequately discharged to ground, induced by ice crystal impacts on anodized surfaces. ECCC and NRC implemented and successfully tested a titanium nitride (TiN) coating to many of the probes' exposed surfaces as a solution.

The series of wind tunnel tests outlined above also revealed a number of other icing issues in high IWC and high LWC environments. ECCC and NASA implemented a number of probe improvements to address these problems, some of which are listed in the HIWC Science Plan. As an example, multiple improvements were made to the Aventech AIMMS-20 probe, which underwent extensive high IWC wind tunnel testing by NASA, Aventech, and ECCC. The major improvements included TiN coating, enhanced de-icing, and a purge system to flush pitot blockages in high IWC conditions. The probe was used successfully on the Convair-580 in Cayenne-15, and improvements were implemented by Aventech in their commercial product line.

APPENDIX B—METHOD OF CALCULATION AND ACCURACY OF IKP-2 TOTAL WATER CONTENT

A description of the development of the IKP-2 TWC Evaporator probe, method of operation, and performance testing has been provided in Appendix A and references [B-1, B2 through B6]. In this appendix, calculations are described, and instrument accuracy is estimated.

B.1 CALCULATIONS OF THE IKP-2 TWC

While a detailed description of the equations used to calculate TWC is available in [B-7], a brief review is provided here. The IKP-2 measures the total hydrometeor + background water vapor (BWV) concentration. The basic measurement of vapor in the IKP-2 is made by a LI-840A hygrometer, with output in the units of ppm. Note that this is a "wet" ppm value, being the ratio of water vapor molecules to dry air + water vapor molecules. Section B.3 Removal of Background Water Vapor in IKP-2 TWC Calculation provides a discussion on the removal of the BWV.

The equation for calculation of TWC in gm^{-3} at isokinetic flow is:

$$\mathrm{TWC_{meas}} = 1000\rho_{\mathrm{amb}}\frac{\omega_{\mathrm{TWC}}}{1+\omega_{\mathrm{amb}}} \tag{B-1}$$

Where ω_{TWC} is the difference between the total mixing ratio in the IKP-2 flow path and the ambient (background) mixing ratio, ω_{amb} is the ambient mixing ratio, and ρ_{amb} is the ambient air density.

The direct measurements of the LI-840A flow path (L_{fp}) and ambient (L_{amb}) concentrations (moles(water vapor)/(moles(water vapor)+moles(dry air)) in ppm are converted to specific humidity values (LD_{fp}, LD_{amb}), and then to the mixing ratios (ω) used in the equation above, by the following:

$$LD_{\mathrm{fp}} = \frac{L_{fp}}{(1-L_{fp}*10^{-6})} \tag{B-2}$$

$$LD_{\mathrm{amb}} = \frac{L_{amb}}{(1-L_{amb}*10^{-6})} \tag{B-3}$$

$$\omega_{\mathrm{TWC}} = k(LD_{fp} - LD_{amb})/10^{6} \tag{B-4}$$

$$\omega_{\mathrm{amb}} = k(LD_{amb})/10^{6} \tag{B-5}$$

Minor corrections for the small departures observed during flight measurements from isokinetic flow are made according to the following:

$$TWC = TWC_{meas} * IKF \tag{B-6}$$

where:

$$IKF = \frac{\dot{m}_{op}}{\dot{m}_{op,IK}} \tag{B-7}$$

and $\dot{m}_{op}$ is the flowpath mass flow rate, measured directly by the IKP-2, and $\dot{m}_{op,IK}$ is the isokinetic flow rate, calculated from the TAS, inlet diameter, air density, and with a small adjustment for the TWC. See [B-7] for details on the calculation of the flow path mass flowrate.

B.2 FIRST ORDER ACCURACY ESTIMATES

This section summarizes accuracy estimates from analytical calculations and from direct testing. These are all relevant to an IKP-2 system in which an acceptable BWV measurement can be made. In section B.3, problems with the removal of BWV and their effects on accuracy estimates during the flight campaigns are discussed.

The system accuracy estimates of [B-7] integrated best estimates of the IKP-2 individual component uncertainties. The analysis showed that due to the increasing magnitude of the BWV with increasing temperature, system accuracy decreases with increasing temperature. Table B-1 shows calculations of ice and water saturation values for the typical tropical atmosphere of Darwin, Australia, which are very similar to the other flight locations. Note that BWV levels at -10 C are of the same order as the TWCs that are expected in high IWC situations, so the accuracy of the subtraction of the BWV is increasingly important at warmer temperatures. Uncertainties in BWV from the hygrometer manufacturer's quoted accuracy dominated the system accuracy estimated for low IWCs and high temperatures. Overall system uncertainties at all temperatures decreased with increasing TWC to about 2-3% at 10 gm^{-3}. At -10, uncertainty at 0.1 gm^{-3} reached 50%, falling below 10% at about 0.5 gm^{-3}, and was about 6% at 1 gm^{-3}. At -30 C, uncertainty was much lower, at about 9%, and 2.5% at 0.1 and 1 gm^{-3}, respectively. At -40 C, uncertainty was about 4% at 0.1 gm^{-3}, falling to a little over 2% by 0.5 gm^{-3}. The system accuracy estimates indicate that the IKP-2 is quite accurate for the high altitude, high IWC environment, but uncertainty can be substantial for the warmer low IWC measurements. The BWV removal processing used in the flight campaigns was not as simple as that assumed in these system accuracy estimates. For example, ice saturation estimates were used rather than actual BWV measurement. The uncertainties associated with this assumption will be addressed in section B.4.

Table B-1. Estimated vapor concentrations for ice and water saturation for a typical Darwin tropical atmosphere

Temperature (C)	Water Saturation gm^{-3}	Ice Saturation gm^{-3}	Water-Ice Saturation gm^{-3}
-10	2.86	2.60	0.26
-20	1.08	0.89	0.19
-30	0.45	0.34	0.11
-40	0.18	0.12	0.06
-50	n/a	0.04	n/a

Accuracy estimates were also obtained by direct comparisons to other measurements [B-1]. The first was obtained using a field calibration cart developed by SEA. The unit injects a metered amount of water directly into the inlet of the IKP-2, while air is sucked through the system at high speed. The liquid water content (LWC) in the flow path is calculated knowing the mass of liquid

injected and the flow path mass flow rate. The calibration method is an end-to-end check of the combined accuracy of almost all the components of the IKP-2, including the hygrometer, the flow control, and the software calculations. The only missing elements are the inlet area and actual flight collection efficiency. A photo depicting the injection of water into the IKP-2 inlet is included in Figure B-1, and a sample calibration is shown in Figure B-2, where the IKP-2 LWC was estimated by regression to be ~ 0.987 of the injected LWC. Note that the calibration spanned LWCs values up to about 35 gm^{-3}. The range of scale factors in seven IKP-2 calibrations was 0.97-1.04 of the injected LWC, with an average of 1.00. Similar results were found for the second copy of the IKP-2.

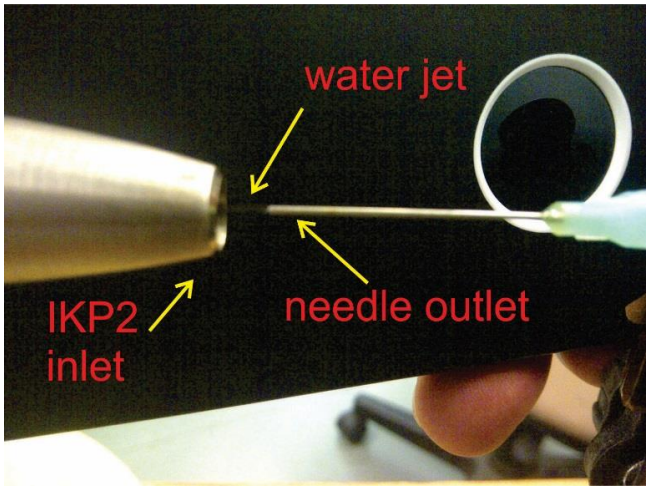

Figure B-1. Injection of liquid droplets into IKP-2 for LWC calibration, using the field calibration cart developed by Science Engineering Associates [B-1]

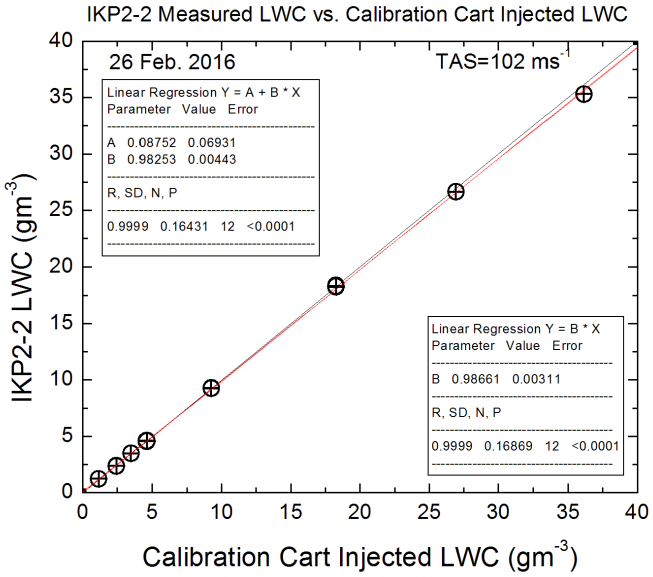

Figure B-2. Example of LWC calibration of the second copy of the IKP-2 using the SEA field calibration cart [B-1]

The second LWC comparison was made in 2014 at the NASA Icing Research Tunnel (IRT). Reference methods for the estimation of LWC in wind tunnels have been fairly well developed for FAR Part 25 Appendix C conditions, and can be traced back to estimates from ice blades and rotating icing tube measurements for which individual uncertainty components have been assessed into an absolute uncertainty estimate of about 5% [B-8, B-9]. The IRT comparisons revealed that the IKP-2 measured approximately 10% higher than the tunnel reference values (Figure B-3). Note also that these comparisons cover a range of median volume diameters from about 15 to 300 µm, and not just FAR Part 25 Appendix C conditions. NASA had obtained a second copy of the IKP-2 by this time, and results from both IKP-2 probes are shown in the figure. From the comparison of data collected by these two probes one day apart, the precision of the IKP-2 for these test conditions was estimated to be ~1%. The IKP-2 team and the IRT staff agreed that the 10% scale difference could be explained by the overall IRT accuracy estimate of 10%, while also noting that systematic uncertainties in the BWV could be elevating IKP-2 estimates somewhat.

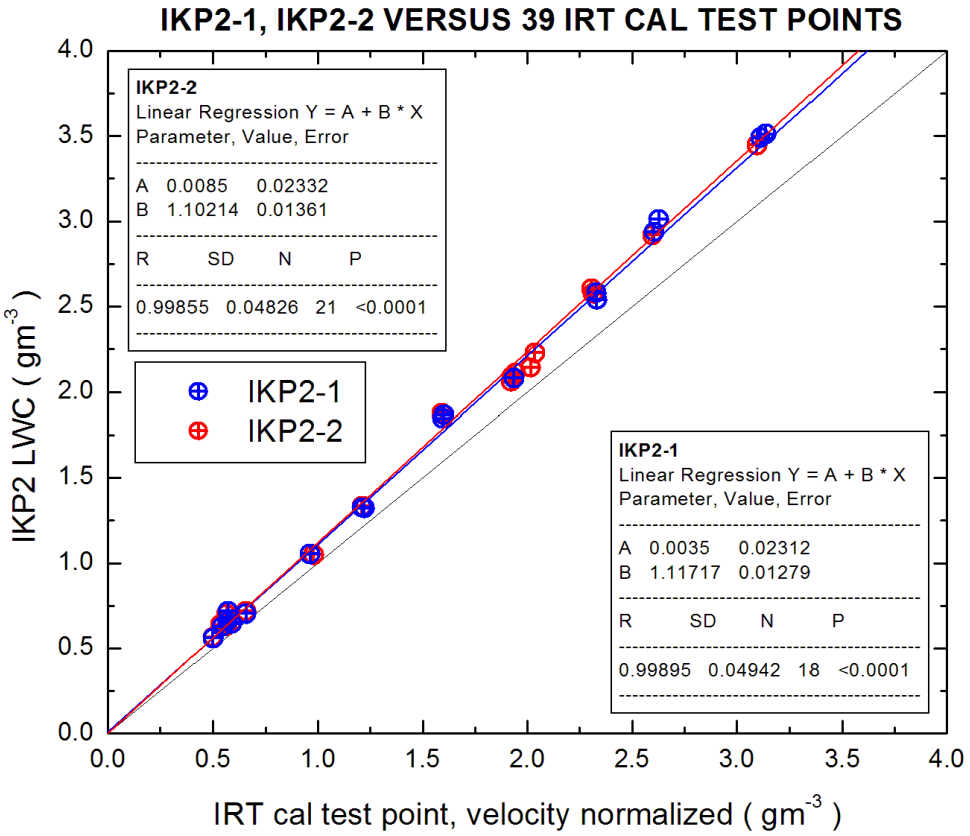

Figure B-3. Comparison of the IKP-2 to tunnel reference values at the NASA IRT in LWC conditions. IKP2-1 and IKP2-2 refer to IKP-2 first and second copies, respectively [B-1]

Reference methods for calibration of IWC measurements are much less developed and documented than for LWC measurements. Comparison to other available airborne IWC instruments was inadequate for IKP-2 accuracy estimates due to their unknown accuracies, especially in high IWC conditions. The IKP-2 team eventually decided that ice capture tubes (ICTs), which had previously been used in European tunnels to estimate IWC, provided the most

practical way in which to collect a reference IWC estimate. Unfortunately, no publications or internal reports documenting the methodology or estimates of their accuracy could be found, so the IKP-2 team conducted its own ICT experiments without benefit of past experience. IWC was estimated by exposing ICTs approximately 11 mm in diameter and 10-20 cm in length, open at one end, to the ice cloud for a measured amount of time. IWC was then calculated from a simple equation [B-1] after measuring the weight of ice collected. A series of tests were performed at the Cox and Co. LeClerc Icing Tunnel and the National Research Council of Canada (NRC) M7 open cell wind tunnel, both of which shave ice blocks to create simulated ice clouds with median mass diameters of roughly 200-300 μm. The ICT method was found to be quite idiosyncratic and results varied according to airspeed, the length of the tube, and the method of extraction of the tube for weighing. Sporadic loss of mass out the mouth of the tube was suspected and sometimes directly observed, leading to some chaotic results[17]. The worst of these mass-loss cases were screened out by comparing duplicate side-by-side simultaneous samples. Observations with transparent tubes helped confirm and explain the different results from different tube lengths, but also suggested that mass loss, probably occurring by ejection out the tube opening and by possible evaporation at the leading edge of the ice plug, would lead to underestimates of the true IWC. It was the opinion of the test team that the IKP-2 was a more accurate reference instrument than the ICT. A photograph of two ICTs installed ahead of the IKP-2 at the NRC M7 open-cell wind tunnel is shown in Figure B-4. Figure B-5 provides comparisons of the IKP-2 to the ICT IWC. The IKP-2 measurements were consistently higher than the ICT measurements by an average ratio of 1.20, improving with increasing IWC, with a regression slope through the origin of 1.14. Given the lack of any other reference IWC methods, the results are believed to be generally positive, and support the 20% accuracy target for the IKP-2 in high IWC conditions, especially considering the strong suspicion of underestimation of the ICT measurements as noted above.

Figure B-4. ICTs installed on mast ahead of the IKP-22, at the NRC M7 open-cell wind tunnel [B-1]

[17] It should be noted that the experiences of [38] may be specific to the methodology used, and may not be experienced in other test facilities.

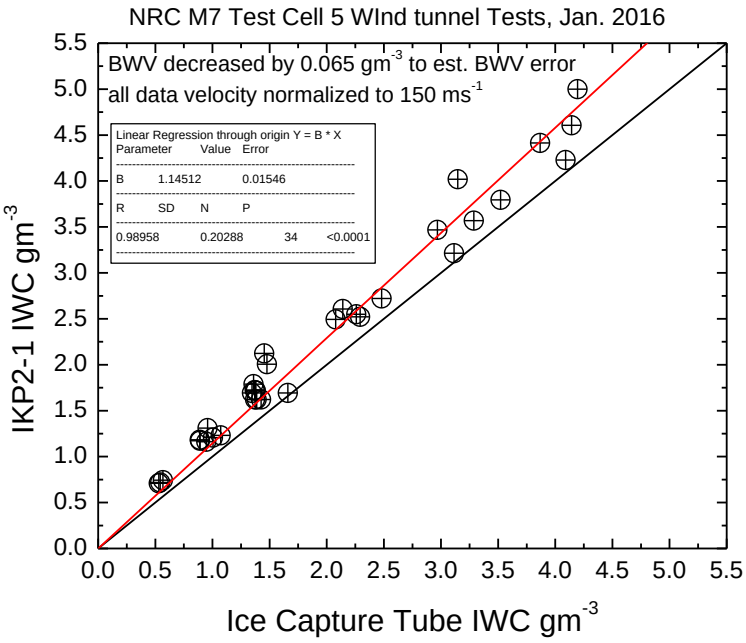

Figure B-5. Summary of comparisons of IKP-2 and reference ICT IWCs, at the NRC M7 open-cell wind tunnel [B-1] ICT

Consolidating the system accuracy and reference comparisons above into a single accuracy statement is not straightforward. Furthermore, due to the importance of BWV removal in the IKP-2 calculation, and the fact that ice saturation estimates have been substituted for actual in-cloud BWV measurements, such a consolidation would provide an incomplete picture of this report's data IKP-2 accuracy. Nevertheless, the following summarizes the discussion above. BWV removal drives system accuracy at the warmer temperatures and lower TWCs, where at -10 C uncertainty can reach as much as 50% at 0.1 gm^{-3}. However, it improves to about 2-3% in high IWC situations at all temperatures. In rough terms, it can be estimated at 2% + 2% of the BWV value. The comparisons to the field calibration cart suggest an absolute accuracy of better than ±5% for high LWC measurement, with no bias to over- or under-read. The comparisons to the IRT LWC reference reveal little scatter but a consistently ~10% higher IKP-2 reading, where the tunnel reference accuracy is estimated to be about 10% by IRT staff. IWC comparisons to those from ICTs, which are highly suspected to underestimate, reveal on the average a 20% higher reading. ICT estimates are not considered sufficiently accurate to represent reference measurements. In sections B.3 Removal of Background Water Vapor in IKP-2 TWC Calculation through B.6 A Combined TWC Error Estimate for the Effects of the Ice Saturation Assumption, and Sampling Uncertainty, the specifics of the IKP-2 BWV removal for the data sets of this report are discussed, and specific accuracy estimates are produced that are particular to the clouds sampled in this data set, and include estimates of statistical uncertainty and bias. It is clear that the accuracy of the IKP-2 is specific to its application.

B.3 REMOVAL OF BACKGROUND WATER VAPOR IN IKP-2 TWC CALCULATION

In this section, an independently *measured* BWV value will be referred to as BWV_m, and BWV estimated from water and ice saturation will be referred to BWV_{wat} and BWV_{ice} respectively. The calculation of the IKP-2 TWC described in section B.1 requires the subtraction of the BWV to obtain hydrometeor TWC. BWV concentrations at the flight programs' four primary measurement levels of -10, -30, -40, and -50 C are approximately 2.1, 0.3, 0.1, and 0.04 gm^{-3}, respectively in ice saturated conditions (Table B-1). At -10 C, they are therefore roughly the same order as the hydrometeor content in high IWC, so calibration differences and synchronization errors between the IKP-2 and BWV hygrometers can lead to substantial errors at this temperature [B-1], limiting the practical use of the IKP-2 in turbulent tropical conditions to temperatures roughly 0 C or colder. As temperatures decrease, errors due to BWV removal eventually become small due to low BWV values (e.g. ~ 0.04 gm^{-3} at -50 C). The BWV removal for the three flight campaigns was unexpectedly problematic, and the following explanation of processes used and associated error estimates is unavoidably tedious and complex.

Falcon-20 and DC-8 BWV removal

In general, many parameters measured on research aircraft correlate and track very well, but have small yet significant instrument calibration errors or other behaviors that lead to relatively stable differences in common measurements. These differences can be reduced or almost eliminated by applying regressions or subtracting simple offsets determined during periods when it is known that the instruments should measure the same. This procedure will be used several times in the following sections describing the Falcon-20, DC-8, and Convair-580 BWV removal.

As discussed in section B.2, the gain of the Falcon-20 LI-COR LI-840A hygrometers (IKP-2 and BWV) used on the Falcon-20 and DC-8 was found to be quite accurate (e.g., field calibration cart results, IKP-2 precision measurements from NASA IRT), and did not vary significantly with time. However, the LI-CORs were subject to baseline drift during flight operations. A fundamental drift with altitude was observed, at times as much as 0.3 gm^{-3} between sea level and 20 KPa. In addition, wetting of inlet lines before takeoff sometimes led to a dry-out period, during which the actual BWV was superimposed on a slowly decreasing baseline offset. Ideally, since the calculation of the TWC involves the subtraction of the IKP-2 flow path and BWV_m concentrations, the offsets in both LI-CORs can be easily removed by a "clear-air calibration" simply by calculating their relative offsets in cloud-free at regular intervals, and then by removing the offset on one of the two units. If a gain difference is suspected, a regression procedure using clear-air data can be used to force one unit to read the same as the other. They are then locked together to give a near zero difference out of cloud. Even if the hygrometers now have a common offset from the true humidity, that offset is removed when they are differenced in cloud. However, as discussed in the following sections, the Falcon-20 and DC-8 in-cloud BWV_m was likely contaminated in an unrecoverable way by ingestion and subsequent evaporation of ice crystals, and it was necessary to substitute BWV at theoretical ice saturation (BWV_{ice}) values for the TWC calculations of this report. An estimate of the errors in this simplification is given in section B.4. The use of BWV_{ice} values requires the removal of any significant absolute offset relative to the IKP-2 flow path LI-COR. The two-step process used for this purpose for the Falcon-20 and DC-8 is described below.

The method for normalizing the Falcon-20 and DC-8 water vapor offsets for the IKP-2 and BWV LI-CORs has been described in [B-1]. An abbreviated description of the procedure is given below, followed by a more detailed description.

- Identify zones in glaciated cloud suspected to be at ice saturation, but with IWC values not conducive to BWV_m contamination from injection of ice crystals into BWV air lines (i.e., quasi-continuous glaciated cloud ~ 0.2 gm^{-3}). Calculate BWV_{ice} from static temperature and pressure. Apply an offset to BWV_m to force it to the BWV_{ice} value.
- Repeat above step for multiple zones in cloud. Interpolate offsets between zones.
- Identify cloud-free zones outside of cloud where IKP-2 LI-COR must equal BWV_m LI-COR. Calculate offset between the two, and subtract from IKP-2 LI-COR, thereby also removing any measurement offset between the IKP-2 LI-COR to the in-cloud ice saturation estimate.
- Repeat above step for multiple zones out of cloud. Interpolate offsets between zones.

Although Environment And Climate Change Canada (ECCC) analysis has shown that high IWC zones would theoretically be the best conditions for ensuring ice saturation, it was decided it would be better to choose the quasi-continuous glaciated cloud at about 0.2 gm^{-3}, where ice crystal BWV_m contamination was suspected to be minimal. The scatter in the BWV_m offsets from ice saturation at a given flight level is an indication of the uncertainty in the method. For example, for the entire Cayenne-15 flight program, the standard deviation of the offsets for the -10 C, -30 C, and -40 temperature levels were 0.023, 0.014, and 0.010 gm^{-3}, respectively. Upon entering cloud, BWV_m was used until the TWC reached 0.2 gm^{-3}, the target TWC at which the BWV_m normalization to ice saturation was performed, and then BWV_{ice} was used for higher TWC values. In general, this in-cloud switchover provided a better TWC estimate at cloud edges, where cloud may be more likely to be sub-saturated with respect to ice, than simply assuming ice saturation over the entire cloud width.

Figure B-6 shows an example of this normalization procedure for a high IWC section of a cloud sampled at -29 C during the Florida-15 project, from [B-1]. The lower panel shows the BWV_{wat} and BWV_{ice} values calculated from the air temperature and pressure, and expressed in gm^{-3}. The green line is the LI-COR BWV_m normalized to the BWV_{ice} value at the two set-points identified in the lower panel (a third one is at an earlier time). In this particular case, the LI-COR BWV_m offsets were very small, and less than 0.01 gm^{-3}. Two of the IKP-2 flow path LI-COR adjustment points (step 2) are also shown near the middle and end of the upper panel, with a third before the start time of the displayed time series. These adjustments to the IKP-2, approximately the same as the IKP-2 and BWV_m LICORs offsets out of cloud, are larger, varying between -0.2 and -0.3 gm^{-3}. Note that adjusted BWV_m estimate (lower panel, green line) is generally near ice saturation when the IWC (red line in top panel) is low, rises as the IWC increases, but is generally between ice and water saturation (blue and black lines, lower panel). BWV in cloud can only exceed water saturation values by a few percent, and much larger excesses provide an indication of contamination due to ice crystals. Such excesses were not observed in this example, but they were in other cases. In this example, the evidence of ice contamination is more subtle and inconclusive[18].

[18] Ice crystal contamination of BWV_m has been confirmed at the NRC M7 wind tunnel by comparison of the differing responses of different inlet designs in high IWC conditions.

It is mainly suggested by the positive correlation of the in-cloud water vapor concentration and the IWC. Figure B-6 displays set-points for ice-saturation normalization of the background LICOR (BWV_m) to ice saturation (BWV_{ice}) are shown in the lower panel, and for the IKP2 LICOR to BWV_m are shown in the upper panel. The upper panel compares the IWC calculated using the adjusted BWV_m measurement (red line), to that using the BWV_{ice} value (blue line). Since the difference between BWV_m and BWV_{ice} values is usually less than 0.1 gm^{-3}, there is little difference between the two TWC estimates in this case. In section B.4, measurements of the Convair-580 provide a better estimate of the uncertainty introduced by using the BWV_{ice} for all IKP-2 TWC values used in this report.

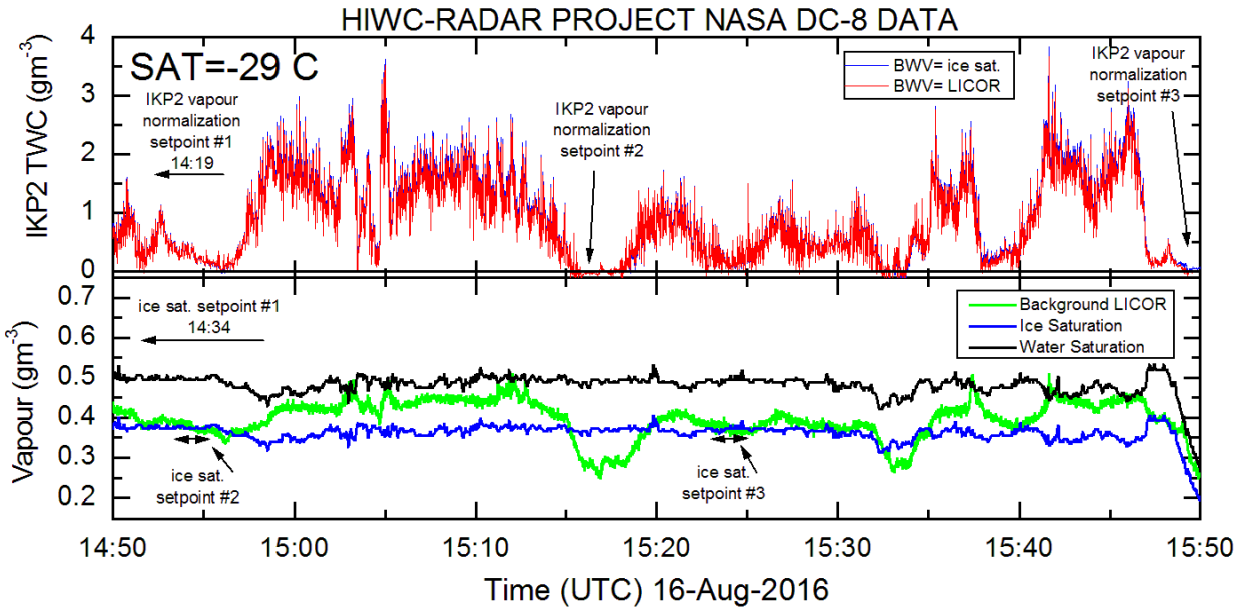

Figure B-6. Illustration of a water vapor normalization procedure for DC-8 during the HIWC-RADAR Florida-15 project [B-1]

Convair-580 BWV removal

The Convair-580 BWV inlet system also suffered from wetting problems for the first eight of the twelve Cayenne-15 flights, strong enough to preclude the recovery of accurate BWV_m values. As in the case of the Falcon-20 and DC-8, use of BWV_{ice} was the only option for the IKP-2 TWC calculation for these eight flights. For the last four flights, ECCC concluded that the Convair-580 BWV_m measurements were accurate, with little or no contamination from ice crystal ingestion. However, in the interest of maintaining consistency in the Falcon-20, DC-8, and Convair-580 IKP-2 data set processing, it was decided to use BWV_{ice} estimate for all flights, but to process the final four Convair-580 flights with both BWV_m and BWV_{ice} to assess the TWC error introduced by the use of the latter. This error assessment is contained in section B.4.

The technique used for the Convair-580 for the four flights using the good BWV_m values follows:

- Time synchronize the IKP-2 flow path LI-COR and the BWV_m LI-COR to minimize phase errors in the subtraction of the two.
- Perform a regression in cloud-free air to remove bias between the IKP-2 flow path LI-COR and the BWV_m LI-COR. IKP-2 LI-COR is chosen as reference. This removes subtraction errors when calculating TWC(BWV_m).
- Calculate TWC(BWV_m) by subtracting BWV_m from flow path water vapor, and by applying equations stated in section B.1. Perform other procedures in next two bullets to support alternate calculation using BWV_{ice} (second set of bullets below).
- Time synchronize the air temperature sensor, to improve data for BWV_{wat} calculations and subtraction. Use transition boundary at cloud edge for rapid changes suitable for synchronization.
- Identify liquid regions in cloud that are known to be at water saturation. Express the BWV_m LI-COR value as a dewpoint, and calculate air temperature offset from the BWV_m LI-COR value dewpoint. Intermittently repeat for liquid zones through cloud. This offset was determined by ECCC to be 0.35 C.

The technique used for the Convair-580 BWV_{ice} estimation and removal was somewhat different than that used for the Falcon-20 and DC-8. Here is an abbreviated description of the procedure:

- Apply the constant offset to air temperature determined in the last bullet above to the air temperature measurements for all twelve flights.
- Calculate the BWV_{ice} with the new in-cloud temperature measurement, and calculate the IKP-2 TWC(BWV_{ice}) for the twelve flights.
- Using the four flights with good background humidity, also calculate the IKP-2 TWC(BWV_m) based on the actual measured background humidity, using the procedure provided in the bullets one paragraph above.
- For the four good flights, perform a regression on the two different TWC estimates (from good background measurements and from ice saturation background estimates), TWC(BWV_m) = a+b* TWC(BWV_{ice}).
- For all twelve flights, correct TWC(BWV_{ice}) using a and b coefficients from above: i.e., $TWC(BWV_{ice})_{final}$= a+b* TWC(BWV_{ice})

- The a and b coefficients used in the final step above were 0.0876 and 0.950, respectively, based on the four-flight regression TWC(BWV_{ice}) =-0.092 +1.0503* TWC(BWV_m).

Note that adjustments are made to the first eight flights based on information obtained from the final four good flights: an air temperature offset is applied, and final TWC values are corrected according to a regression between the two TWC estimates from the last four flights. The TWC(BWV_{ice}) calculation produces negative TWC values outside of cloud because the air is usually sub-saturated with respect to ice out of cloud. This condition also can exist inside cloud when cloudy air is sub-saturated, especially in the edge-regions of clouds. For the purposes of the data set preparation, and to avoid confusion, all such negative TWC values were hard-coded to zero gm^{-3}.

B.4 ESTIMATE OF IKP-2 TWC UNCERTAINTY DUE TO THE USE OF ICE SATURATION BWV IN CLOUD

Due to problems encountered with in-cloud BWV measurement (wetting of airlines, ice crystal ingestion), ice saturation values (BWV_{ice}) have been used for the production of the official IKP-2 TWC data set used in this report. As shown in Table B-1, the level of BWV in cloud increases quickly with temperature. The theoretical adjustment of BWV levels in mixed-phase clouds has been discussed in [B-10], where it was argued that BWV levels will adjust quickly to liquid saturation values when LWC is present. In ice clouds, the steady state equilibrium BWV will tend towards ice saturation, but the adjustment time can be expected to be minutes to tens of minutes in high IWC clouds, and thus the BWV may be both lower and higher than ice saturation. In this section, the uncertainty in IKP-2 TWC estimates due to the assumption of ice saturation in cloud is examined: first, by using direct comparisons available from a limited set of data with reliable BWV measurements that provided IKP-2 calculations from both "true" and ice saturation BWV values, and second, by Monte Carlo simulations of the IKP-2 errors due to the ice saturation assumption over the whole range of conditions of the data set. This Monte Carlo simulation is used in section B.6 to provide a combined error estimate for the ice saturation estimate and sampling uncertainty.

B.4.1 ESTIMATE OF ERRORS IN IKP-2 TWC CALCULATION ALGORITHMS BASED ON A FOUR-FLIGHT INTERCOMPARISON AT -10 C

The analysis of this section is based on preliminary work presented by ECCC at the May 2016 HAIC-HIWC Science Team meeting. There are only four flights from the three flight campaigns (Convair-580 flight nos. 16-19, hereinafter "4 reference CV580 flights") in which in-cloud BWV measurement are thought to be sufficiently accurate to produce a "true" IKP-2 TWC value (hereinafter TWC(BWV_m), or the *reference* TWC). ECCC analyzed the in-cloud variation of the supersaturation with respect to ice for the 4 reference CV580 flights, and proposed that errors in the IKP-2 TWC due to the ice saturation BWV assumption could be estimated from these supersaturation spectra.

Comparisons to the reference TWC will be used to estimate the uncertainty in the IKP-2 TWC measurements based on the two ice saturation BWV algorithms described in section B.3. In addition to the reference TWC, ECCC provided its IKP-2 TWC estimate based on ice saturation (ECCC TWC(BWV_{ice})). Finally, the TWC based on the F20/DC8 ice saturation algorithm

(F20/DC8 TWC(BWV_{ice}) also was calculated. In the following paragraphs, after reviewing some of the in-cloud humidity results provided by ECCC, the TWC results are compared and the first TWC uncertainty results resulting from the ice saturation assumption are provided.

Table B-2 displays a summary of the four flights used in the TWC comparisons. These flights provide the only data with in-cloud background water vapor measurements for the Appendix D assessment that are considered sufficiently accurate for use in IKP-2 calculations. The Appendix D flight campaign archive uses ice saturation estimates in-cloud for consistency. Convair-580 Flight nos. 16-19 are from significantly diverse cloud environments. Flight no. 16 was an afternoon flight in continental convection, where relatively long periods of flight occurred between clouds at relative humidity as low as 20%. This flight was the most challenging for the IKP-2 TWC estimates using ice saturation algorithms, due to the higher occurrence of cloud regions sub-saturated with respect to ice, particularly at the edges of cloud. Flight nos. 17 and 18 were morning and afternoon flights in the same oceanic Mesoscale Convective System (MCS) north of Cayenne, where the aircraft rarely exited cloud, and the relative humidity remained high even at cloud edges. Flight no. 19 was also an oceanic MCS, but in this case the aircraft occasionally exited cloud into relatively low relative humidity. The type of clouds sampled in Flight no. 16 represent about 8% of the clouds sampled for the Appendix D/P assessment. The type of clouds sampled in Flight nos. 17, 18, and 19 represent about 92% of the clouds sampled for the assessment.

Table B-2. Description of final four reference flights of the Convair-580 in the Cayenne-2015 project

Date 2015	Convair Flight#	Data Interval (UTC)	Area	General Comments
25-May	16	19:05:00-21:49:54	Continental French Guiana and Suriname	Very low relative humidity between clouds – very challenging case
26-May	17	09:58:00-12:00:54	Offshore NE French Guiana	More typical oceanic Mesoscale Convective System
26-May	18	14:30:00-16:34:54	Offshore NE French Guiana	Same cloud system as Flight #18
27-May	19	10:00:00-11:39:54	Offshore North of Suriname	Oceanic Mesoscale Convective System

The following analysis was provided by ECCC for the two Convair-580 analysis algorithms (section B.3), comparing ECCC TWC(BWV_{ice}) to the reference TWC. Figure B-7 displays one-second averages of differences in relative humidity (RH) from ice saturation. If all values of IWC are considered (top left panel, IWC> 0 gm^{-3}), the in-cloud data are overall sub-saturated with respect to ice (mean ΔRH_i = -3.52%). Filtering to only cloud points with IWC > 0.4 gm^{-3} (lower right panel), the overall mean supersaturation with respect to ice is near zero. Individual points within cloud can be sub-saturated with respect to ice by more than 20%, and supersaturated by roughly 20%, exceeding liquid saturation at the high end in some cases (not shown). The sub-saturation with respect to ice indicates that subtracting BWV_{ice} in the IKP-2 calculation will sometimes result in negative IKP-2 TWC values. Figure B-8 shows the difference in the measured and ice saturation BWV values expressed in gm^{-3}, illustrating the potential errors in the ice

saturation assumption at -10 C. For all cloud points (top left panel), the measured BWV is on the average higher by about 0.09 gm^{-3}, whereas for clouds with TWC > 0.4 gm^{-3}, the mean error drops to about 0.01 gm^{-3} (bottom right panel). Individual one-second points can be in error by as much as about +1 gm^{-3}, probably at cloud boundaries when the ice saturation TWC estimate is negative. Figure B-9 contains a time history of IKP-2 TWC calculated using the two BWV estimates from a flight where there is a long sustained period of elevated TWC with few out-of-cloud breaks. The blue and red traces show ECCC TWC(BWV_m) and ECCC TWC(BWV_{ice}), respectively. In this case, differences between the two calculations are barely noticeable on the scale of 3 gm^{-3} TWC levels in cloud. Figure B-10 contains the same type of comparison for a flight where the aircraft was frequently going in and out of clouds, with significantly sub-saturated air in between. In this case, sub-saturated cloud regions are much more frequent, particularly on the edges of cloud, leading at times to significantly negative in-cloud IKP-2 readings[19] (note that the in-between cloud regions also appear as negative IKP-2 values). Based on visual inspection of the Convair-580, Falcon-20, and DC-8 time histories, this case is likely an outlier representing perhaps the most severe case of sub-saturation in the data set. A final comparison for all four reference flights is given in Figure B-11. For all points with TWC > 0.2 gm^{-3}, the regression yields: ECCC TWC(BWV_{ice}) = 1.0503 * ECCC TWC(BWV_m) -0.0925. For all points with TWC > 0.2 gm^{-3}, the regression yields: ECCC TWC(BWV_{ice}) = 1.028 * ECCC TWC(BWV_m) -0.059. It is important to note that as a final step in producing the Convair-580 IKP-2 TWC values provided to the HAIC-HIWC archive, ECCC used the inverse of this regression equation to correct the ECCC TWC(BWV_{ice}) values to the reference values for all Convair-580 flights. In the discussions below, this correction has sometimes been removed to enable more straightforward comparisons to the Monte Carlo simulations. ECCC TWC(BWV_{ice}) values with this correction are hereinafter called adjusted values, and those with the correction removed are called unadjusted values.

[19] Negative TWC values have been retained for the analysis of section B.4, including the regressions of Figure B-5, but in order to avoid confusion, such values have been set to zero in the final official IKP-2 TWC dataset.

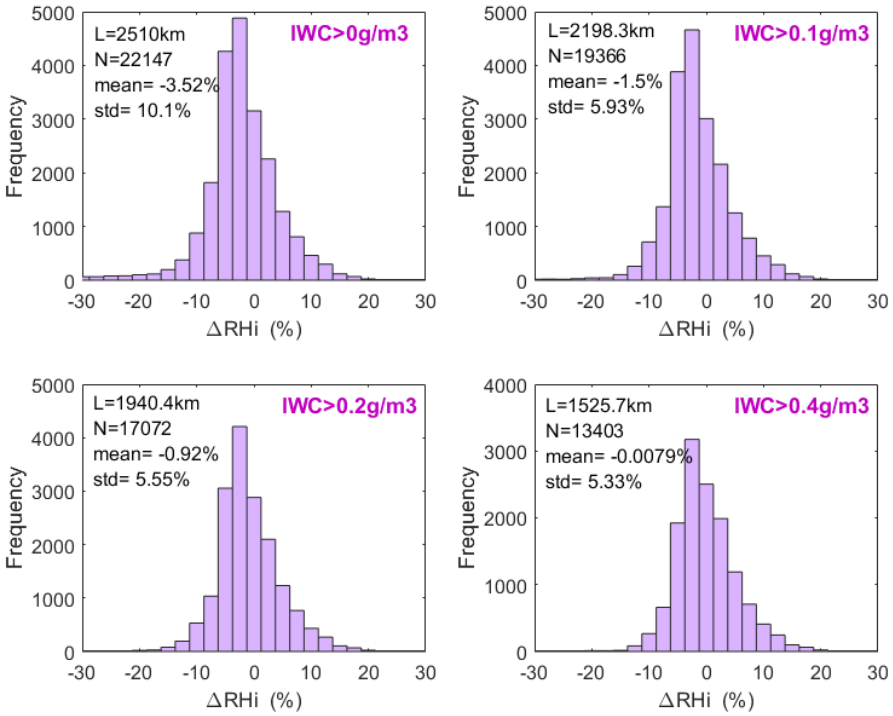

Figure B-7. Frequency distributions for different TWC thresholds of relative humidity (RH) departures from ice saturation for four Convair-580 flights in Cayenne-15 with good background humidity values

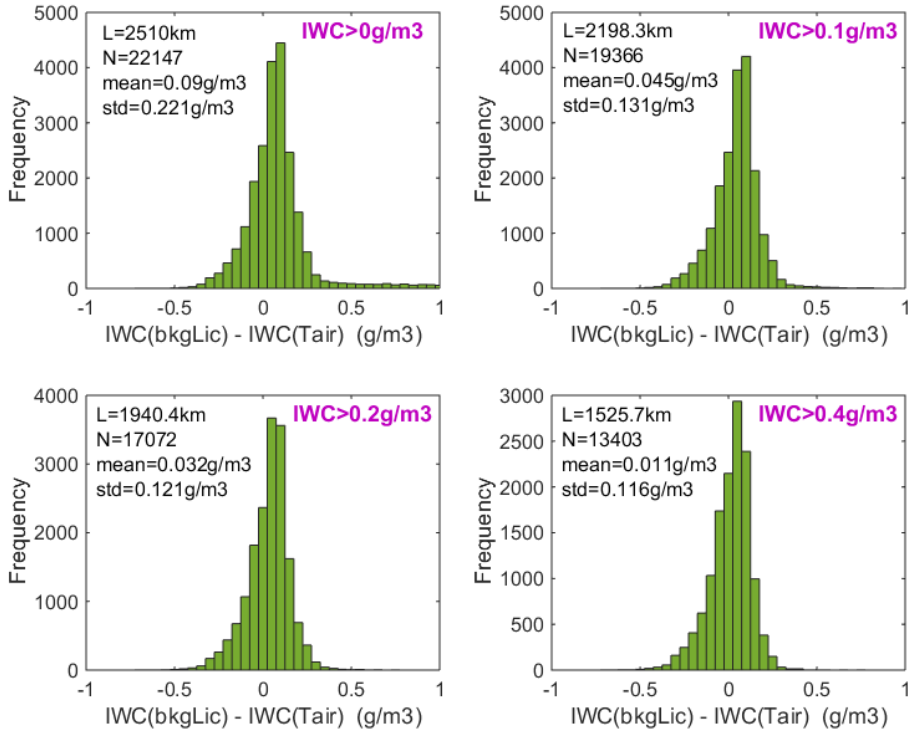

Figure B-8. Frequency distribution for different TWC thresholds of the difference in measured background water vapor and ice-saturation water vapor for four Convair-580 flights in Cayenne-15 with good background humidity values

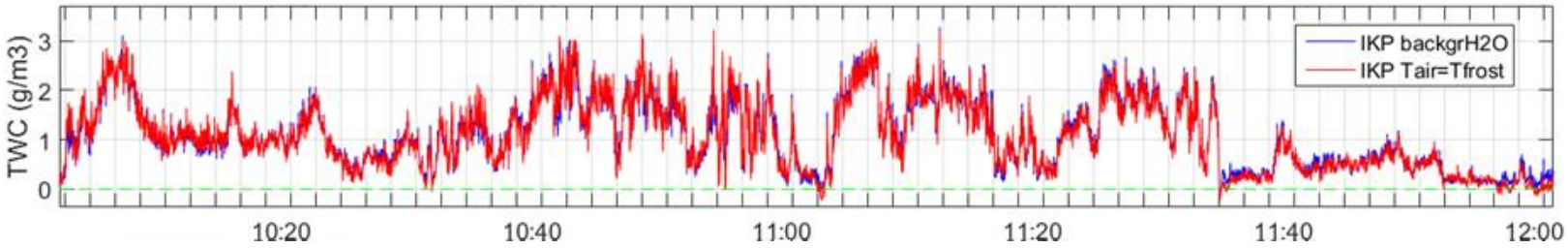

Figure B-9. Time history of IKP-2-computed TWC values using the measured (blue) and ice saturation (red) background water vapor concentrations for the Convair-580 Cayenne-15 flight on 26 May 2015. "IKP backgrH20" corresponds to TWC(BWV_m) (the reference TWC); "IKP Tair=Tfrost," to ECCC TWC(BWV_{ice})

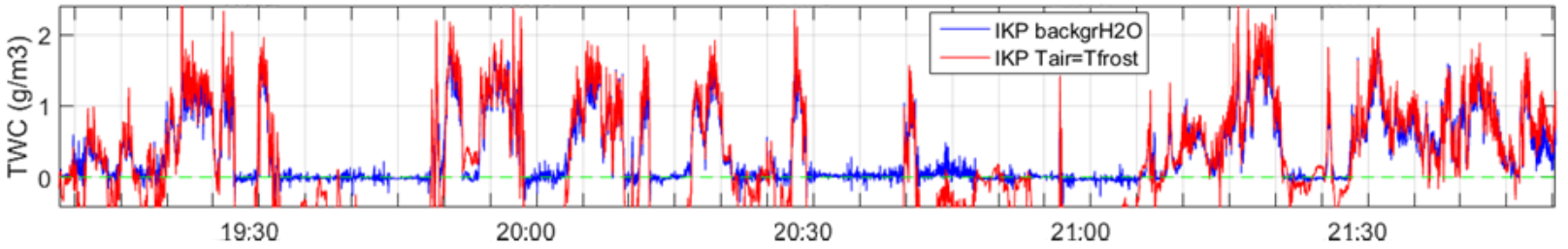

Figure B-10. Convair-580 Cayenne-15 flight on 25 May 2015 per Figure B-9

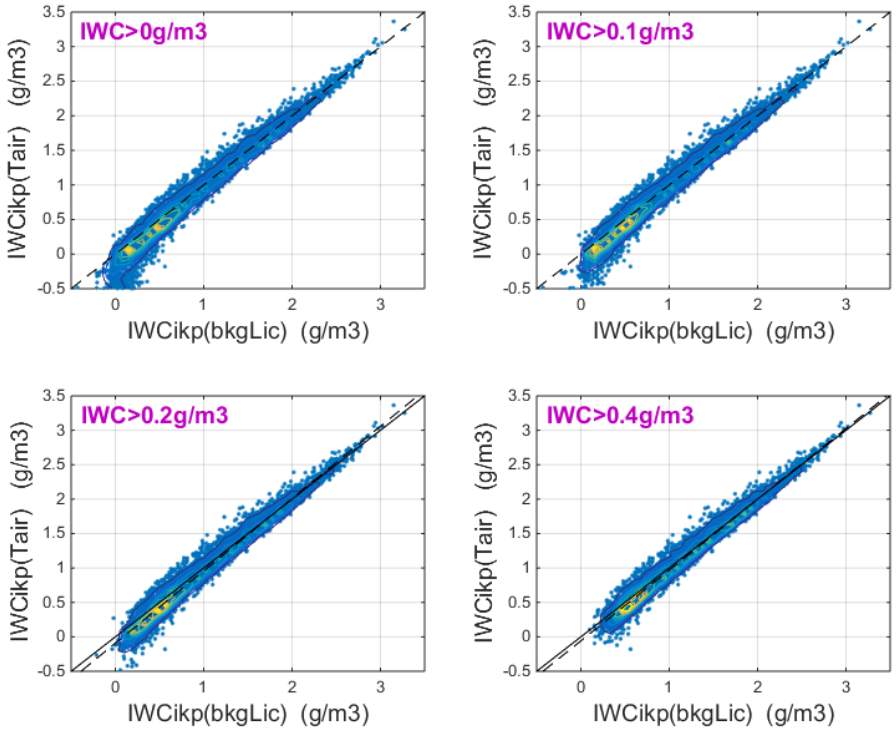

Figure B-11. Scatter diagrams for different TWC thresholds of the IKP-2 TWC calculated using ice saturation (y-axis) and measured (x-axis) background water vapor concentrations. IWCikp(Tair) and IWCikp(bckLic) correspond to ECCC TWC(BWV_{ice}) and TWC(BWV_m) respectively

At low TWC values, ECCC concluded that the ECCC TWC(BWV_{ice}) percentage error greatly increases, and values less than a few tenths of a gm^{-3} should be viewed with caution. However, at the higher TWCs representative of TWC_{99} values in the HAIC-HIWC and HIWC-RADAR flight campaigns, the errors were expected to be relatively small.

To support the further comparison -3of the ECCC and F20/DC8 algorithms in these four reference flights, the F20/DC8 algorithm was first checked to see if the software produced the same results for the same raw IKP-2 and LI-COR BWV measurements as did the ECCC algorithm. Results were nearly identical (not shown). Next, the four flights were processed using the F20/DC8 techniques described in section B.3 to normalize the measurements to ice saturation, and to produce the F20/DC8 TWC(BWV_{ice}) values. Figure B-12 shows a scatterplot of the 5-second average ECCC TWC(BWV_{ice}) versus the reference TWC for the 4 reference CV580 flights 16-19, the only HAIC-HIWC flights considered to have sufficiently accurate background water vapor measurements. This is essentially the same as Figure B-11 (top left, IWC > 0 gm^{-3}), but limited to the time periods used in the Appendix D/P assessment of section 3.1, and to reference TWCs greater than 0 gm^{-3}. ECCC TWC(BWV_{ice}) estimates are typically lower than the reference values for TWC less than about 1 gm^{-3}, and a little higher at the upper TWC values. The linear regression produces a best fit line of ECCC TWC(BWV_{ice}) = -0.0546+1.0527* ECCC TWC(BWV_m). Figure B-13 shows the corresponding comparison of the F20/DC8 TWC(BWV_{ice}) versus reference TWC,

with a very similar best fit line of F20/DC8 TWC(BWV_{ice}) = -0.008+1.0513* ECCC TWC(BWV_m). Table B-3 shows sample values calculated from the linear regression equations. It uses ice saturation water vapor estimates, versus the "true" TWC calculated using the background water vapor measurements. Relative errors are largest at the low TWC values, and the ice saturation values overestimate by about 3-5% at the highest TWCs. Data are 5-second average points for the 4 CV580 reference flights, during Appendix D assessment periods.

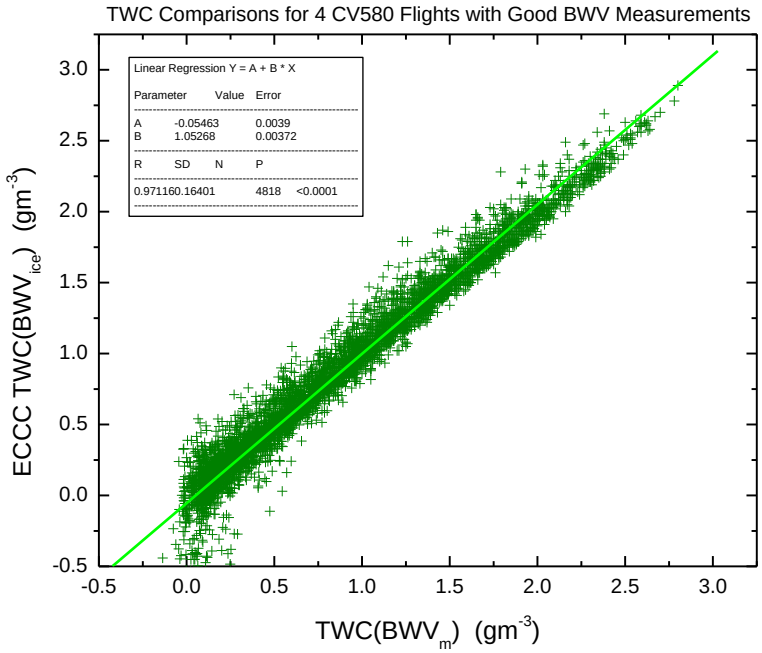

Figure B-12. Scatter plot of ECCC IKP-2 TWC estimate using ice saturation background water vapor (ECCC TWC(BWV_{ice})) vs. the measured background water vapor (TWC(BWV_m))

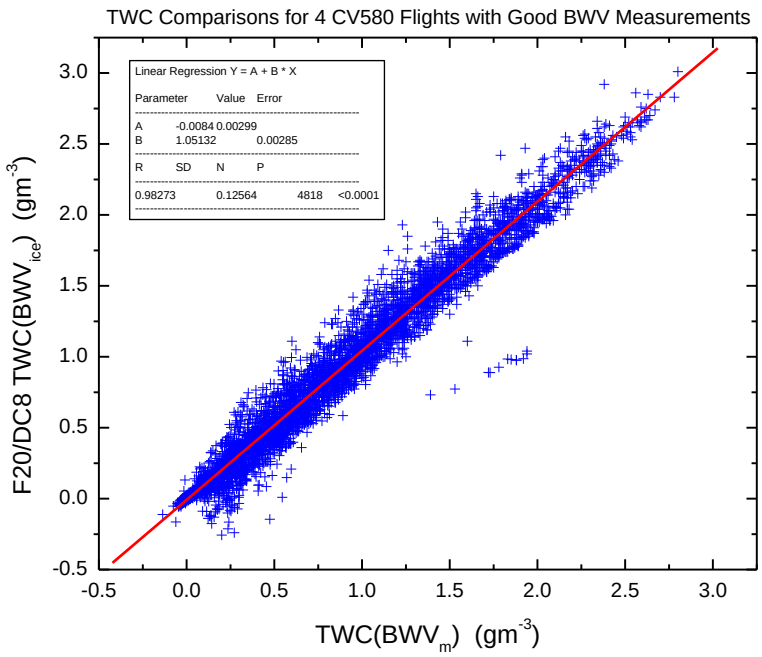

Figure B-13. Per Figure B-12 for the F20/DC8 TWC estimate using ice saturation background water vapor (F20/DC8 TWC(BWV_{ice})) vs. "true" TWC(BWV_m)

Table B-3. Table of values produced by the linear regression equations for ECCC TWC(BWV_{ice}) and F20/DC8 TWC(BWV_{ice}). (also see Figure B-12 and Figure B-13)

Reference TWC(BWV_m)	Adjusted ECCC TWC (BWV_{ice})	F20/DC8 TWC(BWV_{ice})
0	-0.055	-0.008
0.25	0.209	0.254
0.5	0.472	0.517
0.75	0.735	0.780
1	0.998	1.043
1.5	1.524	1.569
2	2.051	2.094
2.5	2.577	2.620
3	3.103	3.146

The time series data were then converted to distance units, and percentiles were calculated over the series of distance scales chosen for the Appendix D/P assessment. Since the primary TWC product of interest in this report is TWC_{99}, the differences in the TWC_{99} values produced by the three TWC calculations have been examined. Table B-4 contains TWC_{99} values for 4 reference CV580 flights, for distance scales between 0.5 and 20 Nm, calculated with the ECCC algorithms using the measured background humidity (TWC99(BWV_m), "truth") and ice saturation (ECCC

TWC_{99} (BWV_{ice}), (columns 3 and 4), and then using the Falcon-20/DC-8 algorithm (F20/DC8 TWC_{99} (BWV_{ice}) (column 8). Column 5 contains an adjusted ECCC TWC(BWV_{ice}) value that is contained in the HAIC-HIWC archive. Columns 6, 7 and 9 contain the ratios of the unadjusted and adjusted ECCC TWC_{99} values and F20/DC8 TWC_{99} values, all using their respective ice saturation BWV estimates, to the reference values, respectively.

Overall, the ECCC unadjusted algorithm tends to overestimate the reference TWC_{99} value by about 1-5% (column 6). The final ECCC correction not surprisingly produces values closer to the reference TWC (column 7). Overall, the F20/DC8 algorithm usually overestimates the reference TWC_{99} by a maximum of about 4%. Table B-4 reveals that, for at least the 4 reference CV580 flights, the use of the BWV_{ice} estimate in the IKP-2 TWC calculation had at most a 4% effect on the TWC_{99} data provided to the HAIC-HIWC and HIWC-RADAR archives.

Table B-4. 99th percentile TWC values (TWC99) for the four CV580 reference flights

			ECCC algorithm				F20/DC8 algorithm	
1	2	3	4	5	6	7	8	9
4 FLIGHTS Distance (Nm)	No. samples	Reference $TWC_{99}(BWV_m)$ (gm^{-3})	unadjusted $TWC(BWV_{ice})$ (gm^{-3})	adjusted $TWC(BWV_{ice})$ (gm^{-3})	col. 4 / col. 3	col. 5 / col. 3	$TWC_{99}(BWV_{ice})$ (gm^{-3})	col. 8 / col. 3
0.5	2922	2.396	2.482	2.387	1.036	0.996	2.435	1.016
1.0	1455	2.349	2.429	2.412	1.034	1.027	2.412	1.027
2.5	567	2.306	2.394	2.321	1.038	1.007	2.394	1.038
5.0	276	2.244	2.375	2.259	1.058	1.007	2.284	1.018
10.0	129	2.096	2.121	2.067	1.012	0.986	2.096	1
15.0	81	1.951	1.976	1.963	1.013	1.006	1.971	1.01
17.4	64	1.956	2.05	1.949	1.048	0.996	1.964	1.004
20.0	56	1.854	1.909	1.814	1.030	0.978	1.841	0.993

B.4.2. MONTE CARLO SIMULATIONS OF THE IKP-2 ERRORS DUE TO THE ICE SATURATION BWV ESTIMATE

The results of the four-flight intercomparisons provide a first estimate of the TWC_{99} errors associated with the assumption of ice saturation BWV in the IKP-2 calculation. However, they are relevant only to the -10 C temperature interval, and they provide insight specifically to the four-flight data set. BWV errors are expected to decrease with decreasing temperature due to the overall decrease in BWV levels, and thus the component of the IKP-2 total water vapor that is being subtracted from the in-cloud signal. In this section, a Monte Carlo simulation is used to estimate the uncertainty due to the ice saturation estimate for the full HAIC-HIWC and HIWC RADAR data sets.

The Monte Carlo simulation starts with a TWC frequency spectrum at 0.1 gm^{-3} intervals for each of the individual data subsets for which error estimates are to be made (Darwin-14 Falcon-20, Cayenne-15 Falcon-20, Cayenne-15 Convair-580, and Florida-15 DC8), and at each of the temperature intervals and distance scales for which data are available. For each simulation (e.g., Darwin-14 Falcon-20, -30 C, 17.4 Nm), data points of a "true: TWC are generated in the simulation according to the observed TWC frequency spectrum, and a temperature is generated random-

normally using the computed mean and standard deviation measured from the data subset. Normal distribution fits of the error spectra of the BWV, derived from the 4 reference CV580 flights, described in more detail below, are injected random-normally into the simulation, and used to calculate a TWC estimate that subtracts BWV with characteristics as in the reference flight data. The simulation is run for a large number of data points (~1,000,000), and the final spectrum of TWC is compared to the input "true" TWC spectrum.

A few assumptions to this simulation should be addressed at the outset. First, the spectrum of BWV errors, which in the case of the ECCC algorithm is equivalent to the in-cloud spectrum of supersaturation with respect to ice (SS_i), is based on the 4 reference CV580 flights only, which were conducted at an average temperature of -9.57 C, and with data in sufficient quantity to provide error spectra up to a TWC of about 2.5 gm^{-3}. Since many of the data sets exceeded 2.5 gm^{-3}, it was necessary to assume that the BWV error spectrum remained constant above 2.5 gm^{-3} TWC. As seen in Figure B-14, the BWV error spectra leveled off somewhat at high TWC, providing some support for this approximation. Second, it is unknown how the spectrum of in-cloud SS_i changes with temperature. Based on the general observation in the data set of reduced mixed-phase cloud with decreasing temperature (Appendix D), it is reasonable to assume that average values of SS_i may decrease with decreasing temperature, and application of the -9.57 C data from the 4 reference CV580 flights to colder temperatures would be conservative, and lead to higher simulated TWC errors. A complicating factor is that the relative difference between water and ice saturation ($(e_w(gm^{-3})-e_i(gm^{-3}))/e_i(gm-^{3})$) increases with decreasing temperature. Application of the -9.57 C SS_i data to -30 C, for example, would produce in-cloud BWV that reaches a lower fraction of the distance between water and ice saturation, which may seem to some like a non-intuitive result. To address this, the BWV error spectra have been scaled to the relative difference between water and ice saturation. Although not based on hard evidence, this, again, is a conservative adjustment that will tend to increase TWC simulation errors. Since the errors will be shown to be very low at the colder temperatures, whether this adjustment is valid is somewhat of a moot point. Third, the BWV error spectra will be applied at distance scales similar to that from which they were derived, but also at much longer distance scales. An investigation of the distance-scale change in the 4 reference CV580 flight error spectra, limited by the decreasing number of points with longer distance scales, revealed little change between 5-second and 25-second averages, but the latter corresponded only to about 1.5 Nm. It is perhaps reasonable to assume that longer distance averages would tend to average out BWV error variations, and application of 5-second (~0.3 Nm) BWV errors to 100 Nm simulations might overestimate error variations, but this is speculation. Finally, the perturbed TWC spectrum produced by the simulation is relative to the input spectrum derived from the flight data, the latter of which is actually a perturbed spectrum. Although the simulation could be performed repeatedly until the final spectrum matched the input flight data, this would be very time-consuming. Given the relatively small differences to be shown, it was concluded that sufficiently accurate errors could be derived without such a repetitive solution.

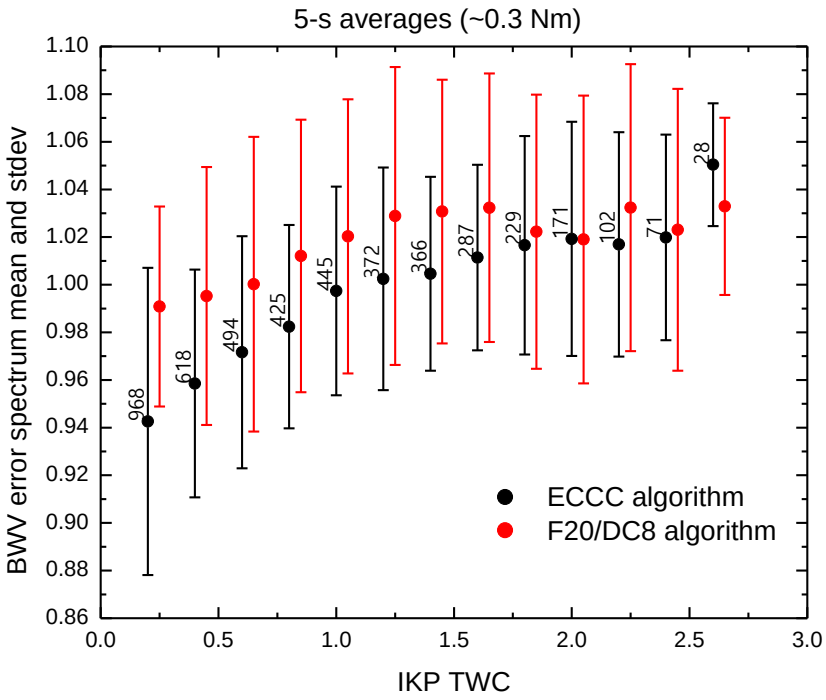

Figure B-14. Average and standard deviations of BWV error spectra from 4 reference CV580 flights based on IKP-2 TWC for the ECCC (black) and F20/DC8 (red) algorithms. Data points per TWC interval shown next to standard deviation bar (see text analysis)

As discussed earlier, the ECCC analysis concluded that the data set showed significant variations in cloud humidity, from sub-saturation with respect to ice, to supersaturation with respect to water. However, on the average, the humidity could be slightly sub-saturated to about saturated with respect to ice, depending on the minimum TWC thresholds used to filter the data in that study. This indicated that average IKP-2 errors due to the assumption of ice saturation, particularly at high IWC, would likely be minor, particularly for high IWC values. The Monte Carlo simulation described here uses in-cloud BWV spectra to estimate the spectrum of errors associated with the ECCC and F20/DC8 algorithms, respectively. In the case of the unadjusted ECCC algorithm, the IKP-2 TWC error is simply derived from the observed SS_i spectrum. In the case of the F20/DC8 algorithm, it is more complicated due to the switching between BWV_m and BWV_{ice} at a TWC of ~0.2 gm^{-3}, but the differences between the ECCC and F20/DC8 algorithm have been carefully traced, and the following equations describe the spectrum of errors:

ECCC algorithm (unadjusted) spectrum of BWV errors:

R1 =spectrum of BWV_m/ BWV_{ice} (i.e. the SS_i spectrum)

F20/DC8 algorithm spectrum of BWV errors:

Case 1: (ice saturation chosen, IWC ~>0.2 gm^{-3})

R2=spectrum of (BWV_m + ΔIKPLicor)/ BWV_{ice} (SS_i spectrum enhanced by IKP-2 Licor offset relative to ECCC algorithm)

Case 2: (adjusted BWV_m chosen, IWC ~<0.2 gm^{-3})

R3= spectrum of (ΔIKPLicor – Δ BWV_m +BWV_{ice})/ BWV_{ice} (equivalent to the spectrum of difference between the BWV_m and BWV_{ice}, taking into account the offsets applied to the IKP-2 and BWV Licors)

The final spectrum R4 is comprised of contributions from R2 and R3, according to which applied to a particular data point. In the Monte Carlo simulation, the TWC modified by the BWV error is given by the following:

$$TWC_m = TWC_{true} + R(i) * BWV_{ice} - BWV_{ice} \quad \text{(B-8)}$$

where R(i) is a BWV error value chosen random-normally from the distribution of BWV errors for which the simulation is being performed (i.e., from R1 for the ECCC algorithm, or R4 for the F20/DC8 algorithm). One can see from the above equation, that the R(i) error value can be thought of as a fraction of the ice saturation value, or a BWV error *relative* to the ice saturation value. To avoid repetitive lengthy terms, these spectra will be referred to below simply as "BWV error spectra".

The above error spectra were computed using the 5-second data from the 4 reference CV580 flights. It was important to compute these spectra as a function of TWC, to determine whether, for example, a higher BWV error might be associated with a higher TWC value (i.e., a higher SS_i). Error spectra were determined in 0.2 gm^{-3} intervals up to 2.5 gm^{-3}, above which the frequency of TWC points quickly decreased, and there were insufficient points to fit normal distributions. It was this necessary to apply a single error spectrum for all TWC values > 2.5 gm^{-3}. A typical example of error spectra for each algorithm for the approximate midpoint of the range in TWC values (1.3-1.5 gm^{-3}) is shown in Figure B-15. Note that the ECCC algorithm shows a mean error very close to unity (i.e., the ECCC algorithm shows the mean in-cloud humidity right at ice saturation, with on the average insignificant TWC error). The F20/DC8 algorithm shows a mean error of about 1.0307, corresponding to a mean positive TWC error of about 0.06 gm^{-3} in the 1.3-1.5 gm^{-3} interval, a relatively small value. Normal fits also are shown for the two distributions in Figure B-15. The means and standard deviations of these fits are used in the Monte Carlo simulation to reproduce the error spectra within this TWC interval. Figure B-14 shows the error spectra means and standard deviations as a function of TWC in the 0.2 gm^{-3} TWC intervals described above. For the ECCC algorithm, the average error rises from about 0.94 of the BWV_{ice} value to about 1.02 at 2.4 gm^{-3}, with a jump to about 1.05 in the final bin representing > 2.5 gm^{-3} TWC. The F20/DC8 average BWV error rises from about 0.99 to level off at about 1.02-1.03

above 1.5 gm^{-3}. The lower errors at low TWCs for the F20/DC8 algorithm are due to the normalization of the BWV at ice saturation in continuous cloud with IWC ~0.2 gm^{-3}. Such cloud is usually found to be sub-saturated with respect to ice using the ECCC algorithm, which normalizes in-cloud humidity in regions of water-saturated cloud. Nevertheless, the takeaway from this figure is that the relative BWV errors are quite low for both algorithms, and on the average would tend to produce TWC errors of minor relative importance except for the lowest TWCs. The standard deviations of the errors are similar between the two algorithms. The effect of the BWV variations (standard deviations) are revealed later in the Monte Carlo simulations.

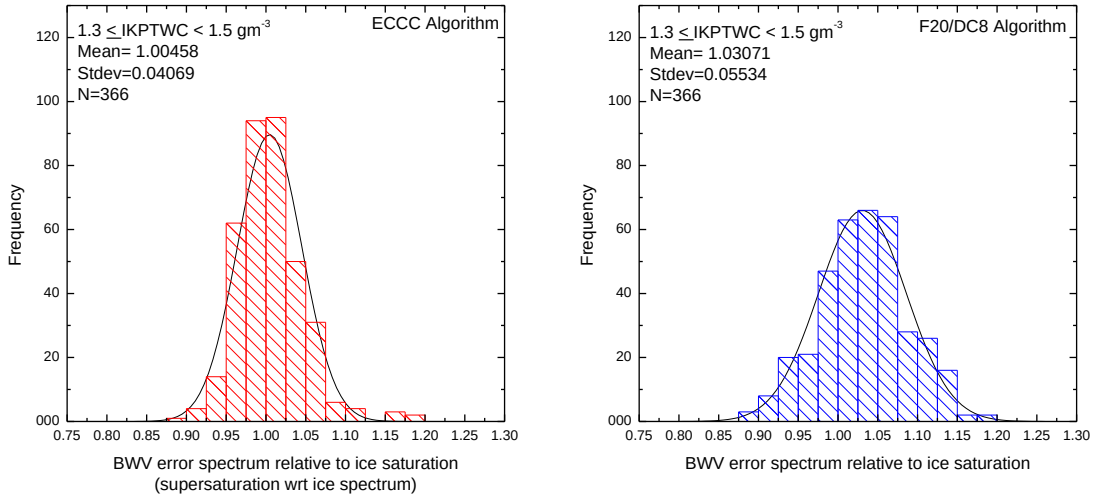

Figure B-15. Spectra of BWV errors for the ECCC (left) and F20/DC8 (right) algorithms for the 1.3-1.5 gm-3 TWC interval. Similar spectra derived in 0.2 gm-3 intervals with normal distribution fits and parameters shown in text inserts

To apply these error spectra to temperatures other than -9.57 C, the following scaling procedure has been applied to the spectra to account for the relative increase in the difference between water and ice saturation concentrations with decreasing temperature (see earlier discussion this section).

$$C1 = \frac{\left(e_w(T) - e_i(T)\right) e_i(T_{ref})}{\left(e_w(T_{ref}) - e_i(T_{ref})\right) e_i(T)} \quad \text{(B-9)}$$

Where:

e_w, e_i are the water saturated and ice saturated vapor concentrations expressed in gm^{-3}

T_{ref} = -9.57 C for our case (avg. temperature of 4 reference CV580 flights)

Then the temperature-scaled error spectra average and standard deviations are:

$$Avg(R(T)) = 1 + C1 * (Avg(R(T_{ref})) - 1) \quad \text{(B-10)}$$

$$\sigma(R(T)) = C1 * \sigma(R(T_{ref})) \quad \text{(B-11)}$$

Testing of Monte Carlo simulation on 4 reference CV580 flights

Table B-5 is a test of the ability of the Monte Carlo simulation to re-create flight values. This table contains results of the Monte Carlo simulation for the 4 reference CV580 flights. Percentiles of the input and output cumulative frequency distributions (CFDs) of TWC are provided. Column A contains the reference TWC CFD, which the Monte Carlo simulation is trying to reproduce as an input. Column B shows the actual Monte Carlo simulation CFD. The CFDs are quite similar but not identical. This is not critical, because more important are the comparisons of Monte Carlo output to Monte Carlo input, and flight data algorithm output to flight data reference values. Column C shows the unadjusted ECCC TWC(BWV_{ice}) percentiles, and column G their ratios to the reference values. Column H shows the corresponding ratios of the Monte Carlo ECCC TWC(BWV_{ice}) to actual simulation input values. (Note that the final ECCC adjustment step for ECCC TWC(BWV_{ice}) based on its linear regression with ECCC TWC(BWV_m) was removed.) The ratios in columns G and H (flight versus Monte Carlo) are almost the same until about the 60^{th} percentile, above which the simulation underestimates the flight ratios by about 2%. Columns I and J contain the ratios of the F20/DC8 algorithm TWCs to the flight data reference values and Monte Carlo actual input values. Except at the lower percentiles, the Monte Carlo ratios are typically a little lower than the flight ratios (typically about 2% lower for percentiles higher than the 50^{th}). This underestimation of the errors by the Monte Carlo simulation for both the ECCC and F20/DC8 algorithms should be kept in mind in the subsequent comparisons for the other data sets. Note, however, that the magnitude of both the flight data and simulation ice-saturation assumption errors are relatively small, being less than about 5% at -9.57 C, and these are predicted to be even lower for colder temperatures.

Table B-5. Percentiles of TWC values from 4 reference CV580 flights and for Monte Carlo simulations, for all Appendix D/P assessment time periods, and a 0.5 Nm distance scale. Values shown for ECCC and F20/DC8 algorithms (see text analysis)

	A	B	C	D	E	F	G	H	I	J
	Flight data	M. Carlo	Flight data	Flight data	M. Carlo	M. Carlo	ECCC flight	ECCC M. Carlo	F20/DC8 flight	F20/DC8 M. Carlo
	Reference ECCC TWC(BWV_m)	input TWC to MC	Unadjusted ECCC TWC(BWV_{ice})	F20/DC8 TWC (BWV_{ice})	ECCC TWC (BWV_{ice})	F20/DC8 TWC (BWV_{ice})	Column C / Column A	Column E / Column B	Column D / Column A	Column F / Column B
max	2.811	2.900	3.069	2.992	3.209	3.317	1.047	1.107	1.064	1.144
10th	0.132	0.141	0.012	0.100	-0.007	0.108	0.091	-0.050	0.758	0.766
20th	0.223	0.239	0.141	0.195	0.144	0.221	0.632	0.603	0.874	0.925
30th	0.351	0.368	0.279	0.338	0.291	0.352	0.795	0.791	0.963	0.957
40th	0.511	0.524	0.456	0.499	0.459	0.524	0.892	0.876	0.977	1.000
50th	0.704	0.722	0.677	0.739	0.682	0.745	0.962	0.945	1.050	1.032
60th	0.928	0.939	0.912	0.957	0.922	0.977	0.983	0.982	1.031	1.040
70th	1.146	1.162	1.181	1.223	1.170	1.228	1.031	1.007	1.067	1.057
80th	1.431	1.447	1.482	1.531	1.464	1.519	1.036	1.012	1.070	1.050
90th	1.760	1.774	1.827	1.854	1.807	1.838	1.038	1.019	1.053	1.036
99th	2.396	2.400	2.482	2.435	2.465	2.494	1.036	1.027	1.016	1.039
Tavg	-9.57	-9.57								
Tstde	1.79	1.79								
Pavg	463.3	460.1								

Monte Carlo simulations of ice saturation assumption errors in the Appendix D/P TWC assessment data sets

In Table B-6, Column A contains the input cumulative frequency distribution. The Monte Carlo simulation produces a slightly different input CFD, as shown in column B. The outputs of the Monte Carlo simulation for the ECCC and F20/DC8 algorithms are provided in columns C and D, respectively, with their ratios to the "true" Monte Carlo TWCs (column B) in columns E and F. TWCs are given in units of gm-3.

In the following tables, examples of the errors in the full HAIC-HIWC and HIWC-RADAR IKP-2 data set CFDs, including the TWC_{99} values, are estimated using the Monte Carlo simulation. Table B-6 through Table B-9 contain error estimates for the composite -10 , -30, -40, and -50 C temperature interval data sets, for the 0.5 Nm and 17.4 Nm distance scales (left and right table sections, respectively). The 0.5 and 17.4 Nm errors tend to be quite similar, so the discussion below focuses on the 17.4 Nm reference scale results. The TWC error estimates referred to below are contained in columns K and L for the ECCC and F20/DC8 algorithms, respectively. Note that ECCC algorithm was not used for any of the Appendix D/P TWC assessment points in the -30, -40, or -50 C temperature intervals, but are provided here for documentation and discussion.

In the -10 C interval (Table B-6), the unadjusted ECCC algorithm provides lower TWCs at the lower percentiles, and reaches a maximum TWC overestimate of about 4% at the 99th percentile. The F20/DC8 algorithm similarly underestimates the TWC at the lower percentiles, to a lesser degree than the ECCC algorithm, and reaches a maximum overestimate of about 7% at the 70th percentile. The TWC underestimates at the lower percentiles largely result from in-cloud points produced from the BWV error spectra that are sub-saturated with respect to ice, and have a greater relative effect at low TWC values. The overestimate of the TWC_{99} value is about 3%. Thus, both algorithms tend to overestimate the TWC_{99} values by less than about 4%.

In the -30 C interval (Table B-7), there is less underestimate of the low percentile TWC values than at -10 C. The ECCC and F20/DC8 algorithms reach maximum overestimates of about 2% at the 99th percentile and 4% at the 80th percentile, respectively, and the F20/DC8 algorithm TWC_{99} overestimate is about 3%. Both algorithms overestimate TWC_{99} by less than 3%.

In the -40 C interval (Table B-8), errors drop significantly. The maximum TWC overestimates using the ECCC and F20/DC8 algorithms are about 0.3% and 1%, respectively. At the 99th percentiles, the errors are about 0.3 and 0.6%, respectively.

In the -50 C interval (Table B-9), errors continue to decrease. The maximum TWC overestimates for the ECCC and F20/DC8 algorithms are only 0.1% and 0.2% respectively, and at the 99th percentile are both about 0.1%.

Table B-6. Monte Carlo simulation error CFD estimates, including TWC99, for the composite data set in the -10 C interval (see text description and analysis)

	0.5 Nm distance scale, -10 C interval, composite data set						17.4 Nm distance scale, -10 C interval, composite data set					
	A Flight data	B M. Car.	C M. Car.	D M. Car.	E M.Car.	F M. Car.	G Flight data	H M. Car.	I M. Car.	J M. Car.	K M. Car.	L M. Car.
	CV580 and F20/DC8 TWC(BWV_{ice})	input TWC-to M.Car.	Unadjusted ECCC TWC(BWV_{ice})	F20/DC8 TWC (BWV_{ice})	Col. C / Col. B	Col. D / Col. B	CV580 and F20/DC8 TWC(BWV_{ice})	input TWC-to M.Car.	Unadjusted ECCC TWC($BWVi_{ce}$)	F20/DC8 TWC (BWV_{ice})	Col. I / Col. H	Col. J / Col. H
10th	0.080	0.102	-0.045	0.075	-0.441	0.735	0.201	0.210	0.061	0.166	0.290	0.790
20th	0.192	0.208	0.107	0.191	0.514	0.918	0.291	0.301	0.222	0.290	0.738	0.963
30th	0.319	0.340	0.260	0.322	0.765	0.947	0.436	0.452	0.374	0.436	0.827	0.965
40th	0.482	0.504	0.434	0.500	0.861	0.992	0.587	0.602	0.544	0.609	0.904	1.012
50th	0.677	0.697	0.655	0.721	0.940	1.034	0.765	0.773	0.736	0.802	0.952	1.038
60th	0.919	0.938	0.923	0.982	0.984	1.047	0.953	0.964	0.955	1.012	0.991	1.050
70th	1.216	1.234	1.247	1.305	1.011	1.058	1.156	1.182	1.203	1.266	1.018	1.071
80th	1.591	1.604	1.631	1.677	1.017	1.046	1.516	1.560	1.579	1.622	1.012	1.040
90th	2.092	2.097	2.142	2.157	1.021	1.029	1.975	1.955	1.998	2.008	1.022	1.027
99th	2.913	2.929	3.046	3.011	1.040	1.028	2.684	2.730	2.842	2.803	1.041	1.027

Table B-7. Composite data set in the -30 C interval per Table B-6

	0.5 Nm distance scale, -30 C interval, composite data set						17.4 Nm distance scale, -30 C interval, composite data set					
	A Flight data	B M. Car.	C M. Car.	D M. Car.	E M.Car.	F M. Car.	G Flight data	H M. Car.	I M. Car.	J M. Car.	K M. Car.	L M. Car.
	F20/DC8 TWC (BWV_{ice})	input TWC-to M.Car.	Unadjusted ECCC TWC(BWV_{ice})	F20/DC8 TWC (BWV_{ice})	Col. C / Col. B	Col. D / Col. B	F20/DC8 TWC (BWV_{ice})	input TWC-to M.Car.	Unadjusted ECCC TWC(BWV_{ice})	F20/DC8 TWC (BWV_{ice})	Col. I / Col. H	Col. J / Col. H
10th	0.086	0.101	0.017	0.083	0.168	0.822	0.134	0.143	0.064	0.129	0.448	0.902
20th	0.156	0.175	0.110	0.166	0.629	0.949	0.242	0.242	0.182	0.229	0.752	0.946
30th	0.247	0.266	0.213	0.254	0.801	0.955	0.349	0.352	0.304	0.342	0.864	0.972
40th	0.360	0.377	0.332	0.372	0.881	0.987	0.448	0.470	0.426	0.468	0.906	0.996
50th	0.499	0.520	0.482	0.519	0.927	0.998	0.604	0.628	0.596	0.631	0.949	1.005
60th	0.686	0.707	0.686	0.722	0.970	1.021	0.748	0.768	0.750	0.788	0.977	1.026
70th	0.929	0.948	0.943	0.973	0.995	1.026	0.947	0.948	0.942	0.973	0.994	1.026
80th	1.262	1.286	1.296	1.331	1.008	1.035	1.218	1.224	1.233	1.268	1.007	1.036
90th	1.773	1.792	1.814	1.823	1.012	1.017	1.612	1.634	1.647	1.672	1.008	1.023
99th	2.804	2.816	2.879	2.857	1.022	1.015	2.371	2.391	2.439	2.457	1.020	1.028

Table B-8. Composite data set in the -40 C interval per Table B-6

	0.5 Nm distance scale, -40 C interval						17.4 Nm distance scale, -40 C interval					
	A Flight data	B M. Car.	C M. Car.	D M. Car.	E M.Car.	F M. Car.	G Flight data	H M. Car.	I M. Car.	J M. Car.	K M. Car.	L M. Car.
	F20/DC8 TWC (BWV_{ice})	input TWC-to M.Car.	Unadjusted ECCC TWC(BWV_{ice})	F20/DC8 TWC (BWV_{ice})	Col. C / Col. B	Col. D / Col. B	F20/DC8 TWC (BWV_{ice})	input TWC-to M.Car.	Unadjusted ECCC TWC($BWVi_{ce}$)	F20/DC8 TWC (BWV_{ice})	Col. I / Col. H	Col. J / Col. H
10th	0.102	0.106	0.081	0.101	0.764	0.953	0.142	0.148	0.127	0.144	0.858	0.973
20th	0.160	0.169	0.150	0.166	0.888	0.982	0.214	0.220	0.201	0.217	0.914	0.986
30th	0.240	0.247	0.230	0.244	0.931	0.988	0.31	0.317	0.304	0.315	0.959	0.994
40th	0.349	0.359	0.344	0.357	0.958	0.994	0.451	0.450	0.436	0.448	0.969	0.996
50th	0.495	0.501	0.491	0.501	0.980	1.000	0.561	0.573	0.564	0.574	0.984	1.002
60th	0.672	0.675	0.667	0.677	0.988	1.003	0.739	0.738	0.732	0.743	0.992	1.007
70th	0.879	0.888	0.884	0.893	0.995	1.006	0.938	0.932	0.931	0.939	0.999	1.008
80th	1.171	1.172	1.173	1.182	1.001	1.009	1.172	1.170	1.170	1.180	1.000	1.009
90th	1.544	1.549	1.553	1.560	1.003	1.007	1.51	1.516	1.519	1.524	1.002	1.005
99th	2.465	2.472	2.481	2.484	1.004	1.005	2.112	2.164	2.171	2.177	1.003	1.006

Table B-9. Composite data set in the -50 C interval per Table B-6

	0.5 Nm distance scale, -50 C interval, composite data set					
	A Flight data	B M. Car.	C M. Car.	D M. Car.	E M.Car.	F M. Car.
	F20/DC8 TWC (BWV_{ice})	input TWC-to M.Car.	Unadjusted ECCC TWC(BWV_{ice})	F20/DC8 TWC (BWV_{ice})	Col. C / Col. B	Col. D / Col. B
10th	0.065	0.064	0.061	0.063	0.953	0.984
20th	0.118	0.126	0.123	0.126	0.976	1.000
30th	0.179	0.186	0.182	0.185	0.978	0.995
40th	0.267	0.275	0.271	0.275	0.985	1.000
50th	0.386	0.388	0.385	0.388	0.992	1.000
60th	0.534	0.539	0.538	0.539	0.998	1.000
70th	0.718	0.723	0.722	0.724	0.999	1.001
80th	1.009	1.015	1.015	1.017	1.000	1.002
90th	1.413	1.417	1.417	1.418	1.000	1.001
99th	2.106	2.106	2.107	2.108	1.000	1.001

	17.4 Nm distance scale, -50 C interval, composite data set					
	G Flight data	H M. Car.	I M. Car.	J M. Car.	K M. Car.	L M. Car.
	F20/DC8 TWC (BWV_{ice})	input TWC-to M.Car.	Unadjusted ECCC TWC($BWVi_{ce}$)	F20/DC8 TWC (BWV_{ice})	Col. I / Col. H	Col. J / Col. H
10th	0.102	0.160	0.240	0.349	0.495	0.672
20th	0.15	0.160	0.157	0.159	0.981	0.994
30th	0.232	0.240	0.236	0.239	0.983	0.996
40th	0.328	0.333	0.331	0.333	0.994	1.000
50th	0.416	0.418	0.415	0.417	0.993	0.998
60th	0.569	0.561	0.559	0.561	0.996	1.000
70th	0.766	0.773	0.772	0.773	0.999	1.000
80th	1.03	1.038	1.038	1.039	1.000	1.001
90th	1.296	1.297	1.298	1.300	1.001	1.002
99th	1.809	1.818	1.820	1.820	1.001	1.001

The comparisons of the ECCC and F20/DC8 results reveal that both algorithms produce similar overestimates of the TWC_{99} values in all temperature ranges due to the assumption of ice saturation BWV in the IKP-2 calculation, and that the differences between the two algorithms decrease with decreasing temperature. In the -40 and -50 C temperature intervals, the TWC_{99} errors are less than 1% or so, and can essentially be ignored. In the -30 C and -10 C intervals, simulations overestimate TWC_{99} by less than 3% and 4%, respectively. However, it is prudent to widen these to 5 and 6% to roughly account for the observation that the Monte Carlo simulation somewhat underpredicted the higher percentile TWCs by 1-2% for the 4 reference CV580 flights (Table B-5).

As shown in the next section, overestimate of the TWC_{99} values is somewhat counteracted by a statistical underestimate due to the finite number of data points available from the flight campaigns. In order to provide a final TWC_{99} bias correction and confidence intervals for each of the TWC_{99} values and CFDs, incorporating both ice saturation assumption and sampling uncertainty, the Monte Carlo simulation will be used again in section B.6.

B.5 STATISTICAL SAMPLING UNCERTAINTY OF TWC_{99} ESTIMATES

During Engine Harmonization Working Group (EHWG) discussions in 2007, an industry statistician provided an analysis of the statistical sampling uncertainty of TWC_{99} values calculated for the 1950s RAE data [B-11]. The data set of 2381 values was repeatedly subsampled using different sample sizes following a "bootstrap" approach. The analysis revealed two forms of uncertainty due to reduced sample size. First, a fairly insignificant low-bias in the TWC_{99} values was observed that exceeded 10% only for sample sizes less than 50. Second, there was a range of TWC_{99} values calculated at each randomly sub-sampled size. The standard deviation σ of the TWC_{99} values increased rapidly for sample sizes less than 100, indicating an estimated 95% confidence interval ($\pm 2\sigma$) of about ±17% of the mean TWC_{99} value at 100 samples. The EHWG decided that 20% should be the target upper limit for the sampling uncertainty, and thereafter established 100 data points as the target objective for flight campaign data collection of 17.4 Nm data points at each temperature level. Table 18 lists the actual number of 17.4 Nm points collected during the flight campaigns, indicating that the 100-point target was achieved at all primary temperature levels, varying between 263 at -50 C, and 445 at -30 C. In this section, the calculations performed by the EHWG are replicated as closely as possible with the current flight campaign data set. The results estimate the statistical uncertainty of sampling TWC_{99} values where the population is defined by the data set itself, and may not be representative of the true total population of suitable clouds that were available for sampling during the flight programs. Further review by a statistician may yield additional insights.

B.5.1. LOW BIAS OF TWC_{99} ESTIMATES

Details of the bootstrap procedure follow. The procedure was performed on the composite data sets for each of the four temperature intervals, and each of the thirteen distance intervals chosen for the Appendix D/P TWC assessment. For each data set (e.g., -30 C, Darwin-14 Falcon-20 + Cayenne-15 Falcon-20 + Florida-15 DC-8, 0.5 Nm distance scale), a subset (n) of the total available TWC values (N) was sampled randomly and with replacement 5000 times. From these 5000 repeated samples, the mean and standard deviation of the TWC_{99} values was calculated. The process was repeated for subset sizes from the maximum number of points available (n=N) to n=10. Due to the computation time required, the subset sizes were reduced in steps of 10 rather

than 1, and if the total number of points was greater than 5000, the largest subset size was 5000. For example, for the -30 C, 0.5 Nm data set sampling, there are 17838 points, so the subset sizes were 5000, 4990, 4980, …. 10. Similarly, for the -50 C interval, 5 Nm data set, there are 1000 points, so the subset sizes were 1000, 990, 980, …. 10.

The low-bias ratio LBR(*n,d*), for subset size *n* and distance scale *d* , was first computed for the shortest distance scale (0.5 Nm) with the largest number of points, as follows:

$$LBR(n,0.5\ Nm) = TWC_{99}(n,0.5\ Nm)/\ TWC_{99}(N,0.5\ Nm) \quad \text{(B-12)}$$

where *N* is the total number of data points available at the distance scale in question. Note that this is simply the ratio of the TWC_{99} computed at the subset size *n* to the corresponding value computed for the largest subset size *N*. At the maximum sample size (*n=N*), it has a value of 1, and for this short distance scale, TWC_{99} is assumed to have negligible error.

An example for the -30 C interval is given in Figure B-16. The sub-sampled TWC_{99} values decrease by about 5% at 100 points, and 20% by about 20 points. The decrease in the TWC_{99} value is less than 1% for sample sizes greater than about 1700. As the same procedure is repeated for longer distance scales (different lines in Figure B-17), the maximum number of available points decreases. As noted above, at the maximum sample size, the LBR value is by definition 1, so the first point of every line starts on the LBR=1 line, and the rest of the line more or less falls off at the same rate as the other lines. But the 0.5 Nm curve predicts that these lines will already have a low bias even at their maximum number of points. Taking the 30 Nm line as an example (the first line with dots in the progression from left to right), the line starts at 232 points and an LBR value of 1. However, the low-bias ratio at 232 points for the 0.5 Nm line is 0.974, suggesting that the 30 Nm should be adjusted down. A further scale factor was thus applied, assuming that the 0.5 Nm bias-versus-sample size applied to all distance scales

$$LBR(n,d) = (TWC_{99}(n,d)/\ TWC_{99}(N,d))*LBR(n,0.5\ Nm) \quad \text{(B-13)}$$

The above equation simply forces the first point of distance scale *d* to start along the 0.5 Nm LBR line, which has a very large number of points for definition. The results for the -30 C interval are shown in Figure B-18, and for the other temperature intervals in Figure B-19, Figure B-20, and Figure B-21. The curves at the different distance scales now line up reasonably well, and the low biases can be more accurately approximated, particularly for 100 points and larger. At the reference distance scale of 17.4 Nm, for example, the low bias at the -10, -30, -40, and -50 C intervals (271, 445, 434, and 263 points) is almost negligible at < 2%. Low bias at 100 points varies between about 5 and 8%, quite a bit larger than estimated from the RAE data set for the EHWG, but still relatively small. Low bias reaches 20% with sample sizes between about 10-20.

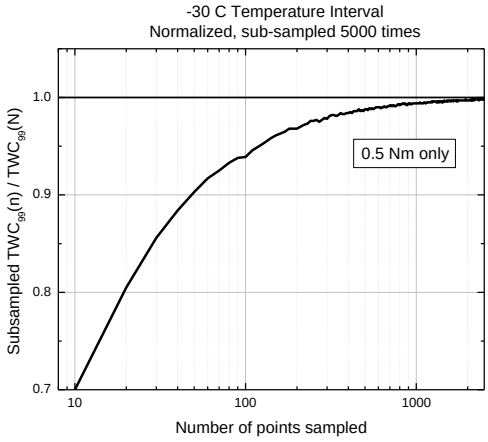

Figure B-16. Low-bias ratio for TWC99 values computed by sub-sampling 59132 0.5 Nm TWC values in the -30 C temperature interval

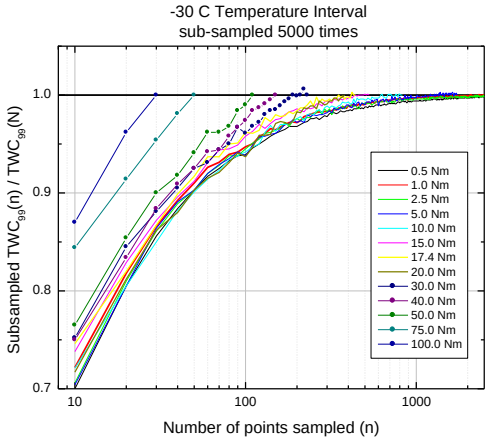

Figure B-17. Different distance scales with fewer points per Figure B-16. Distance scales ≥ 30 Nm represented by lines and points

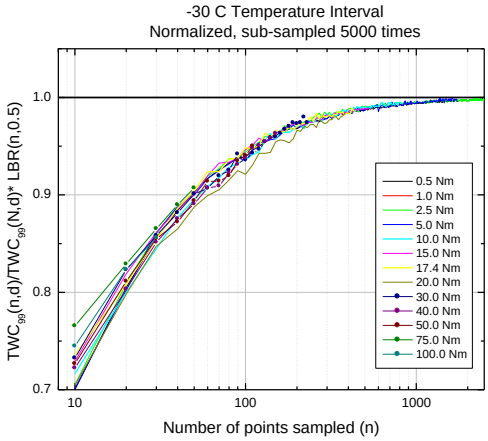

Figure B-18. Additional starting bias ratio applied to first point from 0.5 Nm data per Figure B-17, as in equation (B-9)

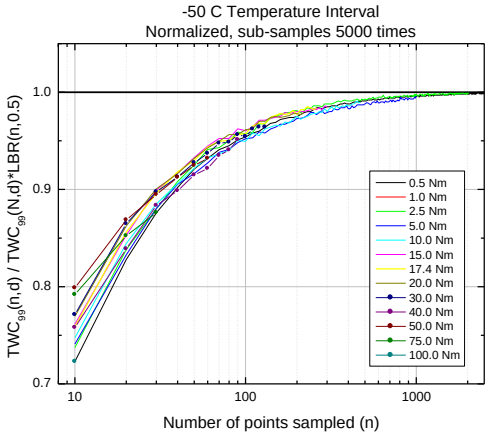

Figure B-19. -50 C temperature interval per Figure B-18

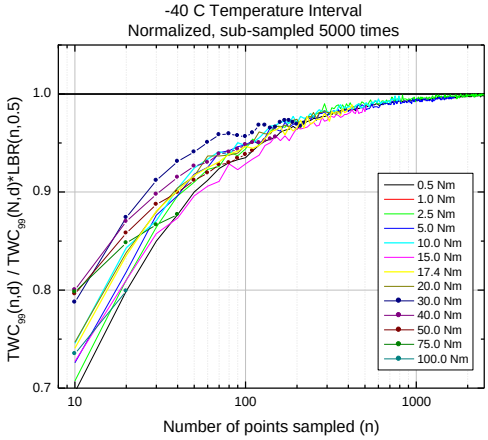

Figure B-20. -40 C temperature interval per Figure B-18

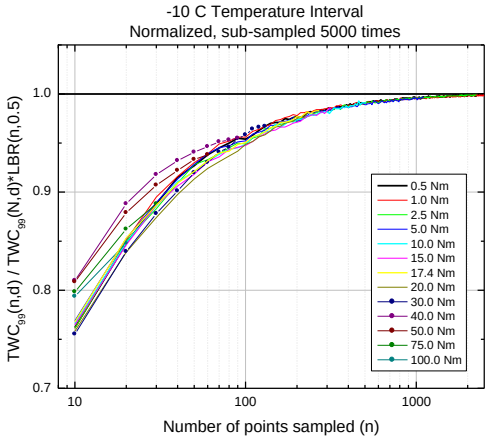

Figure B-21. -10 C temperature interval per Figure B-18

B.5.2. STANDARD DEVIATION (UNCERTAINTY) OF TWC_{99} ESTIMATES

Standard deviations of the TWC_{99} values were also calculated during the sub-sampling procedure described in section B.5.1. Starting again with the -30 C temperature interval, results for the lowest distance scale (0.5 Nm, 59132 points) are provided in Figure B-22. The standard deviation σ increases with decreasing sample size as expected, with values of about 0.04, 0.26, and 0.56 gm^{-3} at 5000, 100, and 10 points, respectively. At 100 points, the 2σ value is about 18% of the best estimate of the "true" TWC_{99} (at 5000 points), about the same as found by the EHWG for the RAE data set.

A certain fraction of the data set contributing to the analysis is lost at each distance scale. For example, a cloud with a characteristic size of 20 Nm will contribute data points up to the 20 Nm distance scale, but none above. This is illustrated in Figure B-23(a-b), where the number of flights and cloud runs contributing to the data set as a function of distance scale are shown for the different

temperature intervals. At the 17.4 Nm distance scale, some flights and runs have already been excluded, with about 90-100% of flights and 70-80% or runs represented, depending on temperature interval. At 50 Nm, 80-90% of flights and 37-55% of runs are represented. The data set becomes less diverse with increasing distance scale. The variability in the data set points also decreases due to the averaging, as illustrated in the reduction of the TWC maximum and standard deviation with distance scale (Figure B-23(c-d) respectively). These factors all interact in influencing the final standard deviation estimates for the uncertainty of the TWC_{99} values.

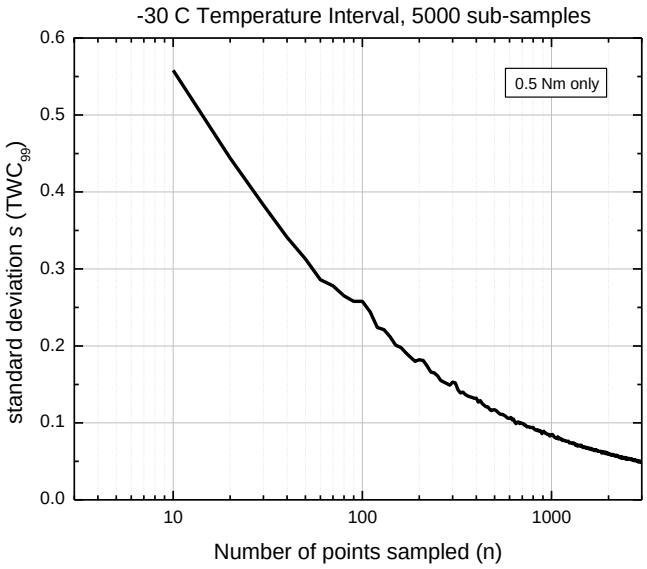

Figure B-22. Standard deviation of TWC_{99} values computed by sub-sampling 59132 0.5 Nm TWC values in the -30 C temperature interval

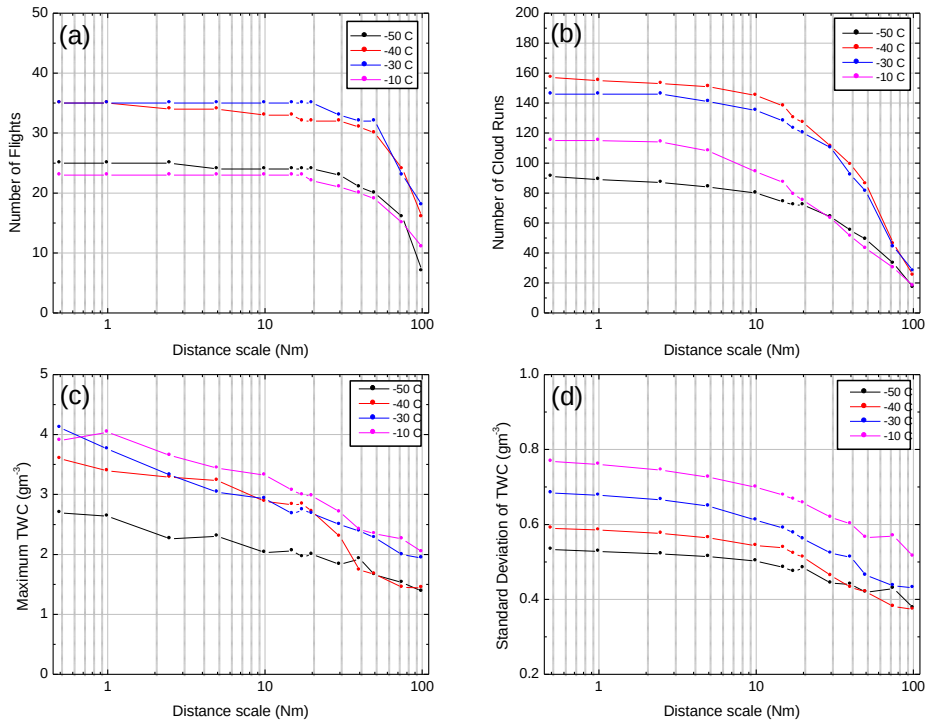

Figure B-23. Change in composition of data set with increasing distance scale

Figure B-24 displays the standard deviations of the 1.0-100 Nm distance scale TWC_{99} values (symbols) for the -30 C interval, sampled 5000 times with all the data points available at the given distance scale, and over-plotted on the 0.5 Nm line. The symbols represent the sampling uncertainty at that distance scale estimated by this repeated random re-sampling procedure. In general, the standard deviations are scattered around the 0.5 Nm line. Figure B-25 through Figure B-27 contain the corresponding data for the -50, -40, and -10 C intervals. A similar behavior is observed from 1.0 Nm to about the 30 Nm distance scale, above which standard deviations tend to be much lower than the 0.5 Nm line. It is believed the behavior at the longer distance scales is due to the factors noted above: the decrease in variation due to averaging and the loss of data runs with increasing distance. For the purposes of this report, uncertainty estimates in Appendix F and Table F-1 through Table F-5 are provided whenever possible, but caution should be used in the interpretation of these uncertainty estimates, particularly for distance scales longer than 30 Nm.

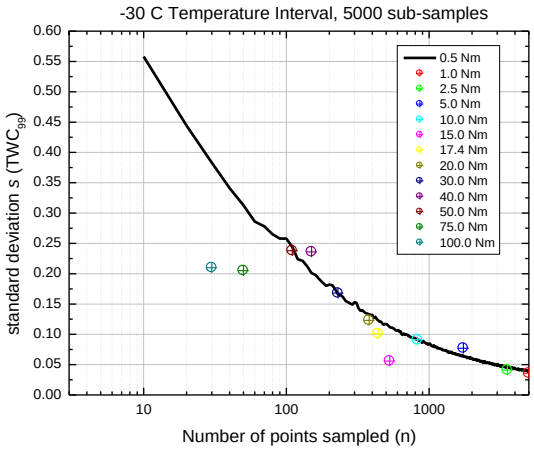

Figure B-24. Adding different distance scales with fewer points per Figure B-22

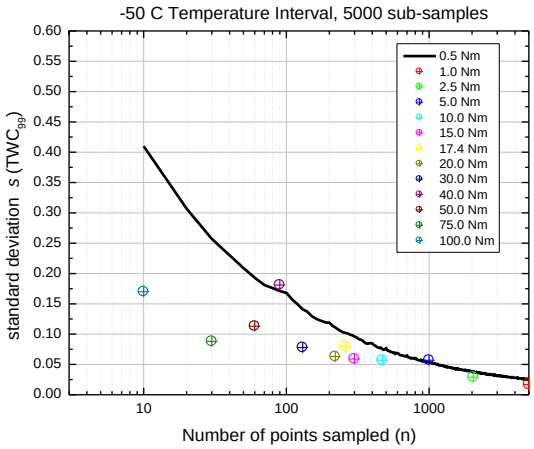

Figure B-25. -50 C temperature interval per Figure B-22

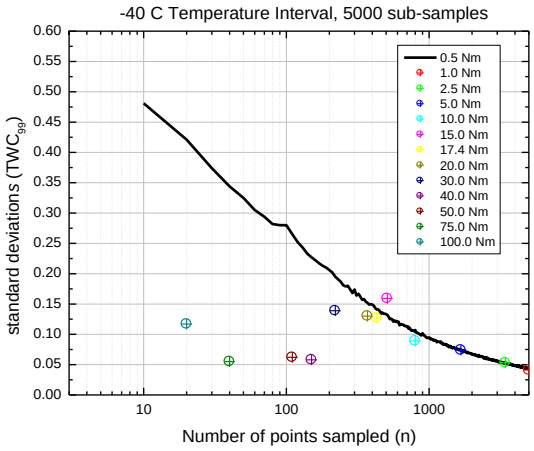

Figure B-26. -40 C temperature interval per Figure B-24

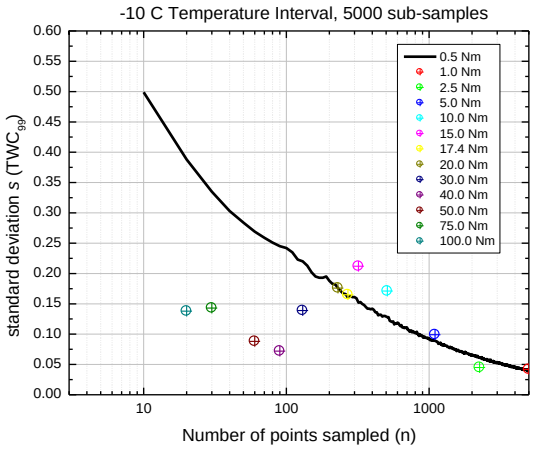

Figure B-27. -10 C temperature interval per Figure B-24

Table B-10 and Table B-11 contain the low-bias ratios and TWC_{99} standard deviations for the composite data sets, at each of the four temperature intervals and thirteen distance scales. TWC_{99} values corrected for low bias are included for illustration[20]. Table B-12 contains the corresponding estimates for all temperature intervals combined. For project documentation, these are shown as uncertainty bars ($\pm 2\sigma$) to the TWC_{99} versus distance plots in Figure B-28(a-d). The solid blue symbols indicate the bias-corrected TWC values. Note that at the short distance intervals (e.g., 0.5 Nm), data points are abundant, uncertainty bars are narrow, and the bias-corrected TWC_{99} is about the same as that calculated directly from the data points (blue dots versus open circles). As the

[20] Final corrected TWC_{99} values, for sampling low bias and the ice saturation BWV assumption, are provided in Appendix F—Supplementary Tables of TWC_{99} Analysis Parameters.

number of data points decreases with increasing distance scale, the bias-corrected values are farther from the straight TWC_{99} calculation, and the uncertainty bars widen.

Table B-10. (see Figure 28(a,b)) Low bias and standard deviation of TWC99 values of flight campaign composite data sets predicted by bootstrap resampling (TWC99 adjusted for bias for the -10 C (left) and -30 C (right) temperature intervals)

	-10 C temperature interval bootstrap results only						-30 C temperature interval bootstrap results only					
Distance Scale (Nm)	# of datapts	Straight TWC_{99}	Avg. TWC_{99} 5000 resamples	Low-Bias ratio	TWC_{99} adjusted for bias	standard deviation of TWC_{99}	# of datapts	Straight TWC_{99}	Avg. TWC_{99} 5000 resamples	Low-Bias ratio	TWC_{99} adjusted for bias	standard deviation of TWC_{99}
0.5	11524	2.913	2.912	1.000	2.912	0.041	17960	2.804	2.806	1.000	2.806	0.039
1	5738	2.885	2.876	1.000	2.876	0.042	8948	2.782	2.781	1.000	2.781	0.036
2.5	2263	2.857	2.858	0.999	2.861	0.044	3540	2.733	2.734	0.998	2.737	0.039
5	1098	2.804	2.791	0.996	2.802	0.098	1742	2.664	2.656	0.994	2.664	0.077
10	517	2.726	2.739	0.991	2.764	0.169	837	2.559	2.562	0.988	2.577	0.090
15	328	2.720	2.678	0.985	2.719	0.209	532	2.434	2.431	0.982	2.458	0.058
17.4	273	2.685	2.634	0.983	2.680	0.166	449	2.371	2.396	0.975	2.430	0.101
20	230	2.685	2.675	0.978	2.735	0.176	381	2.375	2.361	0.973	2.402	0.127
30	139	2.598	2.558	0.969	2.640	0.129	234	2.236	2.187	0.958	2.245	0.165
40	90	2.325	2.315	0.953	2.429	n/a	157	2.304	2.147	0.938	2.232	n/a
50	66	2.308	2.266	0.941	2.408	n/a	118	2.077	1.976	0.922	2.082	n/a
75	34	2.234	2.141	0.896	2.390	n/a	53	1.778	1.707	0.867	1.884	n/a
100	20	2.010	1.924	0.841	2.288	n/a	30	1.796	1.701	0.805	1.989	n/a

Table B-11. (see Figure 28(c,d)) -40 C (left) and -50 C (right) temperature intervals per Table B-10 (Figure 28(a,b))

	-40 C temperature interval bootstrap results only					
Distance Scale (Nm)	# of datapts	Straight TWC_{99}	Avg. TWC_{99} 5000 resamples	Low-Bias ratio	TWC_{99} adjusted for bias	standard deviation of TWC_{99}
0.5	17399	2.465	2.466	1.000	2.466	0.044
1	8651	2.422	2.423	1.000	2.423	0.042
2.5	3425	2.376	2.378	0.999	2.380	0.053
5	1675	2.291	2.289	0.997	2.296	0.074
10	808	2.201	2.183	0.993	2.198	0.088
15	514	2.271	2.232	0.988	2.259	0.151
17.4	435	2.112	2.103	0.984	2.137	0.130
20	370	2.051	2.060	0.983	2.096	0.132
30	221	1.745	1.770	0.969	1.827	0.140
40	154	1.659	1.655	0.957	1.729	n/a
50	111	1.662	1.624	0.942	1.724	n/a
75	48	1.438	1.410	0.894	1.577	n/a
100	25	1.411	1.328	0.823	1.614	n/a

-50 C temperature interval bootstrap results only					
# of datapts	Straight TWC_{99}	Avg. TWC_{99} 5000 resamples	Low-Bias ratio	TWC_{99} adjusted for bias	standard deviation of TWC_{99}
10318	2.106	2.098	1.000	2.098	0.026
5151	2.083	2.082	1.000	2.082	0.017
2042	2.023	2.023	0.999	2.025	0.028
1002	1.995	1.994	0.996	2.002	0.056
478	1.946	1.921	0.99	1.940	0.055
308	1.849	1.841	0.985	1.869	0.059
263	1.809	1.790	0.983	1.821	0.081
224	1.824	1.818	0.979	1.857	0.060
134	1.685	1.688	0.965	1.749	0.078
95	1.689	1.677	0.951	1.763	n/a
68	1.543	1.505	0.938	1.604	n/a
35	1.497	1.448	0.888	1.631	n/a
17	1.351	1.206	0.795	1.517	n/a

Table B-12. All temperature intervals combined per Table B-10 (Figure 28(a,b))

	All temperature intervals bootstrap results only					
Distance Scale (Nm)	# of datapts	Straight TWC_{99}	Avg. TWC_{99} 5000 resamples	Low-Bias ratio	TWC_{99} adjusted for bias	standard deviation of TWC_{99}
0.5	59346	2.700	2.697	1.000	2.697	0.043
1	29553	2.690	2.681	1.000	2.681	0.044
2.5	11689	2.641	2.639	1.000	2.639	0.047
5	5720	2.566	2.564	1.000	2.564	0.042
10	2738	2.482	2.486	1.000	2.486	0.054
15	1742	2.415	2.409	0.999	2.411	0.040
17.4	1469	2.349	2.366	0.998	2.371	0.066
20	1247	2.367	2.365	0.997	2.372	0.075
30	753	2.273	2.268	0.994	2.282	0.117
40	513	2.248	2.230	0.990	2.253	n/a
50	376	2.165	2.151	0.987	2.179	n/a
75	173	2.045	2.019	0.967	2.088	n/a
100	93	1.945	1.891	0.938	2.016	n/a

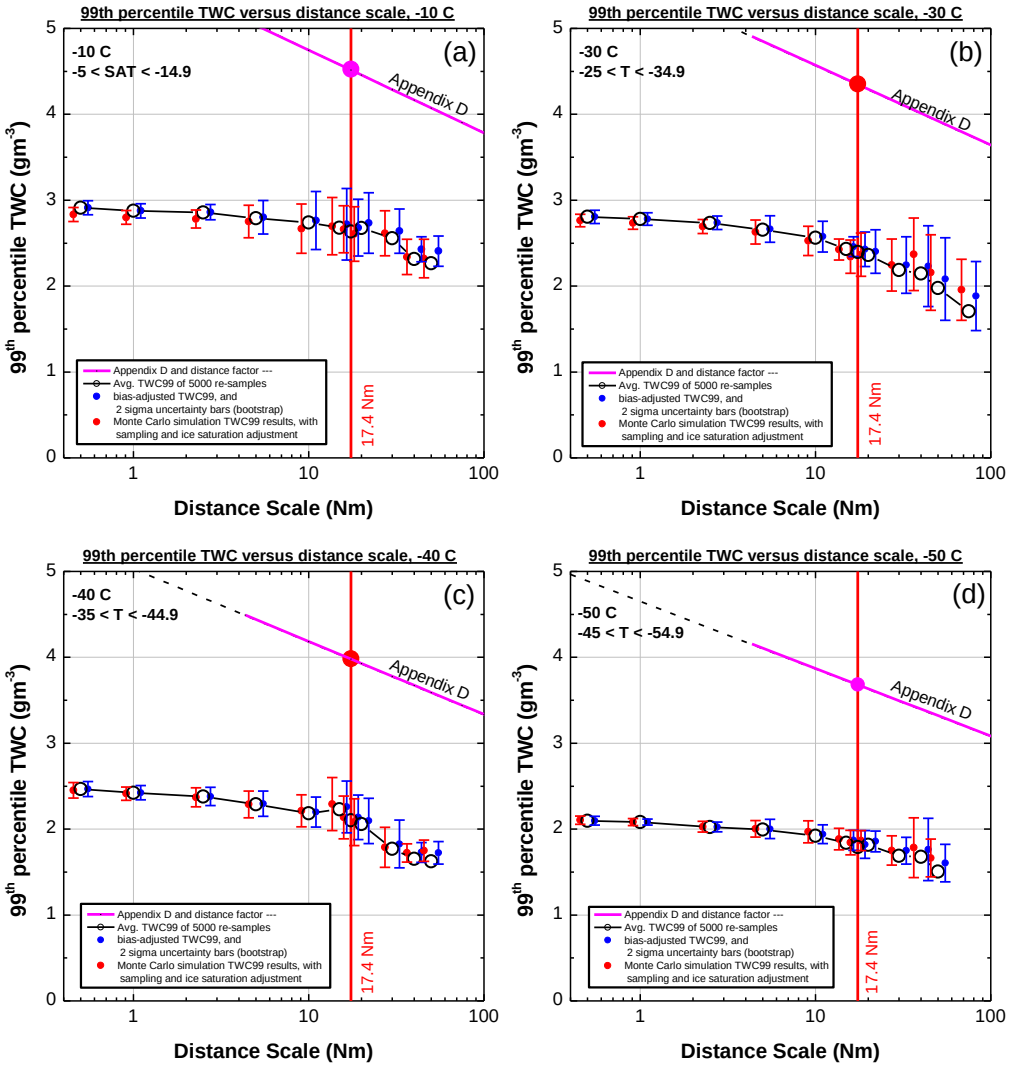

Figure B-28. Uncertainty estimated from random resampling procedure of sections B.5 and B.6. Vertical bars are sampling ±2σ uncertainty from 5000 TWC99 resamples. Red symbols and ±2σ uncertainty are for the Monte Carlo simulations of section B.6

The TWC_{99} values and sampling uncertainties in this report are specific to the Type 1[21] data points (section 3.1), the use of which was agreed upon during discussions with the EHWG. Other point definition options may offer advantages in certain areas. For example, the Boeing Co. has proposed using only a single point per cloud run, the highest TWC at that distance scale, derived from overlapping data points translated at the fundamental 0.5 Nm distance scale. Exploration of other data point definitions is beyond the scope of this report, and will be left for future studies if deemed appropriate. Regardless of the data point definition, the TWC_{99} values are fundamentally dependent of whether the data set properly represents a natural population of clouds. Statistical

[21] The choice of Type 1 data points for the Appendix D/P assessment was deliberate, and at the time interpreted to be consistent with discrete icing cylinder collections used to develop the FAR Part 25 Appendix C envelope. Further discussions are ongoing.

bias and uncertainty estimates can only reflect the random errors of sampling from whatever data set is collected.

B.5.3. COMPARISON TO OUTPUT OF STATISTICAL PACKAGE "R"

The TWC_{99} values and statistical uncertainties presented in this report were calculated with custom user-written software. In order to cross-check these values for accuracy, the TWC_{99} results for the combined four project data sets and the four different temperature intervals at the 17.4 Nm distance scale were also analyzed with the software package "R" [B-12] for comparison. TWC_{99} values were found to be nearly identical, agreeing within 0.05%, The spans of the 95% confidence intervals also were found to be in good agreement as follows (the R results are given first, then the value for this report): -10 C, 0.56 and 0.66; -30 C interval, 0.39 and 0.40; -40 C interval, 0.50 and 0.51; and -50 C interval, 0.26 and 0.32. The reason for the small discrepancies in the confidence interval spans may be due to the estimation of two times the standard deviation of the resampled TWC_{99} estimates in the case of the report values, rather than direct determination from its cumulative frequency distribution that is likely provided by the R software.

B.6 A COMBINED TWC ERROR ESTIMATE FOR THE EFFECTS OF THE ICE SATURATION ASSUMPTION, AND SAMPLING UNCERTAINTY

Sections B.5.2. Standard Deviation (Uncertainty) of TWC_{99} Estimates and B.5.3. Comparison to Output of Statistical Package "R" provide separate uncertainty estimates for the IKP-2 TWC due to the assumption of ice saturation BWV, and sampling statistics, respectively. In this section, a combined correction and uncertainty estimates are obtained using the Monte Carlo simulations described in section B.4.2. These simulations provide a large number of IKP-2 data-point calculations with TWC frequency distributions specified by the actual HAIC-HIWC and HIWC RADAR data subsets, and with BWV error spectra as measured during the 4 reference CV580 flights. Section B.4.2. Monte Carlo Simulations of the IKP-2 Errors due to the Ice Saturation BWV Estimate summarizes the assumptions made in the Monte Carlo simulation. The Monte Carlo simulations were performed for each of the data subsets and distance intervals (312 simulations). The sub-sampling was performed using the same bootstrap procedure described in section B.5, but using the Monte Carlo simulation data sets as input rather than the actual aircraft data.

Figure B-28 has already been discussed in section B.5 in context of corrections and uncertainties provided by simple bootstrap resampling of the composite HAIC-HIWC/HIWC RADAR data set (blue circles and blue $\pm 2\sigma$ uncertainty bars). This figure also contains results of the corresponding re-sampling of the Monte Carlo simulations, shown with red circles and red $\pm 2\sigma$ uncertainty bars. The X-position of the input data (black open circles), the simple bootstrap, and the Monte Carlo simulations are deliberately displaced to enable visual separation. The input data here are very close to the TWC_{99} data computed directly from the data sets. They have simply been re-sampled with replacement 5000 times, and the average TWC_{99} value has been plotted. The first general observation related to the Monte Carlo simulations is that the results are quite similar to the simple bootstrap results. Like the latter, the $\pm 2\sigma$ uncertainty levels of the Monte Carlo simulations are narrow at short distance scales due to the large number of points, and widen to about 0.2-0.3 gm^{-3} at the reference distance of 17.4 Nm. The simple bootstrap results show an increasing TWC_{99} correction for low bias with increasing distance scale, evident in the difference between the small

blue circles and the open black symbols. For the Monte Carlo results, the low-bias is counteracted by the correction for the overestimate of the TWC_{99} due to the ice saturation BWV estimate, which is most noticeable at -10 C due to the higher BWV levels. Note that in Figure B-28(a), the red circles are lower than the open circles at the shorter distance scales, due to the correction for the ice saturation BWV assumption dominating over the negligible sampling low-bias correction. At the higher distance scales, the low-bias correction, working in the opposite direction, overtakes the ice saturation correction, and the red circles are higher than the open black circles.

The magnitude of the ice saturation BWV correction decreases with decreasing temperature. By -50 C (Figure B-28(d)), the red and blue circles are nearly identical, a reflection of its negligible effect. There is almost no correction at all for distance scales less than about 20 Nm, and some modest correct, almost completely due to sampling statistics, at the larger distance scales.

The results of the Monte Carlo simulations are thus consistent with the interaction between ice saturation BWV and sampling statistics corrections, and there is some cancellation of error. The width of the $\pm 2\sigma$ uncertainty bars do not appear to be significantly changed by the assumption of ice saturation BWV. Note that the results of Figure B-28 are for the composite data sets, with their fairly large numbers of data points. Biases and error bars are naturally expected to increase for the smaller data subsets.

For documentation, in Appendix F, Table F-1 through Table F-14 contain the final corrections and uncertainties of the composite data sets and the project subsets in the four temperature intervals, as well as all temperature intervals combined. These correction and uncertainty estimates have been used in the TWC_{99} versus distance plots shown in section 3.

APPENDIX C—PARTICLE SIZE DISTRIBUTION METHOD OF CALCULATION, ACCURACY STATEMENT

The processing of the cloud particle data from the three flight campaigns was performed by the UBP/ Laboratoire De Météorologie Physique (LaMP) for the Falcon-20 and DC-8 data sets, and by Environment And Climate Change Canada (ECCC) for the Convair-580 data set. The details of the algorithms are presented in this appendix. In sections C.1 Particle Sizing through C.6 MM Estimation, the post-processing of 2D images of optical array probe (OAP) probes is reviewed, from the sizing of particles to the computation of Particle Size Distribution (PSDs), mass size distributions (MSDs) and median mass diameters (MMDs). Finally, section C.7 is dedicated to the sensitivity study of MMD with respect to TWC threshold and distance scale chosen for MMD statistics, and a statement on absolute accuracy. More details on the analysis and results of the PSD studies can be found in refs. [C-1,C-2]].

C.1 PARTICLE SIZING

As discussed in section 2.2, the 2D-S and precipitation imaging probe (PIP) probes capture two-dimensional images of particles passing through a laser beam (Figure C-1). Two probes are needed in order to cover the broad range of particle sizes in natural clouds: the 2D-S probe samples particles in the range of 10 to 1280 µm with a 10 µm resolution, whereas the PIP captures images of particles with sizes between 100 µm and 6.4 mm, with a 100 µm resolution. Examples of ice crystal images captured during the HAIC-HIWC field campaigns were previously provided in Figure 16.

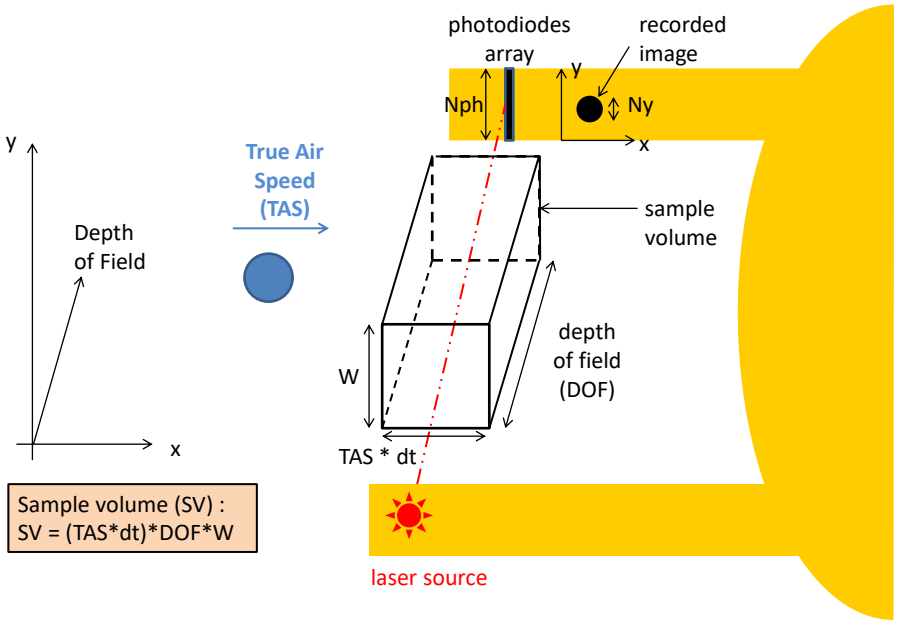

Figure C-1. Schematic of an Optical Array Probe (OAP)

Two simple dimensions can be derived from a rectangular box that fully encloses a particle image [C-3]: the size L_y is the box dimension along the direction of the photodiode array, and L_x is the

box dimension along the direction perpendicular to the photodiode array (along the axis of the forward movement of the aircraft). Knowing the total area of shaded pixels (A), the 2D area equivalent diameter D_{eq} is defined as the diameter of a circle of the same area as the 2D particle image:

$$D_{eq} = \sqrt{\frac{4*A}{\pi}} \tag{C-1}$$

See Figure C-2 for illustrations of these size definitions. Finally, many studies use a "maximum" dimension D_{max} (not shown), but its definition is unfortunately ambiguous. Definitions vary from one study to another, possibly leading to significant differences in the final PSDs (factor of 6 in number concentration for sizes smaller than 200 µm) and in integrated values (factor of 3 for IWCs) [C-4].

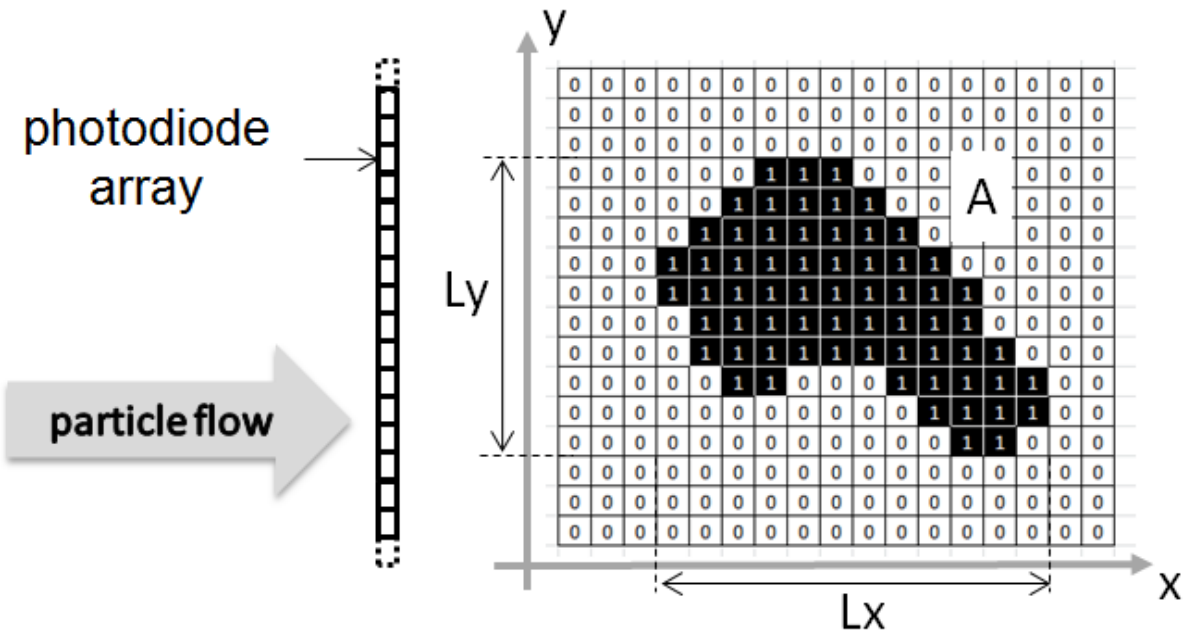

Figure C-2. Various size definitions that can be derived from a particle's image as recorded by the 2D-S or the PIP (adapted from [C-5])

In our processing, L_y was used to compute the sample volume (see section C.3) but particles were then processed into PSDs according to their area equivalent diameter D_{eq}. D_{eq} is preferred to D_{max} in this application for several reasons:

- the D_{eq} definition is unambiguous, which could facilitate comparison with other studies.
- Particle images truncated on either one or both edges of the diode array due to the finite width of the laser were processed according to [C-6] in order to retrieve an estimate of reconstructed full-image sizes. This method uses the simplification of a circular image in order to reconstruct/compute the "true" particle dimension. For truncated ice images, the true maximum size cannot be exactly retrieved, as part of the particle image are missing, and it is very likely that maximum dimensions derived from reconstruction can be

significantly underestimated. This underestimation is on the average smaller when using the D_{eq} definition.

- A comparison of 2D-S and PIP concentrations in the overlapping size range gave a better agreement for D_{eq} than for D_{max}, particularly when the fraction of large truncated particles was high. This supports the previous statement above. Moreover, the PSD overlap between the 2D-S and PIP for the D_{max} size definition was also very good when a smaller fraction of 2D-S images were truncated (i.e., populations of smaller ice particles).

C.2 ARTIFACT REMOVAL

Not all images recorded by OAPs are naturally occurring cloud particles. Some are measurement artifacts that need to be identified and either removed or carefully processed before further analysis.

Splashing and Shattering

It has been known for some time that during sampling a certain fraction of cloud particles inevitably hits the housing of probes forward of the sample volume and may break up into multiple fragments that are recorded by the cloud probe [C-7 through C-9]. This breakup effect is called splashing for droplets and shattering for ice particles. See Figure A-1 for a conceptual illustration of this effect for ice particles. From the fragmented image, there is no reliable way to infer the initial particle size. Thus, all images corresponding to a shattering or a splashing event must be removed; otherwise, measurements of PSDs and subsequently derived microphysical properties would be incorrect. Figure C-3 shows an example of an image showing a shattering event. This event shows fragments of an initially large particle that broke up during sampling.

Figure C-3. Example of shattering event (largest image near center of frame) as recorded by the 2D-S probe

When such a fragmentation event occurs, the probe usually records either a sequence of images with atypically short inter-arrival times, a large image frame with multiple disconnected images, or a combination of both. Most of the images related to a fragmentation event can be removed by a careful analysis of the ratio between the particle's shaded pixel area and the product of it sizes in the x and y directions ($L_x * L_y$, as defined in Figure C-2), and analysis of the inter-arrival times [C-10 through C-13]. Both techniques were used in the processing of all 2D image data sets for this report.

Out of focus particles

The object plane of an OAP imaging system is designed to be near the midpoint between the probe's arms. The probe's electronic system is set such that particles are sampled not only when they cross the beam at the object plane, but also some finite distance away from it, where the probe generates an out-of-focus image. Examples of typical out-of-focus images are shown in Figure C-4. The maximum length along the laser beam where the out-of-focus images of a particle with size D is still registered by the probe is referred to as a depth-of-field. The out-of-focus problem mostly affects the 2D-S probe.

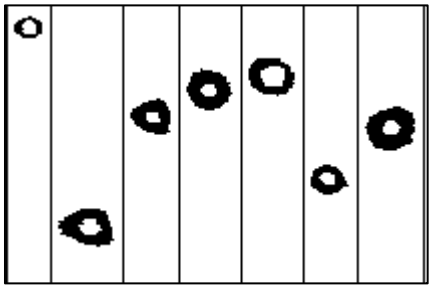

Figure C-4. Examples of out-of-focus images recorded by the 2D-S probe

Using the Fresnel diffraction approximation, the response of spherical particles recorded on an OAP has been theoretically modelled [C-14]. These results show that out of focus spherical particles have a donut-like appearance with a central Poisson spot void of shadowed pixels, and where the outside diameter of the donut exceeds the real particle size. For this study, the lookup tables of [C-14] were used to retrieve the predicted correct particle sizes for measured area ratios of the Poisson spot over the apparent out-of-focus particle size, assuming spherical particles.

Noisy pixels and two particle images

Optical contamination or malfunctioning of the probe's electronics may cause triggering of a single or a group of the same image pixels. This results in the generation of artificial images, which are usually referred to as "noise." Examples of noisy pixels are shown in Figure C-5 (left frame). Even though noisy pixels were uncommon in the HAIC-HIWC data set, such pixels for the 2D-S and PIP were eliminated by a software algorithm.

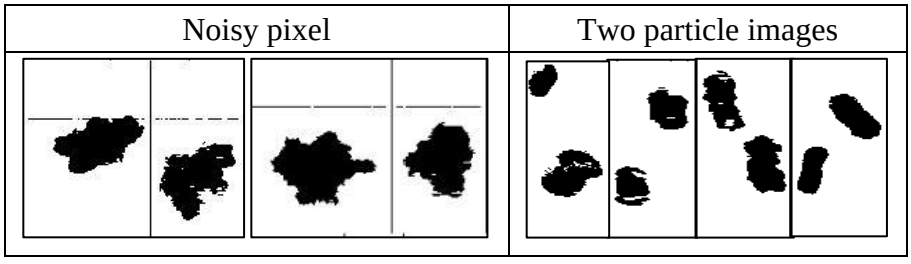

Figure C-5. Example of 2D-S image with a noisy pixel (left) or with two particles on the same image (right)

Due to the typical high concentration of ice particles associated with the high IWC environment, the HAIC-HIWC data set was affected more than in past experience by the double-image or multiple-image problem, i.e., when two or more particles are recorded within the same image frame (Figure C-5, right frame). Such images were identified and only the largest particle was kept for further analysis.

C.3 PROBE SAMPLE VOLUME

PSD computation requires both the individual raw bin counts and the sample volume (SV) of the probe, which is the product of the sample area (SA), the true airspeed (TAS), and the sample time (Δt) [C-15]:

$$SV = SA * TAS * \Delta t \tag{C-2}$$

Sample time excludes "dead time," otherwise known as overload time, i.e., the time when the probe is unable to record images while unloading particle image data. While the technical details of probe dead time vary somewhat according to the probe and data system, in an environment with high concentrations of particles, many probes are subject to this dead-time condition. The sample time is measured directly by the 2D-S. For the PIP, the probe continues to count the number of all particles passing through the beam even during the dead time. Thus, for this probe, an estimate of the image sample time is obtained by comparing the number of recorded images to the total number of counted particles.

In order to compute the SA, the depth of field (DOF) and the effective beam width W are needed (Figure C-1), which are both size-dependent [C-16]:

$$SA = DOF * W \tag{C-3}$$

The DOF was taken directly from that recommended in the manufacturers' technical manuals (SPEC, 2001 and Droplet Measurement Technologies, 2009). Since both complete and partial images were included, the width was defined as:

$$W=(N_{PH}+L_y-1)*\Delta x \tag{C-4}$$

where N_{PH} is the number of photodiodes across the array, Δx the probe's pixel size resolution and L_y is defined as in Figure C-2.

C.4 MERGING OF 2D-S AND PIP PSDS

The 2D-S and PIP PSDs were merged to produce one single composite size distribution ranging from 10 µm up to more than 1 cm [C-17]. The 2D-S was used in the composite distribution for sizes smaller than 800 µm. Likewise, the PIP was used for sizes larger than 1200 µm. Between 800 and 1200 µm, the composite distribution is a linear weighted mean of the two distinct distributions:

$$\boldsymbol{N(D) = (1-\omega)\, N_{2D-S}(D) + \omega\, N_{PIP}(D)} \text{ for } D\in[800;\ 1200] \tag{C-5}$$

where

$$\omega = \frac{D(\mu m) - 800}{1200 - 800}$$

In order to increase the probe sample volume and improve the statistics for the largest particles, the composite PSDs were produced at a 5s time resolution. For user convenience, a final composite size distribution with a uniform 10 µm size resolution was produced, using linear interpolation within the PIP size bins.

C.5 VALIDATION OF POST-PROCESSING

The post-processing software from UBP/LaMP was compared with those from ECCC and University of Illinois, based on data collected during flight 23 from Darwin-14 campaign.

Figure C-6 presents mean composite PSDs for two different periods of the flight. On the left, PSDs are from a stratiform part of the sampled cloud system, whereas the PSD on the right are from a convective part of the cloud with much higher concentrations of small particles. UBP/LaMP results (red) agree well with results from ECCC (blue) and University of Illinois (green).

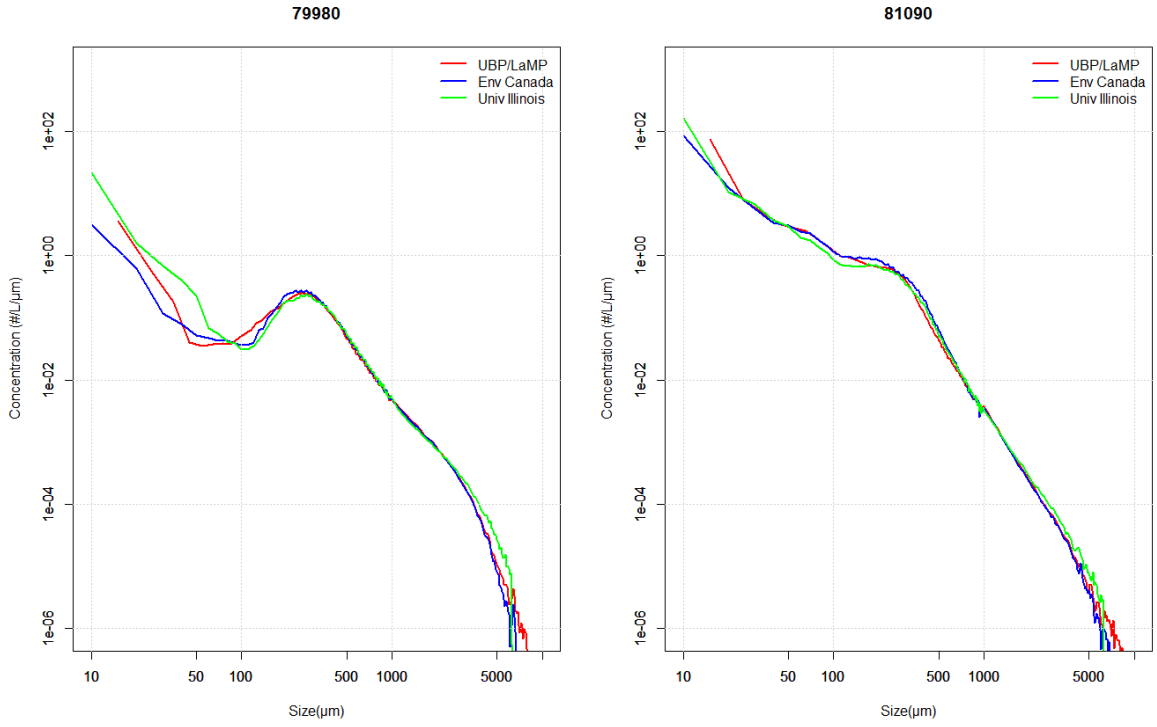

Figure C-6. Mean composite PSDs for different periods of flight 23 of Darwin-14 campaign for the three groups participating in the algorithm intercomparison study

C.6 MM ESTIMATION

In order to convert PSDs into mass size distributions, mass-size relationships are commonly applied and are usually represented as a power law relationship of the form $m = \alpha D^{\beta}$. Then, the

MMDs are deduced from the mass distributions. The MMD **is the size** at which 50% of the ice mass is contained in smaller particles, and 50% in larger particles:

$$\int_0^{MMD} \alpha D^{\beta} N(D) dD = \frac{1}{2} \int_0^{\infty} \alpha D^{\beta} N(D) dD \quad \text{(C-6)}$$

Power-law, mass-size relationships are common in the literature [C-17, C-18 through C-23] and have often been established for different crystal types (or shapes) present in the atmosphere, although, in practice, single values of α and β are most commonly used for all ice crystal data of an entire flight, regardless of any changes in crystal type.

The sensitivity of the MMD to the chosen mass-size relationship has been studied [C-5], and MMDs have been demonstrated to be quite sensitive to the value of the β parameter. Therefore, the value of the β exponent should be determined with caution. For this reason, a method has been developed to deduce β from the projected area-size A(D) and the perimeter–size P(D) relationships that can be directly deduced from OAP image populations [C-55].

Three-dimensional ice crystals models of various shapes and their projections on a 2D plane were used to produce 2D binary images in a manner similar to that of OAP probes [C-17]. These simulated images were used by these authors to study the relationships between their 3D volume and various 2D parameters (area, perimeter, size, etc.). From these simulations, a relationship between the exponent β in the m(D) relationship and the exponent σ of the area-size relationship $A(D) = \gamma D^{\sigma}$ (where A is the 2D area of the binary particle image) was established, one that can be extracted from simulated (as well as "real") 2D binary images [C17].

For the former study, the maximum dimension D_{max} was computed from the binary OAP images. Because of the use of D_{eq} in this study, the m(D) retrieval method was modified and extended, making it more general and applicable to other size definitions [C-5]. To do so, the dependency of β on particle shape was strengthened by studying both the surface-size A(D) and the perimeter-size P(D) relationships($P = \delta D^{\tau}$, [C-24]). This enabled the extension of the method to the area equivalent diameter D_{eq} where by definition σ=2 for all particle images while β varies.

Once β was determined, α was derived by matching the IKP-2 TWC (the TWC reference measurement during flight tests campaigns) with the TWC integrated from the PSD using the mass-size relationship:

$$\mathbf{TWC(IKP)} = \sum_{\mathbf{i}} \mathbf{N(i)} \boldsymbol{\alpha} \mathbf{D_{eq}(i)}^{\boldsymbol{\beta}} \quad \text{(C-7)}$$

As a consequence, α and β are no longer unique and constant values to be applied for an entire data set, but vary dynamically with time (e.g., along the flight trajectory, from one flight to another, etc.), according to variations in the OAP ice crystals shapes.

Figure C-7 gives a summary of the MMD computation process from the probe images used for this report.

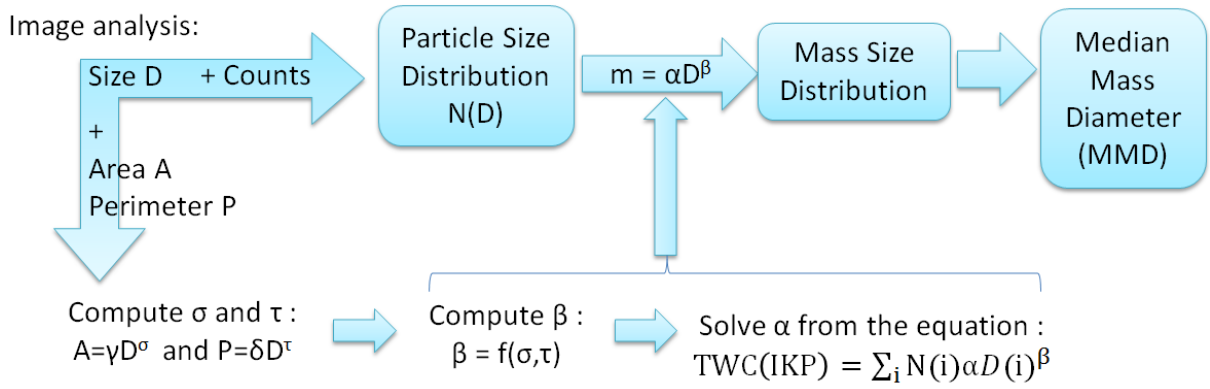

Figure C-7. Summary of main steps to compute the median mass diameters (MMDs) from the particle images and the TWC from the IKP-2

C.7 SENSITIVITY AND ACCURACY ESTIMATES OF MMD AND CUMULATIVE FREQUENCY DISTRIBUTIONS

Table C-1 and Table C-2 present the results of a study of MMD sensitivity to chosen TWC thresholds and distance scales, for the Falcon-20, DC-8, and Convair-580 data sets. TWC thresholds of 0.7, 1.0 and 1.5 gm^{-3} and distance scales of 0.5, 17.4 and 30 Nm were considered. The top value in the table cells gives the MMD for the column's specified distance scale, TWC threshold, and temperature. The middle value gives its percent difference from the reference MMD (at a threshold of 1 gm^{-3} and 0.5 Nm distance scale, at the specified temperature). The bottom value gives the number of data points available for the computation of the statistics.

The majority of the sensitivity tests show MMD percent differences from the reference TWC threshold and distance scale of less than 5%, and more than 95% of the tests show relative differences below 10%. There are only three tests with differences slightly larger than 10%; these all have a relatively small number of data points. Therefore, the values presented in the main body of this report, for a TWC threshold of 1 gm^{-3} continuously detected over 0.5 Nm, are considered to be adequately representative of high IWC cloud regions at higher thresholds and distance scales. They are based on a larger number of data points, and are thus the most statistically representative.

Table C-1. Results of sensitivity tests of MMD to TWC threshold, distance scale, and temperature. Reference case = red values for Falcon-20 (F-20) data set. Top value in cell = MMD, middle value = % difference from reference conditions, bottom value = # of data points. MMD % difference: green < 5%, light green 5 - 10%, light orange > 10%

F-20 data set		Temperature (°C)			
Distance scale (Nm)	TWC Threshold (gm^{-3})	-50	-40	-30	-10
0.5	0.7	325 µm 2.8% 544	411 µm 2.6% 5006	485 µm 2.0% 3662	770 µm 3.1% 1376
	1.0	316 µm - 378	401µm - 3227	476µm - 2472	747µm - 2252
	1.5	303 µm -4.2 % 181	393 µm -1.8% 1473	466 µm -2.0% 1412	694 µm -7.0% 1376
17.4	0.7	334 µm 5.6% 13	418 µm 4.2% 85	486 µm 2.2% 55	796 µm 6.6% 55
	1.0	324 µm 2.3% 8	406 µm 1.4% 46	467 µm -1.8% 34	783 µm 4.9% 37
	1.5	319 µm 0.7% 3	391 µm -2.4% 13	442 µm -7.0% 12	694 µm -7.8% 19
30	0.7	337 µm 6.5% 8	426 µm 6.2% 39	485 µm 2.0% 25	818 µm 9.5% 27
	1.0	333 µm 5.4% 4	396 µm -1.2% 18	472 µm -0.8% 9	803 µm 7.5% 17
	1.5	334 µm 5.6% 1	373 µm -6.9% 4	541 µm 13.9% 2	733 µm -1.8% 7

Table C-2. DC-8 and Convair-580 data sets per Table C-1

		DC-8			Convair-580
		Temperature (°C)			
Distance scale (Nm)	TWC Threshold (gm^{-3})	-50	-40	-30	-10
0.5	0.7	344 µm -4.4% 1793	407 µm 6.9% 1473	522 µm 5.7% 2831	667 µm 5.8% 1677
	1.0	329 µm - 1169	381 µm - 971	493 µm - 1857	630µm - 1125
	1.5	319 µm -3.0% 446	346 µm -9.3% 299	448 µm -9.1% 998	581 µm -7.8% 648
17.4	0.7	337 µm 2.3% 45	402 µm 5.5% 40	507µm 2.7% 49	667 µm 5.9% 63
	1.0	324 µm -1.5% 27	373 µm -2.3% 22	480 µm -2.8% 29	620 µm -1.7% 37
	1.5	304 µm -7.8% 7	346 µm -9.2% 4	443 µm -10.3% 15	568 µm -9.9% 21
30	0.7	335 µm 1.9% 24	404 µm 6.0% 19	500 µm 1.3% 24	644 µm 2.2% 32
	1.0	324 µm -1.6% 14	366 µm -4.1% 10	486 µm -1.4% 13	618 µm -1.9% 20
	1.5	311 µm -5.5% 1	348 µm -8.6% 3	439 µm -11.1% 9	605 µm -4.0 9

It should be recalled here that there is no direct method to measure PSD MMD, which is dependent on the variation of particle density with size. There is only indirect information on this variation in the two-dimensional imagery provided by the probes. MMDs are instead estimated with the rather complex processing summarized above, that includes application of a modified mass-diameter relationship to deduce the mass-size distribution. Such relationships are in general difficult to relate back to any absolute mass measurements relevant to aircraft data that may have quite variable particle characteristics. There also are no MMD reference standards such as are available for liquid water content in calibrated wind tunnels that could provide adequate algorithm comparisons. It is therefore very difficult, as it would be for any other researcher in the atmospheric science community involved in such studies, to provide a rigorous absolute MMD accuracy

estimate for this report. Accuracy is instead usually inferred from comparisons to other similar methods, or from comparisons of independent bulk estimates to integrated PSD estimates, for example the IKP-2 IWC to the PSD IWC. In general, such comparisons do tend to correlate well with only moderate scale factor differences, providing qualitative support for the MMD estimates. In the end, it can be stated that the algorithms described above represent a state-of-the-art in PSD analysis. The estimates are not expected to have large errors in absolute terms, and the MMD estimates are likely as accurate as could possibly be provided by the community at this time. Moreover, using the same methods and definitions described in this appendix, it should be possible for others to estimate MMD to a high level of relative accuracy.

APPENDIX D—ESTIMATION OF MIXED-PHASE PROPERTIES

The estimation of the properties of mixed-phase regions of clouds encountered during the flight campaigns is examined in this appendix. A comprehensive review of the current status of knowledge of the mixed phase in clouds is provided in [D-1]. As discussed in section 3.4, the determination of mixed-phase is a difficult problem due to the high levels of IWC observed in the flight campaign data sets, and the contaminating effect of ice crystals on the instruments that normally measure cloud LWC. The use of multiple instruments to deduce the components of LWC and IWC in mixed-phase clouds has been discussed in references [D-2, D-1], but mostly in stratus, stratocumulus, and clouds associated with mid-latitude, synoptic-scale weather systems. The problem is more challenging for the data sets of this report due to a higher level of IWC. The analyses will be presented here first for the Cayenne-15 Convair-580 data set, then for the Darwin-14 and Cayenne-15 Falcon-20 data sets, and finally, for the Florida-15 DC-8 data set.

D.1 CAYENNE-15 CONVAIR-580 MIXED-PHASE ANALYSIS

The mixed phase analysis for the Cayenne-15 Convair-580 data set reported below was provided by Environment And Climate Change Canada (ECCC). The Convair-580 carried the largest suite of cloud in-situ microphysical probes, and collected the most comprehensive set of data from which to make conclusions about the occurrence and properties of mixed-phase. Nevertheless, such analysis is not straightforward and requires a high level of understanding of the idiosyncratic and sometimes peculiar response of the various instruments. In conventional clouds dominated by liquid in small droplets, hot-wires provide an accurate estimate of the LWC. However, it has been previously noted that LWC hot-wires also react to ice crystals, adding a false response of the order of 10% of the IWC to the LWC measurement, and one that has dependencies that have not been fully characterized (Appendix A). In the HAIC-HIWC and NASA/FAA HIWC-RADAR flight campaigns, where the IWC can exceed 3 gm^{-3}, the uncertainty in removing this false component poses a significant problem. The Convair-580 data were examined in this regard. The Nevzorov LWC sensor was found to have a false response in glaciated conditions that varied between about 7 and 11%. For example, in 3 gm^{-3} of IWC, this corresponds to a false response of the LWC sensor between 0.21 and 0.33 gm^{-3}. Given that LWC levels during the flight campaigns were rarely higher than a few tenths of a gm^{-3}, it was concluded the variability of this fraction would lead to insufficient accuracy in LWC identification and quantification in high IWC mixed-phase conditions.

There were two scattering probes on the Convair-580 that measured the cloud droplet spectra: the Droplet Measurement Technologies (DMT) CDP-2 (2-50 μm) and the PMS Forward Scattering Spectrometer Probe (FSSP) (2-47 μm). If these instruments are well calibrated, they can provide relatively accurate estimates of LWC in conventional small droplet clouds.

Figure D-1 shows measurements from the Convair-580 CDP-2 and FSSP probes in a small-droplet liquid cloud on 16 May 2015: ConcCorF96 = FSSP total number concentration, ConcCorCDP = CDP-2 total number concentration, ExtF96 = extinction calculation from FSSP, ExtCDP = extinction calculation from CDP-2, NvzLWCp-1= LWC from Nevzorov LWC sensor#1, NvzLWCp-2= LWC from Nevzorov LWC sensor#2, LWCF96= FSSP spectrum LWC calculation, LWCCDP= CDP-2 spectrum LWC calculation, icefq= ice detector frequency.

Figure D-1 shows: (a) a time history of total droplet concentration from the two probes; (b) extinction estimates from the two probes compared to an ECCC bulk extinction probe; (c) LWC comparisons for the 2 probes and the Nevzorov LWC and TWC hot-wire probes; and (d) the response of the Rosemount ice detector[22]. The main conclusion from this plot is that the CDP-2 and FSSP probes provided quite comparable LWC estimates to the hot-wires in small droplet clouds. However, it also was found that the FSSP and CDP-2 reacted differently in ice clouds. The CDP-2 was found to measure concentrations that increased with increasing size up to its upper size limit, and this was not observed on the FSSP. In the overlap region with the 2D-S probe, this CDP-2 "tail" was greatly in excess of the 2D-S and the mass continually increased with size, whereas the 2D-S concentrations were decreasing with size as expected. The spurious tail on the CDP-2 in ice clouds is suspected to be caused by shattering of ice crystals (Appendix A, section A.2) on the leading edge of the tips and subsequent measurement of the debris. Although both the CDP-2 and the FSSP were equipped with special anti-shattering tips, only the FSSP appeared to be effective in high IWC conditions. In fact, upon inspection of glaciated high IWC conditions up to 4 gm^{-3}, where insignificant mass of ice crystals smaller than 50 µm would be expected, the FSSP was found to measure a maximum-inferred LWC of only 0.002 gm^{-3} where the CDP-2 measured up to 0.08 gm^{-3} (both likely due to ice crystal debris). It was, therefore, concluded that the FSSP could provide the most sensitive estimate of LWC in mixed-phase clouds, and one adequate for the purposes of this report.

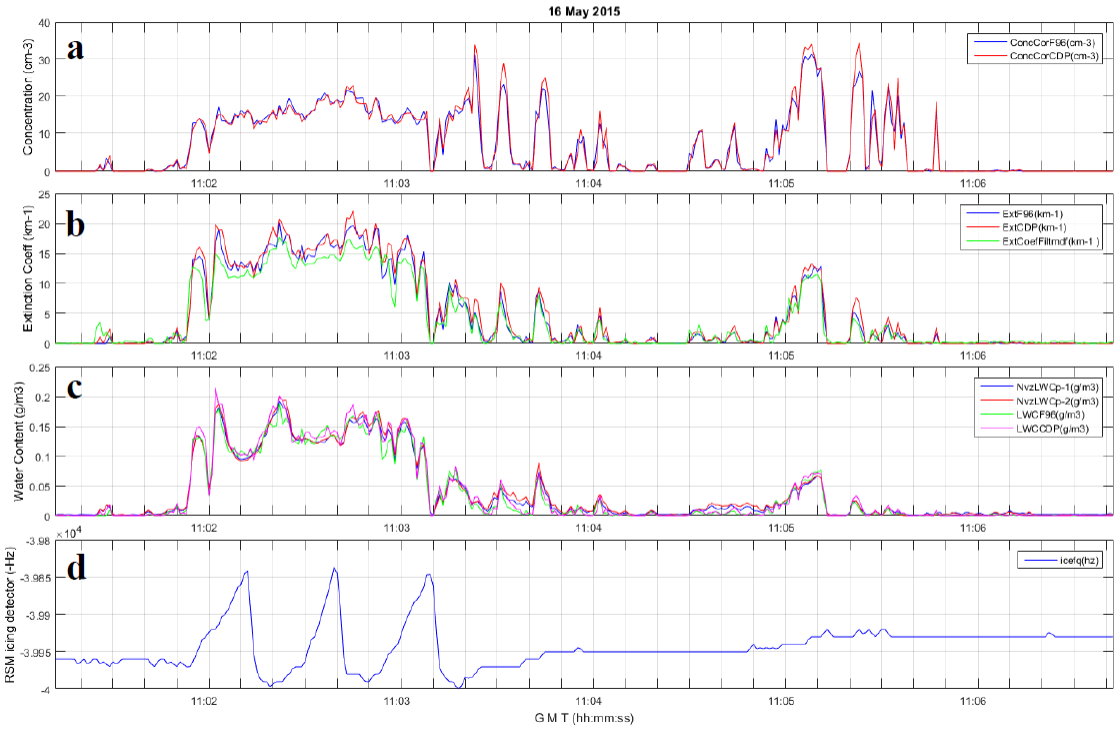

[22] Note the scale for the icing detector is reverse to the plots later provided for the Falcon-20.

Figure D-1. Measurements from the Convair-580 CDP-2 and FSSP probes in a small-droplet liquid cloud on 16 May 2015

Figure D-2 shows a sample time history of the identification of mixed-phase periods for Convair-580 flight 16 on 25 May 2015. These data are all within the -10 ±5 C Appendix D/P temperature interval. Panel (a) shows the TWC estimates "TWC2D" from mass-size distributions (MSDs) derived from the 2D-S and Precipitation Imaging Probe particle probes[23], and the LWC derived from the FSSP probe. Panel (b) shows the estimated LWC fraction (FSSP LWC/TWC2D). Panel (c) shows the inverted response of the Rosemount ice detector, and panel (d) shows the SAT. The mixed-phase periods are identified by the ice detector up deflections (ramp-like excursions from the baseline value) on the plot, and the non-zero FSSP LWC values. Note that the mixed-phase periods are short in duration, fairly infrequent, and low in LWC. In general, mixed-phase periods were identified by this combination of ice detector deflection and significant FSSP LWC values. In one exception on 14 May, instead of conventional small droplet liquid cloud, the liquid was contained only in large drizzle drops that were not in the size range of the FSSP. The ice detector displayed a deflection, but the FSSP LWC was not significant, and it was necessary to estimate LWC from the Nevzorov probe instead.

[23] The PSDs in this figure are derived using the "Ly" size dimension, and mass distributions are derived using the mass-diameter relationship $m(D)=\alpha D^{\beta}$, where $\alpha= 7.0044 \times 10^{-12}$, $\beta=2.3$, M(D) in g, and D in μm.

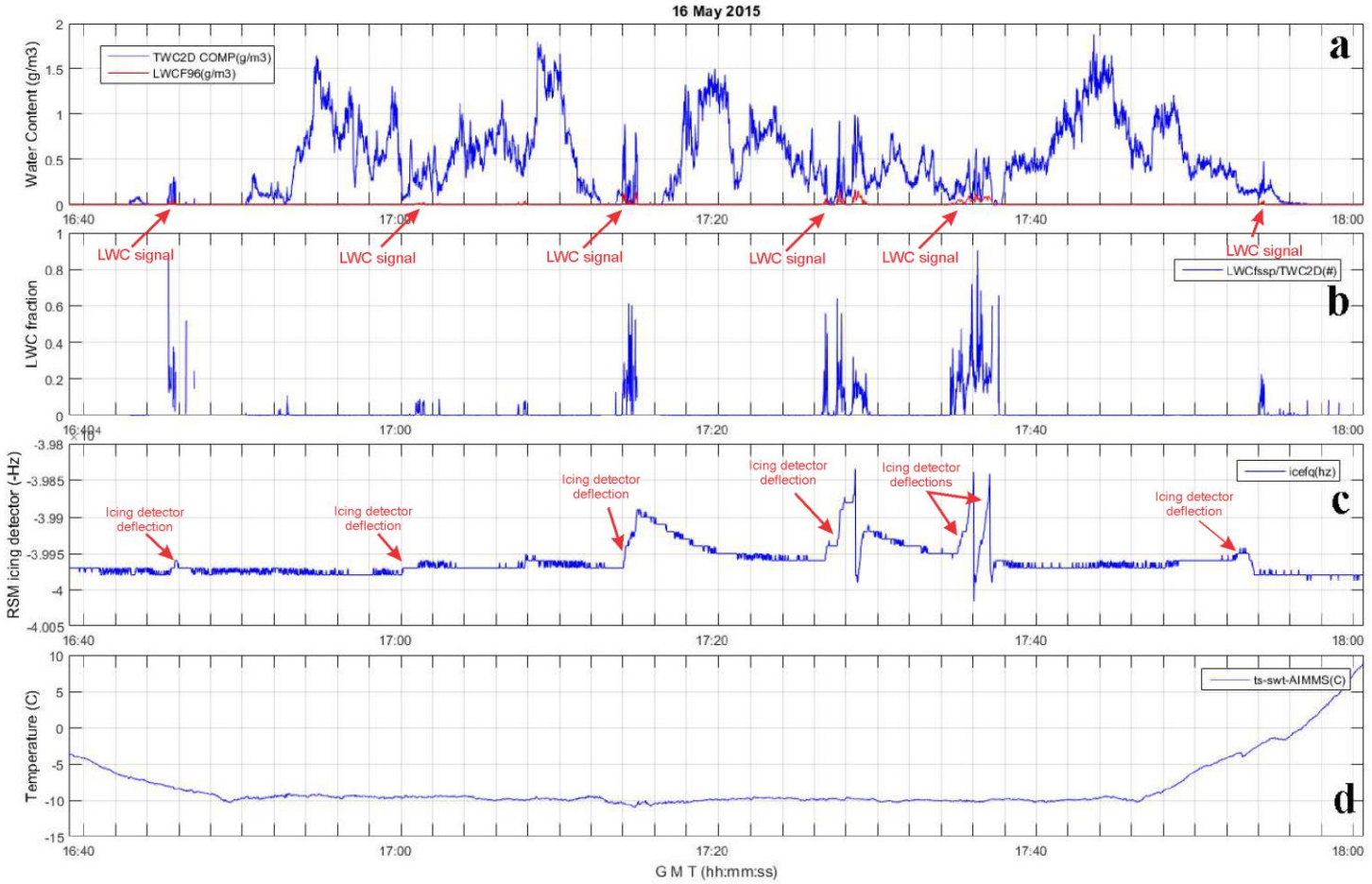

Figure D-2. Mixed-phase periods for section of flight on 16 May 2015. TWC2D= TWC estimated from PSD (see text), LWCF96= FSSP spectrum LWC calculation, LWCFSSP/TWC2D= estimated LWC fraction = LWC96/TWC2D, icefq= ice detector frequency, ts_swt_AIMMS = SAT from AIMMS-20 system

All flights from 15–27 May 2015 were analyzed as in Figure D-2, and the following results were obtained. Mixed-phase periods were found in relatively narrow regions usually less than a few nautical miles wide. LWC estimated from the FSSP was usually lower than 0.1 gm^{-3} and never exceeded 0.25 gm^{-3}. The liquid fraction was usually less than 20% of the TWC. The spatial fraction of mixed-phase periods with LWC greater than 0.1 gm^{-3} was estimated at approximately 5%.

D.2 DARWIN-14 AND CAYENNE-15 FALCON-20 MIXED-PHASE ANALYSIS

A smaller number of instruments were available on the Falcon-20 than the Convair-580, and the mixed-phase analysis is somewhat more speculative. Like the Convair-580, during the Darwin-14 campaign the Falcon-20 collected data from a hot-wire LWC probe, in this case a SEA probe that is routinely used to measure LWC in conventional small-droplet clouds. Unfortunately, the probe was mounted on the belly of the aircraft close to the fuselage, in what has been concluded to be an area with IWC enhanced by about a factor of 2 by ice crystal impact debris streaming down from the nose of the aircraft. The false response on the probe in glaciated conditions was found to be about 10% of the free-stream IWC, and correction for the effect is exacerbated by the unknown characteristics of the nose debris. Furthermore, a variety of sensor diameters and geometries were used, complicating the derivation of any general corrections. As in the case of the Convair-580, it was concluded that the uncertainty in the ice crystal false response results in unacceptable errors in hot-wire-derived LWC. As noted above, the Convair-580 analysis instead made use of FSSP LWC readings to quantify LWC sections in mixed-phase clouds. The Cloud Droplet Probe on the Falcon-20 was a DMT CDP-2 probe, with a similar operating principle to the FSSP. The CDP-2 probe on the Convair-580 displayed a larger response in the glaciated clouds than the FSSP (section D.1) probably due to shattering debris from ice crystal impacts on the probe tips. On the Falcon-20, the CDP-2 also often displayed high number and mass concentrations in high IWC clouds. An example is shown in Figure D-3, where the CDP-2 concentrations rise to nearly 20 cm^{-3} and 0.23 gm^{-3} in the vicinity of glaciated cloud where the IKP-2 TWC peaks at approximately 4 gm^{-3}. Data are from the Falcon-20, flight 13, 15 May 2015. The PSD for the period between the green vertical bars is shown in Figure D-4. Figure D-4 shows the average MSDs for the 2DS+PIP probes (red line), and the CDP-2 (black line) for a 20-second period bracketing this region, between the green vertical bars in Figure D-3. Panels as follows: (a) SAT; (b) CDP-2 total number concentration; (c) IKP-2 TWC and CDP-2-calculated LWC; and (d) Goodrich Ice Detector vibration frequency. The CDP-2 shows the same tendency noted in the ECCC analysis, with mass continually rising up to its maximum size bin, and poor overlap in this region with the 2D-S size distribution. The observations strongly suggest that elevated CDP-2 concentrations could be caused by shattering debris rather than a genuine response to a liquid cloud, and the probe therefore cannot be used by itself to identify liquid section of mixed-phase cloud in high IWC situations.

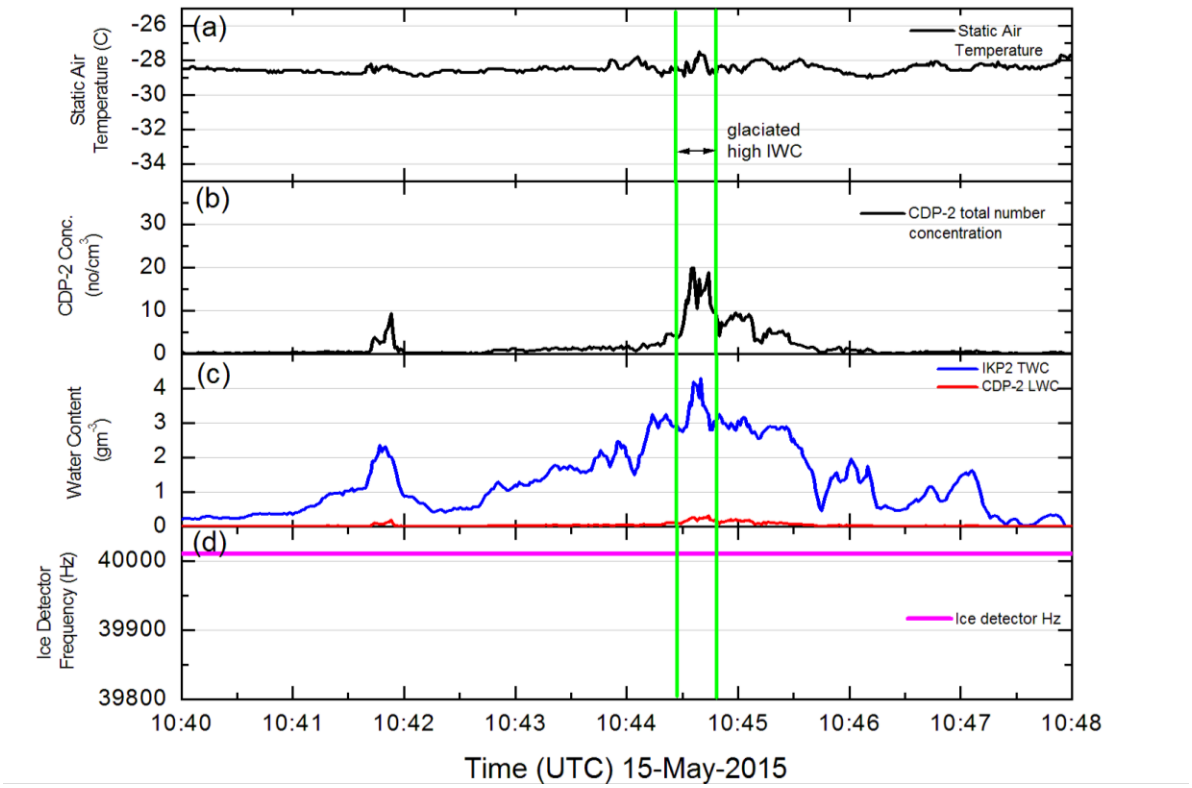

Figure D-3. Period of high IWC glaciated cloud during Cayenne-15 flight program

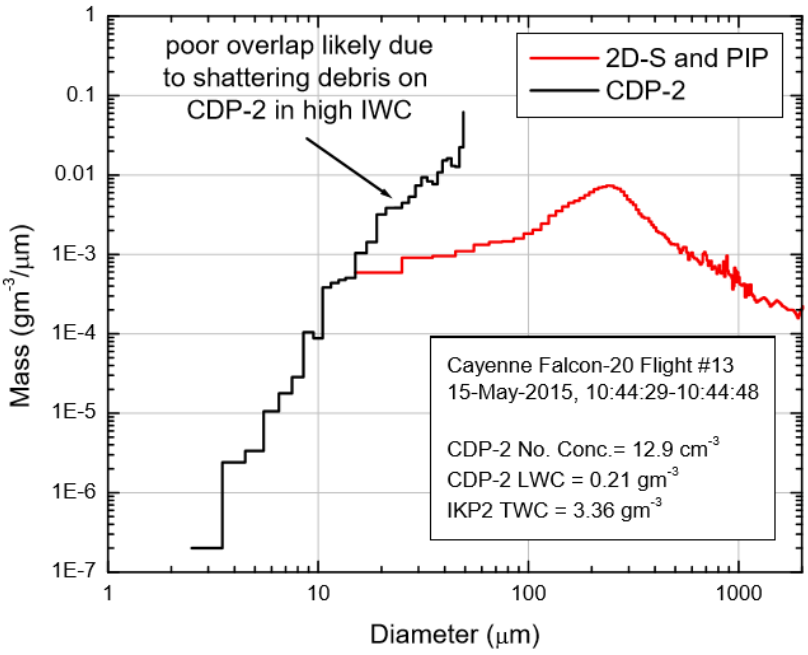

Figure D-4. Illustration of probable ice crystal shattering debris on the CDP-2 measurements in a glaciated section of high IWC cloud

Periods of mixed-phase were then estimated as follows. Time histories were visually examined and periods with ice detector deflections were identified. In addition, periods in which the CDP-2 total number concentration exceeded 10 cm^{-3} (hereinafter $CDPconc_{>10}$) were also identified, and if the spectra showed minimal indication of contamination by ice crystals, these periods also were identified. This was a manual procedure performed by UBP/Laboratoire De Météorologie Physique. The resulting list of time periods is dominated by ice detector deflection events. Periods of $CDPconc_{>10}$ were not uncommon in high IWC clouds, most being filtered out by examination of the CDP-2 and 2D-S spectrum overlap. Because of the potential for contamination of the CDP-2 LWC calculation in the mixed-phase cloud, the LWC estimates used in the following mixed-phase analysis were derived from the rate of change of the ice detector frequency, the method of which is described in the next paragraph. The use of the ice detector for estimating LWC is usually not recommended, particularly when other conventional instruments provide more accurate estimates. However, due to instrument shortcomings in conventional instruments that are amplified in high IWC situations as noted above, it was decided for this report that the ice detector would provide less ambiguous results. Furthermore, its estimates were usually within a factor of 2 of the CDP-2 LWC, the only practical alternative. A linear regression of the event-average ice detector-derived LWC as a function of the CDP-2 LWC yielded a slope of 0.82, an offset of 0.048, and a correlation coefficient of 0.61. On the average, the two estimates were very similar. Some of the scatter may be due to some LWC being outside the size range of the CDP-2, as found by ECCC for the Convair-580 analysis, and some is inevitably due to the shortcomings of the ice detector-derived LWC. For the purposes of this report, there is no claim that these ice detector derived LWC estimates are more accurate than a factor of 2, but this uncertainty has little effect on the main conclusions related to short duration and low LWC levels of mixed-phase regions in the data set. Results and conclusions would be similar if the CDP-2 LWC had been used.

The ice detector measures the frequency of a vibrating rod that accretes ice when exposed to supercooled LWC. The frequency decreases with the amount of ice that has been accreted. Once the ice accumulation reaches a set point, the rod is automatically heated to shed the mass, and the cycle restarts. The rate of change (slope) of the vibration frequency provides an estimate of the cloud LWC (e.g., [D-3,D-4]). In order to provide an approximate LWC calibration of the ice detector, a section of mostly liquid cloud was identified and the scale factor relating change in ice frequency to LWC was estimated. The cloud was from an initial climb from Darwin on 18 May 2014, and is not included in the Appendix D/P analysis. Figure D-5 shows time histories of relevant parameters. The figure illustrates some key points discussed later in this section. First, there are three main cloud regions of ice detector deflection, shown as A, B, and C in panel (d). The first one is a small and short deflection (A) on entry into the first cloud. In panel (c), the CDP-2-calculated LWC and the IKP-2 TWC indicate that this was a mostly ice cloud with the narrow LWC region near the entrance side. The second and third deflections (B and C) are during an approximately 2-minute traverse through a second mostly-liquid cloud. The ice detector accretes to its set point, ice is shed, and a second deflection cycle is started in the second half of the cloud. The mixed-phase section "C" has been used here to provide the change in ice detector frequency to LWC scale factor. The CDP-2 LWC is approximately the same as the IKP-2 TWC here, and the (PSDs reveal that the IWC minimizes to about 0.1 gm^{-3} (not shown). Using the CDP-2 LWC as the reference LWC, the following estimation of LWC from the ice detector was derived:

$$GICELWC\ (gm^{-3}) = \frac{\Delta f * 8}{V \Delta t} \qquad \text{(D-1)}$$

where Δf is the change in ice detector frequency in Hz, Δt is the time interval in seconds, and V is the aircraft TAS in ms^{-1}.

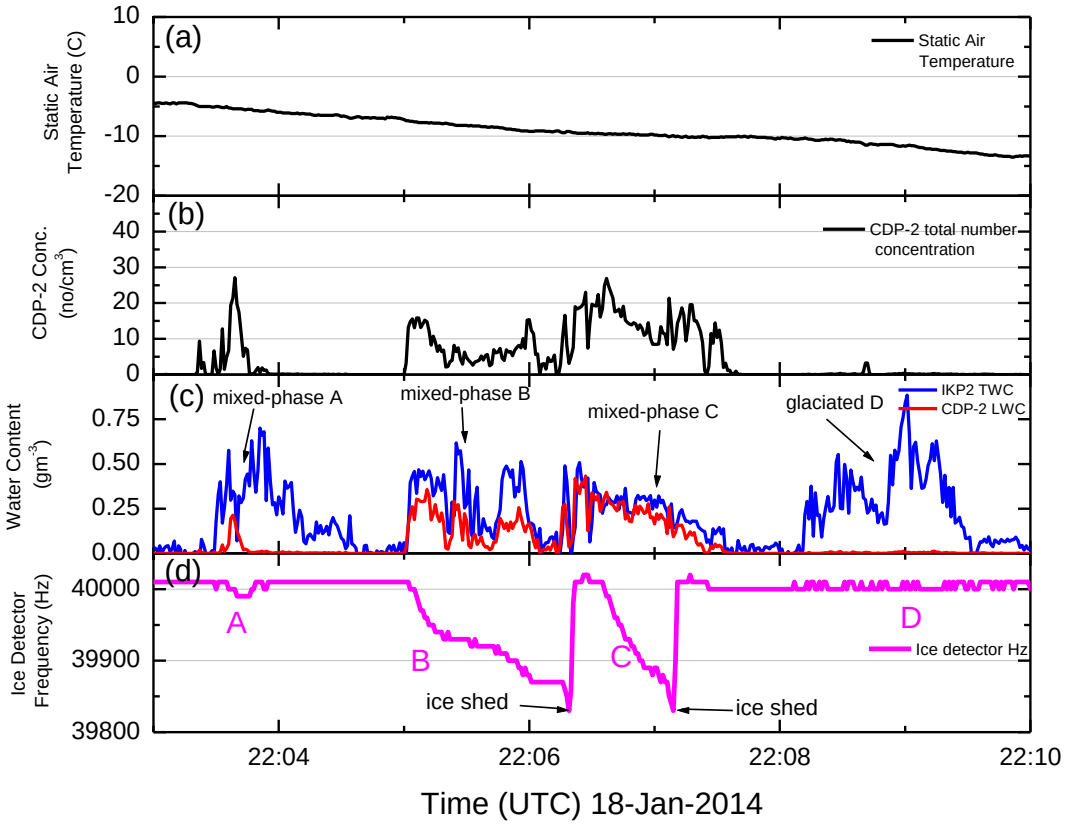

Figure D-5. Rough calibration of ice detector Δ frequency versus LWC in mostly LWC section "C", Darwin-14, 18 Jan 2014. Panels per Figure D-3

The last cloud region "D" is presumably glaciated. There is no deflection on the ice detector, and negligible CDP-2 LWC or number concentration. Also note the CDP-2 total number concentrations in panel (b). In the sections where the CDP-2 concentrations rise above10 cm^{-3}, one also observes the significant downward deflections in the ice detector frequency. In the glaciated section "D", the CDP-2 concentrations are close to zero. This observation is due to the fact that liquid is primarily formed in cloud by nucleation of cloud droplets within the size range of the CDP-2, and in concentrations much higher than ice particles. Liquid regions tend to have much higher CDP-2 particle number concentrations than glaciated regions, unless they are composed only of drizzle or rain.

The Darwin-14 and Cayenne-15 data that were within the selected cloud runs used in the Appendix D/P assessment were visually inspected to identify all periods with a significant ice detector deflection. The ice detector raw measurement of frequency is given in 10 Hz increments and has a noise level of about one 10 Hz step, so the minimum resolution of a deflection was about 20 Hz. In Darwin, observations of deflections were rare, with only three such events during the entire project. The events were 0.92, 1.05, and 3.35 Nm across, and with average ice-detector-derived LWC (GICELWC from equation above) of 0.05, 0.05, and 0.06 gm^{-3}. None were in high IWC

regions, but rather were adjacent to but outside such regions. In Cayenne, there were 33 ice deflection events, varying in width from 0.6 to 7.9 Nm, with a median width of 1.7 Nm. The median and maximum period-average GICELWCs were 0.08 and 0.32 gm^{-3}, respectively. The majority (n=27) of these deflections were in the -10 ±5 C interval, accounting for most of the difference in the number of events between the Cayenne and Darwin data sets, as there were little data collected at -10 C in Darwin. Most of the deflections (n=25) occurred at the edges of high IWC areas, or in isolated small clouds. In only five cases were deflections deeply embedded in high IWC zones. Figure D-6 shows a time history of the second-most significant LWC event in a high IWC cloud in the Darwin-14 and Cayenne-15 Falcon-20 data sets. The mixed-phase region is bracketed by the green vertical lines. TWC values vary between about 0.8 and 1.5 gm^{-3} (blue trace, panel c). CDP-2 number concentrations are typically 30 cm^{-3} and peak at 60 cm^{-3} (panel b), although these values may be subject to contamination due to ice particle shattering. The ice detector deflection is about 110 Hz (panel d), and the ice detector-derived LWC is 0.26 gm^{-3}. The most significant LWC event of both data sets was observed in a cloud about five minutes earlier, but is not shown because an ice-detector reset occurred in the middle of the short 20-second event, complicating the estimation of the GICELWC. For the short period before the reset, the GICELWC was estimated at 0.32 gm^{-3} in a region of cloud with a TWC of about 1.5 gm^{-3}.

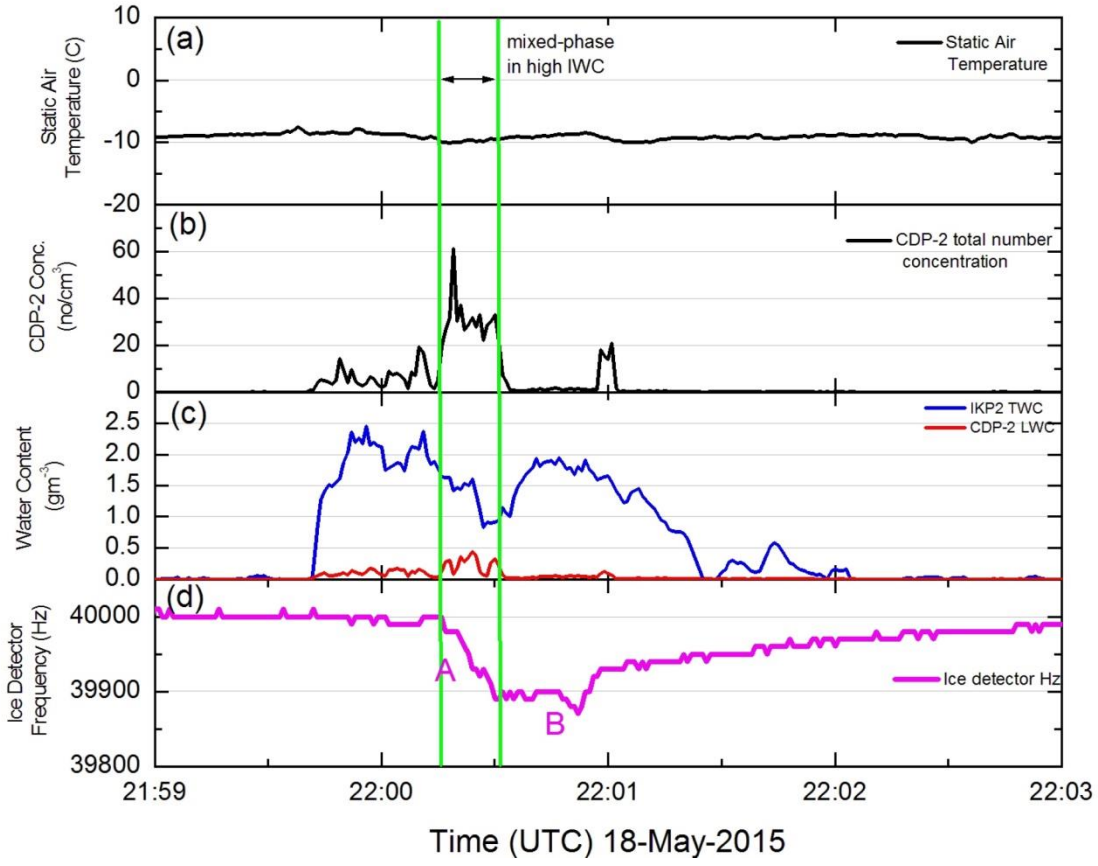

Figure D-6. Mixed-phase period in high IWC cloud, bracketed by the vertical green lines. Panels per Figure D-3.

Taking the two Falcon-20 data sets together, the ice detector deflection distances relative to the total distance flown are summarized in Table D-1. Summary statistics are for periods contributing to the Appendix D/P assessment. The top table shows statistics based of Goodrich Ice Detector deflection only. The bottom table includes periods of ice-detector deflections, and periods of CDP-2 concentration > 10 cm-3 when the PSD did not show contamination by ice crystals. The percentage of distance in cloud with ice detector deflections decreases with decreasing temperature as expected, from 2.8% at -10 ± 5 C, to 0 for temperatures < -35 C. Adding those cases in which a seemingly valid $CDPconc_{>10}$ value was observed with no ice detector deflection, the numbers increase slightly, yielding 3.0%, 0.80%, and 0.65% of the distance travelled in the -10, -20, and -30 ±5 C intervals, with no observations of LWC for < 35 C. Median exposure length was 0.7 Nm with a maximum of 6.2 Nm. Median and maximum event-average GICELWC values were 0.08 and 0.32 gm^{-3}, respectively.

Table D-1. Statistics on occurrence of mixed-phase events from the Falcon-20 Darwin-14 and Cayenne-15 data sets

Just Ice Detector Deflection Events									
	Darwin-14 Falcon-20			Cayenne-15 Falcon-20			Both Data Sets		
Temp. interval	total Nm	GICE Nm	GICE %	total Nm	GICE Nm	GICE %	total Nm	GICE Nm	GICE %
-10	273.8	0	0.00	1995.6	63.94	3.20	2269.4	63.94	2.82
-20	402.5	0	0.00	547.8	3.38	0.62	950.3	3.38	0.36
-30	2826.3	6.75	0.24	2670.1	4.37	0.16	5496.4	11.12	0.20
<-35	3611.9	0	0.00	2362.1	0	0.00	5974	0	0.00

Ice Detector Deflection + CDP-2 >10 cm^{-3} Events (see caption)									
	Darwin-14 Falcon-20			Cayenne-15 Falcon-20			Both Data Sets		
Temp. interval	total Nm	GICE & CPD>10 Nm	GICE & CPD>10 %	total Nm	GICE & CPD>10 Nm	GICE & CPD>10 %	total Nm	GICE & CPD>10 Nm	GICE & CPD>10 %
-10	273.8	0	0.00	1995.6	68.2	3.42	2269.4	68.2	3.01
-20	402.5	0	0.00	547.8	7.6	1.39	950.3	7.6	0.80
-30	2826.3	7.26	0.26	2670.1	28.6	1.07	5496.4	35.86	0.65
<-35	3611.9	0	0.00	2362.1	0	0.00	5974	0	0.00

The above results assume that the Goodrich ice detector is a reliable indicator of supercooled LWC even in high IWC situations, where erosion by ice particles could conceivably counteract the accumulation of rime ice on the vibrating rod. There is no detailed information on this effect, although some discussion about the likelihood if erosion on ice formations was included in the FAA mixed-phase icing review [D-5], and erosion has been observed by these authors in wind tunnel tests in very high IWC conditions at the National Research Council of Canada M-7 test cell 5. The observations of Figure D-6 indicate that a significant ice detector deflection can be observed on a high-speed aircraft in a 1-1.5 gm^{-3} TWC cloud that appears to be dominated by IWC.

However, there is insufficient information to conclude whether erosion is a factor here, and it could be reducing the mixed-phase summary statistics provided in the previous paragraph

D.3 FLORIDA-15 DC-8 MIXED-PHASE ANALYSIS

The DC-8 aircraft carried a similar instrument suite to the Falcon-20, but the Goodrich ice detector data was only retrieved for Florida-15 flights 8, 9, and 10. Furthermore, it was determined that the ice detector deice circuit was not operational for these three flights, so ice accretion events could cause a deflection of the vibration frequency[24], but the rod would not have deiced if the deice frequency threshold had been reached. However, for these three flights, there were no ice-detector deflections in the data periods used for the Appendix D/P assessment, permitting a valid conclusion that there were no ice accretion events during data periods at least for these flights. The lack of a complete record of ice-detector data left very limited options for assessing the occurrence of mixed phase on the DC-8. Nevertheless, the data were examined to see what could be concluded. One additional data set from the SEA Ice Crystal Detector (a dual hot-wire LWC/TWC system) was used in a few cases to infer additional information. The starting point was to examine all periods of $CDPconc_{>10}$ within the time periods selected for the Appendix D/P evaluation, and at temperatures warmer than -40 C. As far as can be concluded with the limited information, the frequency and length scales of periods of elevated CDP-2 data are similar to those in the Falcon-20 data. Occurrences of $CDPconc_{>10}$ were small in number and short in distance. Many occurred in high IWC cloud, most likely like on the Falcon-20 due to shattering contamination rather than reliable mixed-phase measurements. Occurrences in the -10 C interval amounted to a total of 9.6 Nm out of a total of 111.7 Nm samples, or 8%. That is higher than the approximately 3% observed on the Falcon-20 in Darwin-14 and Cayenne-15, but may simply be due to the very short distance sampled at -10 C in Florida. One interesting observation was a liquid-dominated narrow cloud of about 0.8 Nm with peak LWC estimated by the ICD of about 1 gm^{-3}, higher than any of the other observations of the four data sets. The only other possible mixed-phase periods in the DC-8 data were observed in the -30 C interval, with 30.2 Nm of $CDPconc_{>10}$, or about 0.8% of its total in-cloud distance. This percentage is similar to the Falcon-20 at -30 C, but 27.1 of this 30.2 Nm distance was in high IWC cloud, and therefore suspected to be due to particle shattering contamination rather than true liquid cloud.

[24] A deflection of the vibration frequency was observed on descent during flight 9, confirming that the rod was responding.

APPENDIX E—DIURNAL VARIATIONS IN CONVECTION AT PROJECT LOCATIONS

In Section 4.2 , the issue of daytime-only data sampling and its potential effects on the TWC_{99} statistics of this report due to potential diurnal cycles of convective cloud is described. Results of that section are condensed from the more detailed specific analysis provided below. Refer to section 4.2 for introductory remarks related to this issue.

In the following sub-sections, the occurrence of deep convective clouds, as identified by the relative IR satellite cloud top areas at selected temperature thresholds, are presented by time of day, in both a climatological analysis and a storm-specific analysis. Climatological analyses were performed to derive time-of-day statistics within fixed geographical boxes. Storm-specific analyses followed the evolution of cloud within a box encapsulating the entire cloud system for a 24-hour period starting at midnight. The times with the maximum cold cloud-top areas were compared to flight times, and some in-situ data were examined in one case of two flights being performed at different stages of the life cycle of a cloud system. Time is reported in solar time, converted from UTC using a longitude adjustment, unless otherwise noted.

E.1 CLIMATOLOGICAL DIURNAL ANALYSIS OF DEEP CONVECTION NEAR CAYENNE

A total of seven geographical boxes were identified for the IR cloud top area frequency study (Figure E-1): four open ocean boxes (OCEAN1, OCEAN2, OCEAN3, and OCEAN4); two coastal boxes (COAST1 and COAST2); and one overland box (CONT). The two coastal boxes were chosen due to the possible added influence of diurnal land-sea breezes in triggering convection. Based on pre-project visual inspection of satellite images, COAST 1 and OCEAN1 were expected to have the highest frequency of oceanic convection, possibly due to coastal convergence of the easterly circulation when encountering the Brazilian coast. OCEAN3 and OCEAN4 were in regions to the north where the South American coastline is more parallel to the dominant flow, and presumably more representative of open ocean conditions.

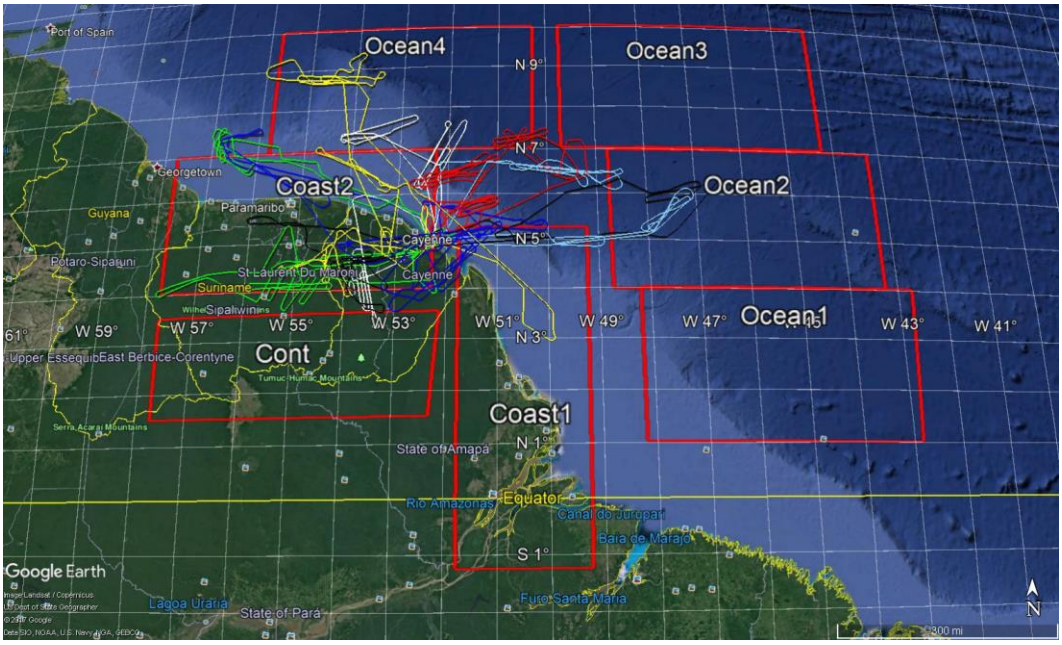

Figure E-1. Geographical boxes chosen for 20-year IR cloud top temperature analysis for the Cayenne-205 flight campaign area

The following plots are based on 20 years of IR satellite GOES-13 images, nominally twice per hour, for the month of May only. The separate lines on each graph represent the relative area of cloud colder than a series of IR temperature thresholds spanning from $\leq$ -40 C to $\leq$ -80 C (e.g. magenta line $\leq$ -75 C). Since the area of cloud reduces greatly with decreasing temperature, superimposition of the cloud fractions of the different temperature thresholds in the box on a single graph does not permit effective identification of the time-of-day maxima. Consequently, each line has been normalized to its maximum 20-year average value for the day. The actual proportion of cloud area for a given temperature threshold relative to the $\leq$ -40 C threshold is given in the legend of each figure for reference.

Figure E-2 shows the CONT results. Convection starts in the early afternoon and reaches a peak at around 18:00 local time for most temperature levels. The coldest cloud maximizes later at around 21:00 (black line, $\leq$ -80 C). Clouds diminish during the night and reach a minimum in the morning at about 10:00-11:00.

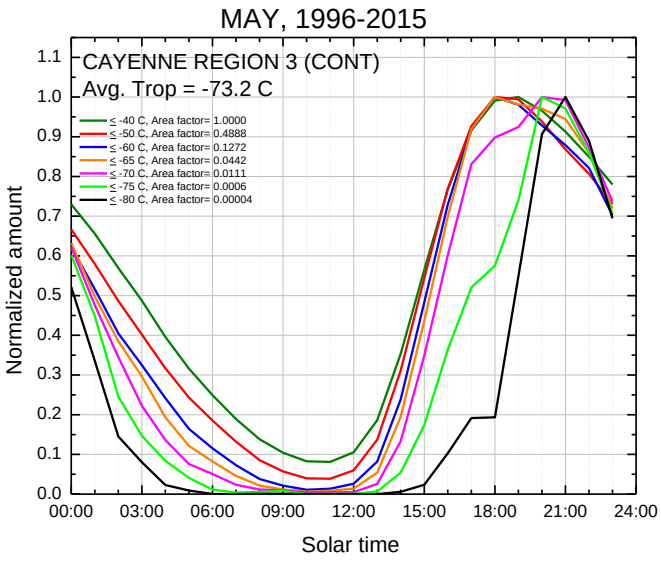

Figure E-2. Frequency of IR cloud area colder than specified temperature thresholds for May only for the period of 1996-2015. Each line normalized to the max value for day. Ratios of areas for each line relative to the < -40 C line in legend. Results are for the CONT geographical box shown in Figure E-1

Figure E-3 shows the COAST2 results. Note that a very similar continental peak is observed at about 17:00 and later. This is undoubtedly related to continental convection that forms over the land in this box, which straddles both land and ocean surfaces. There is little evidence of an early morning peak that might be associated with oceanic convection. Figure E-4 shows the COAST1 results. The mid-late afternoon continental behavior is similar to COAST2, but here we see a secondary maximum in the early morning maximizing between 01:00-06:00, depending on the temperature threshold. As mentioned earlier, COAST1 is suspected to be in an area more favored for oceanic convection due to coastal convergence, where the mean flow is nominally normal to the Brazilian coast.

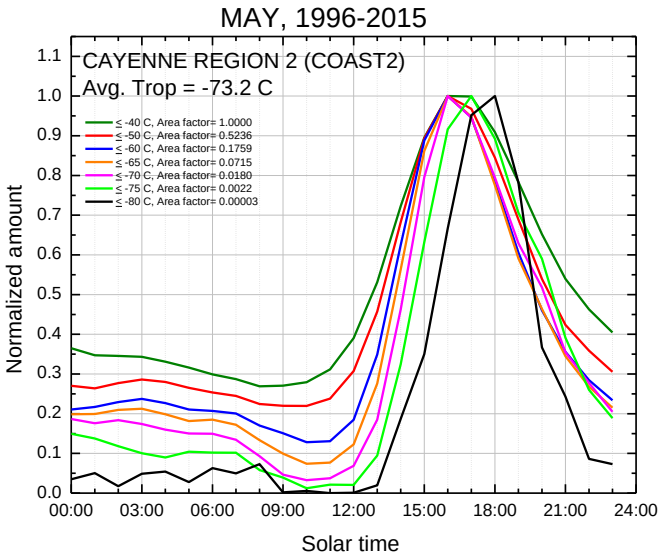

Figure E-3. COAST2 geographical box per Figure E-2

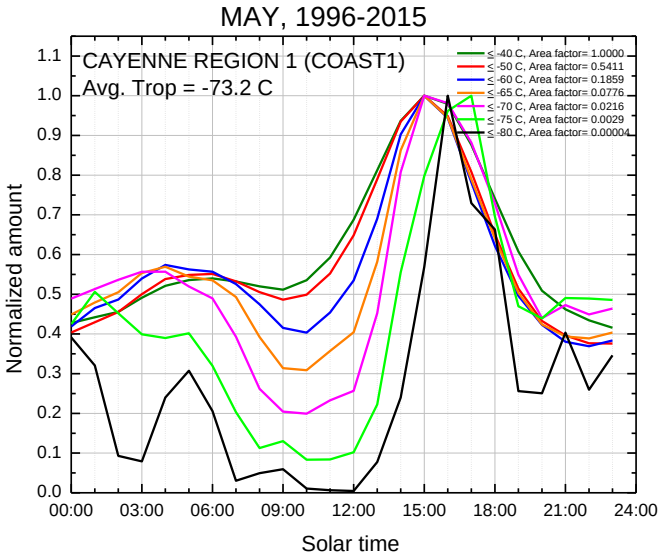

Figure E-4. COAST1 geographical box per Figure E-2

The results for OCEAN1, OCEAN2, OCEAN3, and OCEAN4 are all similar, but somewhat noisier than their coastal and continental counterparts. They are presented as combined results in Figure E-5. A bimodal trend is observed. There are clear early morning maxima (00:00-06:00) for all temperature thresholds colder than -60 C, while a second smaller mode is observed for each of these later in the morning (e.g. ≤ -70 C, magenta line at 13:00). The importance of the second mode increases with increasing temperature. For the dark green line (≤ -40 C), the second mode is dominant. This behavior may indicate a superimposition of two independent convective triggers, rather than a more simple translation of the first mode to later times in the day for warmer cloud temperatures. The mechanism forming the second mode may be that suggested by [E-1]: warming

of the sea surface temperature and boundary layer by direct solar heating after sunrise destabilizes the boundary layer and triggers convection. For Figure E-5, it is suggested the decrease in the later afternoon may result from increased cloud cover and decreased solar intensity and ocean surface solar heating after mid-day. Cloud-top warming by direct sunlight also may be a factor. This bimodal diurnal pattern will be observed again in the Florida investigation below.

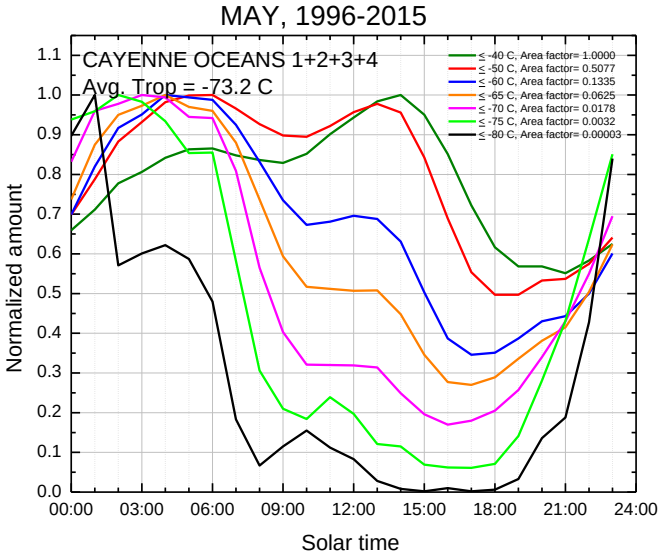

Figure E-5. Combined geographical boxes of OCEAN1, OCEAN2, OCEAN3, and OCEAN4 per Figure E-2

Figure E-6 shows the combined OCEAN results for May 2015 only. The single year results for May tend to be noisier due to having 20 times less data, particularly for the lowest-frequency cloud at the coldest temperatures. The same two modes in the early morning and around noon as in Figure E-5 are observed, at least for the plots ≤ -40 C to ≤ -65 C. The coldest cloud appears in the late evening to around midnight. This could be a climatological anomaly due to a small number of single events during May 2015, although this suggestion was not pursued.

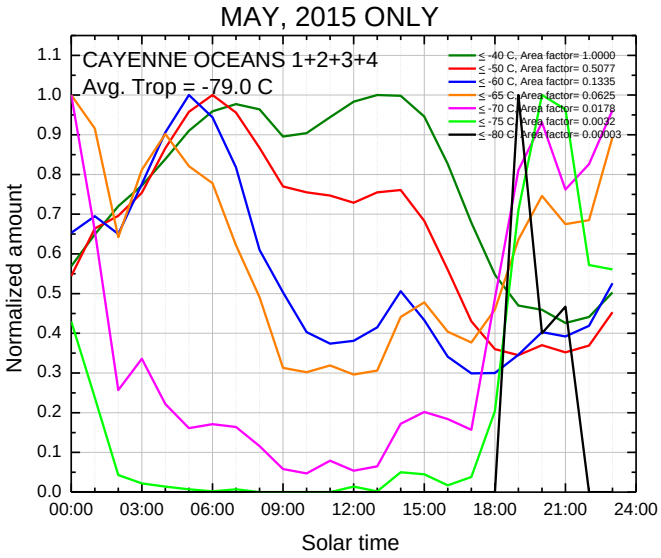

Figure E-6. Combined geographical boxes of OCEAN1, OCEAN2, OCEAN3, and OCEAN4 for May 2015 only per Figure E-2 and Figure E-5

Figure E-7(a) shows the average area percentage of cloud in the boxes versus the temperature threshold, for the separate and combined Cayenne oceanic regions. The percentage of cloud cover $\leq$ -40 C is lowest for OCEAN3 at about 3.2%, and highest for OCEAN1 at 7.7%, presumably for the reasons discussed earlier, with a combined four-box average of 3.9%. At the average MERRA tropopause temperature of -72 C, cloud area fractions are down about two orders of magnitude relative to $\leq$ -40 C. Figure E-7(b) also shows the fraction cloud area at a given temperature threshold, this time relative to the amount at $\leq$ -40 C, to illustrate the relative amounts of cold cloud, box to box. The results reveal that the proportion of the coldest cloud is highest in OCEAN1, and lowest in OCEAN3. Thus, not only do these boxes contain the highest and lowest cloud fractions, but also the highest and lowest proportions of the deepest cloud.

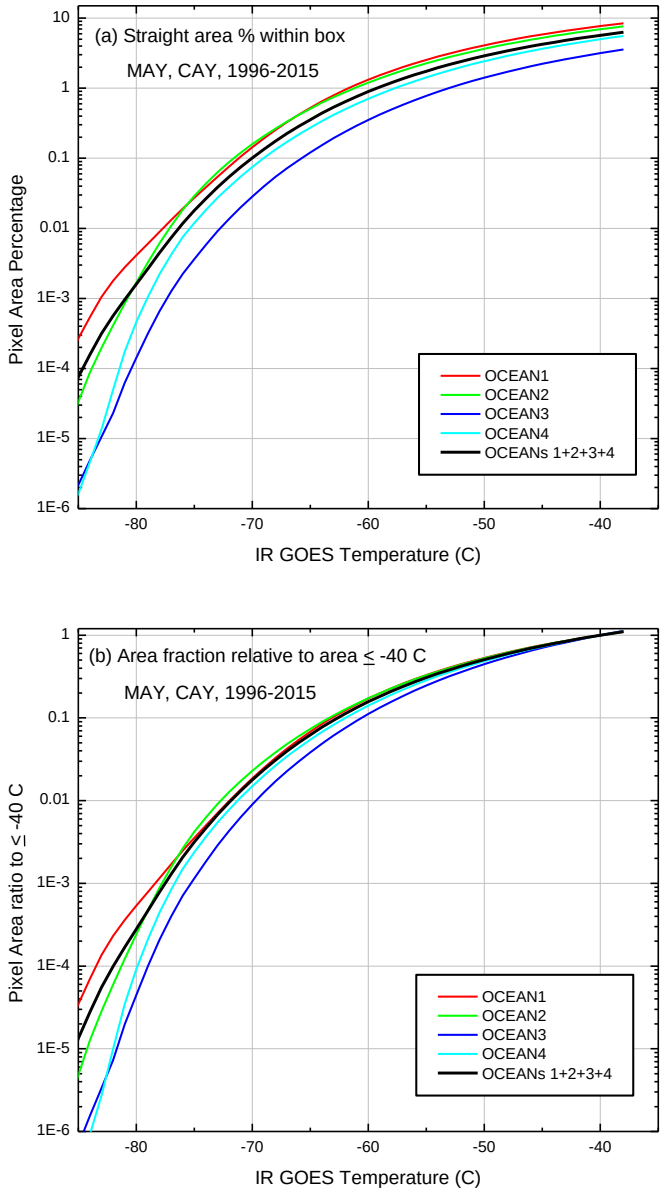

Figure E-7. (a) Percentage areas of cloud colder than threshold IR temps and (b) percentage areas normalized to the percentage area at temp threshold < -40 C. Data for 20-year climatological averages for May only in 4 Cayenne oceanic boxes and combined oceanic box

The question arises as to how significant these coldest cloud areas are in terms of potential flight campaign data collection. It is desirable to sample clouds not too close to their tops, due to the variations in the height of the top of the cloud, and potential TWC thinning close to the top. The cloud percentages of Figure E-7(a) include non-cloudy days and are thus biased low relative to flight days. Assume that in a 3º x 5 º box (~180 x 300 Nm) there is instead a 15% cloud cover ≤ -40 C, and that the coldest cloud is concentrated in a single cloud system. A rough indication of the size of the colder cloud elements can then be obtained by scaling them relative to ≤ -40 C using Figure E-7(b). Results are contained in Table E-1. The effective cloud sizes are not insignificant,

remaining above 10 Nm to ≤ -70 C, and the effective sizes may in fact be larger if contributed by a small number of exceptional events. However, as indicated by Figure E-5, climatologically these areas would be expected before about 9:00 a.m.

Table E-1. Rough estimate of effective diameter of cloud colder than the given temp threshold in a 180 x 300 Nm box, assuming 50% cloud cover for T < -40 C, and cloud area scaling for temp per Figure E-7(b). Cloud assumed concentrated into a single large cloud

	Area Diameter (Nm)				
Temperature Threshold ≤ °C	OCEANALL	OCEAN1	OCEAN2	OCEAN3	OCEAN4
-85	0.4	0.6	0.2	0.1	0.1
-80	1.7	2.4	1.6	0.7	1.0
-75	5.7	6.1	6.6	3.4	5.0
-70	13.5	13.9	15.4	9.6	12.4
-60	40.2	42.1	42.2	33.9	38.1
-50	72.4	74.0	73.7	67.9	70.7
-40	101.6	101.6	101.6	101.6	101.6

E.2 CLIMATOLOGICAL DIURNAL ANALYSIS OF DEEP CONVECTION NEAR FLORIDA

Three geographical boxes were chosen for a 20-year climatological analysis similar to that performed for Cayenne in section E.1. These boxes are representative of the widely separated areas flown by the DC-8 in the Florida-15 campaign, and are shown in Figure E-8. Although all boxes are expected to contain mostly oceanic convection, boxes 1 and 3 can potentially be directly impacted by continental convection due to their proximity to the Florida coastline and neighboring islands, respectively.

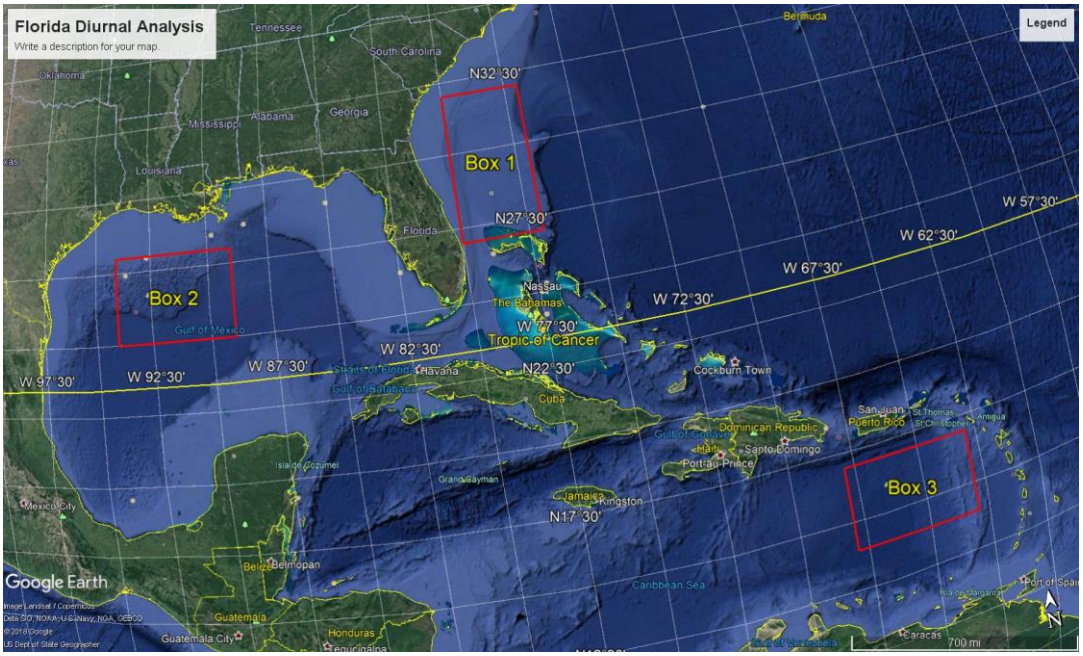

Figure E-8. Geographical boxes chosen for Florida 20-year IR cloud-top temp IR analysis, representing areas of measurement collection for FL-2015 flight campaign

Time-of-day animations of the 20-year climatological spatial distribution of cloud anvil fractions covering the regions of the three boxes were constructed by NASA Langley for other purposes in preparation for a 2018 flight campaign. These animations contain both warmer (e.g., -50 C) and colder anvils, nevertheless, they are revealing and pertinent to this discussion. Box 1 displays what is most likely a land-sea breeze effect, triggering a band of convection parallel to the coast around midnight. Convection spreads to the east through the morning and peaks in areal coverage by about 11:00. The anvil fraction minimizes by about 19:00. Box 2 displays some indication of a less defined land-sea breeze trigger in the early morning, with the anvil fraction increasing until around noon, and thereafter declining. Box 3 does not exhibit a late night impulse, but rather a gradual buildup of cloud from the early morning until about 13:00, followed by decreasing amounts. This box differs from the other two in that it is more frequently influenced by easterly waves, which can include tropical storms, which have a weaker diurnal cycle, and perhaps have a disruptive effect on climatological diurnal trends. The coastal areas near all three boxes exhibit a suppression of convection offshore, strongest around the time that neighboring continental convection reaches its maximum. For box 3, the offshore coastal minimum extends through the whole day, but does not appear to reach the southern boundary of the box. For box 1, it affects a minor fraction of the area at the western and northwestern sections. The effect does not appear to reach the edges of box 2.

Figure E-9 contains the 20-year (August only) climatological relative fractions of IR cloud-top areas for different temperature thresholds for box 1, by time of day. As in Figure E-2 through Figure E-6, each temperature threshold is normalized to its maximum for the day, and its area fraction relative to the $\leq$ -40 C threshold is provided in the figure legend. A similar bimodal diurnal cycle is observed as in the oceanic regions near Cayenne. There is a peak in the cloud amounts for the colder temperature thresholds ($\leq$ -60 C and colder) in the early morning hours. A second lesser

peak is observed between 09:00 and 12:00. For the ≤ -40 and ≤ -50 temperature thresholds, only the second mode is observed. Cloud amounts decline after noon, reaching a minimum around 19:00. There is some indication of another cold impulse at around 19:00-20:00, possibly due to continental influence in the southwest corner of the box. The early morning maximum of the coldest cloud is thought to be due possibly to the sea-breeze convective impulse observed in the animations described early, but may also be attributed to, or augmented by, nighttime IR cooling and de-stabilizing of cloud tops. Figure E-10 contains the 20-year climatological data for Florida box 2. In this region, the first early morning mode is not as strong, and the diurnal pattern is dominated by the second mode, the mid-day maximum. Figure E-11 displays the corresponding data for box 3, which is geographically closest to Cayenne. This region experiences the early morning and mid-day modes, the former observed mainly for temperature thresholds of ≤ -60 and colder. Additional modes are observed at about 19:00, perhaps due to continental convection over the neighboring islands, and near midnight, for reasons unknown. The other boxes experience near minima around midnight.

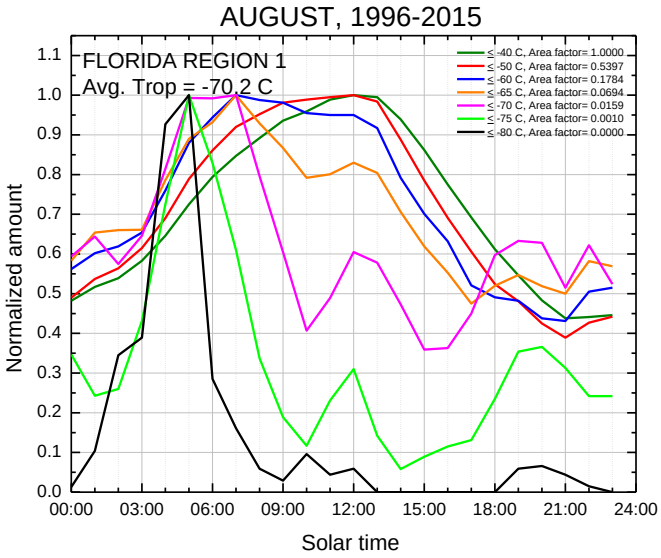

Figure E-9. Florida-2015 box 1 as defined in Figure E-8 per Figure E-2

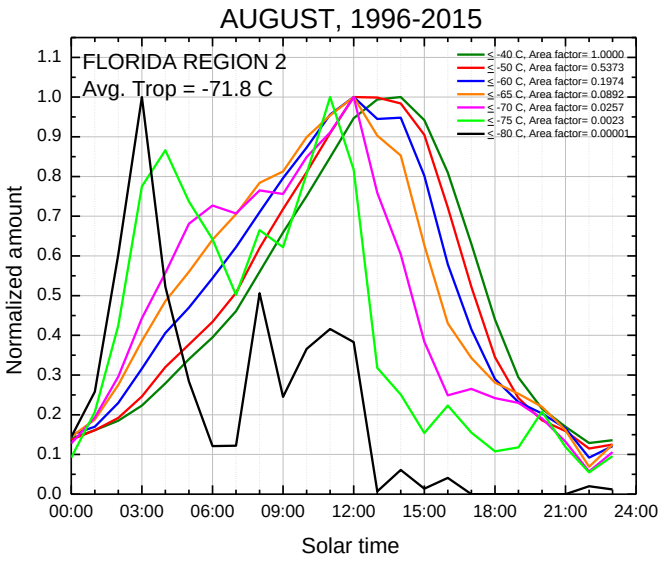

Figure E-10. Florida-15 box 2 as defined in Figure E-8 per Figure E-9

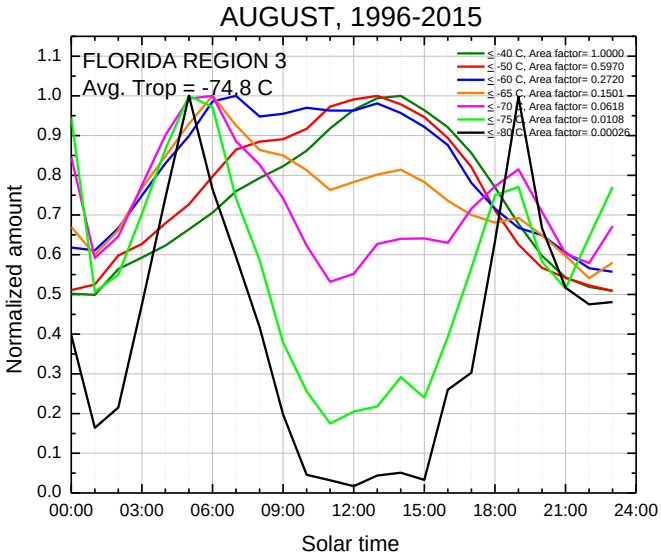

Figure E-11. Florida-15 box 3 as defined in Figure E-8 per Figure E-10

Thus, although all three boxes are oceanic, they exhibit some distinctly different diurnal variations in the amounts of cold cloud. In Figure E-12, the three regions are combined for an indication of the overall diurnal trend, although given their differences, the results should be viewed with caution. Once again, two primary modes are observed, one in the early morning maximizing before 06:00-07:00, and a second one maximizing at 12:00-13:00. In this composite picture, the early mode dominates only for temperature thresholds $\leq$ -70 C and colder.

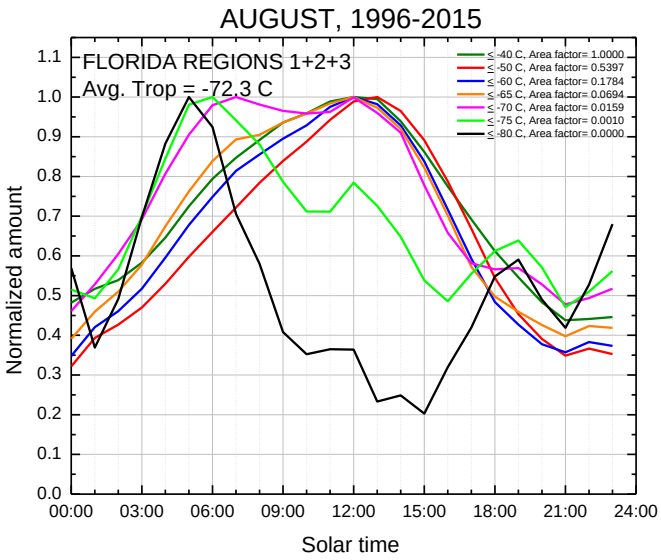

Figure E-12. Combined cloud fractions of Florida-15 boxes 1, 2, and 3 as defined in Figure E-8 per Figure E-11

Figure E-13 displays the box 1+2+3 composite results for August 2015 only, to determine if 2015 differed from the 20-year climatology. The first early morning mode is not well defined here, perhaps due to the poorer statistics of a single year. The second mode near noon is clear. Another fairly sharp mode at around 22:00 is observed, especially for the colder clouds, and may again be influence of continental convection experienced in 2015, but perhaps due to "statistical events" not climatologically expected at these levels. In summary, the dominant main mid-day mode is observed, but other features are either absent or added, perhaps due to the influence of the smaller sample size.

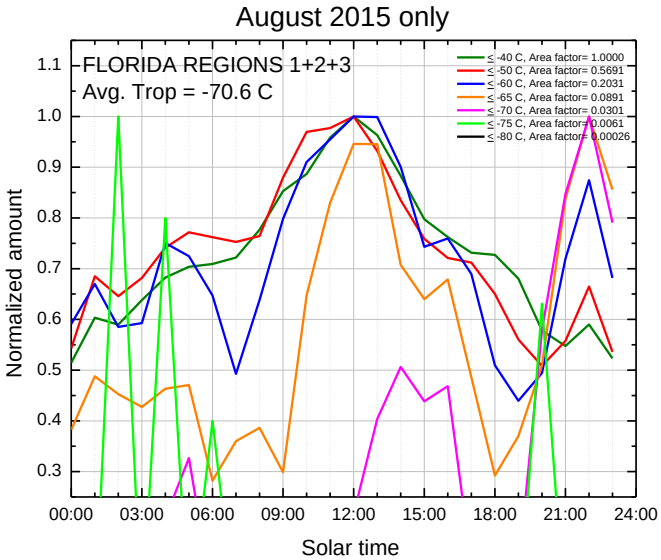

Figure E-13. For August 2015 only per Figure E-12 instead of the 20-year Aug. climatology

Figure E-14(a) displays the climatological average cloud area percentages as a function of the temperature threshold. Individual box results and composite results are shown. The average percentage of cloud ≤ -40 C varies between 3.8% for box 3 and 6.8% for box 1, with a composite average of 4.9%. At colder temperatures, the proportions reverse, from 0.19% to 0.25 % for boxes 1 and 3, respectively, with an average of 0.27 %. As for the Cayenne analysis above, the ratios of the area percentages to those in the ≤ 40 C threshold are plotted in Figure E-14(b), in order to better display the proportion of cold cloud to warmer cloud. At the ≤ 70 C threshold, box 3 has the highest relative percentage, box 1 the lowest (a factor of 5 higher), and the trend continues for colder cloud.

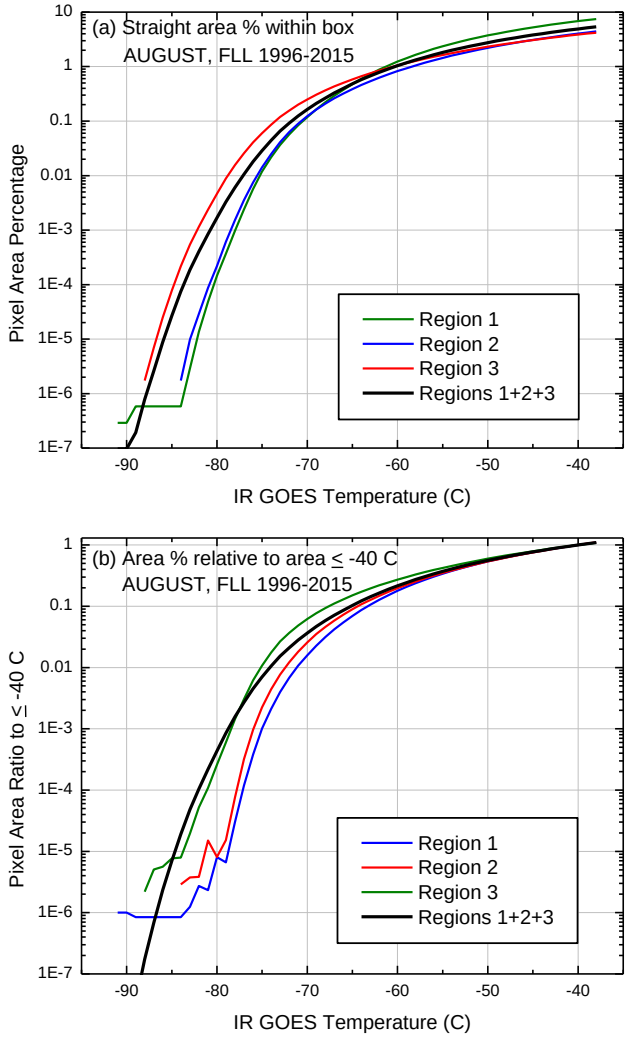

Figure E-14. (a) Percentage areas of cloud colder than threshold IR temps and (b) percentage areas normalized to the percentage area at temp threshold < -40 C. Data for 20-year climatological averages for August only in the 3 Florida boxes and combined box

E.3 CLIMATOLOGICAL COMPARISON OF CAYENNE AND FLORIDA OCEANIC REGIONS

Figure E-7 and Figure E-14(a) reveal that the overall Cayenne (May) versus Florida (August) average percentages of cloud in the oceanic geographical boxes chosen for these studies are not vastly different, and in fact, the inter-box variability at a particular location appears more significant than any Cayenne-Florida differences. These plots are on a logarithmic scale, and somewhat difficult to compare. In Figure E-15(a-c), the Cayenne (red) and Florida (dark cyan) results are presented as bar graphs on a linear IR area percentage scale for temperature thresholds of $\leq$ -40, $\leq$ -60, and $\leq$ -75 C, respectively. For Cayenne, all three temperature thresholds display an inter-box variability of at least a factor of 2 in the area percentages. The relative percentages for each box do not appear to vary greatly from temperature to temperature. The Florida boxes similarly show a significant variability from box to box, although the behavior changes with temperature. As discussed earlier, Florida box 3 has the lowest area percentage of the three boxes for $\leq$ -40 C and the highest for $\leq$ -75 C, whereas the reverse behavior is observed for box 1. The Cayenne and Florida composite oceanic boxes show similar area percentages at all three temperature thresholds. The results suggest that regional influences such as land-sea breezes and exposure to tropical waves dominate the inter-box differences in the absolute amount of cloud, the relative amount of the deepest cloud, and presumably the diurnal behavior. Although the climatological results for the composite boxes in both locations show that the pre-dawn morning hours contain the highest amounts of the deepest clouds (Figure E-5 and Figure E-12), the larger influence being in Cayenne, this maximum can almost be completely absent in a specific box (e.g., Florida box 2, Figure E-10).

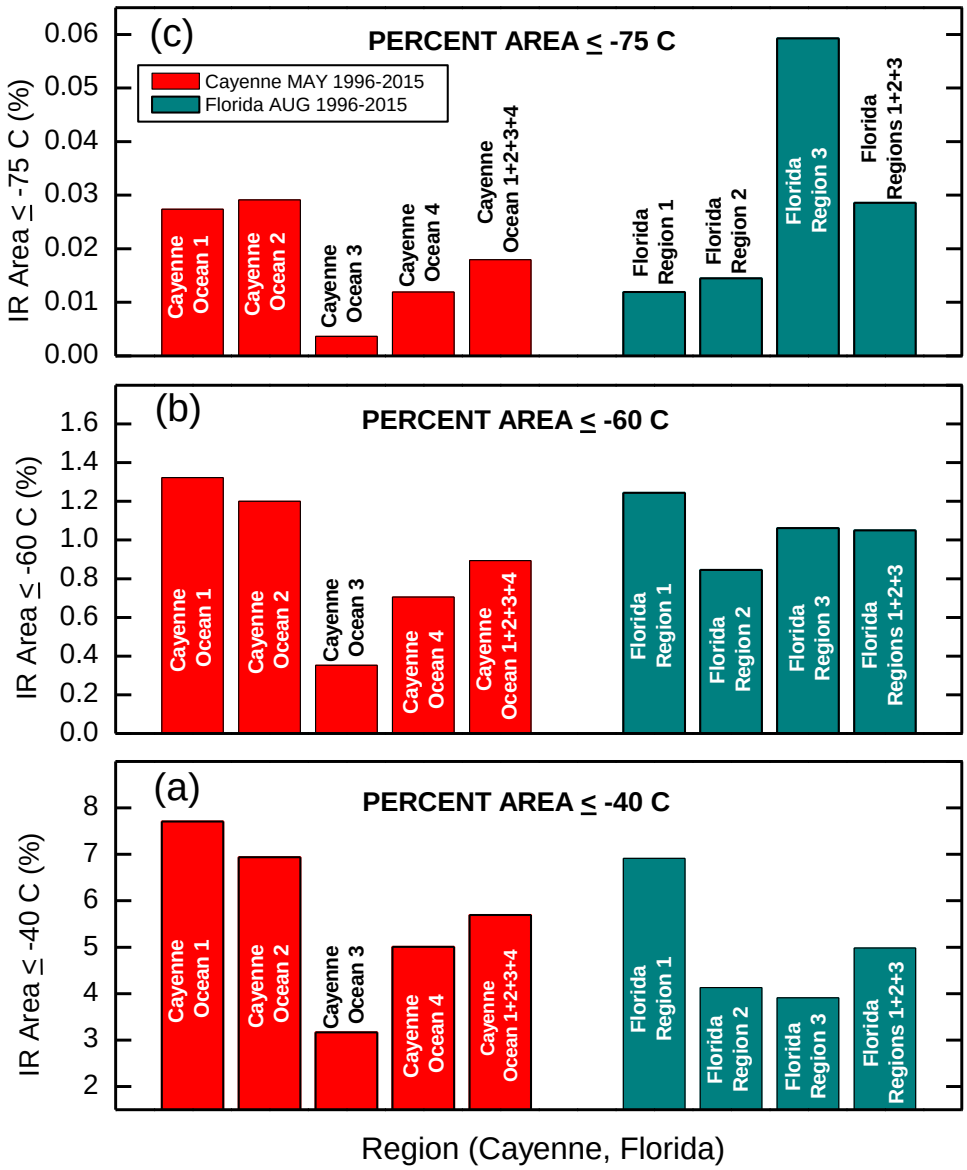

Figure E-15. Climatological average areas of cloud colder than (a) -40 C, (b) -60 C, and (c) -75 C, for each of four ocean regions and composite for Cayenne (red) and three ocean regions and composite for Florida (dark cyan). 20-year data averages

E.3.1. CLIMATOLOGICAL DIURNAL ANALYSIS OF DEEP CONVECTION NEAR DARWIN

A climatological analysis of oceanic convection has not been performed as of the time of this report. It may be added in the future if the need develops or the opportunity arises.

E.3.2. DARWIN DIURNAL ANALYSIS OF FLIGHT CAMPAIGN CLOUDS

Sections E.1 Climatological Diurnal Analysis of Deep Convection Near Cayenne through E.3 Climatological Comparison of Cayenne and Florida Oceanic Regions provide climatological

information on the diurnal variability of cold cloud amounts for Cayenne and Florida. Although these climatological studies are revealing, an equally important factor is when in the lifecycle of a sampled storm the measurements were taken. Were the measurements taken when the TWC was expected to be highest and/or at its greatest spatial extent? As discussed in the introductory remarks of section 4.2, the first order hypothesis is that this the optimum sampling time would be the time of maximum area of the coldest cold cloud tops, although as discussed below, this may not be the optimum *practical* time for cloud sampling, if copious lightning and/or high reflectivity at altitude is characteristic for this stage of the storm.

In order to study the storm-specific diurnal evolution of the Mesoscale Convective Systems (MCSs) sampled during Darwin-14, the evolution of the cloud top of each system was studied for 24 hours starting from midnight solar time. A latitude-longitude box was chosen that contained the MCS in question over the entire period. Using similar approach to the climatology studies (sections E.1 Climatological Diurnal Analysis of Deep Convection Near Cayenne, E.2 Climatological Diurnal Analysis of Deep Convection Near Florida), areas of cloud top colder than threshold temperatures of -40, -50, -60, -70, -80, and -90 C versus time within the box were produced. The satellite data were rapid-scan Multifunctional Transport Satellites IR images specially provided for the project at 10-minute resolution by the Japanese Meteorological Agency. In addition, lightning data were provided by the Australian Bureau of Meteorology. Figure E-16 shows an example of the 260x260 Nm box defined for the MCS of Darwin-14 flight 2. The time evolution of the area of the satellite-observed cloud top colder than the above temperature thresholds is provided in Figure E-17, along with the frequency of lightning strikes. As in the case of the 20-year climatology figures of sections E.2 Climatological Diurnal Analysis of Deep Convection Near Florida and E.3 Climatological Comparison of Cayenne and Florida Oceanic Regions, the data were normalized to the maximum value for the day to facilitate easier comparison of the different temperature thresholds. This example exhibits some characteristics common to many Darwin-14 cases. The coldest cloud-top area ($\leq$ -90 C) typically maximized earliest, followed roughly in sequence for each warmer temperature threshold. In this case, the $<$ -90 C time trend is somewhat sporadic due to the small number of pixels, and the $\leq$ -80, $\leq$ -70, and $\leq$ -60 C traces show two modes in the early hours, the second of which tends to line up better with this sequencing. In general, the time of maximum lightning frequency tended to occur during at the time of the coldest cloud maxima ($\leq$ -90, $\leq$ -80 C) , and by the time of the $\leq$ -70 C area maximum, lightning was typically subsiding. Since experience during the Darwin-14 flight program demonstrated that it was often difficult to operate in areas of high IWC with abundant lightning, it can be surmised that the best data (in the most active cells that could still be directly sampled) would probably have been collected after the maximum of the coldest cloud tops, and during the period bracketing the $\leq$ -70 C IR area maximum. In Figure E-17, the $\leq$ -70 C maximum of the two early morning modes are 01:20 a.m. and 03:50 a.m. local time, and the flight measurements were taken between about 6:30 a.m. and 8:00 a.m. More precisely, the midpoint of the flight measurements was 5.2 or 3.4 hours after the $\leq$ -70 C area local maximum, depending on which mode was used as reference.

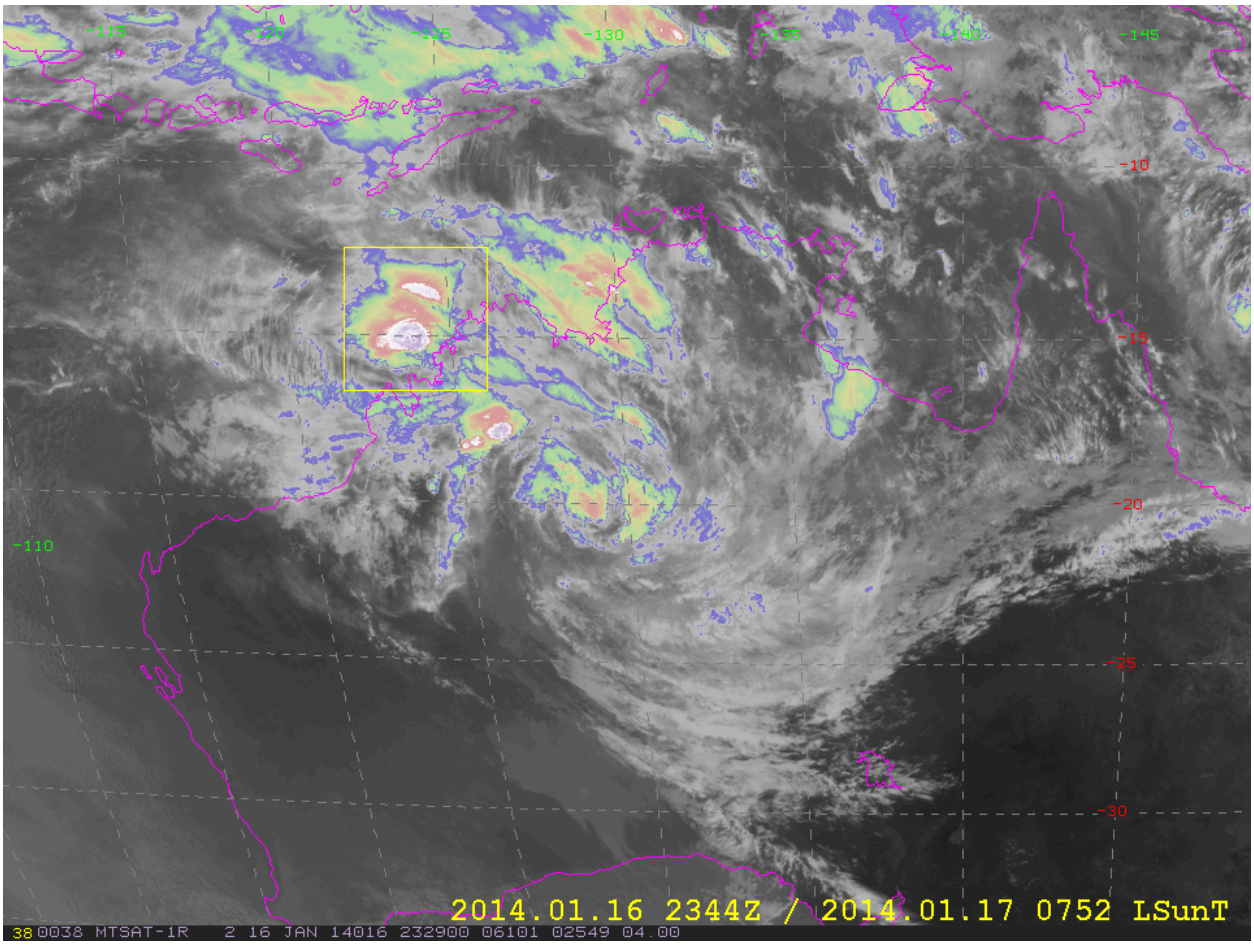

Figure E-16. Example of box defined to track 24-hour evolution of MCS sampled during Darwin-14 campaign

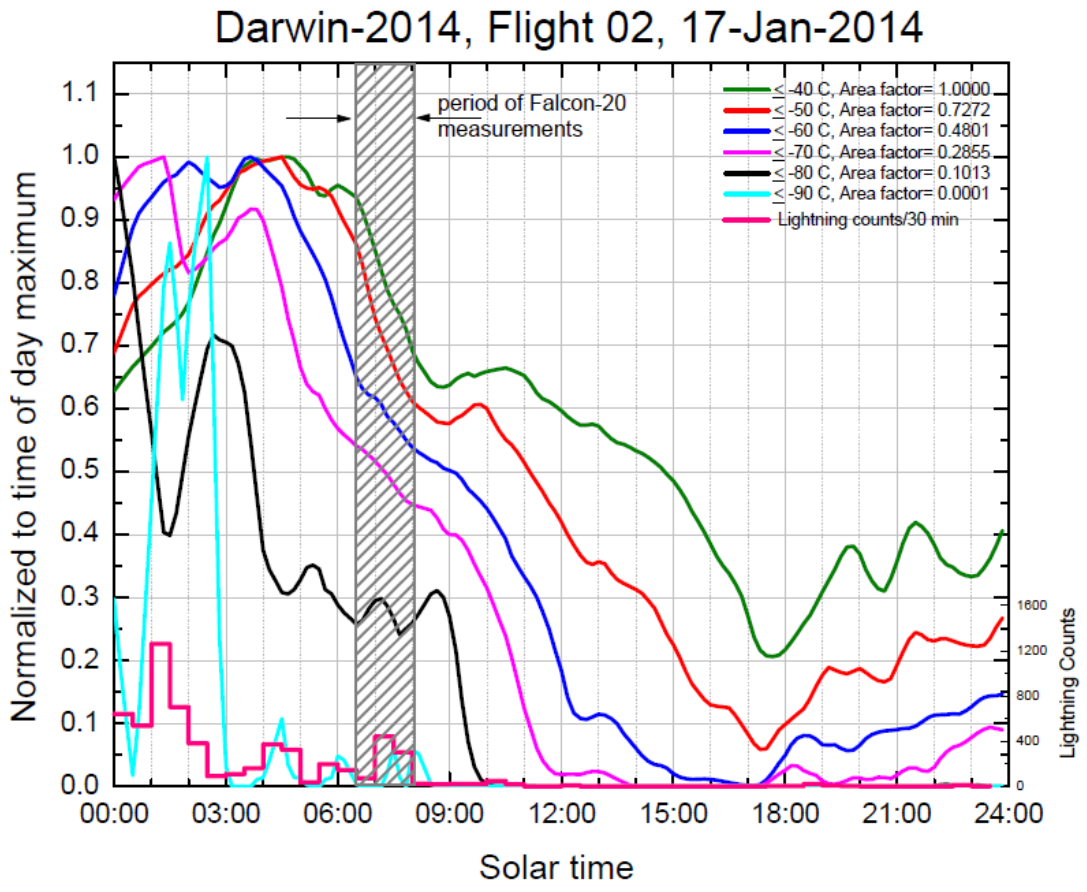

Figure E-17. Area of cloud colder than threshold temps of each line normalized to the time-of-day maximum for temp, Darwin-14 Flight 2. Falcon-20 measurements shown as grey hatched box. Cumulative lightning counts in 30-min. intervals shown by pink line

A similar analysis was performed for all 17 Darwin-14 flights contributing to the Appendix D/P analysis, and the results are summarized in Table E-2. It was recognized early in the campaign that it would be necessary to plan cloud sampling as early as possible within the constraints of daytime sampling. Excluding the two-flight days of local date 3 February 2014, the median start of Falcon-20 sampling was 06:20 a.m., with the earliest at 05:03 a.m. Table E-2 also shows that the ≤ -70 C cloud area maximum was often in the pre-dawn morning (median 4:40 a.m.). In 14 of the 17 flights the measurements were taken after the ≤ -70 C area maximum, an average of 2.6 hours later (median 2.9 hours) including all flights. If the time of the ≤ -80 C maximum was instead chosen as reference, the average time difference increased to about 3.3 hours. In the three cases of negative time differences, in which the aircraft sampled before the day's ≤ -70 C area maximum, takeoff time was chosen in response to the cloud target as it appeared at the early morning briefing, and a regeneration of the cloud occurred during or after the aircraft sampling.

Table E-2. Timing of Falcon-20 flights relative to time of the maximum of MTSAT IR temperatures colder than -70 C

UTC Date	Flt#	Takeoff-landing locations	Time of Max. Area ≤-70 C solar time	Time of midpt of F20 sampling solar time	Difference between sampling and ≤-70 C Area (hours)	≤-70 C cloud area ratio Flt-time/Max-time (ratio)
16-Jan-14	2	DRW-BME	1:20	7:13	5.9	0.51
17-Jan-14	3	BME-DRW	1:10	11:43	10.6	0.03
18-Jan-14	4	DRW-DRW	3:50	7:51	4.0	0.24
23-Jan-14	6	DRW-DRW	1:50	6:18	4.5	0.74
24-Jan-14	7	DRW-DRW	2:20	5:46	3.4	0.27
27-Jan-14	8	DRW-DRW	8:40	6:44	-1.9	0.64
28-Jan-14	9	DRW-DRW	4:00	7:19	3.3	0.35
29-Jan-14	10	DRW-GOV	6:20	6:58	0.6	0.89
2-Feb-14	12	DRW-DRW	4:50	6:43	1.9	0.69
3-Feb-14	13	DRW-DRW	19:30	13:40	-5.8	0.36
4-Feb-14	14	GOV-GOV	7:10	7:16	0.1	0.53
5-Feb-14	15	GOV-GOV	7:30	10:00	2.5	0.71
7-Feb-14	16	DRW-BME	6:40	7:08	0.5	0.94
8-Feb-14	18	DRW-DRW	0:00	6:31	6.5	0.42
9-Feb-14	19	DRW-BME	0:30	6:53	6.4	0.58
17-Feb-14	22	DRW-DRW	9:20	7:42	-1.6	0.96
18-Feb-14	23	DRW-DRW	4:40	7:32	2.9	0.20

This table also includes the ratio of the cloud ≤ -70 C area at the midpoint of the Falcon-20 sampling time to that at the time of the ≤ -70 C area maximum. This value is as low as 0.03 for Flight 2, sampled unusually late between 11:24 and 12:04, but the median value is 0.53. The value decreases to 0.22 if ≤ -80 C was chosen as reference. This is further explored below.

One can only speculate on the implication of these results to the Darwin data that contributes to this report's TWC_{99} statistics. Experience during the flight program showed that high TWCs were associated with active cells that in turn were associated with the coldest cloud tops. Clouds with greater areas of these coldest cloud tops tended to have longer exposures to high TWC, as long as active cells were still present. This is consistent with the observations during engine events, which favor long traverses across MCS with cloud reaching the convective equilibrium level or higher [E-2], and traverses in the vicinity of local cloud overshoots and close to the time of their peak spatial extent [E-3]. The Darwin-14 flight campaign contains only one case during which two flights were performed the same day at different stages during the storm's lifecycle. Darwin-14 flights 12 and 13 were conducted in the same tropical storm, approximately seven hours apart. The first flight sampled the cloud about 1.9 hours after the early morning peak of cloud area colder than -70 C, and the second flight sampled during a regenerating stage of the storm, about three

hours after the minimum between stages, and about 5.8 hours before the -70 C second stage maximum. Both stages had active cells during the time of sampling. Figure E-18 shows the evolution of the IR cloud areas throughout the entire day at the same temperature thresholds as Figure E-17. The periods of the Falcon-20 measurements are depicted with the pink vertical lines. The different temperature threshold data here are not normalized to time of day, but rather are shown as absolute area values on the three different subplots (a), (b), and (c). A comparison of the different IR temperature threshold plots again shows the tendency for the coldest maxima to occur first, followed in sequence by the warmer maxima. Small thumbnails satellite images are shown along the bottom of the diagram for reference. The second and fourth thumbnails show the cloud system around the time of the two flights. The visual impression is that the system was larger and more intense at the time of the earlier flight. Table E-3 contains statistics for five traverses (runs) for flights 12, and six for flight 13, all at about -36 C. The ratios of the IR cloud areas colder than -70 C relative to the morning maximum were 0.69 and 0.36, suggesting as a first-order approximation that the TWC length scales at the time of the morning maximum could have been a factor 1.2 ($(1/0.69)^{0.5}$) higher than during flight 12, and a factor of 1.7 ($(1/0.36)^{0.5}$) than during flight 13. Furthermore, under this approximation, flight 12 would have TWC length scales of the order of about a factor of 1.4 ($(0.69/0.36)^{0.5}$) longer than flight 13. Unfortunately, these run length scales cannot be accurately compared using in-situ data, because during both flights, turns defining the end of runs were often terminated before exiting cloud, sometimes when the TWC was still in excess of 1 gm^{-3} (i.e., cloud widths were underestimated by the run length). Nevertheless, the average run lengths of 53.7 and 39.8 Nm for flights 12 and 13 are shown in Table E-3, perhaps fortuitously indicating flight 12 run lengths to be a similar factor of 1.3 higher than flight 13. Table E-3 also shows the average of the TWC_{avg} values, where TWC_{avg} is the average TWC for an individual run. Due to the premature termination of runs, the comparison of these values for flight 12 and 13 may be misleading, although they are interestingly almost identical at 1.06 gm^{-3}. The TWC_{max} values provide a more convincing comparison. The table contains the average of the five and six TWC_{max} values for flights 12 and 13, respectively. Values are derived from 0.5 Nm non-overlapping TWC data points (approximately 5-second averages). The maximum values are almost the same, at 2.87 and 2.80 gm^{-3}, respectively. When comparing the single 0.5 Nm maxima over these runs, flight 12 and 13 values are 3.32 and 3.50 gm^{-3}, respectively, again very similar. In summary, this single comparison of TWC characteristics at two stages during a cloud's lifecycle shows some weak evidence that run-average TWCs were not greatly affected, but were observed over a longer length at the stage closer to its maximum. More convincingly, the maximum TWC values appeared to be about the same during both stages. This is assumed to be due to the fact that during both flights, active cells were sampled, and results might have been different had active cells not persisted. During flight 12, the NASA Langley overshooting top (OT) algorithm estimated that the Falcon-20 passed within 0.1 and 8.9 Nm of an OT each run (average for all runs 5.3 Nm). For flight 13, the Falcon-20 passed within 2.8 and 37.7 Nm of an OT (average 16.4 Nm), again confirming the existence and proximity of active cells during the runs.

Table E-3. Comparison of Falcon-20 in-situ measurements for Flights 12 and 13 in the same cloud system on same day and at different periods in the cloud intensity lifecycle. Run avgs. are avg. values from beginning of run across cloud until the end using run start and end time per Appendix D/P analysis. 0.5 Nm values contiguous non-overlapping 0.5 Nm segments; 5-sec. centered averages (approx. 0.5 Nm) overlapping values at 1-sec. resolution

	Darwin-14 Flight 12	Darwin-14 Flight 13
≤-70 C cloud area ratio: Flt-time/morning max	0.69	0.36
Number of runs across center of cloud (~-36 C)	5	6
Average Temperature (C)	-36.0	-35.7
Average run length (Nm)	53.7	39.8
Average of the run TWC_{avg} values (gm^{-3})	1.06	1.06
Average of run 0.5 Nm TWC_{max} values (gm^{-3})	2.87	2.80
Single maximum of all 0.5 Nm TWC values (gm^{-3})	3.32	3.60

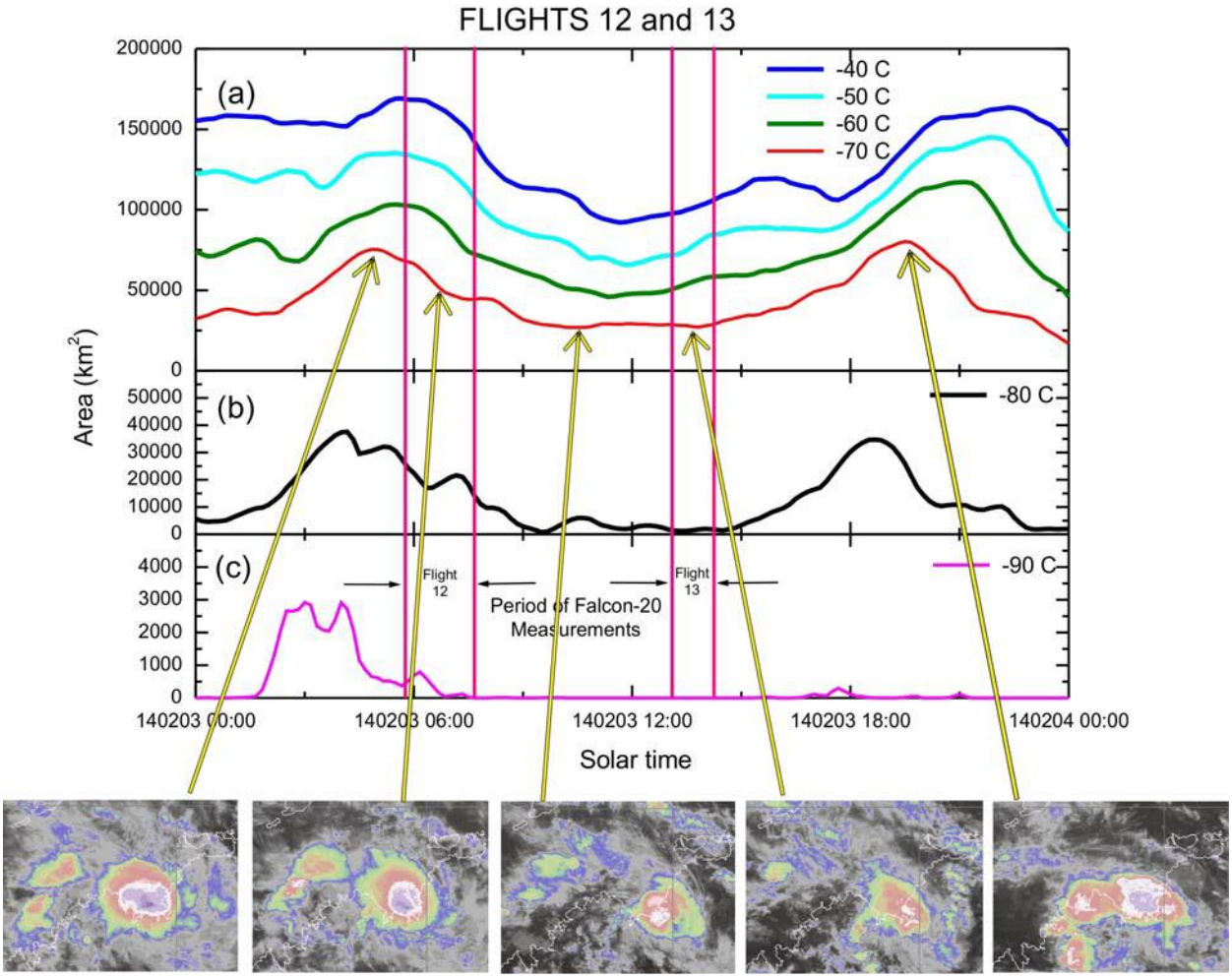

Figure E-18. Time history of satellite IR cloud areas colder than (a) -40, -50, -60, -70 C, (b) -80 C, and (c) -90 C for the local day 3 Feb 2014, Falcon-20 flights 12 and 13. Thumbnails of the satellite IR pictures for selected times shown at bottom

APPENDIX F—SUPPLEMENTARY TABLES OF TWC_{99} ANALYSIS PARAMETERS

Tables containing the maximum, 50^{th} and 99^{th} percentile TWCs (TWCMax, TWC50 and TWC99), SAT, and pressure altitude for a series of distance scales from 0.5 to 100 Nm when available. Data are shown for each flight campaign data set (DRW14 F20 = Darwin-14, Falcon-20; CAY15 F20 = Cayenne-15, Falcon-20; similarCAY15 CV580 = Cayenne-15, Convair-580; and FLL15 DC8 = Florida-15 DC-8) and each temperature interval. The -20 C interval is also included, although data collection was sparse. The 99^{th} percentiles are shown as cautionary red when the number of points is less than 100. Unadjusted TWCs refer to straight calculations from the data set. Adjusted TWCs include an estimated correction for the ice saturation, background water vapor assumption in cloud and for sampling bias, using a Monte Carlo simulation of the IKP2 calculation described in sections B.5 Statistical Sampling Uncertainty of TWC_{99} Estimates and B.6 A Combined TWC Error Estimate for the Effects of the Ice Saturation Assumption, and Sampling Uncertainty. Bootstrap resampling of the Monte Carlo results provides the uncertainties ($\pm 2\sigma$) shown for the adjusted TWC50 and TWC99 values. Adjusted results are not available for the -20 C interval due to the small number of points.

Table F-1. Maximum, and final 50th and 99th TWC percentiles, SAT, and pressure altitude, as a function of distance scale for all 4 data sets combined, for all temperatures (top) and for -50 C(bottom)

ALL Data Sets, All temperatures													
		IKP2 unadjusted		IKP2 adjusted				SSAT(deg C)			Palt (ft)		
Scale (Nm)	npoints	TWC99	TWCMax	TWC50	± 2σ	TWC99	± 2σ	avg	min	max	avg	min	max
0.5	59105	2.700	4.11	0.502	0.023	2.657	0.084	-31.8	-52.5	-1.2	30629	15940	39014
1	29429	2.690	3.90	0.506	0.023	2.653	0.086	-31.8	-52.5	-1.2	30627	15944	39013
2.5	11634	2.641	3.65	0.516	0.023	2.602	0.092	-31.9	-52.2	-1.2	30640	15951	38970
5	5691	2.566	3.44	0.527	0.023	2.520	0.088	-31.9	-52.0	-1.4	30656	15994	38954
10	2720	2.482	3.32	0.555	0.033	2.446	0.112	-32.0	-52.0	-1.5	30698	16010	38946
15	1729	2.415	3.07	0.591	0.037	2.397	0.092	-32.0	-51.8	-4.5	30714	16838	38929
17.4	1461	2.349	2.99	0.578	0.041	2.317	0.134	-32.1	-51.9	-4.3	30764	16866	38930
20	1239	2.367	2.98	0.600	0.047	2.350	0.154	-32.2	-51.8	-4.4	30792	16843	38927
30	748	2.273	2.71	0.613	0.049	2.247	0.231	-32.1	-51.8	-4.5	30740	16861	38926
40	510	2.248	2.41	0.639	0.059	2.246	0.182	-32.5	-51.8	-4.8	30924	16961	38924
50	373	2.165	2.35	0.645	0.070	2.175	0.233	-32.3	-51.7	-4.7	30831	16940	38924
75	173	2.045	2.26	0.653	0.085	2.108	0.288	-32.3	-51.7	-8.8	30798	19745	38924
100	93	1.945	2.04	0.688	0.112	2.043	0.300	-31.6	-50.9	-8.8	30551	19743	37017

ALL Data Sets, -50 C interval													
		IKP2 unadjusted		IKP2 adjusted				SSAT(deg C)			Palt (ft)		
Scale (Nm)	npoints	TWC99	TWCMax	TWC50	± 2σ	TWC99	± 2σ	avg	min	max	avg	min	max
0.5	10312	2.106	2.70	0.386	0.017	2.104	0.049	-47.8	-52.5	-45.0	36873	34968	39014
1	5147	2.083	2.64	0.388	0.018	2.082	0.041	-47.8	-52.5	-45.0	36871	34974	39013
2.5	2040	2.023	2.26	0.393	0.028	2.028	0.063	-47.8	-52.2	-45.0	36870	35024	38970
5	1000	1.995	2.30	0.409	0.038	2.004	0.096	-47.8	-52.0	-45.0	36868	35025	38954
10	477	1.946	2.03	0.414	0.048	1.969	0.128	-47.8	-52.0	-45.0	36876	35472	38946
15	307	1.849	2.06	0.408	0.074	1.884	0.126	-47.7	-51.8	-45.0	36868	35042	38929
17.4	263	1.809	1.96	0.416	0.071	1.844	0.142	-47.8	-51.9	-45.0	36863	35033	38930
20	224	1.824	2.00	0.462	0.095	1.866	0.117	-47.7	-51.8	-45.0	36870	35478	38927
30	134	1.685	1.83	0.463	0.106	1.751	0.171	-47.7	-51.8	-45.0	36852	35477	38926
40	95	1.689	1.92	0.511	0.117	1.784	0.348	-47.7	-51.8	-45.0	36874	35927	38924
50	68	1.543	1.66	0.494	0.139	1.664	0.220	-47.8	-51.7	-45.0	36879	35930	38924
75	35	1.497	1.53	0.543	0.234	1.717	0.184	-47.8	-51.7	-45.0	36894	35932	38924
100	17	1.351	1.38	0.510	0.281	1.857	0.338	-48.0	-50.9	-45.3	36908	35975	37017

Table F-2. -40 C (top) and -30 C (bottom) per Table F-1

ALL Data Sets, -40 C interval													
		IKP2 unadjusted		IKP2 adjusted				SSAT(deg C)			Palt (ft)		
Scale (Nm)	npoints	TWC99	TWCMax	TWC50	± 2σ	TWC99	± 2σ	avg	min	max	avg	min	max
0.5	17385	2.465	3.60	0.495	0.023	2.453	0.090	-40.4	-45.0	-35.0	34544	30499	37009
1	8643	2.422	3.39	0.502	0.023	2.413	0.077	-40.4	-45.0	-35.0	34540	31472	36969
2.5	3422	2.376	3.29	0.516	0.028	2.371	0.110	-40.4	-45.0	-35.0	34540	31489	36999
5	1673	2.291	3.23	0.521	0.040	2.288	0.156	-40.4	-45.0	-35.0	34536	31483	36955
10	806	2.201	2.88	0.552	0.059	2.213	0.187	-40.4	-45.0	-35.0	34545	31491	36937
15	512	2.271	2.83	0.593	0.063	2.292	0.308	-40.4	-45.0	-35.0	34517	31495	36939
17.4	434	2.112	2.84	0.559	0.066	2.136	0.249	-40.4	-45.0	-35.1	34531	32477	36938
20	369	2.051	2.71	0.572	0.072	2.081	0.272	-40.4	-45.0	-35.0	34538	32479	36937
30	220	1.745	2.30	0.599	0.081	1.788	0.232	-40.3	-44.9	-35.1	34506	32480	36932
40	154	1.659	1.74	0.588	0.111	1.723	0.107	-40.5	-45.0	-35.3	34566	32481	36933
50	110	1.662	1.67	0.601	0.110	1.749	0.124	-40.3	-44.9	-35.2	34510	32480	36928
75	48	1.438	1.45	0.615	0.110	1.620	0.135	-40.4	-44.9	-36.2	34501	32997	36926
100	25	1.411	1.44	0.517	0.176	1.763	0.275	-40.6	-44.8	-36.1	34725	33968	36927

ALL Data Sets, -30 C interval													
		IKP2 unadjusted		IKP2 adjusted				SSAT(deg C)			Palt (ft)		
Scale (Nm)	npoints	TWC99	TWCMax	TWC50	± 2σ	TWC99	± 2σ	avg	min	max	avg	min	max
0.5	17838	2.804	4.11	0.500	0.024	2.764	0.073	-29.4	-35.0	-25.0	30079	27903	34821
1	8885	2.782	3.76	0.502	0.023	2.735	0.073	-29.4	-35.0	-25.0	30079	27914	34820
2.5	3513	2.733	3.32	0.511	0.028	2.693	0.082	-29.4	-35.0	-25.0	30076	27923	34801
5	1727	2.664	3.04	0.528	0.039	2.630	0.139	-29.4	-34.9	-25.0	30080	28926	34798
10	828	2.559	2.93	0.555	0.059	2.527	0.170	-29.4	-34.9	-25.2	30073	28933	34797
15	526	2.434	2.68	0.597	0.070	2.425	0.122	-29.4	-34.9	-25.4	30062	28940	34792
17.4	445	2.371	2.74	0.603	0.079	2.342	0.193	-29.3	-34.9	-25.1	30049	28942	34793
20	377	2.375	2.68	0.630	0.080	2.366	0.253	-29.3	-35.0	-25.6	30051	28938	34793
30	232	2.236	2.50	0.620	0.086	2.246	0.303	-29.3	-34.9	-25.4	30030	28941	33985
40	154	2.304	2.39	0.664	0.100	2.371	0.423	-29.3	-34.9	-25.7	30015	28946	33985
50	116	2.077	2.28	0.645	0.122	2.158	0.441	-29.2	-34.8	-25.9	29996	28953	32531
75	53	1.778	1.99	0.650	0.143	1.957	0.356	-29.0	-34.7	-26.4	29970	28970	32529
100	30	1.796	1.94	0.728	0.133	2.044	0.448	-29.0	-30.8	-26.7	29990	28969	31998

Table F-3. -20 C (top) and -10 C (bottom) per Table F-1

ALL Data Sets, -20 C interval													
		IKP2 unadjusted		IKP2 adjusted				SSAT(deg C)			Palt (ft)		
Scale (Nm)	npoints	TWC99	TWCMax	TWC50	± 2σ	TWC99	± 2σ	avg	min	max	avg	min	max
0.5	1950	2.91	3.65	n/a	n/a	n/a	n/a	-21.2	-25.0	-15.0	26596	19990	30002
1	967	2.94	3.61	n/a	n/a	n/a	n/a	-21.2	-25.0	-15.0	26594	22339	29991
2.5	381	2.85	3.36	n/a	n/a	n/a	n/a	-21.2	-25.0	-15.0	26584	22361	29971
5	184	2.85	3.00	n/a	n/a	n/a	n/a	-21.2	-24.9	-15.0	26596	22436	29970
10	89	2.60	2.77	n/a	n/a	n/a	n/a	-21.2	-24.9	-15.0	26623	22567	29970
15	54	1.88	2.07	n/a	n/a	n/a	n/a	-21.3	-24.8	-15.1	26663	22524	29948
17.4	44	2.36	2.53	n/a	n/a	n/a	n/a	-21.4	-24.8	-15.1	26624	22442	29953
20	37	1.80	1.85	n/a	n/a	n/a	n/a	-21.4	-24.9	-15.5	26763	23464	29953
30	21	1.54	1.60	n/a	n/a	n/a	n/a	-21.4	-24.1	-15.5	26644	23465	28013
40	16	1.41	1.43	n/a	n/a	n/a	n/a	-21.3	-24.1	-15.3	26602	23456	28013
50	12	1.48	1.52	n/a	n/a	n/a	n/a	-21.2	-24.2	-15.5	26645	23458	28013
75	3	0.73	0.74	n/a	n/a	n/a	n/a	-22.6	-22.7	-22.4	26968	26964	26972
100	1		0.21	n/a	n/a	n/a	n/a	-22.6	-22.6	-22.6	26965	26965	26965

ALL Data Sets, -10 C interval													
		IKP2 unadjusted		IKP2 adjusted				SSAT(deg C)			Palt (ft)		
Scale (Nm)	npoints	TWC99	TWCMax	TWC50	± 2σ	TWC99	± 2σ	avg	min	max	avg	min	max
0.5	11480	2.913	4.04	0.654	0.032	2.834	0.081	-10.5	-15.0	-5.0	20817	16915	23526
1	5716	2.885	3.90	0.663	0.031	2.799	0.080	-10.5	-15.0	-5.1	20818	16917	23523
2.5	2251	2.857	3.65	0.684	0.045	2.782	0.105	-10.5	-14.9	-5.0	20818	16904	23498
5	1093	2.803	3.44	0.683	0.063	2.752	0.189	-10.5	-14.9	-5.2	20825	16985	23496
10	513	2.725	3.32	0.737	0.092	2.668	0.287	-10.6	-15.0	-5.1	20833	17065	22992
15	326	2.712	3.07	0.763	0.102	2.698	0.332	-10.5	-14.6	-5.8	20839	18455	22987
17.4	271	2.684	2.99	0.738	0.116	2.662	0.273	-10.6	-14.4	-5.8	20860	18571	22990
20	229	2.684	2.98	0.789	0.106	2.606	0.318	-10.6	-14.8	-5.9	20866	18692	22990
30	139	2.598	2.71	0.784	0.133	2.615	0.263	-10.7	-14.9	-7.3	20888	18972	22982
40	90	2.324	2.41	0.824	0.185	2.339	0.205	-10.6	-14.0	-7.7	20889	19139	22983
50	66	2.307	2.35	0.845	0.171	2.321	0.224	-10.7	-14.2	-7.8	20905	19222	22983
75	34	2.233	2.26	0.791	0.286	2.348	0.321	-10.7	-13.7	-8.8	20923	19745	22244
100	20	2.009	2.04	0.860	0.350	2.217	0.374	-10.8	-13.8	-8.8	20950	19743	22175

Table F-4. Darwin-2014 Falcon-20 data set only per Table F-1 all temperatures (top) and -50 C (bottom)

DRW14 F20, All Temperatures													
		IKP2 unadjusted		IKP2 adjusted				SSAT(deg C)			Palt (ft)		
Scale (Nm)	npoints	TWC99	TWCMax	TWC50	± 2σ	TWC99	± 2σ	avg	min	max	avg	min	max
0.5	15531	2.775	3.60	0.588	0.022	2.667	0.189	-34.1	-52.5	-1.2	32638	15940	39014
1	7734	2.769	3.38	0.591	0.021	2.740	0.089	-34.1	-52.5	-1.2	32639	15944	39013
2.5	3062	2.686	3.13	0.605	0.026	2.659	0.121	-34.1	-52.2	-1.2	32639	15951	38970
5	1502	2.594	3.05	0.615	0.037	2.552	0.210	-34.2	-52.0	-1.4	32652	15994	38954
10	723	2.516	2.93	0.646	0.050	2.485	0.295	-34.2	-52.0	-1.5	32671	16010	38946
15	459	2.419	2.83	0.649	0.057	2.416	0.201	-34.3	-51.8	-11.5	32718	22003	38929
17.4	387	2.322	2.84	0.642	0.077	2.311	0.289	-34.4	-51.9	-11.5	32733	22001	38930
20	330	2.283	2.71	0.688	0.081	2.282	0.353	-34.4	-51.8	-11.5	32746	22007	38927
30	199	2.144	2.30	0.708	0.088	2.155	0.370	-34.1	-51.8	-11.5	32643	22007	38926
40	137	1.728	2.25	0.712	0.102	1.694	0.334	-34.6	-51.8	-11.6	32841	22008	38924
50	104	1.665	1.67	0.705	0.134	1.651	0.108	-34.1	-51.7	-11.6	32621	22010	38924
75	47	1.523	1.59	0.759	0.164	1.554	0.148	-34.4	-51.7	-11.8	32663	22009	38924
100	26	1.456	1.46	0.642	0.144	1.546	0.223	-34.4	-44.8	-27.5	32790	29959	36927

DRW14 F20, -50 C interval													
		IKP2 unadjusted		IKP2 adjusted				SSAT(deg C)			Palt (ft)		
Scale (Nm)	npoints	TWC99	TWCMax	TWC50	± 2σ	TWC99	± 2σ	avg	min	max	avg	min	max
0.5	1315	2.170	2.58	0.584	0.030	2.168	0.123	-48.3	-52.5	-45.0	38017	36848	39014
1	653	2.149	2.46	0.591	0.045	2.160	0.154	-48.3	-52.5	-45.0	38017	36851	39013
2.5	258	2.061	2.25	0.610	0.070	2.097	0.186	-48.3	-52.2	-45.0	38014	36863	38970
5	124	2.007	2.18	0.612	0.114	2.090	0.252	-48.3	-52.0	-45.0	38025	36900	38954
10	60	1.772	1.90	0.629	0.193	1.898	0.214	-48.3	-52.0	-45.0	38027	36919	38946
15	38	1.761	1.77	0.668	0.238	1.934	0.159	-48.3	-51.8	-45.0	38014	36922	38929
17.4	30	1.606	1.63	0.619	0.284	1.821	0.236	-48.3	-51.9	-45.0	38019	36922	38930
20	28	1.650	1.67	0.565	0.263	1.869	0.204	-48.3	-51.8	-45.0	38006	36926	38927
30	15	1.187	1.19					-48.3	-51.8	-45.0	38000	36923	38926
40	11	1.300	1.30					-48.9	-51.8	-46.9	38206	37918	38924
50	7	1.263	1.28					-48.2	-51.7	-45.0	38007	36929	38924
75	3	0.772	0.77					-49.3	-51.7	-47.1	38262	37923	38924
100	0												

Table F-5. Darwin-2014 Falcon-20 data set only per Table F-1
-40 C (top) and -30 C (bottom)

DRW14 F20, -40 C interval													
		IKP2 unadjusted		IKP2 adjusted				SSAT(deg C)			Palt (ft)		
Scale (Nm)	npoints	TWC99	TWCMax	TWC50	± 2σ	TWC99	± 2σ	avg	min	max	avg	min	max
0.5	7212	2.623	3.32	0.694	0.022	2.604	0.078	-38.5	-45.0	-35.0	34425	33722	37009
1	3589	2.604	3.17	0.698	0.026	2.592	0.096	-38.5	-45.0	-35.0	34426	33729	36969
2.5	1424	2.555	3.13	0.712	0.038	2.547	0.156	-38.5	-45.0	-35.0	34427	33825	36999
5	699	2.476	3.05	0.717	0.054	2.465	0.221	-38.5	-45.0	-35.1	34428	33926	36955
10	337	2.366	2.88	0.739	0.076	2.386	0.310	-38.5	-45.0	-35.1	34429	33939	36937
15	217	2.415	2.83	0.761	0.099	2.454	0.430	-38.5	-45.0	-35.0	34411	33953	36939
17.4	187	2.287	2.84	0.760	0.114	2.323	0.390	-38.5	-45.0	-35.1	34426	33950	36938
20	155	2.265	2.71	0.762	0.128	2.320	0.423	-38.5	-45.0	-35.2	34438	33946	36937
30	94	1.803	2.30	0.781	0.150	1.909	0.364	-38.5	-44.8	-35.3	34422	33953	36932
40	67	1.722	1.74	0.772	0.138	1.831	0.103	-38.7	-45.0	-35.5	34508	33960	36933
50	50	1.668	1.67	0.778	0.189	1.775	0.106	-38.5	-44.6	-35.6	34410	33958	36928
75	22	1.444	1.45	0.850	0.298	1.692	0.138	-38.8	-44.7	-36.2	34444	33972	36926
100	13	1.426	1.44	0.571	0.213	1.899	0.355	-39.2	-44.8	-36.1	34679	33974	36927

DRW14 F20, -30 C interval													
		IKP2 unadjusted		IKP2 adjusted				SSAT(deg C)			Palt (ft)		
Scale (Nm)	npoints	TWC99	TWCMax	TWC50	± 2σ	TWC99	± 2σ	avg	min	max	avg	min	max
0.5	5634	2.955	3.60	0.451	0.019	2.915	0.055	-29.5	-35.0	-25.0	31045	29809	34076
1	2811	2.953	3.38	0.465	0.026	2.917	0.068	-29.5	-35.0	-25.0	31050	29817	34070
2.5	1112	2.916	3.12	0.472	0.041	2.899	0.153	-29.5	-35.0	-25.0	31045	29845	34050
5	551	2.811	3.03	0.500	0.057	2.795	0.224	-29.5	-34.9	-25.0	31052	29894	34024
10	265	2.759	2.93	0.544	0.081	2.776	0.363	-29.5	-34.8	-25.6	31040	29924	34022
15	168	2.418	2.49	0.541	0.088	2.468	0.222	-29.5	-34.9	-25.6	31018	29940	34017
17.4	141	2.355	2.74	0.510	0.123	2.392	0.456	-29.4	-34.6	-25.6	30983	29933	33981
20	122	2.288	2.68	0.536	0.119	2.343	0.517	-29.5	-35.0	-25.6	31008	29938	33984
30	75	2.164	2.21	0.584	0.145	2.297	0.427	-29.4	-34.8	-25.4	30988	29945	33985
40	49	1.941	2.25	0.647	0.172	2.118	0.509	-29.5	-34.9	-25.7	31018	29946	33985
50	39	1.569	1.62	0.616	0.193	1.730	0.230	-29.4	-31.0	-25.9	30925	29946	31998
75	20	1.512	1.59	0.543	0.204	1.819	0.413	-29.5	-30.9	-27.4	30928	29957	31998
100	13	1.383	1.46	0.728	0.188	1.918	0.713	-29.7	-30.8	-27.5	30901	29959	31998

Table F-6. Darwin-2014 Falcon-20 data set only per Table F-1
-20 C (top) and -10 C (bottom)

DRW14 F20, -20 C interval													
		IKP2 unadjusted		IKP2 adjusted				SSAT(deg C)			Palt (ft)		
Scale(Nm)	npoints	TWC99	TWCMax	TWC50	± 2σ	TWC99	± 2σ	avg	min	max	avg	min	max
0.5	802	2.46	2.65	n/a	n/a	n/a	n/a	-20.4	-25.0	-15.0	26711	24935	30002
1	398	2.37	2.56	n/a	n/a	n/a	n/a	-20.4	-25.0	-15.1	26716	24936	29991
2.5	156	2.12	2.34	n/a	n/a	n/a	n/a	-20.3	-25.0	-15.2	26690	24949	29971
5	75	1.89	2.13	n/a	n/a	n/a	n/a	-20.4	-24.8	-15.3	26718	24955	29970
10	37	1.69	1.72	n/a	n/a	n/a	n/a	-20.5	-24.9	-15.4	26768	24963	29970
15	21	1.27	1.35	n/a	n/a	n/a	n/a	-20.6	-24.8	-15.5	26888	24971	29948
17.4	17	1.30	1.37	n/a	n/a	n/a	n/a	-20.8	-24.8	-15.5	26872	24972	29953
20	15	1.18	1.20	n/a	n/a	n/a	n/a	-20.4	-24.9	-15.5	26721	24970	29953
30	8	1.12	1.15	n/a	n/a	n/a	n/a	-20.0	-24.1	-15.5	26490	24973	28013
40	6	0.80	0.81	n/a	n/a	n/a	n/a	-20.1	-24.1	-15.5	26492	24974	28013
50	5	0.89	0.90	n/a	n/a	n/a	n/a	-20.7	-24.2	-15.5	26794	24974	28013
75	0												
100	0												

DRW14 F20, -10 C interval													
		IKP2 unadjusted		IKP2 adjusted				SSAT(deg C)			Palt (ft)		
Scale (Nm)	npoints	TWC99	TWCMax	TWC50	± 2σ	TWC99	± 2σ	avg	min	max	avg	min	max
0.5	543	2.595	3.06	0.820	0.059	2.499	0.180	-11.6	-14.9	-6.1	21927	18994	23526
1	271	2.503	2.73	0.826	0.089	2.442	0.201	-11.6	-14.9	-6.1	21926	18997	23523
2.5	107	2.457	2.57	0.774	0.115	2.460	0.303	-11.6	-14.5	-6.5	21917	19001	23498
5	51	2.179	2.40	0.856	0.149	2.335	0.536	-11.6	-14.4	-6.8	21925	19003	23496
10	23	1.789	1.90	0.951	0.233	1.960	0.409	-11.7	-12.0	-9.9	21949	20519	22034
15	15	1.384	1.40	0.979	0.244	1.537	0.272	-11.8	-12.0	-11.5	22013	22003	22030
17.4	12	1.341	1.36					-11.8	-11.9	-11.5	22014	22001	22030
20	10	1.324	1.33					-11.8	-12.0	-11.5	22015	22007	22029
30	7	1.217	1.23					-11.8	-11.9	-11.5	22014	22007	22025
40	4	1.140	1.15					-11.8	-11.9	-11.6	22016	22008	22024
50	3	1.136	1.14					-11.7	-11.9	-11.6	22016	22010	22023
75	2	0.870	0.87					-11.8	-11.8	-11.8	22012	22009	22014
100	0												

Table F-7. Cayenne-2015 Falcon-20 data set only per Table F-1 all temperatures (top) and -50 C (bottom)

CAY15 F20, All temperatures													
		IKP2 unadjusted		IKP2 adjusted				SSAT(deg C)			Palt (ft)		
Scale (Nm)	npoints	TWC99	TWCMax	TWC50	± 2σ	TWC99	± 2σ	avg	min	max	avg	min	max
0.5	17304	2.918	4.11	0.361	0.019	2.880	0.088	-30.7	-47.6	-7.4	30127	19928	36641
1	8608	2.899	3.90	0.367	0.019	2.858	0.085	-30.7	-47.6	-7.4	30121	19931	36639
2.5	3401	2.855	3.65	0.385	0.024	2.816	0.087	-30.7	-47.4	-7.6	30120	19940	36575
5	1661	2.807	3.44	0.399	0.035	2.786	0.161	-30.6	-47.3	-7.8	30102	19950	36535
10	791	2.584	3.32	0.415	0.046	2.590	0.211	-30.6	-47.2	-7.9	30090	19954	36512
15	501	2.483	3.07	0.408	0.072	2.426	0.286	-30.5	-46.5	-8.0	30039	19961	36510
17.4	423	2.560	2.99	0.437	0.075	2.545	0.257	-30.4	-46.8	-7.9	30011	19962	36495
20	356	2.551	2.98	0.465	0.086	2.572	0.350	-30.6	-46.7	-8.4	30086	19964	36496
30	214	2.566	2.71	0.529	0.094	2.596	0.398	-30.1	-46.5	-8.3	29868	19965	36475
40	146	2.293	2.41	0.540	0.104	2.355	0.253	-30.6	-46.5	-9.0	30062	19966	36481
50	100	2.288	2.35	0.507	0.126	2.363	0.287	-29.7	-45.5	-8.8	29682	19967	36475
75	42	2.114	2.26	0.551	0.218	2.336	0.405	-29.1	-45.8	-9.3	29372	19967	36474
100	21	1.967	2.04	0.549	0.282	2.352	0.662	-25.7	-45.3	-9.1	27849	19967	35994

CAY15 F20, -50 C interval													
		IKP2 unadjusted		IKP2 adjusted				SSAT(deg C)			Palt (ft)		
Scale (Nm)	npoints	TWC99	TWCMax	TWC50	± 2σ	TWC99	± 2σ	avg	min	max	avg	min	max
0.5	2229	2.131	2.70	0.266	0.019	2.129	0.119	-45.4	-47.6	-45.0	36003	35416	36642
1	1120	2.093	2.64	0.277	0.027	2.099	0.175	-45.4	-47.6	-45.0	36003	35422	36639
2.5	446	1.926	2.21	0.280	0.046	1.962	0.214	-45.4	-47.4	-45.0	36001	35434	36575
5	219	1.726	2.30	0.294	0.072	1.795	0.356	-45.4	-47.3	-45.0	36005	35444	36535
10	103	1.667	1.98	0.290	0.089	1.819	0.476	-45.4	-47.2	-45.0	35999	35472	36512
15	66	1.322	1.35	0.305	0.080	1.512	0.192	-45.4	-46.5	-45.0	35999	35477	36510
17.4	55	1.220	1.29	0.318	0.103	1.415	0.176	-45.3	-46.8	-45.0	35995	35478	36495
20	49	1.241	1.24	0.342	0.149	1.437	0.124	-45.3	-46.7	-45.0	36008	35478	36496
30	29	1.403	1.49	0.444	0.169	1.752	0.453	-45.3	-46.5	-45.0	35984	35477	36475
40	22	0.894	0.95	0.520	0.211	1.220	0.298	-45.3	-46.5	-45.0	36011	35927	36481
50	12	0.866	0.88					-45.2	-45.5	-45.0	36004	35930	36475
75	7	0.931	0.94					-45.3	-45.8	-45.0	36042	35932	36474
100	1		0.22					-45.3	-45.3	-45.3	35975	35975	35975

Table F-8. Cayenne-2015 Falcon-20 data set only per Table F-1
-40 C (top) and -30 C (bottom)

CAY15 F20, -40 C interval													
		IKP2 unadjusted		IKP2 adjusted				SSAT(deg C)			Palt (ft)		
Scale (Nm)	npoints	TWC99	TWCMax	TWC50	± 2σ	TWC99	± 2σ	avg	min	max	avg	min	max
0.5	4706	2.433	3.60	0.279	0.010	2.430	0.109	-42.9	-44.9	-35.0	35349	30499	36560
1	2332	2.329	3.39	0.283	0.015	2.330	0.163	-42.9	-44.9	-35.0	35339	31472	36554
2.5	918	2.270	3.29	0.285	0.024	2.278	0.188	-42.9	-44.9	-35.0	35345	31489	36538
5	446	2.210	3.23	0.302	0.039	2.252	0.239	-42.9	-44.9	-35.0	35332	31483	36505
10	214	2.001	2.21	0.315	0.045	2.078	0.231	-43.0	-44.9	-35.0	35361	31491	36466
15	132	1.683	2.41	0.307	0.076	1.777	0.630	-42.9	-44.9	-35.0	35319	31495	36469
17.4	111	1.898	1.99	0.325	0.084	2.041	0.392	-42.9	-44.9	-35.1	35349	32477	36468
20	95	1.846	2.05	0.313	0.108	2.010	0.432	-43.0	-44.9	-35.0	35364	32479	36463
30	53	1.315	1.43	0.327	0.141	1.493	0.293	-42.9	-44.9	-35.1	35340	32480	36428
40	37	1.296	1.33	0.302	0.100	1.584	0.215	-43.3	-44.9	-35.3	35431	32481	36449
50	25	1.300	1.32	0.344	0.098	1.732	0.324	-43.3	-44.9	-35.2	35411	32480	36034
75	9	0.671	0.68					-43.5	-44.9	-37.9	35587	32997	36023
100	5	0.366	0.37					-44.3	-44.7	-44.1	35856	35447	35994

CAY15 F20, -30 C interval													
		IKP2 unadjusted		IKP2 adjusted				SSAT(deg C)			Palt (ft)		
Scale (Nm)	npoints	TWC99	TWCMax	TWC50	± 2σ	TWC99	± 2σ	avg	min	max	avg	min	max
0.5	5325	2.822	4.11	0.321	0.020	2.786	0.066	-30.2	-34.9	-25.0	30366	27903	34821
1	2644	2.749	3.76	0.324	0.026	2.718	0.107	-30.2	-34.9	-25.0	30359	27914	34820
2.5	1043	2.745	3.32	0.340	0.042	2.728	0.152	-30.2	-34.9	-25.0	30359	27923	34801
5	508	2.520	3.04	0.347	0.064	2.507	0.221	-30.2	-34.9	-26.7	30360	29434	34798
10	240	2.433	2.53	0.379	0.081	2.459	0.214	-30.2	-34.9	-26.8	30360	29450	34797
15	154	2.302	2.48	0.360	0.097	2.408	0.334	-30.2	-34.9	-26.8	30348	29451	34792
17.4	130	2.300	2.36	0.367	0.119	2.389	0.260	-30.2	-34.9	-26.9	30355	29451	34793
20	106	2.118	2.17	0.431	0.138	2.224	0.344	-30.1	-34.9	-26.9	30327	29452	34793
30	66	1.774	1.81	0.510	0.162	1.906	0.197	-30.1	-34.9	-26.9	30287	29453	32533
40	42	1.755	1.78	0.514	0.177	1.940	0.301	-30.0	-34.9	-26.9	30275	29460	32533
50	30	1.411	1.49	0.506	0.179	1.610	0.242	-30.2	-34.8	-26.9	30300	29458	32531
75	10	1.314	1.35	0.468	0.331	1.831	0.559	-29.7	-34.7	-27.0	30206	29471	32529
100	5	0.887	0.90					-29.2	-30.2	-27.3	29912	29573	30005

Table F-9. Cayenne-2015 Falcon-20 data set only per Table F-1
-20 C (top) and -10 C (bottom)

CAY15 F20, -20 C interval													
		IKP2 unadjusted		IKP2 adjusted				SSAT(deg C)			Palt (ft)		
Scale(Nm)	npoints	TWC99	TWCMax	TWC50	± 2σ	TWC99	± 2σ	avg	min	max	avg	min	max
0.5	1091	3.08	3.65	n/a	n/a	n/a	n/a	-21.9	-24.9	-15.0	26565	23429	27958
1	542	2.97	3.61	n/a	n/a	n/a	n/a	-21.9	-24.8	-15.0	26564	23432	27958
2.5	213	3.01	3.36	n/a	n/a	n/a	n/a	-22.0	-24.8	-15.0	26582	23444	27957
5	105	2.88	3.00	n/a	n/a	n/a	n/a	-21.9	-24.9	-15.0	26540	23442	27944
10	50	2.67	2.77	n/a	n/a	n/a	n/a	-21.8	-24.8	-15.0	26548	23455	27927
15	31	1.96	2.07	n/a	n/a	n/a	n/a	-21.9	-23.7	-15.1	26566	23461	27491
17.4	26	2.43	2.53	n/a	n/a	n/a	n/a	-21.9	-23.7	-15.3	26623	23461	27490
20	21	1.82	1.85	n/a	n/a	n/a	n/a	-22.0	-23.7	-15.5	26683	23464	27489
30	13	1.57	1.60	n/a	n/a	n/a	n/a	-22.2	-23.6	-15.8	26738	23465	27485
40	10	1.42	1.43	n/a	n/a	n/a	n/a	-22.0	-23.4	-15.3	26668	23456	27485
50	7	1.50	1.52	n/a	n/a	n/a	n/a	-21.6	-23.4	-15.5	26539	23458	27486
75	3	0.73	0.74					-22.6	-22.7	-22.4	26968	26964	26972
100	1		0.21					-22.6	-22.6	-22.6	26965	26965	26965

CAY15 F20, -10 C interval													
		IKP2 unadjusted		IKP2 adjusted				SSAT(deg C)			Palt (ft)		
Scale (Nm)	npoints	TWC99	TWCMax	TWC50	± 2σ	TWC99	± 2σ	avg	min	max	avg	min	max
0.5	3953	3.196	4.04	0.746	0.051	3.099	0.085	-11.0	-14.9	-7.4	21319	19928	23483
1	1970	3.177	3.90	0.751	0.072	3.095	0.127	-11.0	-14.9	-7.4	21319	19931	23482
2.5	781	3.136	3.65	0.759	0.112	3.079	0.161	-11.1	-14.9	-7.6	21320	19940	23458
5	383	3.078	3.44	0.760	0.166	3.086	0.244	-11.1	-14.9	-7.8	21316	19950	23451
10	184	3.061	3.32	0.929	0.219	3.055	0.317	-11.1	-14.5	-7.9	21308	19954	22992
15	118	2.991	3.07	0.856	0.265	3.041	0.318	-11.0	-14.2	-8.0	21308	19961	22987
17.4	101	2.839	2.99	0.884	0.282	2.876	0.264	-11.0	-14.3	-7.9	21315	19962	22990
20	85	2.919	2.98	0.865	0.289	2.979	0.315	-11.1	-14.3	-8.4	21315	19964	22990
30	53	2.660	2.71	0.915	0.321	2.744	0.244	-11.0	-14.2	-8.3	21296	19965	22982
40	35	2.379	2.41	1.171	0.317	2.486	0.246	-11.1	-14.0	-9.0	21361	19966	22983
50	26	2.330	2.35	1.013	0.353	2.473	0.259	-11.3	-13.9	-8.8	21389	19967	22983
75	13	2.213	2.26	1.210	0.540	2.492	0.414	-11.4	-13.7	-9.3	21391	19967	22024
100	9	2.008	2.04					-11.5	-13.8	-9.1	21451	19967	22024

Table F-10. Cayenne-2015 Convair-580 data set only per Table F-1 all temperatures (top) and -20 C (bottom)

CAY15 CV580, All temperatures													
		IKP2 unadjusted		IKP2 adjusted				SAT(deg C)			Palt (ft)		
Scale (Nm)	npoints	TWC99	TWCMax	TWC50	± 2σ	TWC99	± 2σ	avg	min	max	avg	min	max
0.5	6906	2.558	2.98	0.583	0.029	2.467	0.047	-10.0	-15.8	-3.8	20408	16782	22986
1	3438	2.528	2.91	0.599	0.035	2.430	0.058	-10.0	-15.7	-3.8	20408	16783	22957
2.5	1350	2.443	2.79	0.608	0.055	2.342	0.088	-10.0	-15.5	-3.8	20409	16796	22937
5	653	2.376	2.75	0.623	0.075	2.285	0.118	-10.0	-15.4	-4.0	20407	16820	22921
10	304	2.320	2.49	0.649	0.107	2.257	0.147	-10.0	-15.2	-4.2	20411	16826	22826
15	192	2.273	2.41	0.681	0.123	2.223	0.196	-10.0	-15.1	-4.5	20411	16838	22847
17.4	158	2.222	2.34	0.646	0.128	2.167	0.170	-10.0	-15.1	-4.3	20417	16866	22723
20	133	2.276	2.36	0.707	0.135	2.282	0.200	-10.1	-14.8	-4.4	20428	16843	22747
30	78	2.177	2.22	0.753	0.181	2.213	0.322	-10.1	-14.9	-4.5	20441	16861	22594
40	51	2.174	2.24	0.644	0.184	2.221	0.324	-10.0	-14.0	-4.8	20416	16961	22266
50	37	1.978	2.13	0.701	0.227	2.123	0.370	-10.0	-14.2	-4.7	20390	16940	22331
75	19	2.042	2.19	0.730	0.328	2.499	0.788	-10.2	-13.3	-8.8	20488	19745	22244
100	11	1.844	1.89	0.738	0.364	2.214	0.579	-10.3	-13.1	-8.8	20539	19743	22175

CAY15 CV580, -20 C interval													
		IKP2 unadjusted		IKP2 adjusted				SAT(deg C)			Palt (ft)		
Scale(Nm)	npoints	TWC99	TWCMax	TWC50	± 2σ	TWC99	± 2σ	avg	min	max	avg	min	max
0.5	29	0.78	0.79	n/a	n/a	n/a	n/a	-15.2	-15.8	-15.0	22501	22330	22609
1	15	0.55	0.57	n/a	n/a	n/a	n/a	-15.2	-15.7	-15.0	22500	22339	22609
2.5	7	0.45	0.45	n/a	n/a	n/a	n/a	-15.2	-15.5	-15.0	22501	22361	22591
5	2	0.31	0.31	n/a	n/a	n/a	n/a	-15.2	-15.4	-15.0	22496	22436	22555
10	1		0.20	n/a	n/a	n/a	n/a	-15.2	-15.2	-15.2	22567	22567	22567
15	1		0.24	n/a	n/a	n/a	n/a	-15.1	-15.1	-15.1	22524	22524	22524
17.4	1		0.19	n/a	n/a	n/a	n/a	-15.1	-15.1	-15.1	22442	22442	22442
20	0												
30	0												
40	0												
50	0												
75	0												
100	0												

Table F-11. Cayenne-2015 Convair-580 data set only for -10 C per Table F-1

CAY15 CV580, -10 C interval													
		IKP2 unadjusted		IKP2 adjusted				SAT(deg C)			Palt (ft)		
Scale (Nm)	npoints	TWC99	TWCMax	TWC50	± 2σ	TWC99	± 2σ	avg	min	max	avg	min	max
0.5	6762	2.562	2.98	0.600	0.028	2.469	0.048	-10.1	-15.0	-5.0	20459	16915	22986
1	3364	2.531	2.91	0.614	0.036	2.434	0.058	-10.1	-15.0	-5.1	20460	16917	22957
2.5	1321	2.452	2.79	0.626	0.056	2.352	0.090	-10.1	-14.8	-5.0	20456	16904	22937
5	639	2.378	2.75	0.637	0.075	2.288	0.118	-10.1	-14.9	-5.2	20466	16985	22921
10	297	2.323	2.49	0.663	0.107	2.261	0.146	-10.1	-15.0	-5.1	20474	17065	22826
15	187	2.280	2.41	0.697	0.119	2.243	0.195	-10.1	-14.6	-5.8	20475	18455	22847
17.4	153	2.227	2.34	0.653	0.127	2.174	0.171	-10.2	-14.4	-5.8	20495	18571	22723
20	130	2.281	2.36	0.708	0.133	2.283	0.203	-10.2	-14.8	-5.9	20509	18692	22747
30	76	2.178	2.22	0.752	0.173	2.212	0.320	-10.2	-14.9	-7.3	20534	18972	22594
40	50	2.175	2.24	0.647	0.189	2.222	0.322	-10.1	-14.0	-7.7	20485	19139	22266
50	36	1.982	2.13	0.697	0.226	2.120	0.369	-10.2	-14.2	-7.8	20486	19222	22331
75	19	2.042	2.19	0.721	0.324	2.496	0.787	-10.2	-13.3	-8.8	20488	19745	22244
100	11	1.844	1.89	0.736	0.363	2.211	0.578	-10.3	-13.1	-8.8	20539	19743	22175

Table F-12. Florida-2015 DC-8 data set only per Table F-1 all temperatures (top) and -50 C (bottom)

FLL15 DC8, All temperatures													
		IKP2 unadjusted		IKP2 adjusted				SAT(deg C)			Palt (ft)		
Scale (Nm)	npoints	TWC99	TWCMax	TWC50	± 2σ	TWC99	± 2σ	avg	min	max	avg	min	max
0.5	19364	2.351	3.15	0.513	0.025	2.330	0.092	-38.8	-52.3	-10.6	33108	19983	37186
1	9649	2.356	3.10	0.517	0.026	2.339	0.087	-38.8	-52.2	-10.7	33108	19986	37176
2.5	3821	2.262	2.97	0.528	0.028	2.240	0.096	-38.8	-52.0	-10.9	33115	20004	37145
5	1875	2.215	2.85	0.532	0.042	2.205	0.151	-38.8	-51.9	-11.1	33119	20019	37130
10	902	2.184	2.76	0.547	0.063	2.180	0.230	-38.8	-51.8	-11.6	33117	20026	37078
15	577	2.216	2.68	0.604	0.068	2.244	0.278	-38.9	-51.4	-11.5	33135	20028	37053
17.4	493	2.183	2.62	0.584	0.072	2.194	0.341	-39.0	-51.4	-11.6	33179	20027	37038
20	420	2.290	2.68	0.633	0.077	2.322	0.388	-38.9	-51.4	-11.7	33138	20028	37042
30	257	2.034	2.50	0.610	0.088	2.076	0.396	-38.8	-51.4	-11.6	33118	20033	37034
40	176	2.032	2.39	0.678	0.117	2.109	0.414	-38.9	-51.3	-11.9	33191	20042	37033
50	132	2.029	2.28	0.658	0.114	2.103	0.426	-39.0	-51.1	-12.0	33216	20042	37033
75	65	1.691	1.99	0.653	0.094	1.831	0.330	-39.2	-50.9	-26.4	33385	28970	37027
100	35	1.772	1.94	0.792	0.189	2.022	0.460	-39.8	-50.9	-26.7	33655	28969	37017

FLL15 DC8, -50 C interval													
		IKP2 unadjusted		IKP2 adjusted				SAT(deg C)			Palt (ft)		
Scale (Nm)	npoints	TWC99	TWCMax	TWC50	± 2σ	TWC99	± 2σ	avg	min	max	avg	min	max
0.5	6768	2.075	2.46	0.385	0.018	2.073	0.041	-48.4	-52.3	-45.0	36937	34968	37186
1	3374	2.076	2.39	0.384	0.023	2.079	0.040	-48.4	-52.2	-45.1	36937	34974	37176
2.5	1336	2.024	2.26	0.390	0.037	2.033	0.076	-48.4	-52.0	-45.2	36939	35024	37145
5	657	2.005	2.25	0.408	0.050	2.022	0.088	-48.4	-51.9	-45.0	36938	35025	37130
10	314	1.947	2.03	0.415	0.060	1.977	0.144	-48.4	-51.8	-46.4	36943	36024	37078
15	203	1.887	2.06	0.414	0.101	1.931	0.147	-48.4	-51.4	-45.0	36935	35042	37053
17.4	178	1.871	1.96	0.417	0.096	1.922	0.148	-48.4	-51.4	-45.0	36936	35033	37038
20	147	1.839	2.00	0.465	0.137	1.902	0.108	-48.4	-51.4	-46.6	36941	36038	37042
30	90	1.703	1.83	0.447	0.157	1.788	0.177	-48.4	-51.4	-46.9	36940	36043	37034
40	62	1.771	1.92	0.465	0.186	1.899	0.330	-48.3	-51.3	-47.0	36944	36043	37033
50	49	1.575	1.66	0.480	0.192	1.744	0.226	-48.4	-51.1	-47.0	36933	36049	37033
75	25	1.506	1.53	0.540	0.297	1.803	0.190	-48.3	-50.9	-47.3	36968	36830	37027
100	16	1.352	1.38	0.537	0.287	1.834	0.335	-48.2	-50.9	-47.5	36966	36850	37017

Table F-13. Florida-2015 DC-8 data set per Table F-1
-40 C (top) and -30 C (bottom)

FLL15 DC8, -40 C interval													
		IKP2 unadjusted		IKP2 adjusted				SAT(deg C)			Palt (ft)		
Scale (Nm)	npoints	TWC99	TWCMax	TWC50	± 2σ	TWC99	± 2σ	avg	min	max	avg	min	max
0.5	5467	1.859	2.36	0.417	0.026	1.853	0.043	-40.9	-44.8	-36.1	34004	31980	35066
1	2722	1.846	2.18	0.425	0.034	1.842	0.062	-40.9	-44.8	-36.2	34005	31982	35065
2.5	1080	1.824	2.04	0.433	0.062	1.824	0.078	-40.9	-44.8	-36.4	34006	31993	35060
5	528	1.789	2.03	0.433	0.069	1.797	0.087	-40.9	-44.0	-36.5	34007	32000	35049
10	255	1.695	1.87	0.475	0.100	1.712	0.081	-40.9	-44.5	-38.6	34013	33937	35050
15	163	1.657	1.80	0.522	0.156	1.690	0.129	-40.8	-43.5	-38.6	34009	33954	34082
17.4	136	1.652	1.83	0.484	0.133	1.689	0.155	-40.9	-43.5	-38.7	34009	33954	34087
20	119	1.662	1.78	0.528	0.183	1.713	0.107	-40.9	-43.5	-38.7	34009	33957	34082
30	73	1.610	1.75	0.543	0.135	1.685	0.214	-40.8	-43.4	-38.6	34009	33959	34079
40	50	1.437	1.58	0.562	0.167	1.519	0.228	-40.8	-43.0	-38.8	34003	33960	34075
50	35	1.378	1.40	0.584	0.135	1.513	0.103	-40.8	-43.0	-39.1	34010	33961	34074
75	17	1.237	1.26	0.616	0.104	1.561	0.354	-40.8	-42.3	-39.5	34000	33963	34074
100	7	1.110	1.12					-40.4	-42.2	-39.6	34005	33968	34070

FLL15 DC8, -30 C interval													
		IKP2 unadjusted		IKP2 adjusted				SAT(deg C)			Palt (ft)		
Scale (Nm)	npoints	TWC99	TWCMax	TWC50	± 2σ	TWC99	± 2σ	avg	min	max	avg	min	max
0.5	6879	2.637	3.15	0.712	0.028	2.595	0.055	-28.6	-34.5	-25.0	29066	28818	31069
1	3430	2.608	3.10	0.716	0.032	2.562	0.066	-28.6	-34.4	-25.0	29066	28825	31066
2.5	1358	2.618	2.97	0.731	0.052	2.593	0.109	-28.6	-34.1	-25.0	29065	28854	31004
5	668	2.565	2.85	0.744	0.073	2.540	0.158	-28.6	-33.9	-25.1	29066	28926	30993
10	323	2.563	2.76	0.766	0.093	2.560	0.287	-28.6	-33.6	-25.2	29067	28933	30986
15	204	2.479	2.68	0.751	0.097	2.487	0.237	-28.6	-33.5	-25.4	29059	28940	30971
17.4	174	2.517	2.62	0.754	0.101	2.551	0.316	-28.6	-33.6	-25.1	29064	28942	30971
20	149	2.396	2.68	0.751	0.130	2.438	0.305	-28.6	-33.5	-26.4	29070	28938	30971
30	91	2.349	2.50	0.800	0.182	2.447	0.416	-28.5	-33.3	-25.7	29053	28941	30963
40	63	2.380	2.39	0.824	0.146	2.516	0.474	-28.6	-33.3	-26.1	29061	28946	30962
50	47	2.213	2.28	0.782	0.183	2.391	0.417	-28.4	-30.4	-26.1	29031	28953	29072
75	23	1.868	1.99	0.726	0.274	2.161	0.457	-28.3	-30.1	-26.4	29035	28970	29070
100	12	1.881	1.94	0.971	0.386	2.386	0.571	-28.1	-29.4	-26.7	29035	28969	29071

Table F-14. Florida-2015 DC-8 data set only per Table F-1
-20 C (top) and -10 C (bottom)

FLL15 DC8, -20 C interval													
		IKP2 unadjusted		IKP2 adjusted				SAT(deg C)			Palt (ft)		
Scale(Nm)	npoints	TWC99	TWCMax	TWC50	± 2σ	TWC99	± 2σ	avg	min	max	avg	min	max
0.5	28	2.14	2.17	n/a	n/a	n/a	n/a	-24.0	-24.9	-15.0	28733	19990	29083
1	12	1.53	1.59	n/a	n/a	n/a	n/a	-24.3	-24.9	-23.7	29063	29054	29081
2.5	5	1.31	1.33	n/a	n/a	n/a	n/a	-24.3	-24.8	-23.8	29063	29059	29073
5	2	0.80	0.81	n/a	n/a	n/a	n/a	-24.3	-24.7	-23.9	29064	29062	29066
10	1		0.75	n/a	n/a	n/a	n/a	-24.3	-24.3	-24.3	29064	29064	29064
15	1		1.09	n/a	n/a	n/a	n/a	-24.6	-24.6	-24.6	29063	29063	29063
17.4	0			n/a	n/a	n/a	n/a						
20	0												
30	0												
40	0												
50	0												
75	0												
100	0												

FLL15 DC8, -10 C interval													
		IKP2 unadjusted		IKP2 adjusted				SAT(deg C)			Palt (ft)		
Scale (Nm)	npoints	TWC99	TWCMax	TWC50	± 2σ	TWC99	± 2σ	avg	min	max	avg	min	max
0.5	222	2.222	2.53	0.684	0.084	2.107	0.249	-12.1	-14.7	-10.6	20041	19983	20095
1	111	2.029	2.38	0.689	0.113	1.923	0.255	-12.1	-14.8	-10.7	20040	19986	20094
2.5	42	1.995	2.04	0.658	0.160	2.063	0.312	-12.1	-14.6	-10.9	20041	20004	20058
5	20	1.724	1.73	0.679	0.205	1.849	0.328	-12.1	-14.5	-11.1	20040	20019	20050
10	9	1.534	1.57					-12.2	-14.3	-11.6	20040	20026	20047
15	6	1.385	1.39					-12.2	-13.7	-11.5	20040	20028	20045
17.4	5	1.288	1.29					-12.2	-13.4	-11.6	20040	20027	20047
20	4	1.117	1.13					-12.3	-13.1	-11.7	20039	20028	20043
30	3	1.017	1.02					-12.2	-12.6	-11.6	20039	20033	20043
40	1		0.68					-11.9	-11.9	-11.9	20042	20042	20042
50	1		0.79					-12.0	-12.0	-12.0	20042	20042	20042
75	0												
100	0												